AD

USAAVLABS TECHNICAL REPORT 67-67

INVESTIGATION OF PROPELLER SLIPSTREAM EFFECTS ON WING PERFORMANCE

By

M. George

E. Kisielowski

November 1967

U. S. ARMY AVIATION MATERIEL LABORATORIES
FORT EUSTIS, VIRGINIA

CONTRACT DA 44-177-AMC-394(T)
DYNASCIENCES CORPORATION
BLUE BELL, PENNSYLVANIA

DEPARTMENT OF THE ARMY
U S ARMY AVIATION MATERIEL LABORATORIES
FORT EUSTIS, VIRGINIA 23604

This report has been reviewed by the U. S. Army Aviation Materiel Laboratories and is considered to be technically sound. The experimental program was undertaken to determine the validity of the modified theoretical analysis developed under Contract DA 44-177-AMC-48(T) and published as USAAVLABS Technical Report 65-81.

Task 1F125901A14231
Contract DA 44-177-AMC-394(T)
USAAVLABS Technical Report 67-67
November 1967

INVESTIGATION OF PROPELLER SLIPSTREAM EFFECTS ON WING PERFORMANCE

Dynasciences Report DCR-234

by

M. George
E. Kisielowski

Prepared by

DYNASCIENCES CORPORATION
Blue Bell, Pennsylvania

for

U. S. ARMY AVIATION MATERIEL LABORATORIES
FORT EUSTIS, VIRGINIA

SUMMARY

A theoretical and experimental study was conducted to determine the effects of propeller slipstream on wing performance.

Previously developed theoretical analyses were expanded and modified to account for radial variation of the propeller slipstream velocity.

The experimental program consisted of wind tunnel tests conducted with a motor-propeller system mounted on a semi-span wing model. The wing model utilized has a chord to propeller diameter of 0.46, an aspect ratio of 6.37 (3.18 for semispan), a taper ratio of 1.0, and a NACA 0015 airfoil section. The wing model has eight floating wing segments with and without a 45-degree simulated split flap. Located within each floating wing segment is a three-component strain gage balance to provide measurements of lift, drag, and pitching moment. The measurements of total wing lift, drag, and pitching moment were obtained with the six-component main wind tunnel balance. The test data obtained included the effects of the variation of propeller slipstream velocity by utilizing two propellers of different geometries. Propeller rotation for all tests was down at the wing tip.

The experimental and theoretical results are compared; in general, good correlation was observed.

The results obtained from this investigation substantiate the feasibility of the segmented wing approach for the measurement of the spanwise variation of aerodynamic forces and moments. In addition, it is also shown that significant increases in wing lift can be achieved by suitable propeller and wing design.

FOREWORD

This report presents the results of an investigation of the effect of propeller slipstream on wing performance.

The work was performed by the Dynasciences Corporation, Blue Bell, Pennsylvania, for the U. S. Army Aviation Materiel Laboratories (USAAVLABS), Fort Eustis, Virginia, under Contract DA 44-177-AMC-394(T) during the period from March 1966 through May 1967.

Mr. William Sickles was the Army technical representative. His contribution to this work is gratefully acknowledged. Acknowledgement is also extended to Mr. L. Cherry and other North American Aviation tunnel personnel for their cooperation during the testing phase of this program.

The following Dynasciences Corporation personnel authored or contributed to this report:

Mr. M. George - Project Engineer
Mr. E. Kisielowski - Manager, Aerodynamics
Mr. H. Weiss - Mechanical Engineer
Mr. T. Estes - Aeronautical Engineer
Dr. A. A. Perlmutter - Senior Vice-President

TABLE OF CONTENTS

ILLUSTRATIONS

LIST OF SYMBOLS

A_{m_i}	coefficients of infinite series solution for velocity potential
A_p	propeller disc area, ft.^{2}
A_t	tunnel cross-sectional area, ft.^{2}
AR	wing aspect ratio
a	lift curve slope of a wing of finite span, per radian
a_o	curve slope of infinite aspect ratio wing, per radian
a_{ij}	constants as defined in the text
B_{m_i}	coefficients of infinite series solution for velocity potential
b	wing span, ft.
b_s	distance from wing root to slipstream $\mathfrak{C}$
b_{ij}	constants as defined in the text
C_{m_i}	coefficients of infinite series solution for velocity potential
c	wing chord, ft.
c_f	flap chord, ft.
C_D	drag coefficient, based on wing area and q_o
C_{d_s}	local drag coefficient, based on segment area and q_s
C_{D_s}	wing drag coefficient, based on wing area and q_s

C_{D_s}'	total drag coefficient of wing-propeller configuration, based on q_s
$C_{D_{i_s}}$	wing basic induced drag coefficient, based on q_s
C_{D_O}	wing section profile drag coefficient outside propeller slipstream
$C_{D_{O(s)}}$	airfoil section profile drag coefficient within propeller slipstream
$C_{D_{O_{ss}}}$	profile drag coefficient of wing area immersed in slipstream, based on q_s
$C_{D_{O_{Ws}}}$	profile drag coefficient of wing area not immersed in slipstream, based on q_s
$C_{D_{is}}$	induced drag coefficient increment due to lift coefficient increment of wing area immersed in slipstream, based on q_s
$C_{D_{Ls}}$	contribution to wing drag coefficient by component of lift coefficient increment, based on q_s
C_h	wing chord force, lb.
C_{ℓ_w}	basic wing local lift coefficient, based on q_o
C_{ℓ_s}	local lift coefficient increment due to slipstream, based on segment area and q_s
C_{ℓ_i}	local lift coefficient within a slipstream zone, based on q_o
C_L	lift coefficient, based on wing area and q_o
C_{L_s}'	total lift coefficient of wing-propeller configuration, based on q_s

C_{L_s}	wing lift coefficient, based on wing area and q_s
C_{L_W}	basic wing lift coefficient, based on q_o
ΔC_{L_s}	lift coefficient increment of wing area immersed in propeller slipstream, based on q_s
C_{m_s}	local pitching moment coefficient, based on q_s
C_{M_s}	total wing pitching moment coefficient, based on q_s
C_{T_s}	propeller thrust coefficient, based on q_s, defined as $T_p/q_s A_p$
C_Q	propeller torque coefficient, $Q/\rho n^2 D^5$
C_x	propeller blade chord, inches
D_{m_i}	coefficients of infinite series solution for velocity potential
D_p	propeller diameter, ft.
D_u	measured uncorrected drag, lb.
$D_{1,2,3,\ldots}$	constants as defined in the text
i_w	wing geometric incidence angle, radians
J	propeller advance ratio, Vo/nD
K_L	slipstream lift coefficient parameter as defined in the text
K_1, K_2,...	parameters as defined in the text
L	lift force, normal to the free stream velocity vector

n	propeller rotational speed, r.p.s.
N	force perpendicular to wing chord, lb.
N_p	number of propellers
P_1, P_2,...	pressure output signals from 3-D probes, p.s.f.
q	local dynamic pressure, p.s.f.
q_c	corrected free stream dynamic pressure, $\frac{1}{2} \rho_o V_o^2$, p.s.f.
q_s	slipstream dynamic pressure, $\frac{1}{2} \rho V_s^2$, p.s.f.
q_o	free stream dynamic pressure
q_u	calibrated free stream dynamic pressure, p.s.f.
Q	propeller torque, ft./lb.
R	propeller radius, ft.
R_n	Reynolds number
r	radius to any point within the propeller slipstream, ft
$r_i \ldots r_n$	radii of slipstream velocity zones, ft.
r_s, r_1	radius of fully contracted propeller slipstream, ft.
S	wing area, ft.^{2}
$S_1, \ldots 8$	area of instrumented wing segment, ft.^{2}
T_p	propeller thrust, lb.

u	average propeller induced velocity component in fully developed propeller slipstream, feet per second
$u_i \ldots u_n$	propeller induced velocities in slipstream velocity zones, feet per second
V_o	free stream velocity, feet per second
V_s	average velocity of fully developed slipstream, feet per second
$V_i \ldots V_n$	slipstream velocities in velocity zones, feet per second
y	spanwise distance from fuselage centerline, ft.
y_s	spanwise distance from center of slipstream (positive in direction towards wing tip), ft.
α	effective angle of attack of wing without slipstream, radians
α_{LO}	airfoil section angle of zero lift, radians
α_s	effective angle of attack of wing immersed in propeller slipstream, radians
α_i	local angle of attack of wing elements immersed in propeller slipstream, radians
α_T	angle of attack of propeller thrust axis, radians
α_u	uncorrected wing geometric angle of attack, radians
α_w	wing geometric angle of attack without propeller slipstream, deg.
$\Delta\alpha_Q$	incremental angle of attack due to slipstream rotation, radians

$\Delta\alpha\delta_f$	incremental angle of attack due to trailing edge flap deflection, radians
δ_f	trailing edge flap deflection angle, deg.
ϵ_p, ϵ_s, ϵ_w	blockage correction factors used in tunnel data
$\eta_i \ldots \eta_n$	ratio of radii of slipstream velocity zones
θ	generalized polar coordinate angle, radians
θ_p	pitch angle of slipstream obtained with 3-D probes, degrees
θ_x	propeller blade pitch angle, degrees
$\mu_i \ldots \mu_n$	ratio of free stream to jet velocity (V_i/V_o)
ρ	mass density of air, slugs per cubic foot
ρ_o	mass density of air, standard sea level conditions, slugs per cubic foot
$\Phi_i \ldots \Phi_n$	velocity potentials within propeller slipstream
Φ_{si}	upper surface velocity potential at wing trailing edge.
ϕ_i	slipstream induced angle measured from propeller thrust axis, radians
ψ	yaw angle of slipstream obtained with 3-D probes, degrees

SUBSCRIPTS

i, j	0,1,2,3,...n integer pertaining to velocity zones in propeller slipstream
m	1,2,3,... integer pertaining to infinite series
Γ	pertaining to circulation flow about wing

I. INTRODUCTION

The aerodynamics of wings immersed in propeller slipstreams represents a vital aspect of the performance characteristics of tilt-wing VTOL aircraft. In previous investigations performed by Dynasciences Corporation (References 1 and 2), relatively simple analytical techniques were developed for predicting the performance of wings partially or totally immersed in the propeller slipstream. These investigations showed that an increase in wing lift can be obtained with an appropriate radial velocity distribution within the propeller slipstream.

The program reported herein was undertaken to define more fully the effect of slipstream distribution on wing performance and to give further insight into the stall characteristics of the slipstream-immersed wing. This was attained by a combined analytical and experimental study.

The analytical effort of this program consisted of a modification and expansion of the previously developed theory (Reference 1) to approximate more closely the variations of the induced velocity distribution within the propeller slipstream. This was done by considering that the propeller slipstream consisted of four concentric velocity zones with the velocity in each zone being uniform. A computer program was developed which provides numerical solutions for wing lift as a function of total propeller thrust and slipstream velocity distribution.

The experimental phase of the program was conducted with a specially designed and fabricated semispan, segmented wing model. The tests were performed in the low-speed North American Aviation wind tunnel facilities.

The results of the theoretical investigation are presented in Section II of this report. Section III contains the experimental results and a comparison of the theory with the test data.

Tuft photographs obtained during the tests are presented in the appendix.

II. THEORETICAL ANALYSIS

A. GENERALIZED EQUATIONS

In References 1 and 2, a theory is presented for the determination of the lift and drag of a wing partially or totally immersed in propeller slipstream. The analysis which utilizes the basic concepts of the small aspect ratio theory of Reference 3 results in the following expression for the spanwise lift distribution:

$$\frac{\partial L_i}{\partial y} = 2\rho V_i \Phi_{si} \tag{1}$$

where V_i is the local slipstream velocity, and Φ_{si} is the upper surface velocity potential at the wing trailing edge.

In the analysis of References 1 and 2, the velocity potential Φ_{si} is obtained by solving the two-dimensional Laplace equation with suitable boundary conditions for the case in which it is assumed that the slipstream consists of one or two concentric zones of uniform velocity. Using the two-zone analysis, it is shown in Reference 2 that an increase in lift can be achieved if the inner zone possesses a higher velocity than the outer zone of the slipstream.

In the analysis presented herein, the same concept is applied for a multizone slipstream, and a computer program is prepared for a four-zone analysis.

As in the previous work, it is assumed that the flow is inviscid, irrotational, and axisymmetric within each zone as well as outside the slipstream. The notation utilized is presented in Figure 1. The velocities V_0, $V_1 \ldots V_i$, V_n pertain to zones 0, 1, 2, ...n, etc., and the radii r_0, $r_1 \ldots r_i$, r_n are the distances to the outer boundary of each zone. The subscript 0 refers to the free stream outside of the slipstream, and the subscript n refers to the innermost zone of the slipstream.

The two-dimensional Laplace equation in polar coordinate for the i^{th} zone is given by

$$\frac{\partial^2 \Phi_i}{\partial r^2} + \frac{1}{r}\frac{\partial \Phi_i}{\partial r} + \frac{1}{r^2}\frac{\partial^2 \Phi_i}{\partial \theta^2} = 0 \qquad (2)$$

The general solution to equation (2) is

$$\Phi_i = \sum_{m=0}^{\infty} (o_{m_i} r^m \cos m\theta + b_{m_i} r^m \sin m\theta + c_{m_i} r^{-m} \cos m\theta + d_{m_i} r^{-m} \sin m\theta) \qquad (3)$$

where

m = 1, 2, 3, 4..., an integer representing terms of infinite series

i = 0, 1, 2, 3...n, an integer pertaining to each velocity zone as shown in Figure 1

Equation (3) can be rewritten in its nondimensionalized form as follows:

$$\Phi_i = A_{o_i} + \sum_{m=1}^{\infty} \left[A_{m_i} \left(\frac{r}{r_1}\right)^m \cos m\theta + B_{m_i} \left(\frac{r}{r_1}\right)^m \sin m\theta + C_{m_i} \left(\frac{r}{r_1}\right)^{-m} \cos m\theta + D_{m_i} \left(\frac{r}{r_1}\right)^{-m} \sin m\theta \right] \qquad (4)$$

B. BOUNDARY CONDITIONS

The solution for the velocity potential Φ_i, as given by equation (4), can be obtained by satisfying the appropriate boundary conditions of the flows. These conditions are as follows:

1. The velocity potential outside the propeller slipstream Φ_0 tends to zero as r tends to infinity:

$$\Phi_0 = 0, \text{ when } r \longrightarrow \infty \tag{5}$$

2. The velocity potential at the center of the propeller slipstream is finite:

$$\Phi_n = \text{constant, when } r = 0 \tag{6}$$

3. The normal velocity component at the wing surface must be zero. This implies that for $\theta = 0$ or $Z = 0$,

$$\frac{\partial \Phi_i}{\partial Z} = -V_i \alpha_i = \text{constant} \tag{7}$$

4. The jet boundaries are assumed to be streamlines of the flow in each zone. This implies that the flow between two adjacent velocity zones must be tangent at the boundary. This tangency condition at each jet boundary of $r = r_{i+1}$ can be expressed as follows:

$$V_{i+1} \frac{\partial \Phi_i}{\partial r} = V_i \frac{\partial \Phi_{i+1}}{\partial r} \tag{8}$$

5. The pressure on each side of the jet boundary must be the same. This condition for any jet boundary defined by $r = r_{i+1}$ yields

$$V_i \Phi_i = V_{i+1} \Phi_{i+1} \tag{9}$$

C. THE COEFFICIENTS OF THE INFINITE SERIES

Using the above boundary conditions, we will now proceed to determine the coefficients $Am_i \ldots Dm_i$ of the infinite series solution (equation (4)) for the velocity potential in each velocity zone.

Thus, applying the boundary condition represented by equation (5) to equation (4), we obtain

$$Ao_0 = Am_0 = Bm_0 = 0 \tag{10}$$

Applying the boundary condition expressed by equation (6), we obtain

$$Cm_n = Dm_n = 0 \tag{11}$$

Using the basic relationship between Cartesian and polar coordinate systems, i.e., $Z = r \sin\theta$ and $Y = r \cos\theta$, it can be shown that

$$\left(\frac{\partial \Phi_i}{\partial Z}\right)_{\theta=0} = \frac{1}{r}\left(\frac{\partial \Phi_i}{\partial \theta}\right)_{\theta=0} \tag{12}$$

Thus, differentiating equation (4) with respect to θ and applying the boundary conditions expressed by equation (7), we obtain

$$\left(\frac{\partial \Phi_i}{\partial Z}\right)_{\theta=0} = \sum_{m=1}^{\infty} \left[mBm_i \left(\frac{r^{m-1}}{r_1^{m}}\right) + mDm_i \left(\frac{r^{-m-1}}{r_1^{-m}}\right) \right] \tag{13}$$

$$= -V_i \alpha_i = \text{constant}$$

Examining equation (13), it can be noted that the function $(\partial\Phi_i/\partial Z)_{\theta=0}$ will be a constant, provided that

$$Dm_i = 0 \text{ for all } m \tag{14}$$

and that

$$Bm_i = 0 \text{ for } m \geq 1 \tag{15}$$

It follows also that

$$B_{1i} = -r_i V_i \alpha_i \text{ for } i \geq 1 \tag{16}$$

Substituting equations (10) through (16) into equation (4), we obtain the following relationships for the velocity potentials pertaining to various velocity zones:

Oustide the propeller slipstream (i = 0),

$$\Phi_0 = \sum_{m=1}^{\infty} \left(\frac{r}{r_1}\right)^{-m} \left[Cm_0 \cos m\theta + Dm_0 \sin m\theta\right] \tag{17}$$

Within the propeller slipstream, except the central velocity zone ($i \geq 1$),

$$\Phi_i = Ao_i - r_1 V_i \alpha_i \left(\frac{r}{r_1}\right) \sin\theta \sum_{m=1}^{\infty} \left[Am_i \left(\frac{r}{r_1}\right)^{m} + Cm_i \left(\frac{r}{r_1}\right)^{-m}\right] \cos m\theta \tag{18}$$

For the central velocity zone (i = n),

$$\Phi_n = Ao_n - r_1 V_n \alpha_n \left(\frac{r}{r_1}\right) \sin\theta + \sum_{m=1}^{\infty} Am_n \left(\frac{r}{r_1}\right)^m \cos m\theta \qquad (19)$$

Now, in order to apply the boundary conditions expressed by equation (8), it is necessary to determine the partial differential of Φ_i with respect to r . Thus, differentiating equation (4) with respect to r yields

$$\frac{\partial \Phi_i}{\partial r} = \sum_{m=1}^{\infty} \left\{ \frac{m \cos m\theta}{r_1} \left[Am_i \left(\frac{r}{r_1}\right)^{m-1} - Cm_i \left(\frac{r}{r_1}\right)^{-m-1} \right] + \frac{m \sin m\theta}{r_1} \left[Bm_i \left(\frac{r}{r_1}\right)^{m-1} - Dm_i \left(\frac{r}{r_1}\right)^{-m-1} \right] \right\} \qquad (20)$$

Using the boundary condition expressed by equation (8) together with equation (20), we obtain

$$V_{i+1} \sum_{m=1}^{\infty} \left\{ \frac{m \cos m\theta}{r_1} \left[Am_i \left(\frac{r_{i+1}}{r_1}\right)^{m-1} - Cm_i \left(\frac{r_{i+1}}{r_1}\right)^{-m-1} \right] + \frac{m \sin m\theta}{r_1} \left[Bm_i \left(\frac{r_{i+1}}{r_1}\right)^{m-1} - Dm_i \left(\frac{r_{i+1}}{r_1}\right)^{-m-1} \right] \right\}$$

$$= V_i \sum_{m=1}^{\infty} \left\{ \frac{m \cos m\theta}{r_1} \left[Am_{i+1} \left(\frac{r_{i+1}}{r_1}\right)^{m-1} - Cm_{i+1} \left(\frac{r_{i+1}}{r_1}\right)^{-m-1} \right] + \frac{m \sin m\theta}{r_1} \left[Bm_{i+1} \left(\frac{r_{i+1}}{r_1}\right)^{m-1} - Dm_{i+1} \left(\frac{r_{i+1}}{r_1}\right)^{-m-1} \right] \right\} \qquad (21)$$

Equating coefficients of cos $m\theta$, equation (21), yields

$$V_{i+1} \left[Am_i \left(\frac{r_{i+1}}{r_1}\right)^{m-1} - Cm_i \left(\frac{r_{i+1}}{r_1}\right)^{-m-1} \right] = V_i \left[Am_{i+1} \left(\frac{r_{i+1}}{r_1}\right)^{m-1} - Cm_{i+1} \left(\frac{r_{i+1}}{r_1}\right)^{-m-1} \right] \qquad (22)$$

Multiplying equation (22) throughout by $\left(\frac{r_{i+1}}{r_1}\right)^{m+1}$ yields

$$V_{i+1}\left[Am_i\left(\frac{r_{i+1}}{r_1}\right)^{2m} - Cm_i\right] = V_i\left[Am_{i+1}\left(\frac{r_{i+1}}{r_1}\right)^{2m} - Cm_{i+1}\right] \quad (23)$$

It is convenient to define velocity ratios of various velocity zones as

$$\mu_i = \frac{V_0}{V_i} \quad (24)$$

or

$$\mu_{i+1} = \frac{V_0}{V_{i+1}} \quad (25)$$

Substituting equations (24) and (25) into equation (23) yields

$$\mu_i Am_i\left(\frac{r_{i+1}}{r_1}\right)^{2m} - \mu_{i+1} Am_{i+1}\left(\frac{r_{i+1}}{r_1}\right)^{2m} - \mu_i Cm_i + \mu_{i+1} Cm_{i+1} = 0 \quad (26)$$

Similarly, equating coefficients of sin $m\theta$, equation (21) yields

$$\mu_i Bm_i\left(\frac{r_{i+1}}{r_1}\right)^{2m} - \mu_{i+1} Bm_{i+1}\left(\frac{r_{i+1}}{r_1}\right)^{2m} - \mu_i Dm_i + \mu_{i+1} Dm_{i+1} = 0 \quad (27)$$

For $i = 0$, equations (26) and (27) become

$$\mu_0 Am_0 - \mu_1 Am_1 - \mu_0 Cm_0 + \mu_1 Cm_1 = 0 \quad (28)$$

$$\mu_0 Bm_0 - \mu_1 Bm_1 - \mu_0 Dm_0 + \mu_1 Dm_1 = 0 \quad (29)$$

Since $Am_0 = Bm_0$ (equation (10)), $Dm_i = 0$ (equation (14)), and $\mu_0 = 1.0$ (equation (24)) it follows that

$$Cm_0 = \mu_1 (Cm_1 - Am_1) \tag{30}$$

$$Dm_0 = -\mu_1 Bm_1 \tag{31}$$

From equation (16), it can be noted that only for $m = 1$ does there exist a constant term $B_{1_1} = -r_1 V_1 \alpha_1$; therefore, equation (31) yields

$$D_{1_0} = \mu_1 Bm_i = r_1 V_0 \alpha_1 \tag{32}$$

$$Dm_0 = 0 \text{ for } m > 1.0 \tag{33}$$

Finally, using equation (4) and applying the boundary conditions expressed by equation (9), the following relationship is obtained:

$$V_i Ao_i + V_i \sum_{m=1}^{\infty} \left[Am_i \left(\frac{r_{i+1}}{r_1}\right)^m \cos m\theta + Bm_i \left(\frac{r_{i+1}}{r_1}\right)^m \sin m\theta \right.$$

$$\left. + Cm_i \left(\frac{r_{i+1}}{r_1}\right)^{-m} \cos m\theta + Dm_i \left(\frac{r_{i+1}}{r_1}\right)^{-m} \sin m\theta \right]$$

$$= V_{i+1} Ao_{i+1} + V_{i+1} \sum_{m=1}^{\infty} \left[Am_{i+1} \left(\frac{r_{i+1}}{r_1}\right)^m \cos m\theta + Bm_i \left(\frac{r_{i+1}}{r_1}\right)^m \sin m\theta \right.$$

$$\left. + Cm_{i+1} \left(\frac{r_{i+1}}{r_1}\right)^{-m} \cos m\theta + Dm_{i+1} \left(\frac{r_{i+1}}{r_1}\right) \sin m\theta \right] \tag{34}$$

Since the coefficient Bm_i exists only for $m = 1$ and $i \geq 1.0$ (equation (14)) and the coefficient Dm_i is valid only for $m = 1$ and $i = 0$ (equation (32)), equation (34) can be rewritten as follows:

$$V_i Ao_i + V_i (B1_i + D1_i)\left(\frac{r_{i+1}}{r_1}\right) \sin\theta + V_i \sum_{m=1}^{\infty}\left[Am_i\left(\frac{r_{i+1}}{r_1}\right)^{m} + Cm_i\left(\frac{r_{i+1}}{r_1}\right)^{-m}\right]\cos m\theta$$

$$= V_{i+1}Ao_{i+1} + V_{i+1}B1_{i+1}\left(\frac{r_{i+1}}{r_1}\right)\sin\theta + V_{i+1}\sum_{m=1}^{\infty}\left[Am_{i+1}\left(\frac{r_{i+1}}{r_1}\right)^{m} + Cm_{i+1}\left(\frac{r_{i+1}}{r_1}\right)^{-m}\right]\cos m\theta \tag{35}$$

For the upper half of the slipstream, $0 \leq \theta \leq \pi$, the following expression can be utilized:

$$\sin\theta = \frac{2}{\pi} - \frac{4}{\pi}\sum_{m=2,4,6,\cdots}^{\infty}\frac{\cos m\theta}{m^2-1} \tag{36}$$

Substituting equation (36) into equation (35) yields

$$V_i Ao_i + V_i(B1_i + D1_i)\left(\frac{r_{i+1}}{r_1}\right)\frac{2}{\pi} - \frac{4}{\pi}V_i(B1_i + D1_i)\left(\frac{r_{i+1}}{r_1}\right)\sum_{m=2,4,6,\cdots}^{\infty}\frac{\cos m\theta}{m^2-1} + V_i\sum_{m=1}^{\infty}\left[Am_i\left(\frac{r_{i+1}}{r_1}\right)^{m} + Cm_i\left(\frac{r_{i+1}}{r_1}\right)^{-m}\right]\cos m\theta$$

$$= V_{i+1}Ao_{i+1} + V_{i+1}B1_{i+1}\left(\frac{r_{i+1}}{r_1}\right)\frac{2}{\pi} - \frac{4}{\pi}V_{i+1}B1_{i+1}\left(\frac{r_{i+1}}{r_1}\right)\sum_{m=2,4,6,\cdots}^{\infty}\frac{\cos m\theta}{m^2-1} + V_{i+1}\sum_{m=1}^{\infty}\left[Am_{i+1}\left(\frac{r_{i+1}}{r_1}\right)^{m} + Cm_{i+1}\left(\frac{r_{i+1}}{r_1}\right)^{-m}\right]\cos m\theta \tag{37}$$

Comparing constant terms of equation (37) and using equations (24) and (25) yields

$$Ao_{i+1} = \frac{2}{\pi} \frac{\mu_{i+1}}{\mu_i} \left[\frac{\pi}{2} Ao_i + \left(\frac{r_{i+1}}{r_1}\right)(B1_i + D1_i - \frac{\mu_i}{\mu_{i+1}} B1_{i+1}) \right] \quad (38)$$

For $i = 0$, equation (38) becomes

$$Ao_1 = \frac{2}{\pi} \frac{\mu_1}{\mu_0} \left[\frac{\pi}{2} Ao_0 + (B1_0 + D1_0 - \frac{\mu_0}{\mu_1} B1_1) \right] \quad (39)$$

Substituting equations (10), (16), (24), (25), and (32) into equation (39), we obtain

$$Ao_1 = \frac{2}{\pi} \mu_1 (r_1 Vo \alpha_1 - \frac{1}{\mu_1}(-r_1 V_1 \alpha_1) \quad (40)$$

$$Ao_1 = \frac{2}{\pi} \mu_1 r_1 Vo \alpha_1 \left(\frac{1+\mu_1^2}{\mu_1^2}\right) \quad (41)$$

For $i \geq 1.0$, equation (38) becomes

$$Ao_{i+1} = \frac{2}{\pi} \frac{\mu_{i+1}}{\mu_i} \left[\frac{\pi}{2} Ao_i + \left(\frac{r_{i+1}}{r_1}\right)(B1_i - \frac{\mu_i}{\mu_{i+1}} B1_{i+1}) \right] \quad (42)$$

Substituting equations (14), (24), and (25) into equation (42) and simplifying, we get

$$Ao_{i+1} = \frac{2}{\pi} r_1 Vo \mu_{i+1} \left[\frac{\pi}{2} \frac{Ao_i}{r_1 Vo \mu_i} + \left(\frac{r_{i+1}}{r_1}\right)\left(\frac{\mu_i^2 \alpha_{i+1} - \mu^2_{i+1} \alpha_i}{\mu_i^2 \mu^2_{i+1}}\right) \right] \quad (43)$$

Comparing coefficients of $\cos m\theta$ for all odd values of $m \geq 1.0$, equation (36) yields

$$V_i \left[Am_i \left(\frac{r_{i+1}}{r_1}\right)^{m} + Cm_i \left(\frac{r_{i+1}}{r_1}\right)^{-m} \right]$$

$$= V_{i+1} \left[Am_{i+1} \left(\frac{r_{i+1}}{r_1}\right)^{m} + Cm_{i+1} \left(\frac{r_{i+1}}{r_1}\right)^{-m} \right] \quad (44)$$

Simplifying equation (36), the following relationship is obtained:

$$\mu_{i+1} Am_i \left(\frac{r_{i+1}}{r_1}\right)^{2m} - \mu_i Am_{i+1} \left(\frac{r_{i+1}}{r_1}\right)^{2m}$$

$$+ \mu_{i+1} Cm_i - \mu_i Cm_{i+1} = 0 \quad (45)$$

For $i = 0$, equation (45) becomes

$$-Am_1 + \mu_1 Cm_0 - Cm_1 = 0 \quad (46)$$

Substituting equation (30) into equation (46) yields

$$Am_1 (1 + \mu_1^2) + Cm_1 (1 - \mu_1^2) = 0 \quad (47)$$

Finally, comparing coefficients of $\cos m\theta$ for all even values of $m \geq 2.0$, equation (37) yields

$$-\frac{4}{\pi} V_i (B_{1i} + D_{1i}) \left(\frac{r_{i+1}}{r_1}\right) \frac{1}{m^2-1} + V_i \left[Am_i \left(\frac{r_{i+1}}{r_1}\right)^{m} + Cm_i \left(\frac{r_{i+1}}{r_1}\right)^{-m} \right]$$

$$= -\frac{4}{\pi} V_{i+1} B_{i+1} \left(\frac{r_{i+1}}{r_1}\right) \frac{1}{m^2-1} + V_{i+1}\left[Am_{i+1}\left(\frac{r_{i+1}}{r_1}\right)^{m} + Cm_{i+1}\left(\frac{r_{i+1}}{r_1}\right)^{-m}\right] \tag{48}$$

Simplifying equation (48), the following relationship is obtained:

$$\mu_{i+1} Am_i \left(\frac{r_{i+1}}{r_1}\right)^{2m} - \mu_i Am_{i+1}\left(\frac{r_{i+1}}{r_1}\right)^{2m} + \mu_{i+1} Cm_i - \mu_i Cm_{i+1}$$

$$= \frac{4}{\pi}\left(\frac{r_{i+1}}{r_1}\right) \frac{\mu_{i+1}}{m^2-1}\left[B_{1_i} + D_{1_i} - \frac{\mu_i}{\mu_{i+1}} B_{1_{i+1}}\right]\left(\frac{r_{i+1}}{r_1}\right)^{m} \tag{49}$$

For $i = 0$, equation (49) becomes

$$-Am_1 + \mu_1 Cm_0 - Cm_1 = \frac{4}{\pi} \frac{\mu_1}{m^2-1}\left[D_{1_0} - \frac{1}{\mu_1} B_{1_1}\right] \tag{50}$$

Substituting equations (16), (30), and (32) into equation (50) yields

$$(1+\mu_1^2) Am_1 + (1-\mu_1^2) Cm_1 = -\frac{4}{\pi} \frac{r_1 V_0 \alpha_1}{m^2-1}\left(\frac{1+\mu^2}{\mu_1}\right) \tag{51}$$

For $i \geq 1.0$, equation (49) becomes

$$\mu_{i+1} Am_i \left(\frac{r_{i+1}}{r_1}\right)^{2m} - \mu_i Am_{i+1}\left(\frac{r_{i+1}}{r_1}\right)^{2m} + \mu_{i+1} Cm_i - \mu_i Cm_{i+1}$$

$$= \frac{4}{\pi}\left(\frac{r_{i+1}}{r_1}\right) \frac{\mu_{1+i}}{m^2-1}\left[B_{1_i} - \frac{\mu_i}{\mu_{i+1}} B_{1_{i+1}}\right]\left(\frac{r_{i+1}}{r_1}\right)^{m} \tag{52}$$

Substituting equations (16), (24), and (25) into equation (52) yields

$$\mu_{i+1} Am_i \left(\frac{r_{i+1}}{r_1}\right)^{2m} - \mu_i Am_{i+1} \left(\frac{r_{i+1}}{r_1}\right)^{2m} + \mu_{i+1} Cm_i - \mu_i Cm_{i+1}$$

$$= \frac{4}{\pi} \frac{r_{i+1} Vo}{m^2 - 1} \left(\frac{r_{i+1}}{r_1}\right)^{m} \left(\frac{\mu_i}{\mu_{i+1}} \alpha_{i+1} - \frac{\mu_{i+1}}{\mu_i} \alpha_i\right) \tag{53}$$

D. SOLUTION FOR THE FOUR-ZONE PROPELLER SLIPSTREAM ANALYSIS

Although the analysis presented in sections A through C applies to any number of the velocity zones within the propeller slipstream, the explicit solution is herein obtained for the four-zone analysis. This is achieved by determining the coefficients Ao_i, Am_i, Bm_i, Cm_i, and Dm_i of the infinite series for each velocity zone $i = 0, 1, 2, 3,$ and 4. Thus, using equations (10), (41), and (43), the constant terms of the infinite series (equation (4)) are as follows:

$$Ao_0 = 0 \tag{54}$$

$$Ao_1 = \frac{2}{\pi} \mu_1 r_1 \alpha_1 Vo \left(\frac{1+\mu_1^2}{\mu_1^2}\right) \tag{55}$$

$$Ao_2 = \frac{2}{\pi} r_1 Vo \mu_2 \left[\frac{1+\mu_1^2}{\mu_1^2} \alpha_1 + \left(\frac{r_2}{r_1}\right) \left(\frac{\mu_1^2 \alpha_2 - \mu_2^2 \alpha_1}{\mu_1^2 \mu_2^2}\right)\right] \tag{56}$$

$$Ao_3 = \frac{2}{\pi} r_1 Vo \mu_3 \left[\frac{1+\mu_1^2}{\mu_1^2} \alpha_1 + \left(\frac{r_2}{r_1}\right) \left(\frac{\mu_1^2 \alpha_2 - \mu_2^2 \alpha_1}{\mu_1^2 \mu_2^2}\right) + \left(\frac{\mu_2^2 \alpha_3 - \mu_3^2 \alpha_2}{\mu_2^2 \mu_3^2}\right)\right] \tag{57}$$

$$Ao_4 = \frac{2}{\pi} r_1 Vo \mu_4 \left[\frac{1+\mu_1^2}{\mu_1^2} \alpha_1 + \left(\frac{r_2}{r_1}\right) \left(\frac{\mu_1^2 \alpha_2 - \mu_2^2 \alpha_1}{\mu_1^2 \mu_2^2}\right)\right.$$

$$+\left(\frac{r_3}{r_1}\right)\left(\frac{\mu_2^2\alpha_3-\mu_3^2\alpha_2}{\mu_2^2\,\mu_3^2}\right)+\left(\frac{r_4}{r_1}\right)\left(\frac{\mu_3^2\alpha_4-\mu_4^2\alpha_3}{\mu_3^2\,\mu_4^2}\right)\Bigg] \tag{58}$$

The coefficients Bm_i exist only for $m = 1$ and $i \geq 1.0$ (inside propeller slipstream). These coefficients for all velocity zones can be obtained directly from equation (16) by using $i = 1, 2, 3$, and 4. Similarly, the coefficients Dm_i are all zero except for $m = 1$ and $i = 0$ (outside propeller slipstream). This coefficient is given by equation (32).

Finally, the coefficients Am_i and Cm_i can be obtained from the simultaneous solutions of equations (26) and (45) for all odd values of m or equations (26) and (53) for all even values of m .

Examining equations (26) and (45) for odd values of m , it can be noted that there exists only a trivial solution of $Am_i = Am_{i+1} = Cm_i = Cm_{i+1} = 0$.

Therefore, equations (26) and (53) for even values of m must be utilized to obtain a unique solution for these coefficients. Thus, by using equations (30) and (51) for $i = 0$ and equations (26) and (53) for $i \geq 1.0$, we obtain the following set of eight simultaneous equations with eight unknowns:

$$Cm_0 = \mu_1(Cm_1 - Am_1) \tag{59}$$

$$\mu_1 Am_1\left(\frac{r_2}{r_1}\right)^{2m} - \mu_2 Am_2\left(\frac{r_2}{r_1}\right)^{2m} - \mu_1 Cm_1 + \mu_2 Cm_2 = 0 \tag{60}$$

$$\mu_2 Am_2\left(\frac{r_3}{r_1}\right)^{2m} - \mu_3 Am_3\left(\frac{r_3}{r_1}\right)^{2m} - \mu_2 Cm_2 + \mu_3 Cm_3 = 0 \tag{61}$$

$$\mu_3 Am_3\left(\frac{r_4}{r_1}\right)^{2m} - \mu_4 Am_4\left(\frac{r_4}{r_1}\right)^{2m} - \mu_3 Cm_3 = 0 \tag{62}$$

$$(1+\mu_1^2)Am_1 + (1-\mu_1^2)\,Cm_1 = -\frac{4}{\pi}\,\frac{r_1 Vo\alpha_1}{m^2-1}\,\left(\frac{1+\mu_1^2}{\mu_1}\right) \tag{63}$$

$$\mu_2 Am_1\left(\frac{r_2}{r_1}\right)^{2m} - \mu_1 Am_2\left(\frac{r_2}{r_1}\right)^{2m} + \mu_2 Cm_1 - \mu_1 Cm_2$$

$$= \frac{4}{\pi}\,\frac{r_2 Vo}{m^2-1}\left(\frac{r_2}{r_1}\right)^m\left(\frac{\mu_1}{\mu_2}\alpha_2 - \frac{\mu_2\alpha_1}{\mu_1}\right) \tag{64}$$

$$\mu_3 Am_2\left(\frac{r_3}{r_1}\right)^{2m} - \mu_2 Am_3\left(\frac{r_3}{r_1}\right)^{2m} + \mu_3 Cm_2 - \mu_2 Cm_3$$

$$= \frac{4}{\pi}\,\frac{r_3 Vo}{m^2-1}\left(\frac{r_3}{r_1}\right)^m\left(\frac{\mu_2}{\mu_3}\alpha_3 - \frac{\mu_3}{\mu_2}\alpha_2\right) \tag{65}$$

$$\mu_4 Am_3\left(\frac{r_4}{r_1}\right)^{2m} - \mu_3 Am_4\left(\frac{r_4}{r_1}\right)^{2m} + \mu_4 Cm_3$$

$$= \frac{4}{\pi}\,\frac{r_4 Vo}{m^2-1}\left(\frac{r_4}{r_1}\right)^m\left(\frac{\mu_3}{\mu_4}\alpha_3 - \frac{\mu_4}{\mu_3}\alpha_3\right) \tag{66}$$

Equations (60) through (66) are independent of Cm_0. Therefore, these seven equations can be first solved for the seven unknowns Am_1, Am_2, Am_3, Am_4, Cm_1, Cm_2, and Cm_3. After performing the required algebraical manipulation, the following solutions are obtained:

$$Am_4 = \frac{8\eta_2^{2m}\eta_3^{2m}\eta_4^{2m}K_1}{\mu_1 D_4} - \frac{4\eta_3^{2m}\eta_4^{2m}D_1 K_2}{\mu_2 D_4}$$

$$- \frac{2\eta_4^{2m}D_2 K_3}{\mu_3 D_4} - \frac{D_3 K_4}{\mu_4 D_4} \tag{67}$$

$$Am_3 = \frac{\eta_4^{2m}\left(\frac{\mu_4}{\mu_3}\right)}{D_3}\Big[a_{23}\eta_2^{2m}(b_{01}b_{12} + a_{01}a_{12}\eta_2^{2m})$$

$$+ b_{23}\eta_3^{2m}(b_{01}a_{12} + a_{01}b_{12}\eta_2^{2m})\Big]\,Am_4$$

$$+ \frac{4\eta_2^{2m}\eta_3^{2m}K_1}{\mu_1 D_3} - \frac{2\eta_3^{2m} D_1 K_2}{\mu_2 D_3} - \frac{D_2 K_3}{\mu_3 D_3} \tag{68}$$

$$Am_2 = \frac{\frac{\mu_3}{\mu_2}(\eta_3^{2m} - \eta_4^{2m})(b_{01}a_{12} + a_{01}b_{12}\eta_2^{2m})}{D_2} Am_3$$

$$+ \eta_4^{2m} \frac{\frac{\mu_3}{\mu_2}(b_{01}a_{12} + a_{01}b_{12}\eta_2^{2m})}{D_2} Am_4 + \frac{2\eta_2^{2m} K_1}{\mu_1 D_2} - \frac{D_1 K_2}{\mu_2 D_2} \tag{69}$$

$$Am_1 = \frac{a_{01}\frac{\mu_2}{\mu_1}(\eta_2^{2m} - \eta_3^{2m})Am_2}{D_1} + \frac{a_{01}\frac{\mu_3}{\mu_1}(\eta_3^{2m} - \eta_4^{2m})Am_3}{D_1}$$

$$+ \frac{a_{01}\frac{\mu_4}{\mu_1}\eta_4^{2m}Am_4}{D_1} + \frac{K_1}{\mu_1 D_1} \tag{70}$$

$$Cm_1 = \eta_2^{2m}Am_1 - \frac{\mu_2}{\mu_1}(\eta_2^{2m} - \eta_3^{2m})Am_2 - \frac{\mu_3}{\mu_1}(\eta_3^{2m} - \eta_4^{2m})Am_3$$

$$- \frac{\mu_4}{\mu_1}\eta_4^{2m}Am_4 \tag{71}$$

$$Cm_2 = \eta_3^{2m}Am_2 - \frac{\mu_3}{\mu_2}(\eta_3^{2m} - \eta_4^{2m})Am_3 - \frac{\mu_4}{\mu_2}\eta_4^{2m}Am_4 \tag{72}$$

$$Cm_3 = \eta_4^{2m}Am_3 - \frac{\mu_4}{\mu_3}\eta_4^{2m}Am_4 \tag{73}$$

where $\eta_i = \frac{r_i}{r_i}$, $\mu_i = \frac{V_0}{V_i}$

and $a_{ij} = (\frac{\mu_i}{\mu_j} - \frac{\mu_j}{\mu_i})$, $b_{ij} = (\frac{\mu_1}{\mu_j} + \frac{\mu_j}{\mu_i})$ $i, j = 1,2,3,4$

The constants D_i and K_i are given by

$$D_1 = b_{01} + a_{01}\eta_2^{2m} \tag{74}$$

$$D_2 = b_{01}b_{12} + a_{01}a_{12}\eta_2^{2m} + \left(\frac{\eta_3}{\eta_2}\right)^{2m}(b_{01}a_{12} + a_{01}b_{12}\eta_2^{2m}) \tag{75}$$

$$D_3 = b_{23}(b_{01}b_{12} + a_{01}a_{12}\eta_2^{2m}) + \left(\frac{\eta_4}{\eta_3}\right)^{2m} a_{23}(b_{01}b_{12} + a_{01}a_{12}\eta_2^{2m})$$

$$+ \frac{\eta_4^{4m}}{(\eta_2\eta_3)^{2m}} a_{23}(b_{01}a_{12} + a_{01}b_{12}\eta_2^{2m})$$

$$+ \left(\frac{\eta_4}{\eta_3}\right)^{2m} b_{23}(b_{01}a_{12} + a_{01}b_{12}\eta_2^{2m}) \tag{76}$$

$$D_4 = b_{23}b_{34}(b_{01}b_{12} + a_{01}a_{12}\eta_2^{2m}) + \left(\frac{\eta_4}{\eta_3}\right)^{2m} a_{23}a_{34}(b_{01}b_{12} + a_{01}a_{12}\eta_2^{2m})$$

$$+ \left(\frac{\eta_3}{\eta_4}\right)^{2m} a_{23}b_{34}(b_{01}a_{12} + a_{01}b_{12}\eta_2^{2m})$$

$$+ \left(\frac{\eta_4}{\eta_3}\right)^{2m} a_{23}b_{34}(b_{01}a_{12} + a_{01}b_{12}\eta_2^{2m}) \tag{77}$$

$$K_1 = -\frac{4r_1V_0}{\pi(m^2-1)}\left(\frac{1+\mu_1^2}{\mu_1}\right)\alpha_1 \tag{78}$$

$$K_2 = \frac{4r_1V_0\eta_2^{m+1}}{\pi(m^2-1)}\left(\frac{\mu_1}{\mu_2}\alpha_2 - \frac{\mu_2}{\mu_1}\alpha_1\right) \tag{79}$$

$$K_3 = \frac{4r_1V_0\eta_3^{m+1}}{\pi(m^2-1)}\left(\frac{\mu_2}{\mu_3}\alpha_3 - \frac{\mu_3}{\mu_2}\alpha_2\right) \tag{80}$$

$$K_4 = \frac{4r_1V_0\eta_4^{m+1}}{\pi(m^2-1)}\left(\frac{\mu_3}{\mu_4}\alpha_4 - \frac{\mu_4}{\mu_3}\alpha_3\right) \tag{81}$$

E. ANGLES OF ATTACK IN SLIPSTREAM ZONES

The angles of attack in the slipstream zones, α_i, which appear in the constants K_1, K_2,...K_N are functions of the following:

1. Wing geometric incidence angle relative to the propeller axis.
2. Radial distribution of the axial component of the slipstream velocity.
3. Slipstream swirl.
4. Effect of wing flap.
5. Wing camber.

Using the nomenclature of Figure 2, we obtain

$$\alpha_i = i_w - \alpha_{LO} + \Delta\alpha_{\delta_f} + \phi_i + \Delta\alpha_{a_i} \tag{82}$$

The geometric wing incidence relative to the propeller axis (i_w) and the zero lift wing angle of attack (α_{LO}) are generally known from the design and the airfoil characteristics of the selected wing, respectively.

The contribution of a wing flap to the local wing angle of attack can be determined using Reference 4. Thus,

$$\Delta\alpha_{\delta_f} = \tan^{-1}\left[\frac{\frac{C_f}{C}\sin\delta_f}{(1-\frac{C_f}{C})+\frac{C_f}{C}\cos\delta_f}\right] \tag{83}$$

The angle of attack (ϕ_i) due to the induced velocity in the propeller slipstream can be determined as follows:

Using Figure 2, we obtain the resultant velocity within each velocity zone:

$$V_i = \sqrt{V_0^2 + 2 V_0 u_i \cos \alpha_T + u_i^2} \tag{84}$$

The induced angle, ϕ_i , can then be expressed as

$$\phi_i = \sin^{-1}\left[\frac{V_0 \sin \alpha_T}{\sqrt{V_0^2 + 2V_0 u_i \cos \alpha_T + u_i^2}}\right] \tag{85}$$

The induced velocity, u_i , is a function of the propeller thrust distribution. In order to simplify the analysis, however, it will be assumed that the thrust per unit disc area is a constant. Based on an equivalent axial flow $V_0 \cos \alpha_T$, the induced velocity, u_i , is then given by

$$u_i = u = -V_0 \cos \alpha_T + \sqrt{(V_0 \cos \alpha_T)^2 + \frac{T}{\frac{1}{2}\rho A_P}} \tag{86}$$

The largest aerodynamic contribution to the local angle of attack, at realistic values of thrust coefficient ($C_{T_S} > 0.5$), is that due to propeller slipstream rotation. From Reference 2, the swirl angle due to slipstream rotation is given by

$$\Delta \alpha_{Q_i} = \left[\frac{32\, C_Q \sqrt{1 - C_{T_S}}}{\pi J^2 \left(\cos \alpha_T + \sqrt{\cos^2 \alpha_T + \frac{C_{T_S}}{1 - C_{T_S}}}\right)}\right] \frac{r}{r_1} \tag{87}$$

F. PROPELLER SLIPSTREAM CONTRIBUTION TO WING LIFT

The surface potentials, Φ_{s_i} , are obtained from equations (18) and (19) by letting $\theta = 0$. Hence,

$$\Phi_{si} = Ao_i + \sum_{m=1}^{\infty}\left[Am_i \left(\frac{r}{r_1}\right)^m + Cm_i \left(\frac{r}{r_1}\right)^{-m}\right] \tag{88}$$

$$\Phi_{sn} = Ao_n + \sum_{m=1}^{\infty} Am_n \left(\frac{r}{r_1}\right)^m \tag{89}$$

The lift coefficient, based on the free stream dynamic pressure (q_o) for the wing section located between the radial distances r_i and r_{i+1}, is given by

$$C_{\ell_i} = \frac{4}{\mu_i V_o C} \int_{\frac{r_{i+1}}{r_1}}^{\frac{r_i}{r_1}} \Phi_{s_i} \, d\left(\frac{r}{r_1}\right) \tag{90}$$

Performing the integration of equation (90), the lift coefficient for each velocity zone is as follows:

$$C_{\ell_i} = \frac{8 r_1}{\pi C} \left(\frac{\mu_{i-1}}{\mu_i} - \frac{\mu_i}{\mu_{i-1}}\right) \frac{\eta_i^2}{\mu_{i-1}\,\mu_i} \alpha_i + \frac{4}{\mu_i V_o} \sum_{m=2,4,6}^{\infty} \left[\frac{Am_i}{m+1}\left(\eta_i^{m+1} - \eta_{i+1}^{m+1}\right) - \frac{Cm_i}{m-1}\left(\eta_i^{-m-1} - \eta_{i+1}^{-m+1}\right)\right] \tag{91}$$

The total wing lift coefficient within the propeller slipstream is then given as

$$C_L = \sum_{i=1}^{i=4} C_{\ell_i} \tag{92}$$

Similar to the method utilized in Reference 1, the total lift coefficient increment due to the propeller slipstream based on slipstream dynamic pressure, q_s, is given by

$$\Delta C_{L_s} = \left[C_L - (C_L)_{\mu_i = 1}\right] \frac{q_o}{q_s} \tag{93}$$

Equation (93) was solved with the aid of a digital computer. The results are presented in Figure 3 as plots of the lift factor $K_L = \Delta C_{L_s} C/r_1 a_s$ as a function of propeller thrust coefficient C_{T_s} for six different velocity distributions in the propeller slipstream. Each of these velocity distributions corresponds to a constant design value of propeller thrust.

The results presented for the uniform slipstream velocity distribution ② correspond to those obtainable with the one-zone analysis of Reference 1. Figure 3 shows the comparison of one- and four-zone analyses for both idealized velocity distributions (① , ② , and ③) and more realistic velocity distributions (④ , ⑤ , and ⑥). It can be noted that the one-zone solution yields results within ±6% of those obtainable from the four-zone analysis.

Furthermore, comparing distributions ④ , ⑤ , and ⑥ (four-zone results), it can be noted that distribution ④ (with maximum value towards the center of the propeller) yields a higher lift factor K_L than distribution ⑤ (uniform) or distribution ⑥ (with maximum value towards propeller tip). This conclusion further confirms the results which are based on a two-zone analysis of Reference 2.

G. TOTAL WING LIFT AND DRAG

A rapid method is herein presented for the evaluation of the wing lift and drag inside and outside the propeller slipstream. This method utilizes the computer results based on the four-zone analysis shown in Figure 3, as well as a number of specially developed charts to facilitate numerical computations.

1. Spanwise Distribution of Wing Lift

The local slipstream coefficient based on the slipstream dynamic pressure is given by

$$C_{l_s} = \frac{q_o}{q_s}\left(C_{l_w} + C_{l_{w_s}}\right) + \Delta C_{l_s} \qquad (94)$$

The values of C_{ℓ_w}, $C_{\ell_{w_s}}$, and ΔC_{ℓ_s} can be obtained from the following expressions:

$$C_{\ell_w} = K_5 \left[\left(\frac{o}{o_o} \right) o_o \alpha \right] \tag{95}$$

$$C_{\ell_{w_s}} = K_5 \left[\left(\frac{o}{o_o} \right) o_o \alpha_i \right] \tag{96}$$

$$\Delta C_{\ell_s} = K_6 \left[(0.211 \frac{r_s}{C}) C_{T_s} \alpha_i \right] \tag{97}$$

The parameters K_5, K_6, and r_s/D_p are given as

$$K_5 = \frac{1}{2} + \frac{2}{\pi} \sqrt{1 - \left(\frac{y}{b/2} \right)^2} \tag{98}$$

$$K_6 = \left(\frac{1}{y_s/r_s} - \frac{y_s}{r_s} \right) \ell_n \left[\frac{1 + y_s/r_s}{1 - y_s/r_s} \right] \tag{99}$$

$$\frac{r_s}{D_p} = \sqrt{\frac{1}{8} \left(1 + \sqrt{1 - C_{T_s}} \right)} \tag{100}$$

Values for K_6 and r_s/D_p, as well as for o/o_o, can be obtained from Figures 4, 5, and 6 respectively.

The local slipstream angle of attack, α_i, is given by equation (82), and the angle of attack outside the propeller slipstream is as follows:

$$\alpha = i_w + \alpha_T - \alpha_{L_o} + \Delta\alpha\delta_f \tag{101}$$

2. Total Wing Lift Coefficient

The wing lift slipstream coefficient, C_{L_S}, both inside and outside the slipstream is obtained by

$$C_{L_S} = \frac{q_0}{q_s}(C_{L_W}) + \Delta C_{L_S} \tag{102}$$

where

$$C_{L_W} = o\left[\alpha\left(1 - \frac{r_s}{b/2} + K_7\right) + \alpha_s\left(\frac{r_s}{b/2} - K_7\right)\right] \tag{103}$$

$$\Delta C_{L_S} = \frac{(K_L r_s \alpha_s)}{C} \tag{104}$$

and

$$q_s = q_0 + \frac{T}{A_p} \tag{105}$$

The constant K_L is obtained from Figure 3 for the corresponding value of C_{T_S} and propeller induced velocity distribution, while K_7 is given by

$$K_7 = \frac{1}{\pi}\left[\frac{b_s - r_s}{b/2}\sqrt{1 - \left(\frac{b_s - r_s}{b/2}\right)^2} + \sin^{-1}\left(\frac{b_s - r_s}{b/2}\right)\right. \tag{106}$$

$$\left. - \frac{b_s + r_s}{b/2}\sqrt{1 - \left(\frac{b_s - r_s}{b/2}\right)^2} - \sin^{-1}\left(\frac{b_s - r_s}{b/2}\right)\right]$$

The average angle of attack inside the slipstream is given by

$$\alpha_s = i_w + \phi - \alpha_{L_D} + \Delta\alpha\delta_f \tag{107}$$

The angle ϕ_i as given by equation (85) can be expressed as

$$\phi = \tan^{-1}\left(\frac{\sin\alpha_T}{\sqrt{\cos^2\alpha_T + \frac{C_{T_S}}{1-C_{T_S}}}}\right) \tag{108}$$

Representative values of ϕ have been plotted in Figure 7 in terms of C_{T_S} for constant values of α_T. The incremental angle of attack due to flaps is represented by equation (83).

3. Total Wing Drag Coefficient

The slipstream drag coefficient is given by

$$C_{D_S} = C_{D_{is}} + \Delta C_{D_{is}} + \Delta C_{D_{LS}} + C_{D_{DWS}} + C_{D_{OSS}} \tag{109}$$

where

$$C_{D_{is}} = \frac{\left[\left(\frac{D}{D_D}\right) D_D \alpha\right]^2 (1-C_{T_S})}{\pi R} \tag{110}$$

$$\Delta C_{D_{is}} = K_\theta \frac{N_P D_P^2}{2 r_s C} \alpha_s^2 \tag{111}$$

$$\Delta C_{D_{LS}} = K_\theta \frac{N_P D^2}{2 r_s C} \alpha_s \tag{112}$$

$$C_{D_{OWS}} = + \left[1 - \frac{2\left(\frac{r_s}{D_P}\right) N_P D_P C}{S}\right] (1-C_{T_S})\, C_{D_O} \tag{113}$$

and

$$C_{O_{OSS}} = K_{10}\left(\frac{N_P D_P}{2 r_S}\right) C_{p_{O_S}} \tag{114}$$

The constants K_8, K_9, and K_{10} are given by the following equations:

$$K_8 = 1.10 \left(\frac{r_S}{D_p}\right)^2 (1-\mu^2)^2 \cos(\alpha_T - \phi) \tag{115}$$

$$K_9 = 3.74 \left(\frac{r_S}{D_p}\right)^2 (1-\mu^2) \sin(\alpha_T - \phi) \tag{116}$$

$$K_{10} = 2 \left(\frac{r_S}{D_p}\right) \cos(\alpha_T - \phi) \tag{117}$$

III. EXPERIMENTAL PROGRAM

The experimental phase of this study consisted of low-speed wind tunnel tests of a powered semispan wing model at the North American Aviation, Columbus Division, Aerodynamic Laboratory's (NACAL) low-speed wind tunnel. These tests were conducted to determine propeller slipstream effects on spanwise distribution of wing lift, drag, and pitching moment and total wing forces and moments. Also, a survey of the velocity field in the propeller slipstream was performed.

A. DESCRIPTION OF TEST EQUIPMENT

1. Model Description

The model tested consisted of a right-hand semispan wing, a 40-horsepower electric motor with propeller rotating down at the tip, and a semifuselage. Figure 8 is a photograph of the model with flaps installed. Model nomenclature and dimensional data are given in Table I.

a. Wing

The semispan wing is comprised of eight instrumented segments individually supported from the main spar by a three-component strain gage balance made up of a fore and aft set of normal force beams and a chord force beam. A cross section of the instrumented wing segment showing the three-component balance and the method of attachment to the spar is shown in Figure 9. The instrumented segments were separated by stationary segments which were also attached to the spar. A 1/8-inch gap was incorporated between the rigid and instrumented segments. This gap was sealed with dental dam. The arrangement of the rigid and instrumented segments and the geometry of the overall wing are presented in Figure 10.

b. Propellers

Two propellers designated as P_1 and P_2 were utilized during these tests. Both were 39-inch-diameter, two-bladed, wooden propellers. They differed, however,

in twist and taper so as to provide distinctly different velocity profiles. A Clark-Y airfoil was utilized for the propeller blade sections. Figure 11 shows the characteristics of the first propeller, P_1, which has a relatively constant chord and light twist. Figure 12, on the other hand, presents the characteristics of propeller P_2, showing the severe twist and taper incorporated in its design.

c. Motor

A variable-frequency, water-cooled electric motor rated at 40 horsepower at 7300 r.p.m. was used to power the model. The motor is a six-pole, three-phase Task Corporation Model 11513-1. Its performance characteristics are given in Figure 13. Power for the motor was supplied by a 100-kilowatt (30 to 350 c.p.s.) motor generator set and monitored by polyphase wattmeters.

d. Fuselage

A semifuselage was included with the test model. It was made of Styrofoam and covered with Fiberglas resin. The fuselage height was sufficient to permit rotation of the wing through 90° without overhang.

e. Flaps

Simulated split flaps were attached to the wing for a series of tests. The flaps had a fixed deflection of 45° with respect to the wing chord and a flap chord length equal to one-third of the wing chord.

3. Model Installation

The tests were conducted in the 16-foot-by-14-foot test section of the NACAL low-speed single return tunnel. The model was mounted vertically on the post support system of the tunnel and in line with the MK III C six-component strain gage balance furnished by NACAL. A dimensional sketch of the installation and a photograph of the model with a view looking upwind in the tunnel are shown in Figures 14 and 15,

respectively. The semifuselage was mounted on the reflection plane which was positioned 6 inches below the tunnel centerline. The wing spar passed through the fuselage with an interface provided to minimize air leakage.

A series of tests was conducted with an eight-probe pressure rake to determine the propeller slipstream velocity profile. During these tests, the wing segments were removed and the rake was attached to the spar. A photograph of the installation is given in Figure 16. The probe heads, as shown in Figure 17, were located at the intersection of the quarter chord and the center of each segment. An extension was added to the motor and propeller assembly, increasing the distance between the wing spar and the propeller plane. This extension permitted the probes to be installed far enough from the spar to minimize flow distortion.

3. Instrumentation

a. Main Balance

The NACAL MK III C, 2.5-inch-diameter, internal strain gage balance was used to measure three-component force and moment data for the total wing. The balance was mounted vertically and positioned so that its normal force component measured model normal force, its side force component measured model chord force, and its rolling moment component recorded model pitching moment.

b. Instrumented Segments

The eight wing segments were supported from the spar by three-component strain gage balances which measured normal and chord forces and pitching moment on each of the segments. The balances consisted of 350-ohm four-gage bridges. Calibration of each balance was accomplished at NACAL by using the tunnel data recording system. Each wing segment, including the rubber membrane, was calibrated by loading both plus and minus normal forces at three chord locations and chord force at one location. The resulting calibration constants for each segment are presented in Table II.

During calibration, it was established that each segment calibration was linear and symmetrical through the origin. Furthermore, it was determined that there was no interaction between adjacent wing segments. Table III presents the information on the accuracy of the wing force data as affected by the accuracy of the data acquisition system of ± 4 counts, the calibration slopes of the beams, the excitation voltages, and the full-scale millivolt output ranges used during the test.

c. Propulsive System

A calibrated strain gage beam was incorporated into the aft end of the motor mount. The beam, consisting of a 350-ohm four-gage bridge, provided propeller thrust. The indicated thrust was monitored on a Burkley-Ease analog null meter and was used to maintain the required thrust for each test.

The motor was instrumented with a thermocouple for monitoring temperature, and a frequency counter was used to measure rotational speed.

d. Pressure Probes

An eight-probe pressure rake was used to obtain propeller slipstream velocity profiles. The probe, shown in Figure 18, is a United Sensor and Control Corporation Model DA-125 modified, 1/8-inch-diameter, three-dimensional pressure head. The head of each probe is prism shaped, providing five pressure signal outputs. The pressures were coupled to differential pressure transducers, Statham Instruments Model PM 6 TCB+0.5-350, as well as to a 50-tube manometer board. Due to the location of the model with respect to the recording equipment, a length of approximately 60 feet of plastic tubing was required to connect each pressure probe output to the transducers.

e. Tunnel

The tunnel free stream dynamic pressure was measured by the two wall pitot-static probes connected to the

servo manometer. The tunnel pressure was monitored at the tunnel control console and controlled by adjustment of fan r.p.m. The model angle of attack was measured by a three-turn potentiometer incorporated within the strut yaw drive.

f. Recording System

Force and moment data were recorded simultaneously by the Beckman Automatic Data System on magnetic tape and on the analog X-Y plotters as quick-look data. Pressure data were also recorded by the Beckman Automatic Data System on magnetic tape with pictures taken of the manometer board for backup data.

g. Tuft Photographs

Tufts were installed on the wing upper surface and along the tunnel wall in line with the wing. Photographs of these tufts were taken for each data point.

B. TEST PROCEDURES

The tests were conducted at a tunnel pressure level of 1 atmosphere and a Reynolds number of 0.8×10^6 based on the model wing chord. The conditions investigated included angle of attack ranges from 0° to 90°, at 0° yaw angle and at thrust coefficients, C_{T_S}, ranging from 0 to 0.97. The configurations tested and the operating conditions are presented in Table IV. The conditions for each test were established using the settings of Table V.

The test procedure for each of these conditions was as follows:

1. Tunnel speed was brought up to desired value.

2. The required propeller thrust was set by adjusting input power to the model motor. The propeller thrust, which was a function of thrust beam voltage output, was monitored on the analog null meter.

3. The angle of attack was set with the tunnel yaw drive strut.

4. When steady-state values were established, the data point was recorded.

The above procedure was repeated through the specified angle of attack range, constituting a complete run.

Thrust coefficients of unity, i.e., zero tunnel speed, were not possible due to recirculation of the propeller wake through the closed tunnel. During tests with propeller P_2, instrumented segment failures were encountered at the C_{T_S} of 0.9 test condition (test number 8). The segments were repaired, but no further tests were conducted with the wing and the P_2 propeller for C_{T_S} values greater than 0.5. For $C_{T_S} = 0$ runs, i.e., zero propeller thrust, the windmilling propeller resulted in effective negative thrust coefficients.

C. DATA REDUCTION

1. Tunnel Corrections

Corrections applied to the three-component force and moment data were as follows:

Solid (ϵ_S), wake (ϵ_W), and power (ϵ_P) blockage corrections were applied to the free stream dynamic pressure according to the following equation:

$$(q_C/q_U)_{BLOCKAGE} = (1 + \epsilon_S - \epsilon_P + \epsilon_W)^2 \tag{118}$$

where

$$\epsilon_S = 0.00838 \tag{119}$$

$$\epsilon_P = \frac{T_P}{4A_T q_U \sqrt{1 + \frac{T_P}{A_P q_U}}} \tag{120}$$

$$\epsilon_W = (S/4A_T)\, C_{D_T} \tag{121}$$

$$\epsilon_w = 0.00137\ (D_u + T \cos \alpha_w)/q_u S \qquad \text{(Entire Wing)}$$

$$\epsilon_w = 0.00137\ (D_u)/q_u S_{1\ldots8} \qquad \text{(Segments)}$$

Classical wall corrections were applied to the data as follows:

$$\Delta\alpha/C_{L_\Gamma} = 0.4397 \tag{122}$$

$$\Delta C_D/C_{L_\Gamma}{}^2 = 0.0077 \tag{123}$$

$$\Delta C_M/C_{L_\Gamma} = 0 \tag{124}$$

where

$$C_{L_\Gamma} = (L - T_p \sin \alpha_u)/q_u S \tag{125}$$

No corrections were made for wall effect on slipstream velocity during large angles of attack. As indicated in Reference 5, the effect of ground proximity becomes minimal at heights of 1.5 diameters. Note that at $\alpha_w = 90°$, the distance from the propeller plane to ground is 2.6 diameters.

The only corrections applied to the pressure data were blockage corrections to free stream dynamic pressure according to the following equation:

$$(q_c/q_u)_{BLOCKAGE} = (1 + \epsilon_s - \epsilon_p)^2 \tag{126}$$

2. Wing Aerodynamic Data

Three-component force and moment data for each segment, as well as for the total wing, were reduced from magnetic tape on the IBM 7090 computer facility at NACAL. The data were printed out in terms of the measured normal and chord forces

and were also converted to lift, drag, and pitching moment referenced to the wind axes system with origin at the quarter chord.

The notations and signs of forces and angles are shown in Figure 2. The raw data obtained from NACAL were further reduced as follows:

a. The propeller thrust and the corresponding values of q_s and C_{T_s} for each data point were determined. The thrust was obtained by subtracting the sum of chord forces of all individual segments from the total force of the main balance. The following relationships were utilized:

$$T_p = (C_h)_{MAIN} - (C_h)_{SEGMENT} \tag{127}$$

$$q_s = q_o + \frac{T_p}{A_p} \tag{128}$$

$$C_{T_s} = \frac{T_p}{q_s A_p} \tag{129}$$

The calculation of thrust in this manner became necessary due to the questionable data obtained from the thrust beam. During the tests, it was determined that the thrust beam was affected by nonlinear motor expansion with temperature during sustained operation. Although the thrust beam failure precluded the identical setting of test conditions for each propeller and flap configuration, the test result accuracy is not compromised. The thrust data obtained were converted to the nondimensional coefficient form.

b. The lift, drag, and moment data obtained from individual segments and from the total balance force measurements were converted into coefficient form based on slipstream dynamic pressure q_s and the corresponding segment or wing area. These were subsequently plotted as a function of wing span for constant values of α_w .

c. Numerical integration of the spanwise distribution of lift, drag, and moment coefficients was performed to obtain total wing force and moment coefficients excluding propeller thrust and normal force contributions. Conventional C_{L_s} versus α_w, C_M versus α_w, and C_{D_s} versus C_{L_s} plots have been used for presentation of total wing aerodynamic data.

3. Propeller Slipstream Data

The slipstream pressure data were reduced utilizing NACAL IBM computer program B-4000. This program utilized the appropriate pressure probe calibration data provided by the manufacturer.

The method for determining the average pressure and the flow angle for a typical data point (probe 5 of Figure 17) is given below.

a. Obtain the following measured pressure values in p.s.f. absolute:

$P_1 = 2086.91$
$P_2 = 2082.85$
$P_3 = 2081.26$
$P_4 = 2086.94$
$P_5 = 2084.75$

b. Using the values from step a, compute

$$\bar{P} = \frac{P_2+P_3}{2} = 2082.06 \tag{130}$$

and

$$P_1 - \bar{P} = 4.85 \tag{131}$$

c. Then determine the pressure ratio:

$$\frac{P_2 - P_3}{P_1 - \bar{P}} = 0.329 \qquad (132)$$

d. Using the pressure ratio from step c, enter Figure 19 (typical calibration curve) and read off the flow yaw angle:

$$\psi = 5.2°$$

e. From the above results, also compute

$$\frac{P_4 - P_5}{P_1 - \bar{P}} = 0.453 \qquad (133)$$

f. Using the values of ψ from step d and the pressure ratio from step e, enter Figure 20 and obtain the flow pitch angle:

$$\theta_p = 16.5°$$

g. With the known values of ψ and θ_p from steps d and f, respectively, enter Figure 21 and read off

$$\frac{P_0 - P}{P_i - \bar{P}} = 1.003 \qquad (134)$$

h. Finally compute the slipstream dynamic pressure as

$$q = P_0 - P = 4.86 \text{ p.s.f.} \qquad (135)$$

It should be noted that for the pressure rake installation shown in Figure 16, the angle θ_p obtained in step f corresponds to a negative local angle of attack within the propeller slipstream.

D. TEST RESULTS

Presented in this section are the test results obtained for the semispan wing fuselage model (W_1, B_1), with and without 45° split flaps (F_1) and two propellers, P_1 and P_2.

For each of these model configurations, the test data are presented as plots of:

1. Local wing lift, drag, and pitching moment versus wing span for constant values of C_{T_s}.

2. Total wing lift and pitching moment coefficients versus α_w for constant values of C_{T_s} and wing drag versus wing lift.

3. Local dynamic pressure and local angle of attack within the propeller slipstream versus wing span for constant values of α_w and C_{T_s}.

A discussion of the tuft data given in the appendix is also presented.

1. Spanwise Distributions of Wing Lift, Drag, and Pitching Moment

The spanwise distributions of wing lift, drag, and pitching moment for the configurations tested, as shown in Table IV, are presented in Figures 22 through 45. Figures 22 through 30 show the results obtained for the basic wing fuselage model with no flaps and with the P_1 propeller (configuration P_1, W_1, B_1). Figures 31 through 39 show the corresponding results including 45° split flaps (configuration P_1, W_1, F_1, B_1).

The results obtained with the P_2 propeller and no flaps (configuration P_2, W_1, B_1) are given in Figures 40 through 43,

and the corresponding data with 45° split flaps (configuration P_2, W_1, F_1, B_1) are given in Figures 44 and 45. The test data for the P_2 propeller were limited by flexure beam failures during the tests, as discussed in Section III B.

a. Spanwise Lift Distribution

Examining a typical spanwise lift distribution (e.g., Figure 24), it can be noted that for small wing angles of attack up to $\alpha_w = 20°$, the local wing coefficient is higher on the inboard segments than on the outboard segments. For wing angles of attack larger than $\alpha_w = 30$, opposite trends are indicated. These trends are attributed to the slipstream swirl effects. For the propeller rotation down at the wing tip, the effective wing angle of attack is substantially increased on the inboard portion of the wing and is reduced on the outboard portion, resulting in the corresponding changes in local lift coefficient. As wing angle of attack increases, the slipstream swirl effects result in a more rapid onset of stall on the inboard portion of the wing and delayed stall on the outboard portion of the wing. This result is seen by examining the lift data (Figure 24), which show that the local lift coefficient on the inboard wing segment reaches a maximum value at much lower wing angle of attack than that on the outboard portion of the wing. From these results, it is apparent that variations in wing geometry with either differential twist, camber, or flaps, to take advantage of the changes in effective angle of attack due to swirl, can result in significant advantages in both delay of stall or increased lift. For example, by superimposing the data obtained on the outboard portion of the wing at $\alpha_w = 40°$ on the data obtained on the inboard wing segment at $\alpha_w = 20°$, a net increase of about 30% in lift can be attained as compared to the total wing lift at $\alpha_w = 20°$.

It should be noted that the slight negative lift indicated in these figures for $C_{T_s} \approx 0$ (propeller windmilling) is believed to be due to the misalignment of the wing with respect to the tunnel airstream.

b. Spanwise Drag Distribution

Examining a typical drag distribution, such as that of Figure 25, no significant effects of propeller swirl can be noted. In general, the local drag coefficient increases with an increase in wing angle of attack similar to that for a wing without the propeller slipstream.

c. Spanwise Pitching Moment Distribution

The spanwise distribution of wing pitching moment is shown in Figure 30 for the test configuration P_1, W_1, B_1. This figure indicates that at high propeller thrust coefficients ($C_{T_s} = 0.97$), the effect of wing angle of attack on local pitching moment is less predominant than that for low values of C_{T_s}. Furthermore, the effect of propeller slipstream swirl is also apparent in these data but is not as pronounced as in the lift data.

d. Effect of Propeller Thrust Coefficient

Comparing Figures 22 through 30, it can be noted that the major effect of propeller thrust coefficient on local aerodynamic wing characteristics is to reduce the effectiveness of wing geometric angle of attack, causing a reduction in local lift, drag, and pitching moment coefficients. As can be seen from Figures 28, 29, and 30 for $C_{T_s} = 0.97$, the wing lift, drag, and pitching moment are practically independent of α_w. However, an increase in C_{T_s} results in a larger variation of the induced local angle of attack due to propeller swirl.

e. Effect of Flaps

Comparing Figures 22 through 30 (with no flaps) with Figures 31 through 39 (with flaps), it can be seen that the effect of flaps on wing performance is similar to that experienced with a conventional wing without propeller slipstream. Specifically, the

addition of flaps to the wing segments results in an increase of overall wing force and moment coefficients. Furthermore, the flaps cause a much more rapid onset of wing stall.

f. Effect of Propeller Geometry

The tests utilizing the two propellers, P_1 and P_2, were performed in order to determine the effect of slipstream velocity distribution on wing performance. The P_1 propeller had a velocity distribution peaking at approximately 0.7 propeller radius, thus providing a maximum local dynamic pressure (q) at wing segments 3 and 6 (see Figure 10). On the other hand, the velocity distribution of the P_2 propeller had a maximum value of a propeller radius of about 0.35, providing maximum dynamic local pressure close to the propeller centerline (segments 4 and 5).

Comparing the results of Figure 24 with those of Figure 42 for P_1 and P_2, respectively, it can be seen that, in general, for any constant angle of attack (say $\alpha_w = 10°$), the local lift values obtained with the P_2 propeller are higher than those obtained with the P_1 propeller. Although this increase is partially due to the difference in C_{T_s} coefficients for the two propellers, it is shown later in the text, using the total wing lift data, that a net increase in lift is achievable with the P_2 propeller. In addition, Figures 24 and 42 show that the peak values of local lift correspond closely to the peak values of the slipstream velocity distribution for the two propellers.

It can also be noted that the drag data for the two cases (Figures 25 and 43) are not drastically affected, especially at low wing angles of attack.

The above results indicate that the propeller slipstream velocity distribution with a peak value toward inboard portion of the blade yields an

improved wing performance. The effect of an inboard shift of propeller slipstream on the performance of the propeller itself must, of course, also be considered in the optimization of an overall wing-propeller design.

2. Total Wing Forces and Moments

The local wing lift, drag, and pitching moment distributions discussed in Section 1 were numerically integrated to obtain total wing force and moment coefficients. The results are presented in Figures 46 through 50.

The lift, drag, and pitching moment coefficients obtained with the P_1 propeller and basic wing are given in Figure 46 for constant C_{T_S} values of 0, 0.60, 0.93, and 0.97. The data show that an increase in C_{T_S} reduces slipstream lift and drag coefficient and also delays the onset of overall wing stall. An increase in C_{T_S} is also seen to reduce the lift to drag ratio of the wing at high angles of α_w. The reduction in C_{L_S} and C_{D_S} with increasing C_{T_S} is primarily due to both the reduction in the effective wing angle of attack within the propeller slipstream and the reduction of free stream dynamic pressure outside the slipstream. The reason for the reduction of C_{L_S}/C_{D_S} ratio with increase in C_{T_S} is believed to be due to a more pronounced reduction in C_{L_S} than in C_{D_S}.

The results of the wing with flap and P_1 propeller are summarized in Figure 47. With the exception of the increased forces and moments normally associated with flaps, the same trends indicated in Figure 46 with the basic wing are also observed with flap results. Figures 48 and 49 present the wing aerodynamic data for propeller P_2 without and with flaps, respectively. From the limited data obtained, trends similar to those for the P_1 propeller are shown.

A direct comparison of the effect of the two propellers on total wing lift is made in Figure 50. In this figure, the wing lift coefficient at $C_{T_S} = 0.5$ for propeller P_1 is compared with the lift coefficient of P_2 at the same C_{T_S} value. It should be noted that values for $C_{T_S} = 0.5$ for P_1

were obtained by interpolation of the data of Figure 46. The results indicated in Figure 50 confirm the conclusions reached in Section 2.

Specifically, Figure 50 shows that at a comparable propeller-wing operating condition, the P_2 propeller yields an increase in the total wing lift coefficient of about 5% over the P_1 propeller. This result is also in agreement with the theoretical data presented in Figure 3.

3. Propeller Wake Data

The propeller wake data for the powered wing model are summarized in Figures 51 through 55. Figures 51 and 52 show the dynamic pressure profiles of propellers P_1 and P_2, respectively, at $C_{T_s} = 0.97$. These data are nondimensionalized by q_s and are plotted versus nondiminsional wing span $y/b/2$. Also, these figures show a comparison of the pressure data obtained at the tunnel using the three-dimensional pressure probes versus the corresponding results obtained with a pitot-static probe survey at the contractor's facility. A good correlation between the two sets of results is indicated.

Comparing the pressure distribution of the two propellers, it can be seen that the P_1 propeller has a triangular loading with a peak at approximately 70 percent radius. The P_2 propeller, on the other hand, has a parabolic velocity distribution peaking at approximately 30 percent radius. Although pressure data have been obtained for lower C_{T_s} values, they are not presented herein due to the unavailability of propeller thrust data.

In addition to the pressure data, the slipstream local angles of attack were measured and are presented in Figures 53 through 55. Figures 53 and 54 show the slipstream angles for the P_1 propeller at C_{T_s} of 0.97 and approximately 0.5, respectively. The local wing angle, defined as the angle between the resultant slipstream velocity and the thrust axis, is also plotted versus wing span ratio. The swirl angle effect discussed previously is evident in the data, particularly at the $C_{T_s} = 0.97$ test condition. The effect

of geometric wing angle of attack can be seen to increase the local angle throughout the wing span. This is particularly evident at the $C_{T_s} = 0.5$ test condition.

The local angle of attack resulting with the P_2 propeller is given in Figure 55. Trends similar to those obtained with the P_1 propeller are evident with the P_2 propeller at $C_{T_s} = 0.5$.

4. Flow Characteristics

The tuft photographs of the model are presented in the appendix for all tests conducted. Figures 64 through 74 provide an indication on the development of stall patterns on the wing, and their dependency on propeller thrust coefficient, propeller slipstream swirl, and other variables. As shown in these figures, the tufts were located on the top surface of the wing, and the tunnel wall was in the background.

The major points of interest of the flow characteristics of the wing model are discussed below.

As expected, at high C_{T_s} coefficients, the portion of the wing outside the slipstream is always stalled, while inside the slipstream no stall is evident regardless of wing angle. On the other hand, as C_{T_s} reduces, a stall within the propeller slipstream is indicated even at moderate wing angles of attack.

When the tuft data, such as those shown in Figure 65 for $C_{T_s} = 0.6$ are examined, it can be seen that the stall on the inboard portion of the wing within the propeller slipstream begins at approximately $\alpha_w = 20°$, while the stall on the outboard portion of the wing begins at $\alpha_w = 30°$. At the wing root, separation due to the fuselage is noted even at $\alpha_w = 0$ and progresses outboard with increasing angle of attack. Flow near the wing tip, on the other hand, remains attached until $\alpha_w \approx 30°$ and seems to stall at the same angle as the outboard portion of the wing within the propeller slipstream.

For the windmilling condition with propellers P_1 and P_2 (Figures 64 and 72, respectively), the portion of the wing immersed in the propeller slipstream stalls at approximately 10° of wing angle of attack. The stall begins near the hub and progresses first outboard and then inboard along the wind span. Similar stall characteristics are observed for the wing-flap configuration operating at the same propeller windmilling condition (Figures 68 and 74); however, in this case the stall begins approximately 5° to 10° earlier than that for the wing without flaps.

The effect of flow interaction between the model and the background tunnel wall can be seen from Figure 67, which shows the tuft data for large wing angles of attack and high thrust coefficients. In this figure, the wall tufts indicate a radial flow moving outward from the point of impingement resembling the flow field of a propeller or a rotor hovering in ground effect. For this test configuration, however, the axial distance between the propeller and the tunnel wall was large enough ($x/D_p > 2.0$) to ensure no wall effects on the propeller performance.

Flow characteristics similar to those discussed above can be found in other investigations such as those reported in References 6 and 7.

E. CORRELATION OF THEORY WITH TEST DATA

The theory developed in Section II is correlated with the representative test data discussed in Section D. The correlation is performed utilizing the test data for spanwise wing lift distribution as well as the total wing lift and drag coefficients.

1. Spanwise Lift Distribution

Figures 56 through 60 present a comparison of the theoretically predicted lift distribution versus the corresponding measured data. The correlation is presented in plots of local wing lift versus nondimensionalized wing span for constant values of wing angle of attack and thrust coefficients.

Figures 56, 57, and 58 show the correlation of the results obtained with the P_1 propeller (configuration P_1 W_1 B_1) for C_{T_s} values of 0.6, 0.93, and 0.97 respectively. The results obtained with 45° split flaps for C_{T_s} = 0.46 (configuration P_1 W_1 F_1 B_1) are compared in Figure 59. The correlation of the theoretical and experimental results obtained with the P_2 propeller for C_{T_s} = 0.5 (configuration P_2 W_1 B_1) is shown in Figure 60.

When the results presented in the above figures are examined, it can be noted that, in general, the theoretically predicted results (solid lines) correlate well with the corresponding test data (points). This agreement is particularly evident at high values of C_{T_s}, as indicated by Figures 57 and 58.

Somewhat poorer correlation is indicated by Figure 59 for the data with 45° split flaps (configuration P_1 W_1 F_1 B_1), especially at α_w = 15. The relatively poorer correlation for this test configuration is believed to be due to a premature stall of the inboard portion of the wing with 45° flaps.

2. Total Wing Lift and Drag Coefficients

The correlation between the theoretical results and the test data based on the total wing lift and drag coefficients is presented in Figures 61 through 63. These figures show the plots of C_{L_s} versus α_w and C_{D_s} versus C_{L_s} for exactly the same test conditions as discussed in Section 1. The results presented in these figures show a fair to good correlation between the theoretical values (dotted lines) and the corresponding test data (points).

Based on the preceding correlations, it can be concluded that the theory developed in Section II represents an adequate analytical tool for predicting the performance of a wing immersed in a propeller slipstream.

TABLE I

MODEL NOMENCLATURE AND DIMENSIONAL DATA

Symbol	Description	
B_1	Fuselage	
	Right-hand half fuselage	
	Length	9.33 ft.
	Width (half)	0.50 ft.
	Height	2.00 ft.
F_1	Wing T.E. Flap	
	Full-span split flap	
	Span	3.96 ft.
	Chord	.50 ft.
	Area	1.98 $ft.^2$
	Deflection angle	45°
P_1	Propeller	
	Constant chord, rounded tip, low pitch	
	Number of blades	2
	Diameter	3.25 ft.
	Disc area	8.3 $ft.^2$
P_2	Propeller	
	Tapered, thick hub, high pitch	
	Number of blades	2
	Diameter	3.25 ft.
	Disc area	8.3 $ft.^2$
W_1	Wing	
	Constant chord, 0° sweep, segmented wing	
	Span	4.77 ft.
	Chord	1.5 ft.
	Area	7.15 ft.
	Airfoil section	0015
	Wing span/propeller diameter ratio	1.47
	Wing incidence angle	0

TABLE II

BALANCE CALIBRATION CONSTANTS

$\partial R / \partial L$	N_1	N_2	$+C_h$	N_1	N_2	$+C_h$
	Segment No. 1			Segment No. 2		
R_{N1}	.1130	0.0	.0020	.1258	0.0	-.0017
R_{N2}	0.0	.1160	-.0030	0.0	.11825	.0017
R_{Ch}	-.0005	-.0051	.0834	.0009	-.0025	.0599
	Segment No. 3			Segment No. 4		
R_{N1}	.11475	0.0	.0025	.1152	0.0	.0024
R_{N2}	0 0	.11235	-.0034	0.0	.11275	-.0037
R_{Ch}	.0026	-.0038	.0833	.0032	-.0021	.0844
	Segment No. 5			Segment No. 6		
R_{N1}	.1140	0.0	.0024	.1120	0.0	.0027
R_{N2}	0.0	.1136	-.0034	0.0	.1167	-.0029
R_{Ch}	.0015	-.0019	.0861	.0003	-.0056	.0875

TABLE II (Continued)

	Segment No. 7			Segment No. 8		
$\frac{\partial R}{\partial L}$	N_1	N_2	$+C_h$	N_1	$+N_2$	$+C_h$
R_{N_1}	.1147	0.0	.0023	-.1158	0.0	.0021
R_{N_2}	0.0	.11605	-.0035	0.0	11455	-.0033
R_{C_h}	-.0014	-.0031	.0825	-.0013	-.0052	.0820

NOTES: Eleven volts excitation.
Constants are corrected for effective gage location (electrical centers).
Units of calibration constants are in millivolts per volt excitation per pound (mv./v./lb.).

TABLE III

WING FORCE INSTRUMENTATION ACCURACY

Component	Excitation Voltage	Full Scale M.V.	Accuracy	
			Absolute Value	Percent of Maximum Value Measured
Wing Segments				
N	11	15	±.10 lb.	1.5
C_h	11	5	±.03 lb.	1.5
Main Balance				
N	6	5	±5.88 lb.	7.8
C_h	4	5	±5.96 lb.	7.2
P.M.	4	2	±.25 ft.-lb.	1.3

TABLE IV

LISTING OF TUNNEL TESTING RUNS

Run No.	Configuration	$(q_o)_{nom.}$	α_w Range	Settings				
				C_{T_S}	δ_f	q_s	Prop. R.P.M.	Prop. Thrust
1	P_1 W_1 B_1	0	A		-	8	2700	
2	↓	0	A	0.97	-	8.74	2670	72
3		0.8	A	0.93	-	9.25	2700	72
4		4	B	0.60	-	10.09	2760	50
5		8	B	-0.10	-	7.36	*	-6.4
6	P_2 W_1 B_1	8	B	-0.50	-	5.10	*	-24
7	↓	4	B	0.50	-	7.84	3720	32
8		0.8	A	0.92	-	8.67	3990	66
9	P_1 W_1 F_1 B_1	8	B	-0.01	45	7.63	*	-4.6
10	↓	0.8	A	0.90	45	7.43	2430	55
11		4	B	0.46	45	7.55	2160	30
12		0.8	A	0.90	45	7.52	2430	56
13		0	C	0.97	45	7.79	2400	62
14	P_2 W_1 F_1 B_1	8	B	-0.40	45	5.62	*	-20
15	↓	4	B	0.40	45	7.06	3300	25
16	P_2 B_1	0	C	0.97	-	10.25	4080	85
17	↓	0.8	A	0.9	-		4200	
18		4	B	0.5	-		3300	
19	P_1 B_1	0	C	0.97	-	8.0	2430	66
20	↓	0.8	A	0.9	-		2310	
21		4	A	0.5	-		1710	

* Propeller Windmilling

α_w Range	
A	0,10,15,20,30,40,50,60,70,80,90
B	0,10,15,20,30,40,50
C	0,10,20,40,60,80,90

TABLE V

TEST CONDITIONS

C_{T_s}	Propeller Disc Loading (psf)	Tunnel Dynamic Pressure, q_o (psf)	Slipstream Dynamic Pressure, q_s (psf)	Prop. Thrust (lb.)	Voltmeter Setting (volts)
0	0	8	8	0	0
0.5	4	4	8	33.2	12.1
0.9	7.2	0.8	8	59.7	21.7
1.0	8	0	8	66.3	24.1

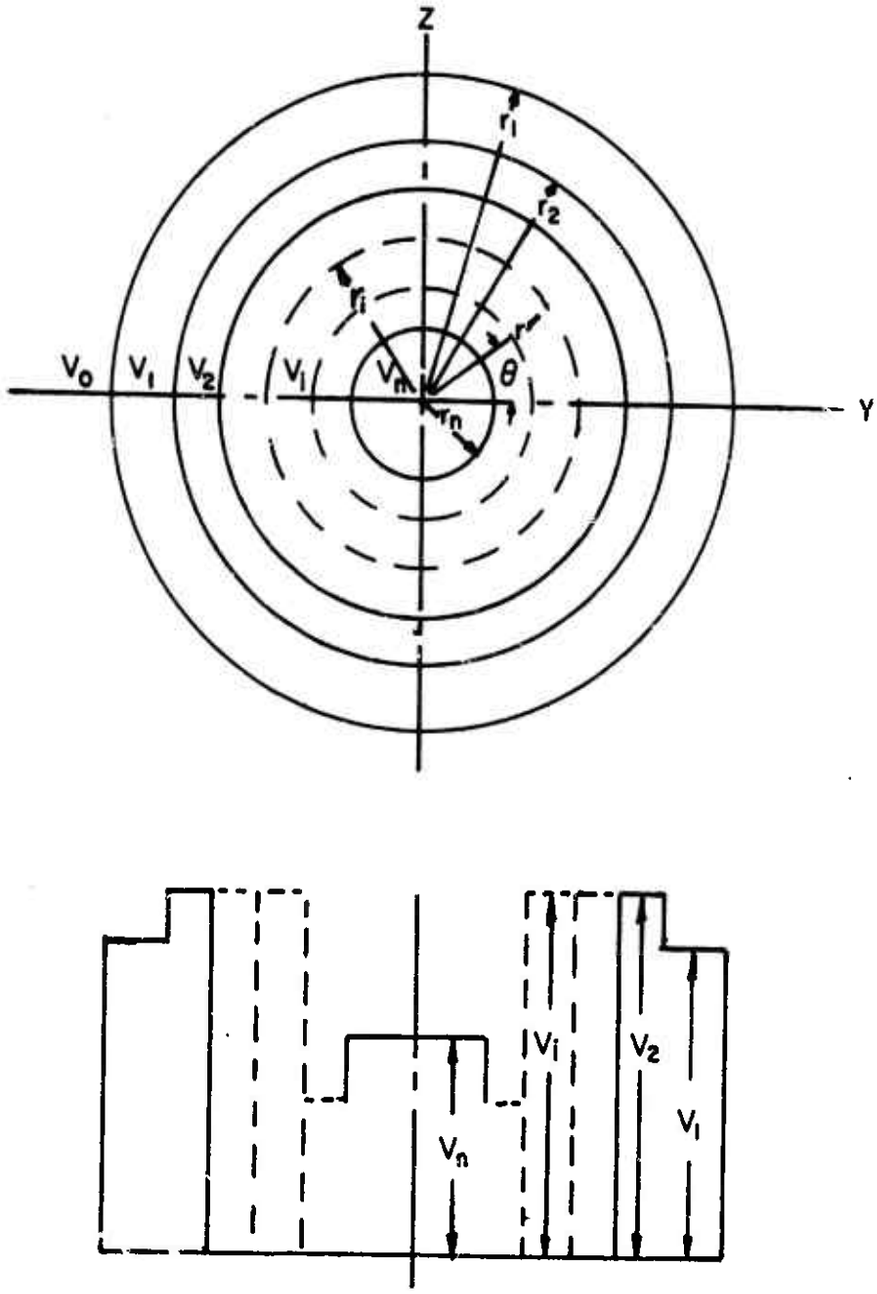

Figure 1. Representation of the Propeller Slipstream Velocity Zones.

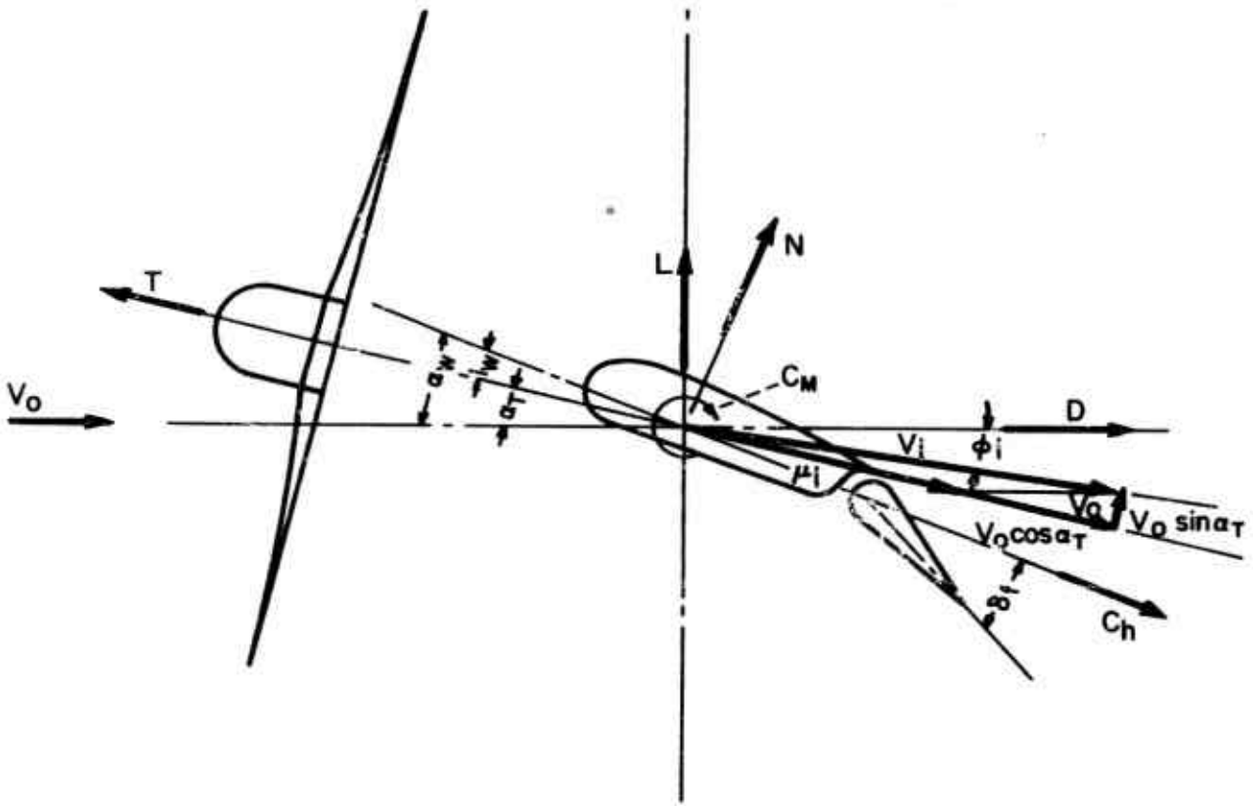

Figure 2. Propeller Slipstream Notation.

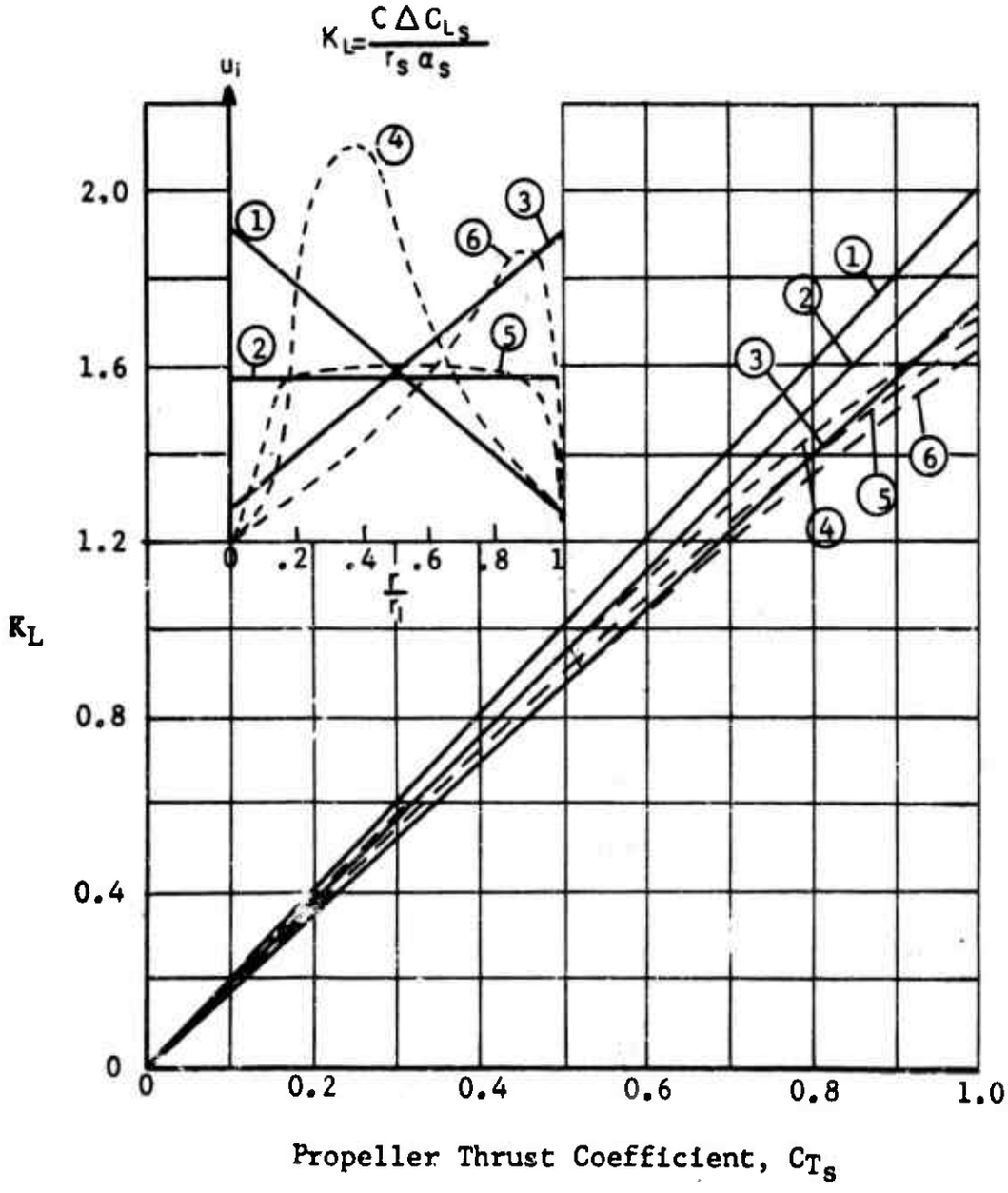

Figure 3. Variation of Lift Coefficient Parameter K_L With C_{T_s} for Various Induced Velocity Profiles.

$$K_6 = \left(\frac{1}{y_s/r_s} - \frac{y_s}{r_s} \right) \ln \left[\frac{1 + y_s/r_s}{1 - y_s/r_s} \right]$$

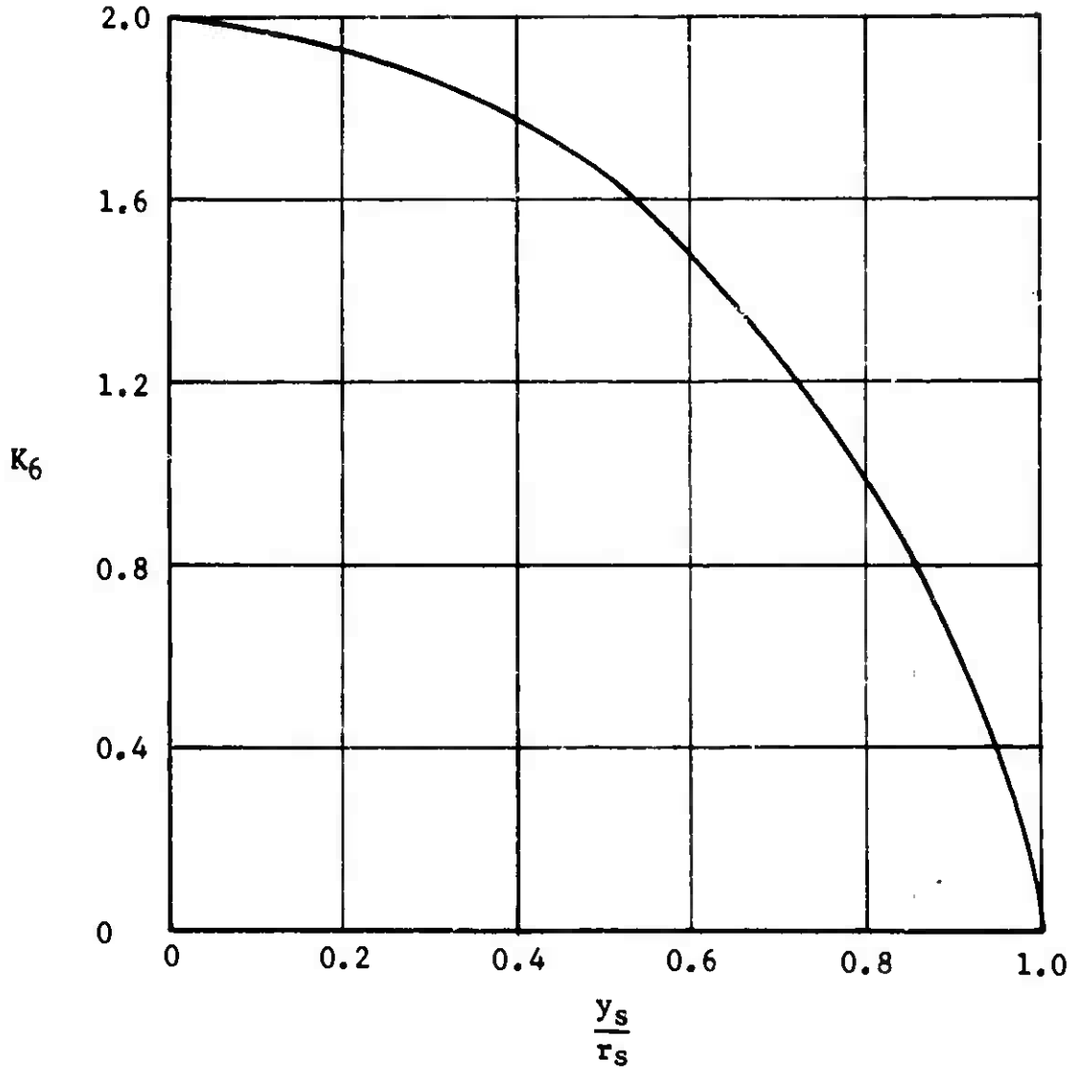

Figure 4. Variation of K_6 With Wing Span Ratio $\frac{y_s}{r_s}$.

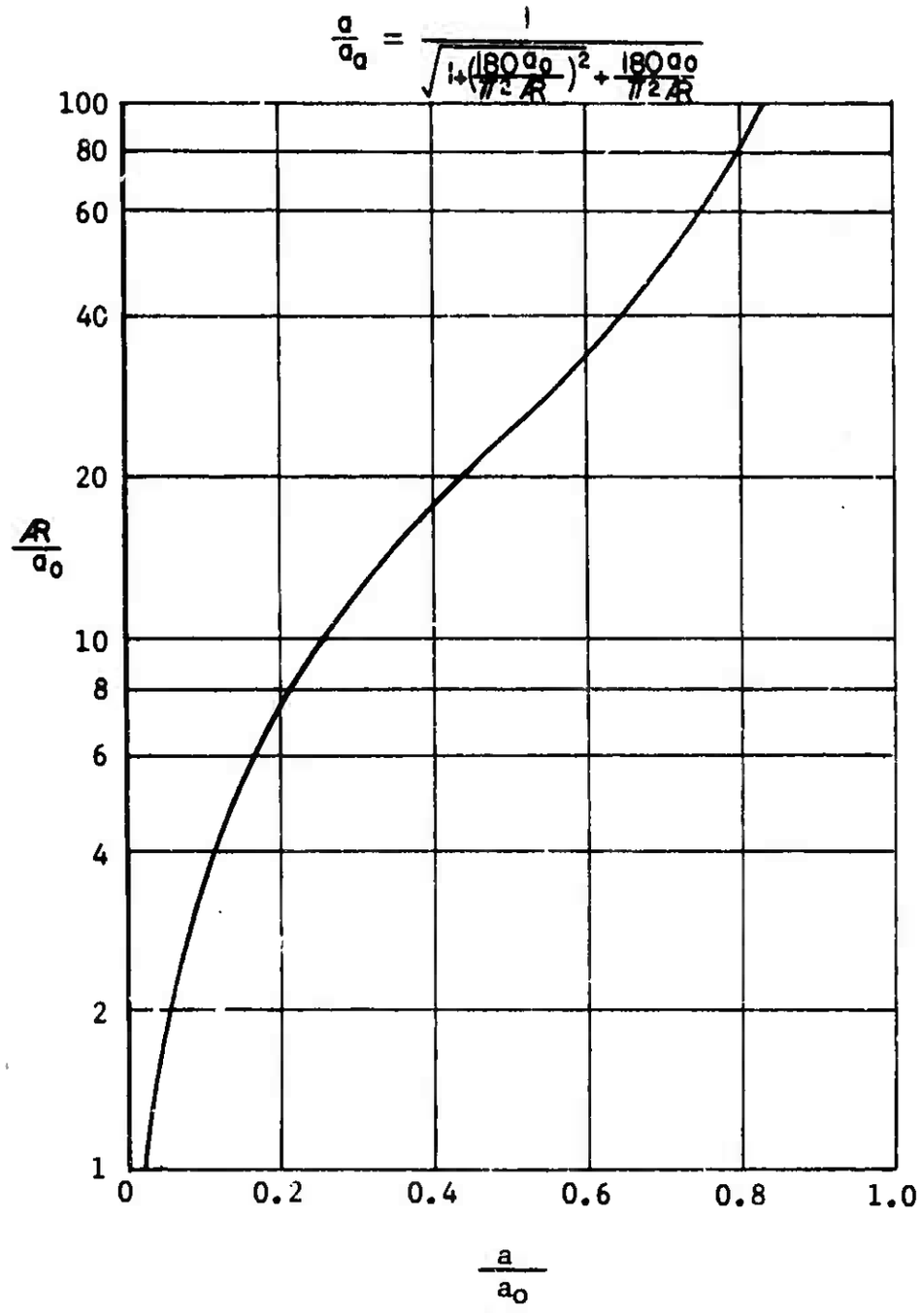

Figure 5. Variation of Lift Curve Slope $\frac{a}{a_0}$ With Aspect Ratio $\frac{AR}{a_0}$.

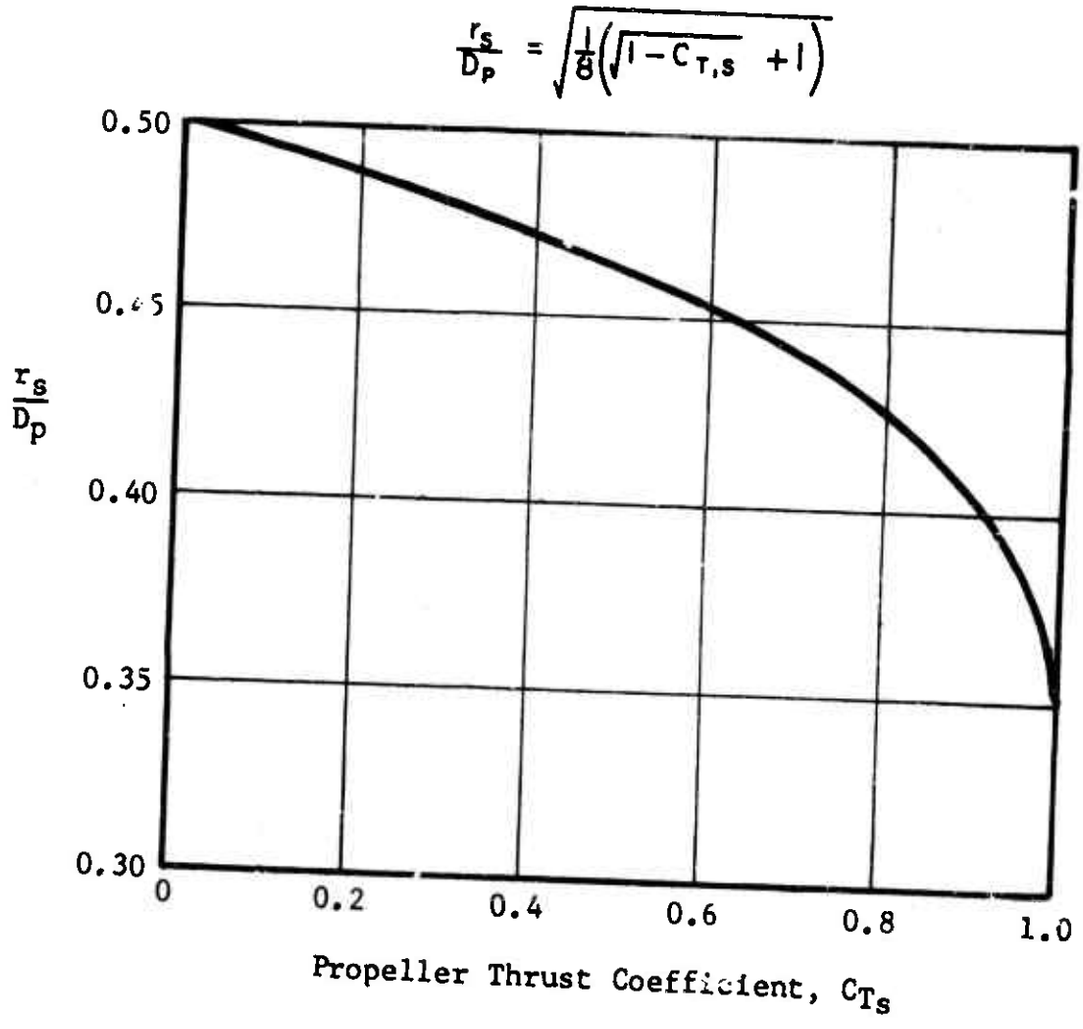

Figure 6. Variation of Propeller Slipstream Radius With Propeller Thrust Coefficient.

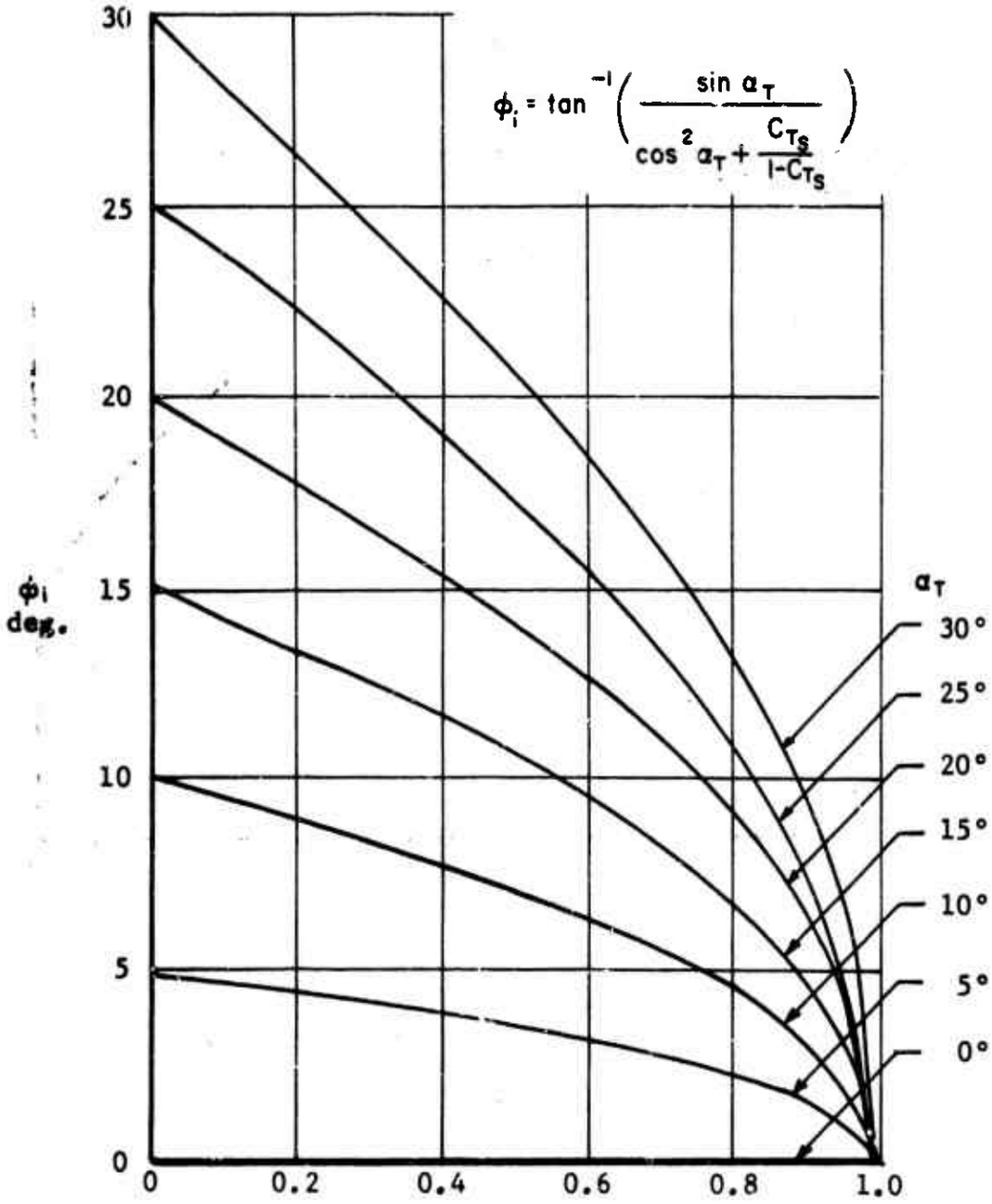

Figure 7. Variation of Propeller Slipstream Induced Angle ϕ_i With Propeller Thrust Coefficient C_{T_S} for Constant Values of α_T.

Figure 8. Front-Quarter View of Bottom Side of Wing With Split Flap. Configuration: P_2 W_1 F_1 B_1.

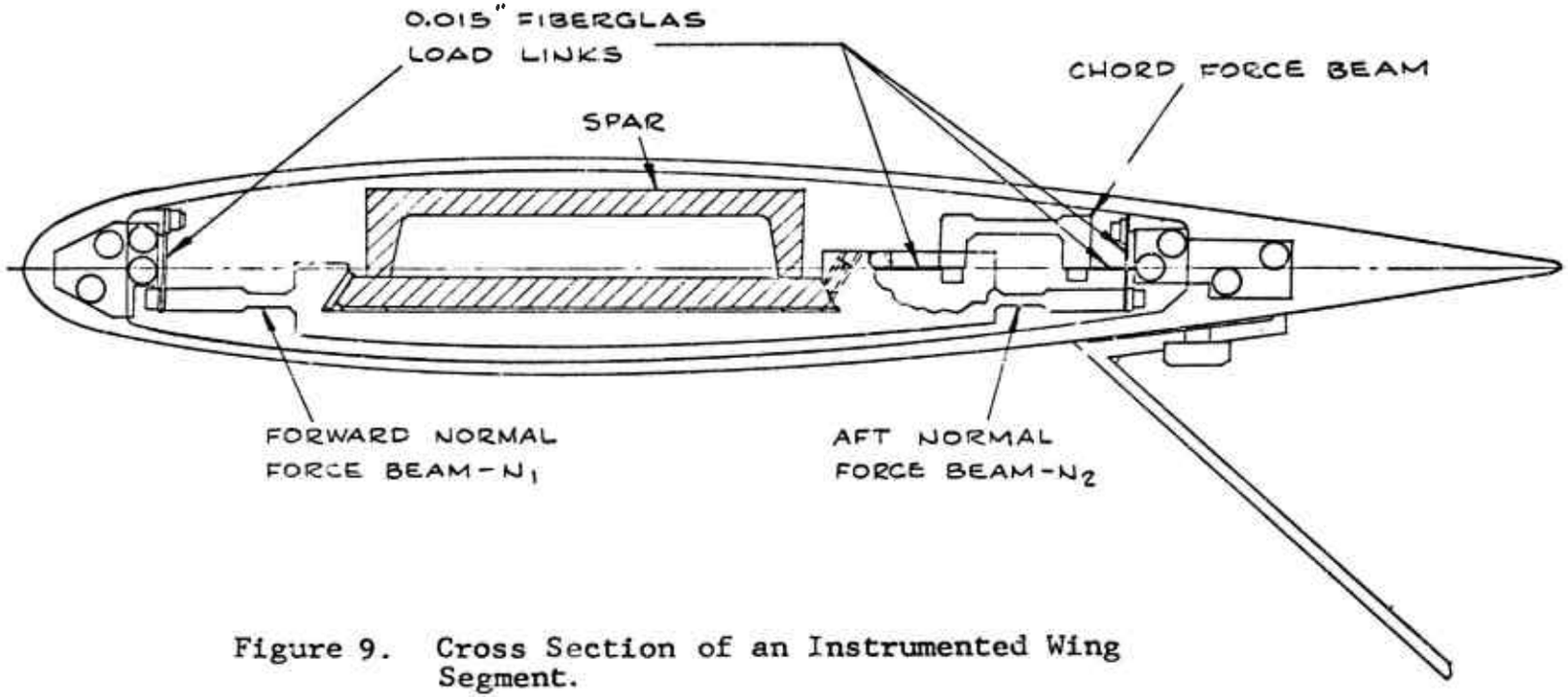

Figure 9. Cross Section of an Instrumented Wing Segment.

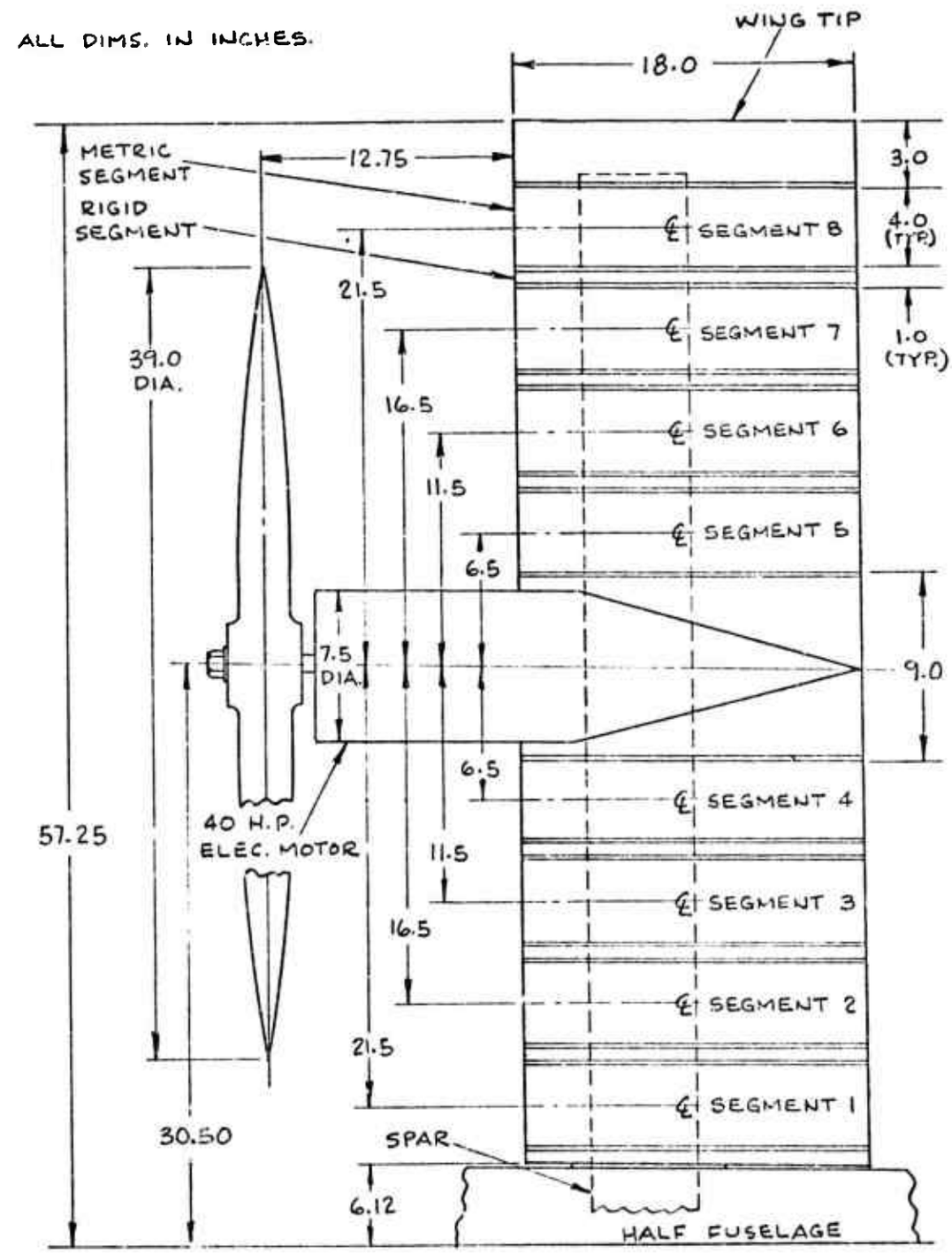

Figure 10. Powered Wing Model Geometry.

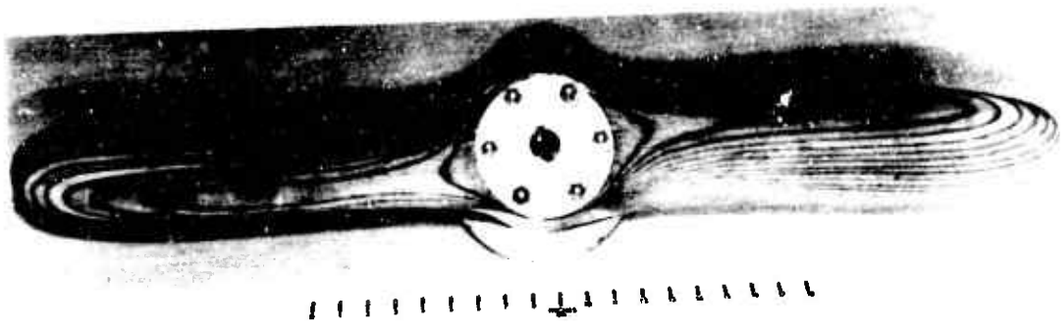

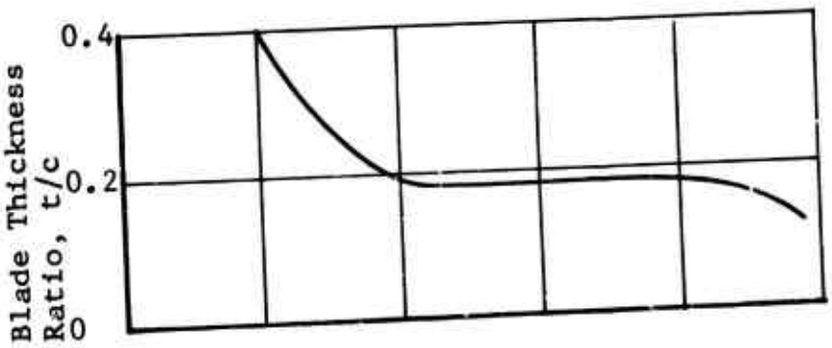

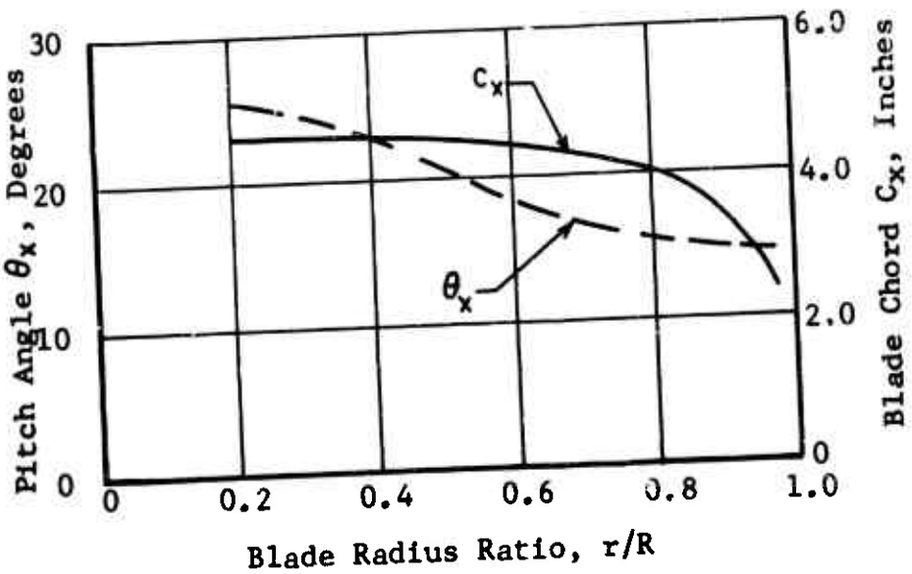

Figure 11. Propeller P_1 Blade Characteristics.

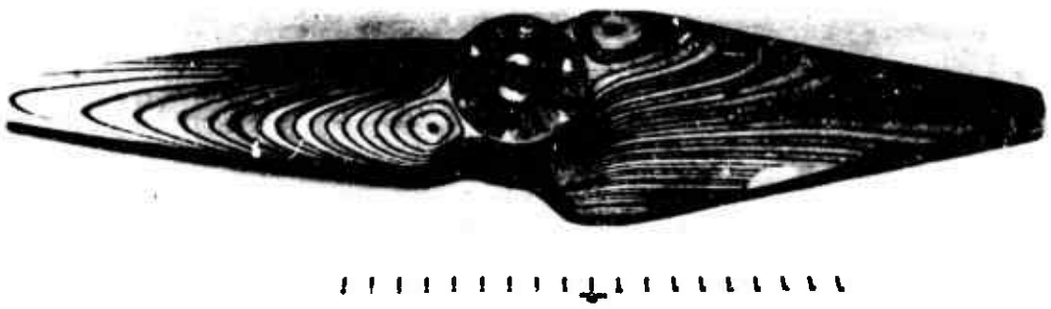

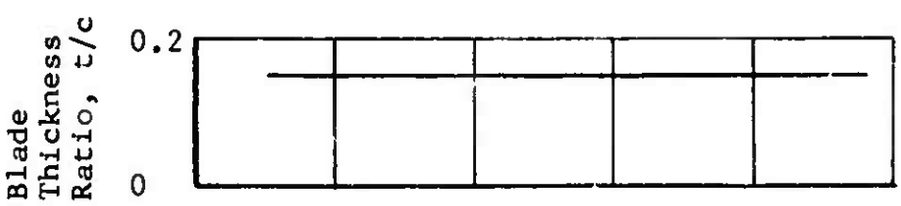

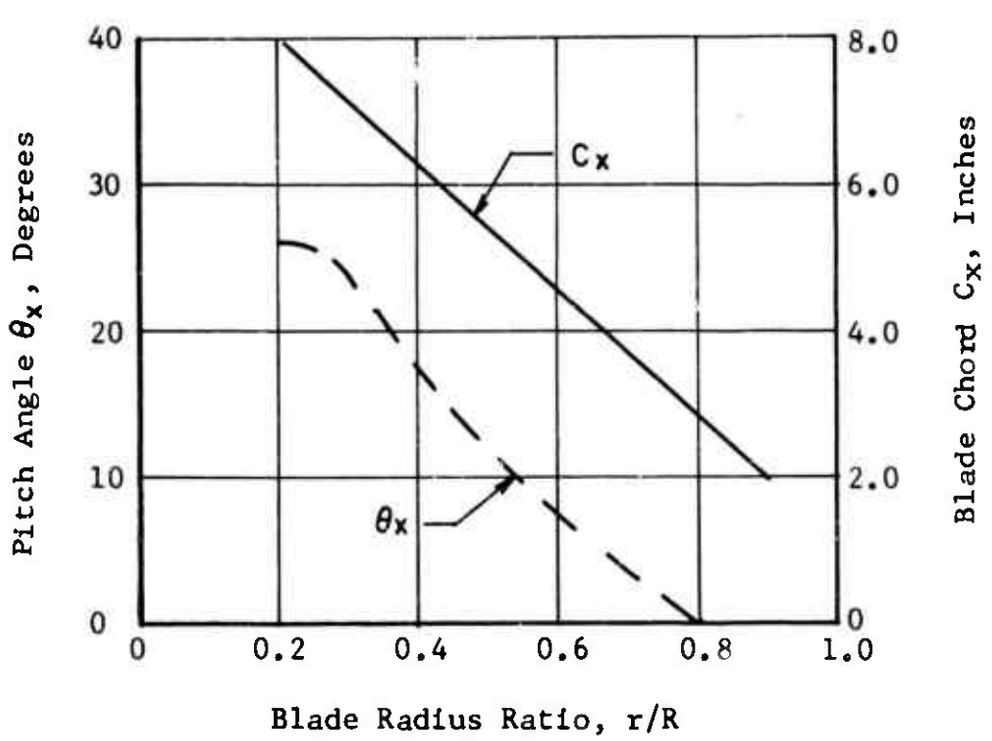

Figure 12. Propeller P_2 Blade Characteristics.

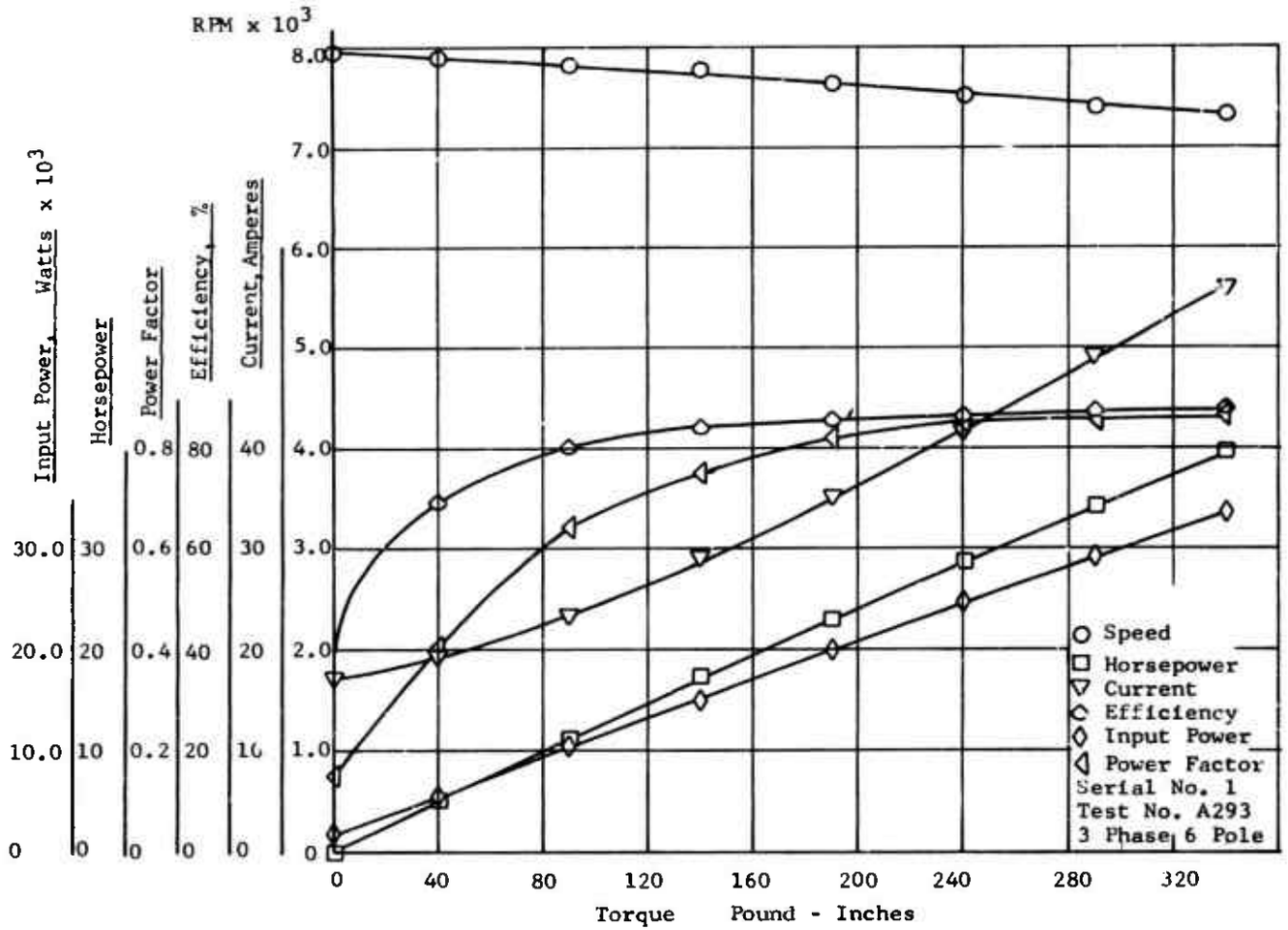

Figure 13. Calibration Curves of Task Model 11513-1 Motor.

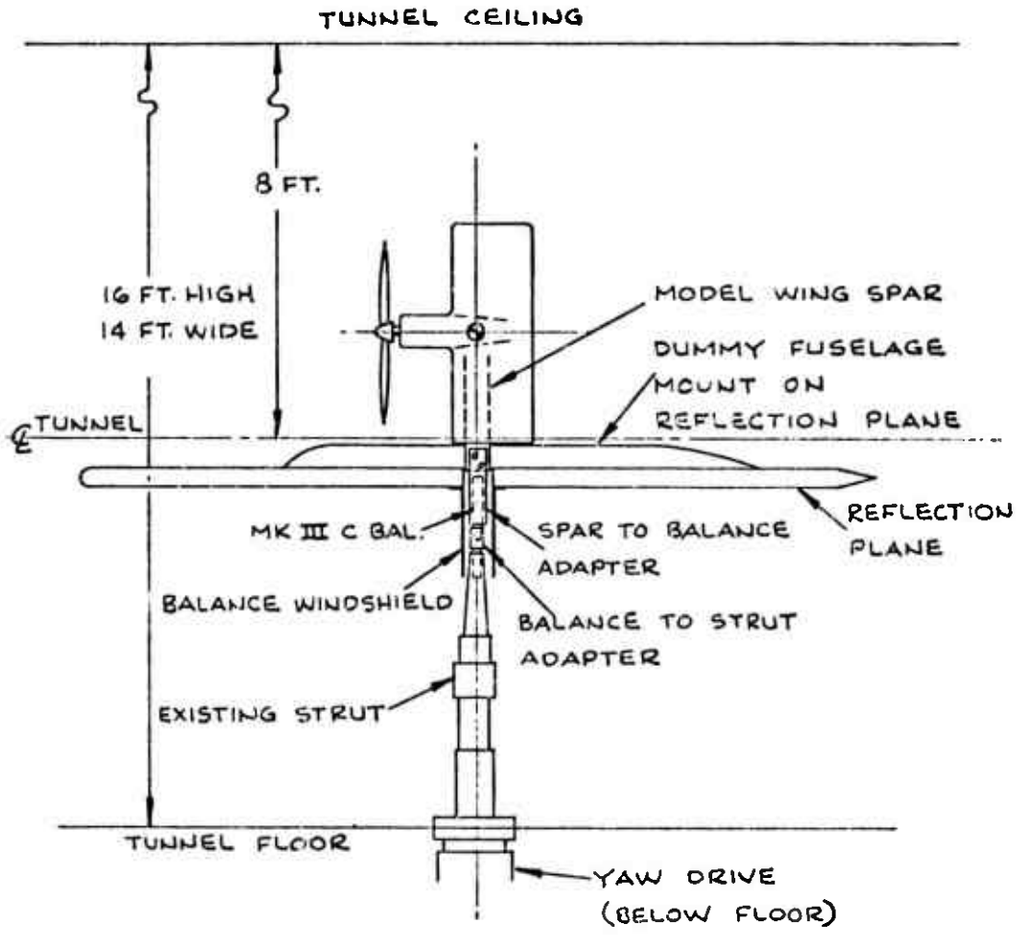

Figure 14. Model Installation in NACAL Tunnel.

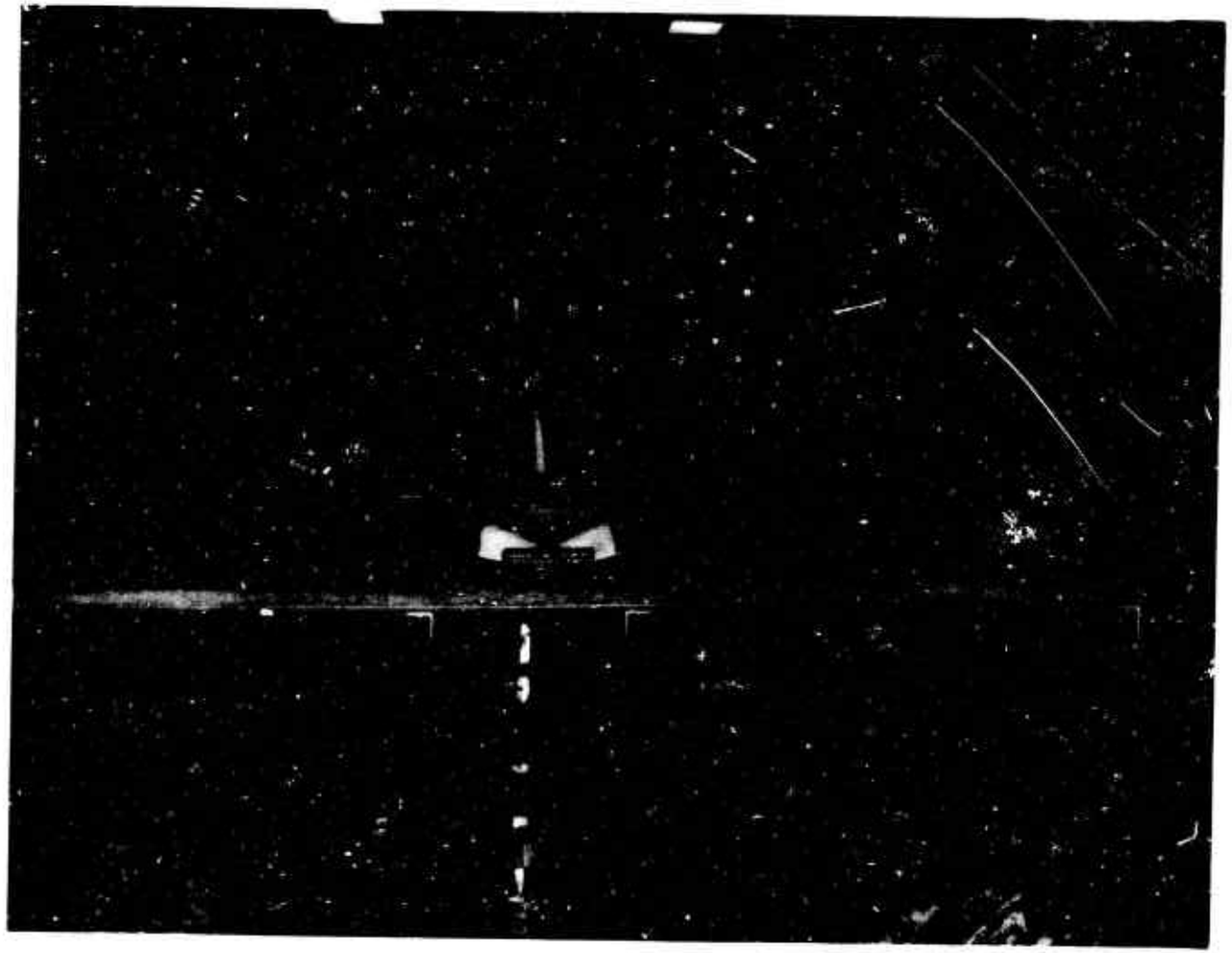

Figure 15. Rear View Showing Model Installed in 16-Foot-by-14-Foot Test Section of NACAL Wind Tunnel.

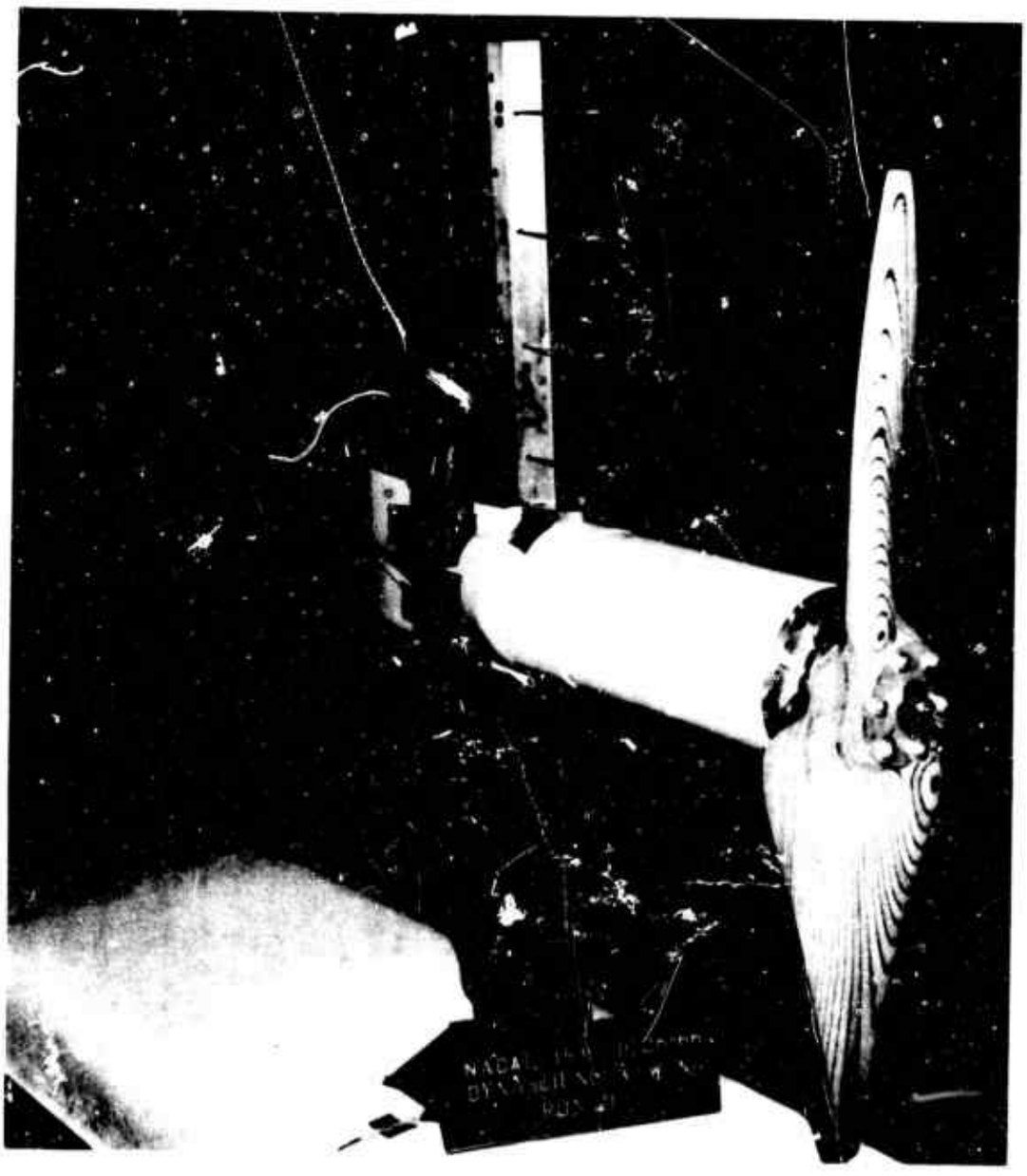

Figure 16. Front-Quarter View Showing Top Side of Wing Spar With Pressure Probes: P_2 B_1.

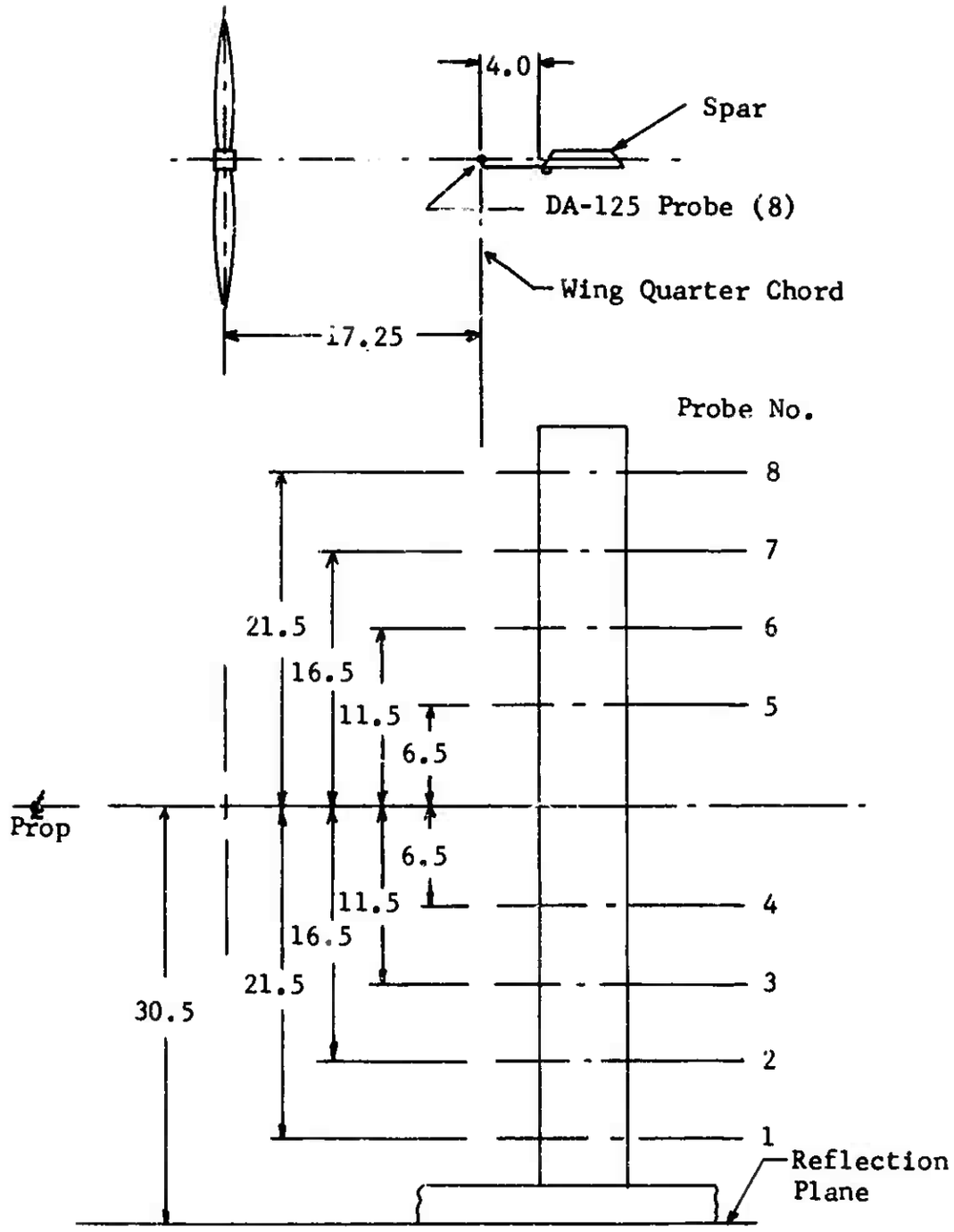

Figure 17. Pressure Probe Rake Arrangement.

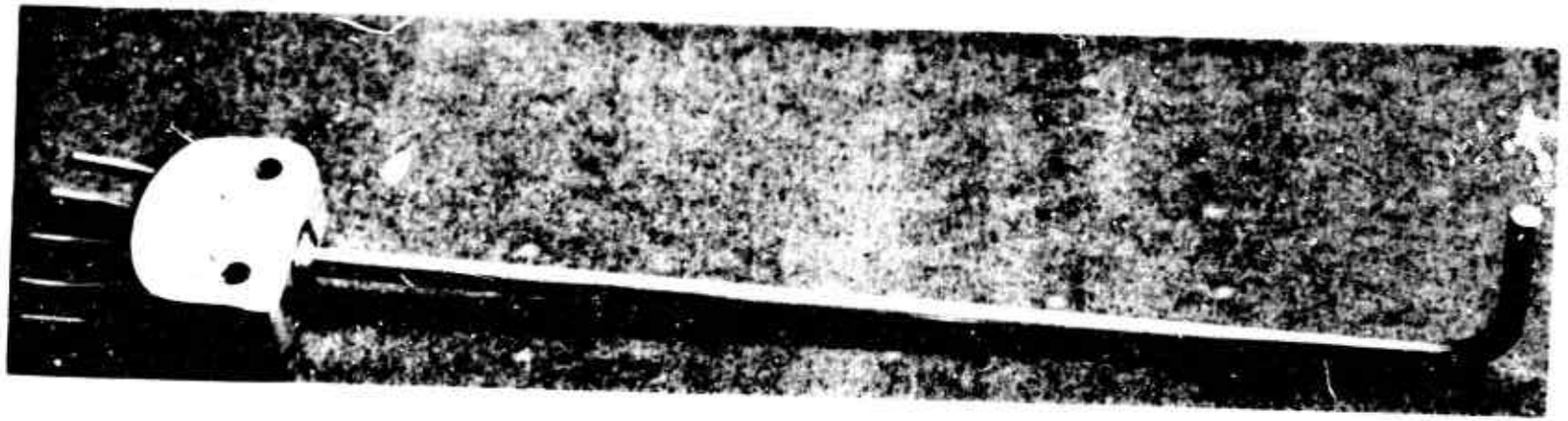

Figure 18. United Sensor 3-D Probe Model DA-125.

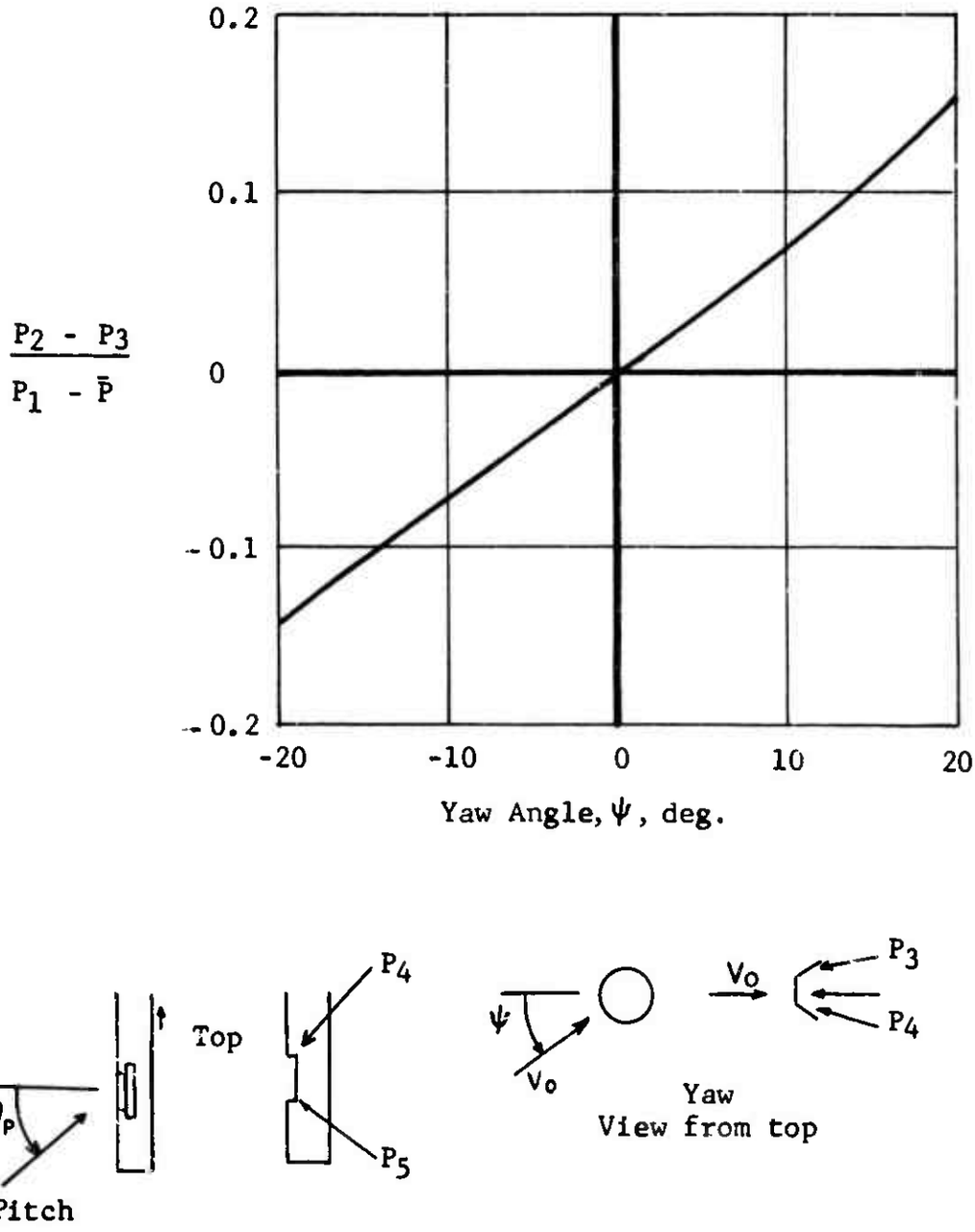

Figure 19. 3-D Pressure Probe, Yaw Angle Calibration (Probe #5).

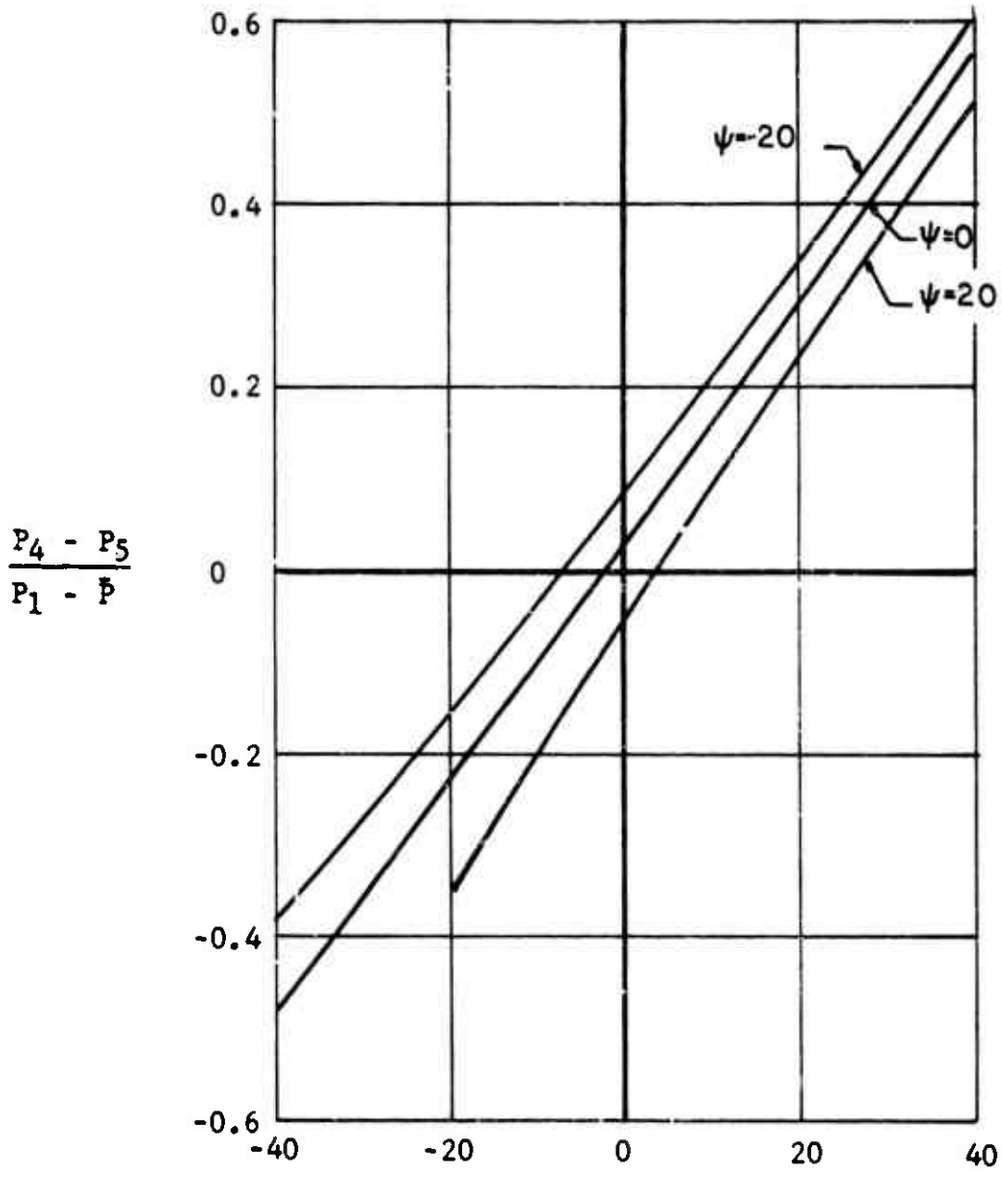

Figure 20. 3-D Pressure Probe, Pitch Angle Calibration (Probe #5).

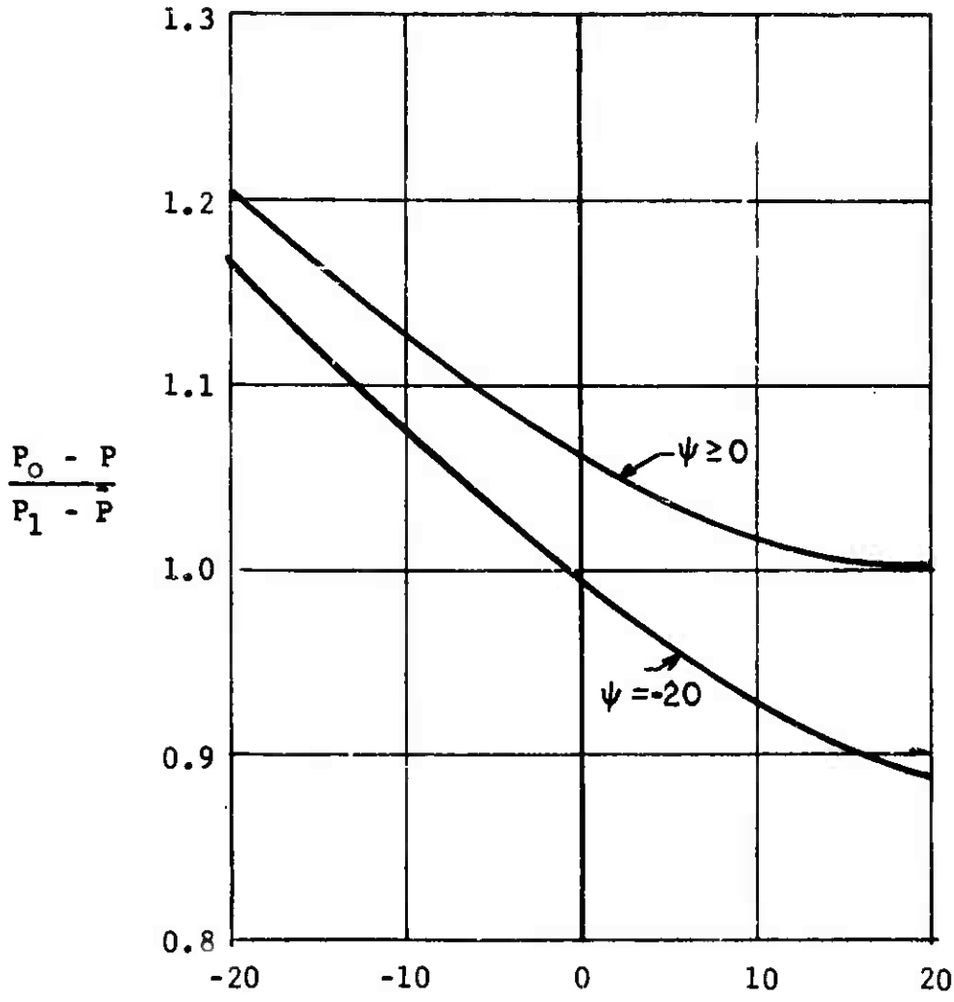

P_o - Stagnation Pressure
P - Static (True) Pressure

Figure 21. 3-D Pressure Probe, Velocity Head Calibration (Probe #5).

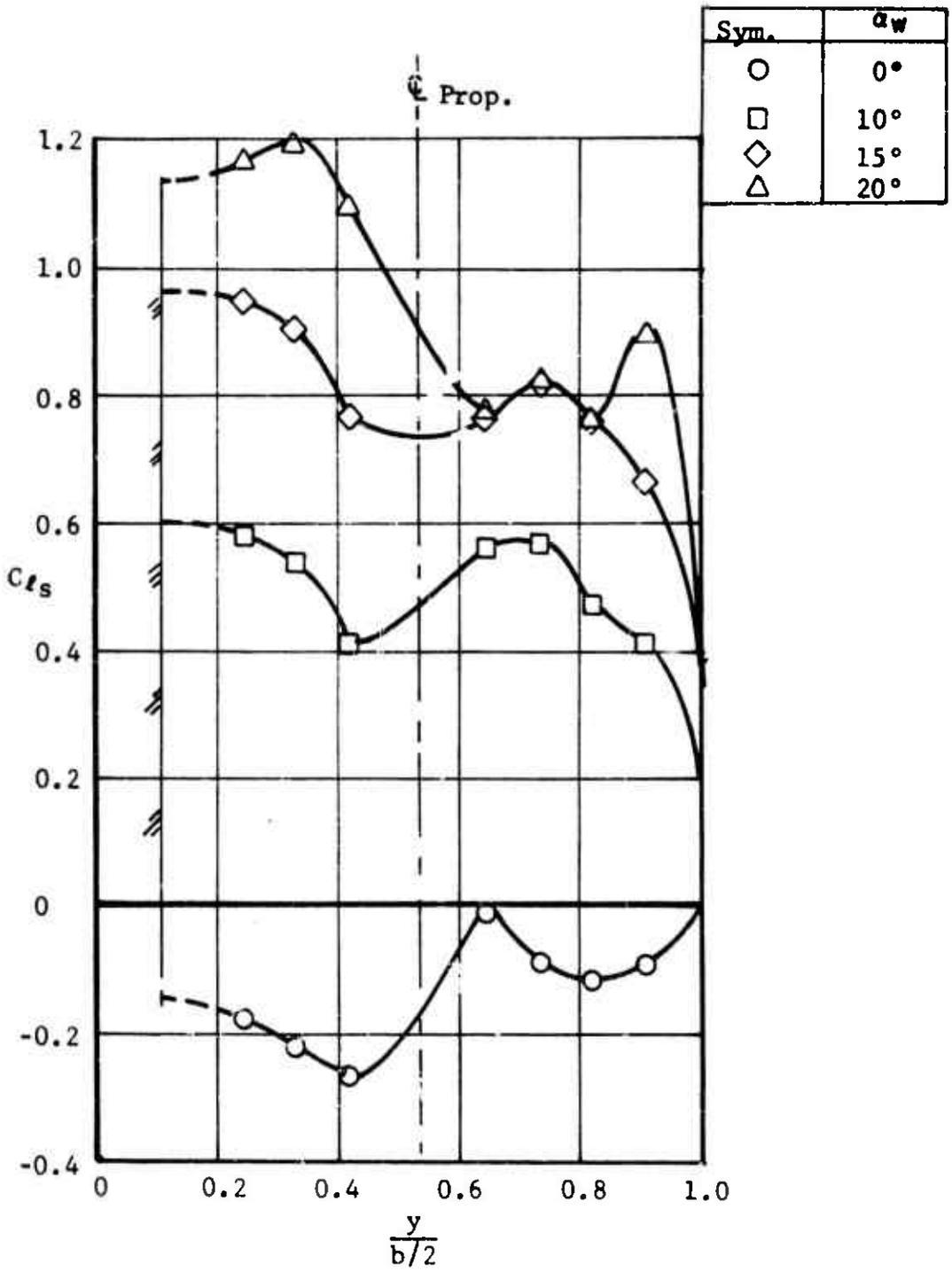

Figure 22. Spanwise Distribution of Slipstream Lift Coefficient, C_{ℓ} = -0.1.

Configuration: P_1 V_1 B_1.

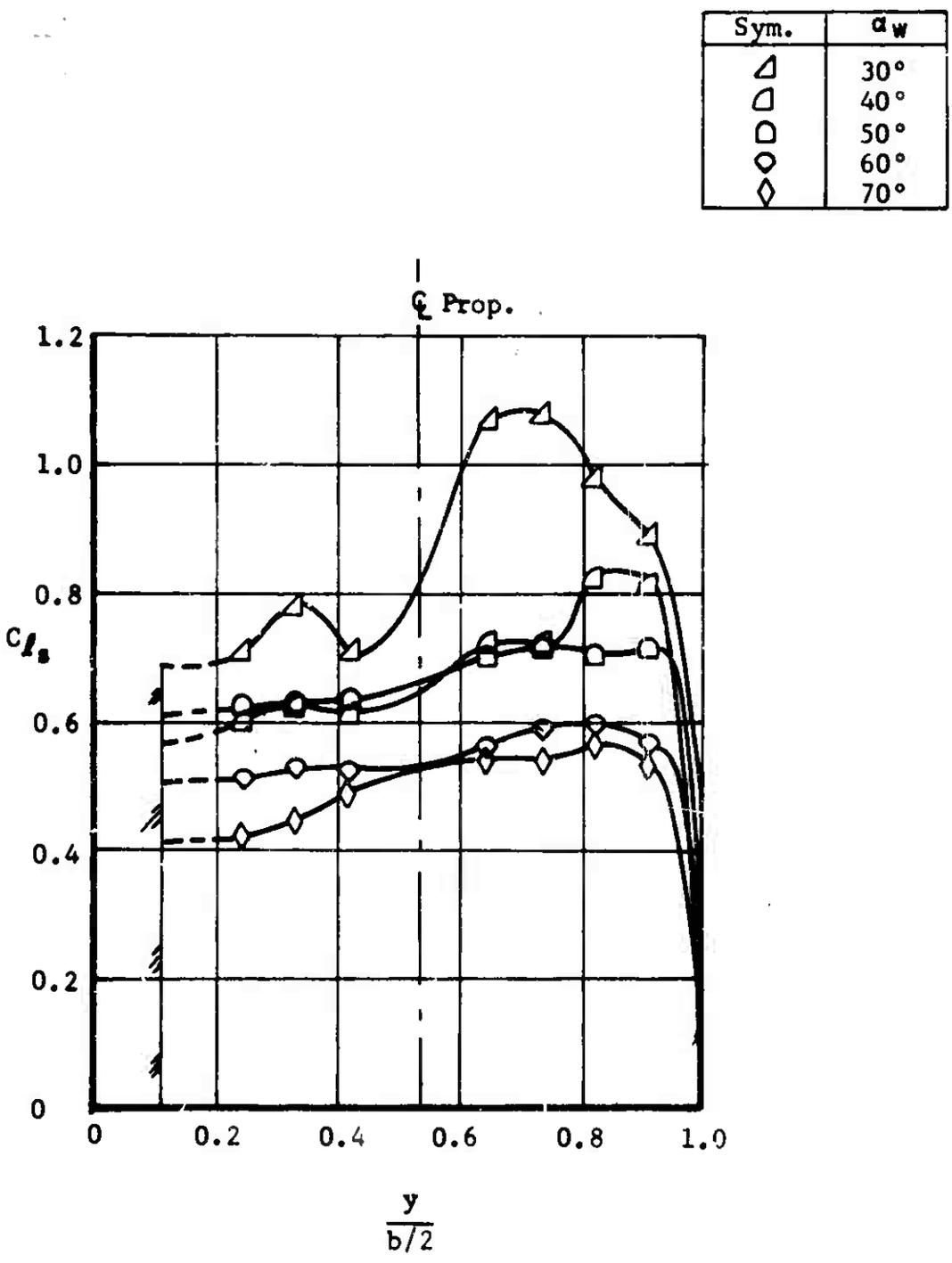

Figure 22. (Continued).

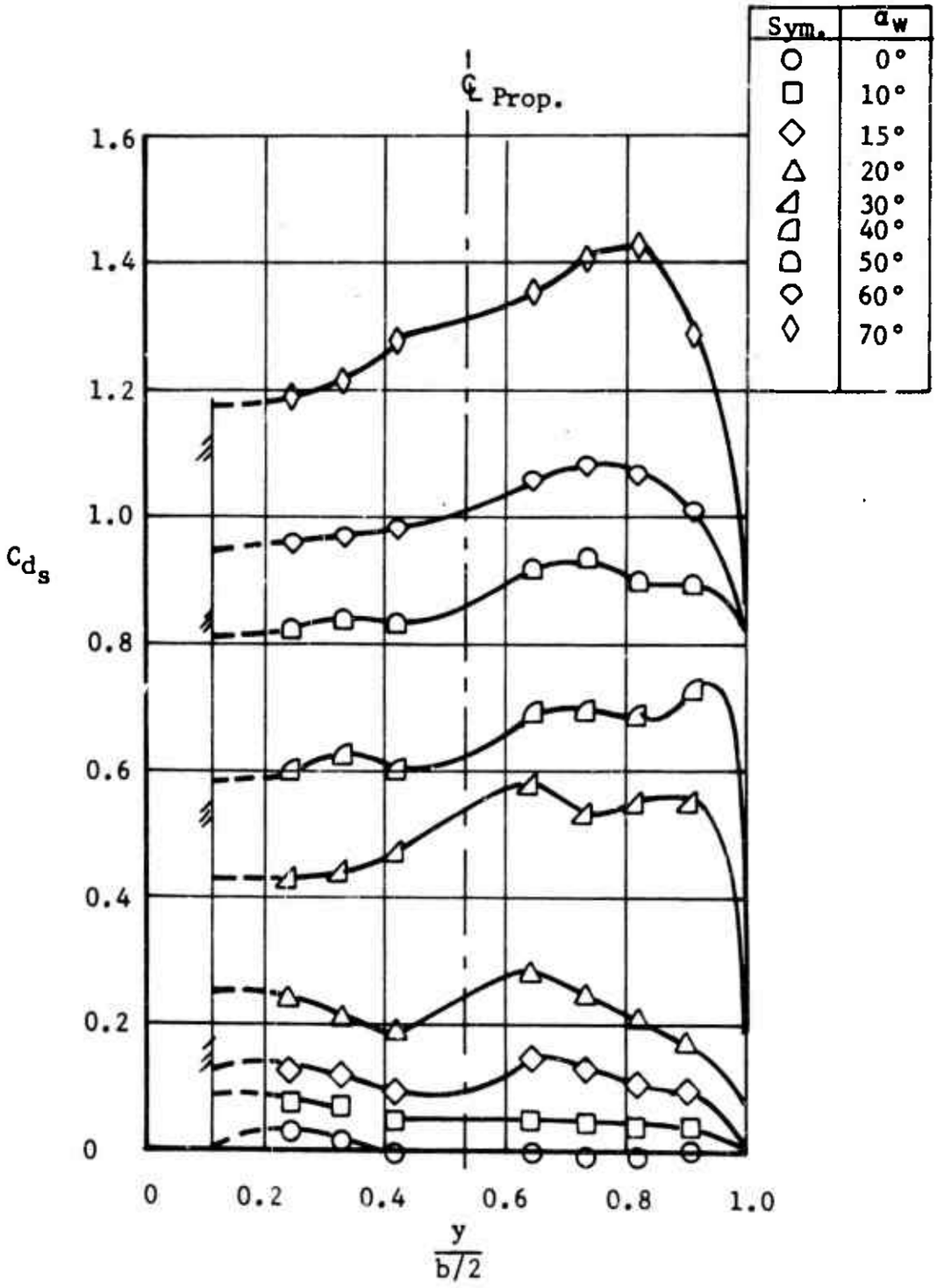

Figure 23. Spanwise Distribution of Slipstream Drag Coefficient, $C_{T_s} = -0.1$. Configuration: P_1 W_1 B_1.

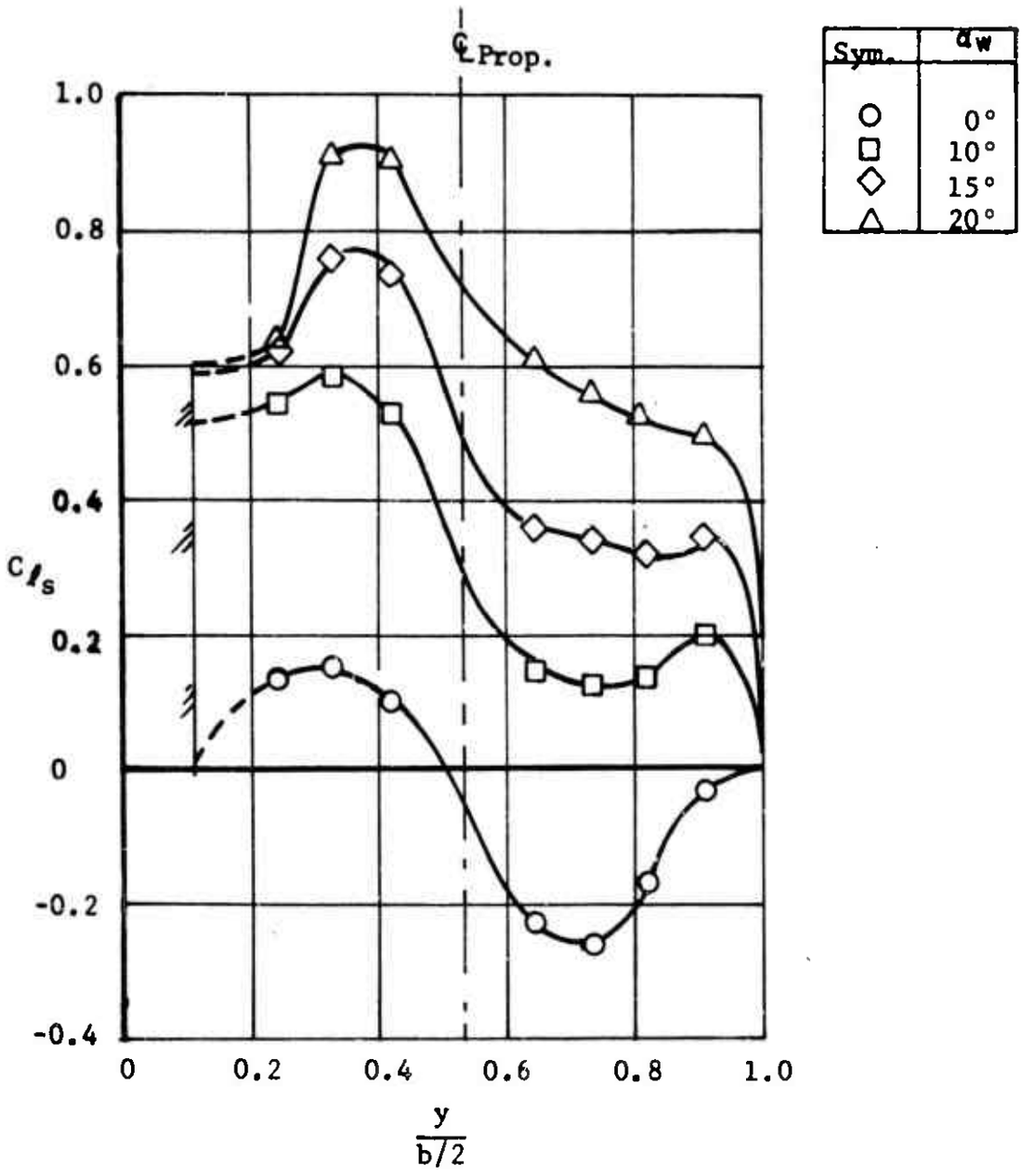

Figure 24. Spanwise Distribution of Slipstream Lift Coefficient, $C_{T_s} = 0.6$.
Configuration: P_1 W_1 B_1.

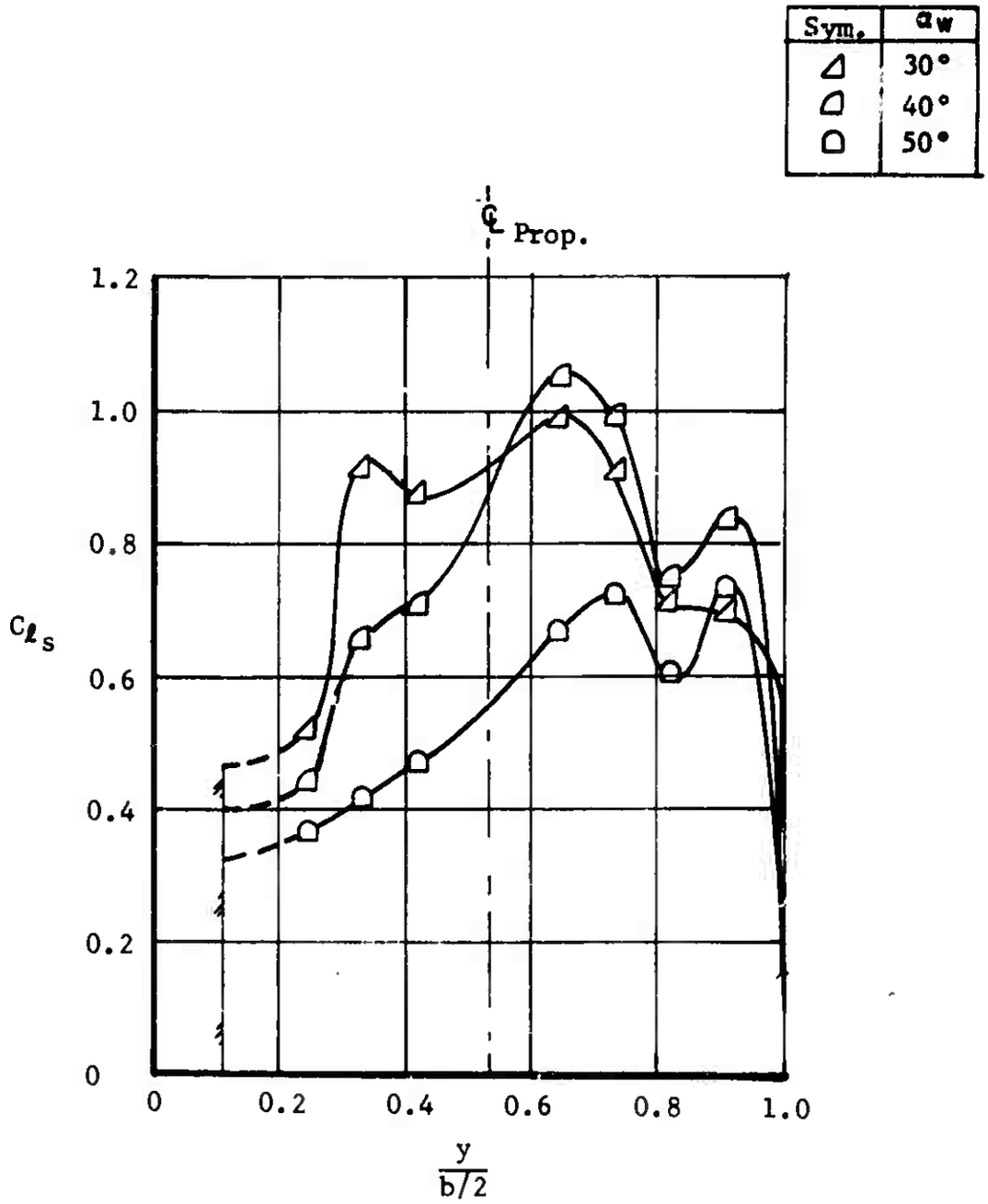

Figure 24. (Continued).

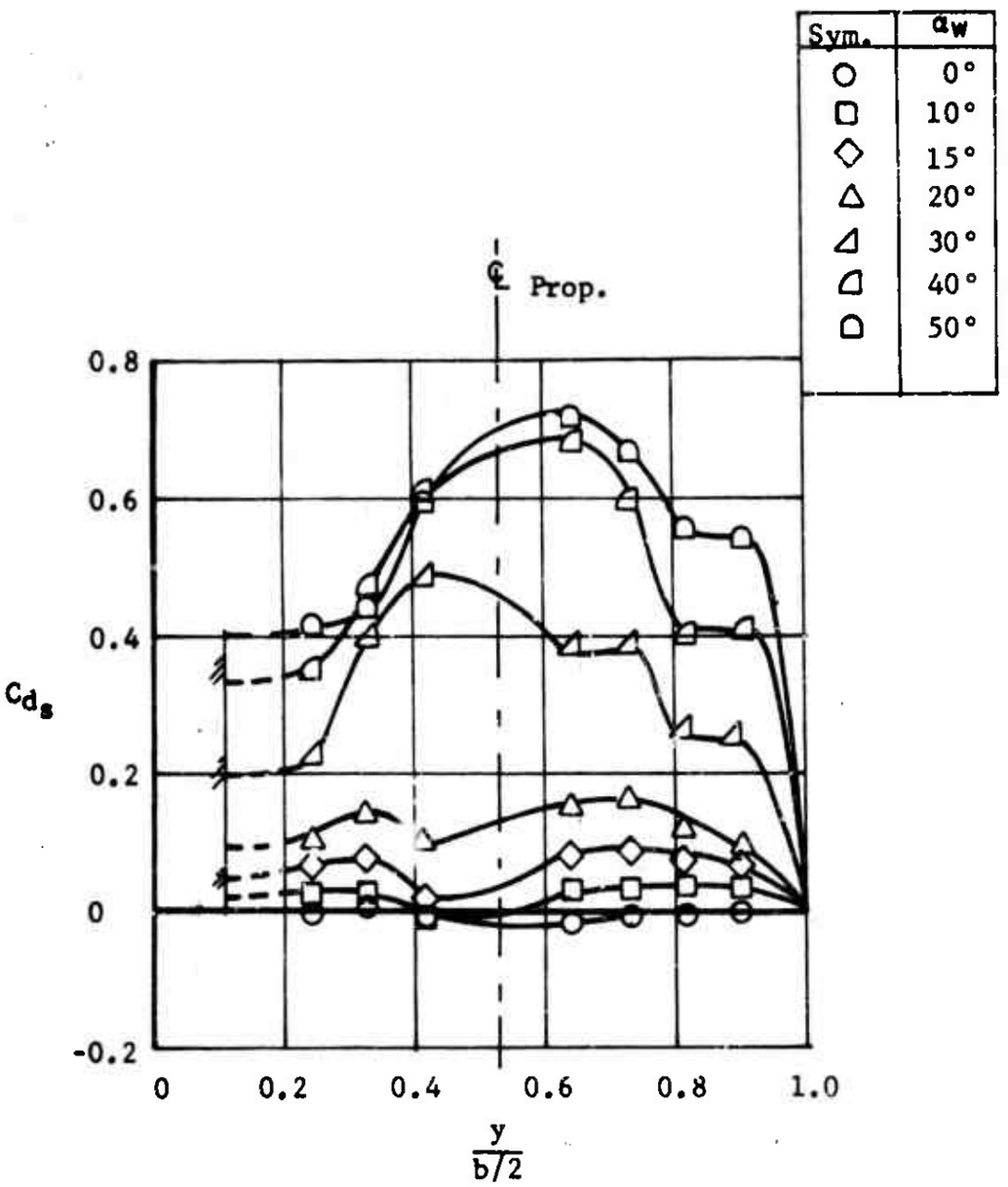

Figure 25. Spanwise Distribution of Slipstream Drag Coefficient, $C_{T_s} = 0.6$.
Configuration: P_1 W_1 B_1.

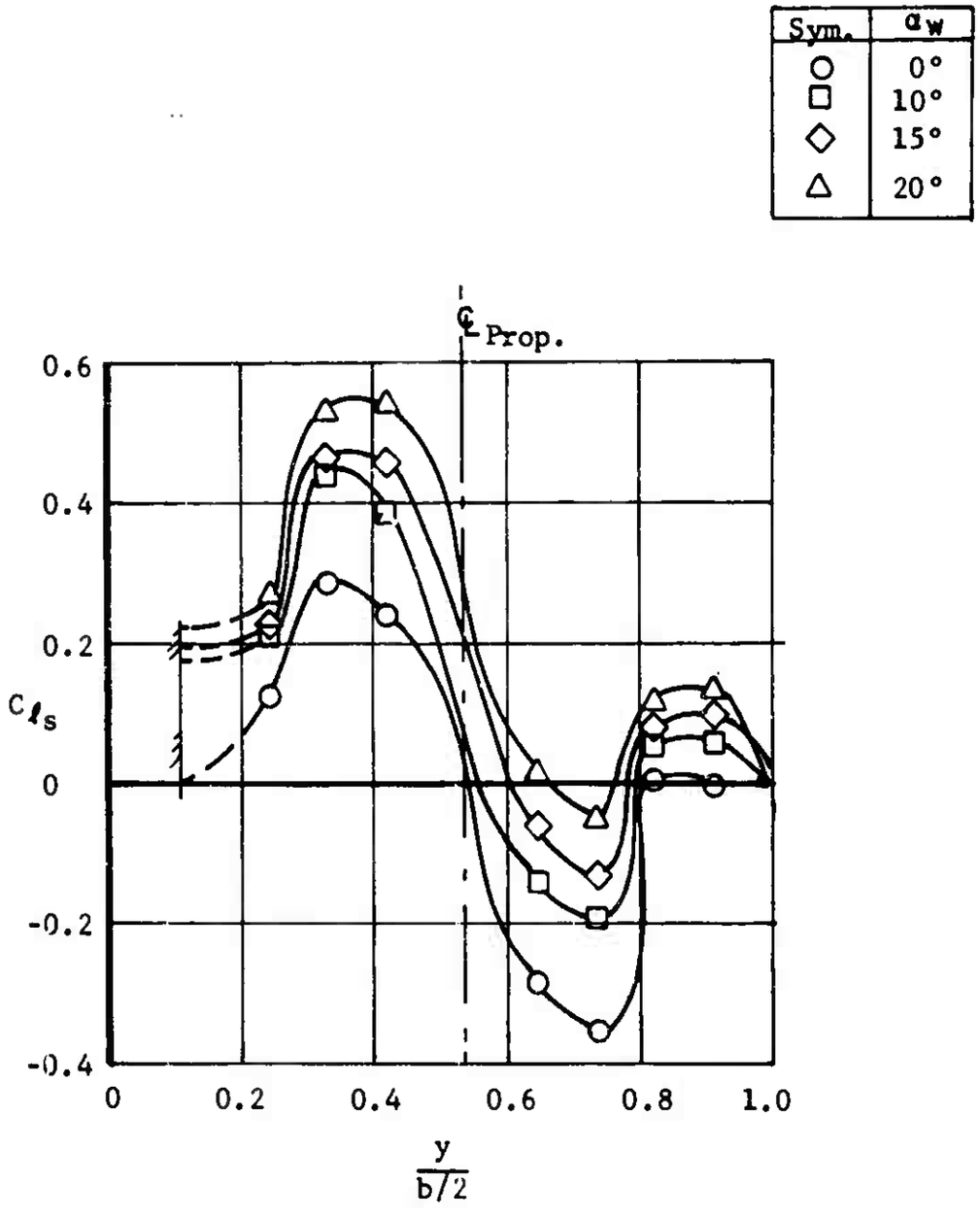

Figure 26. Spanwise Distribution of Slipstream Lift Coefficient, $C_{T_s} = 0.93$.
Configuration: P_1 W_1 B_1.

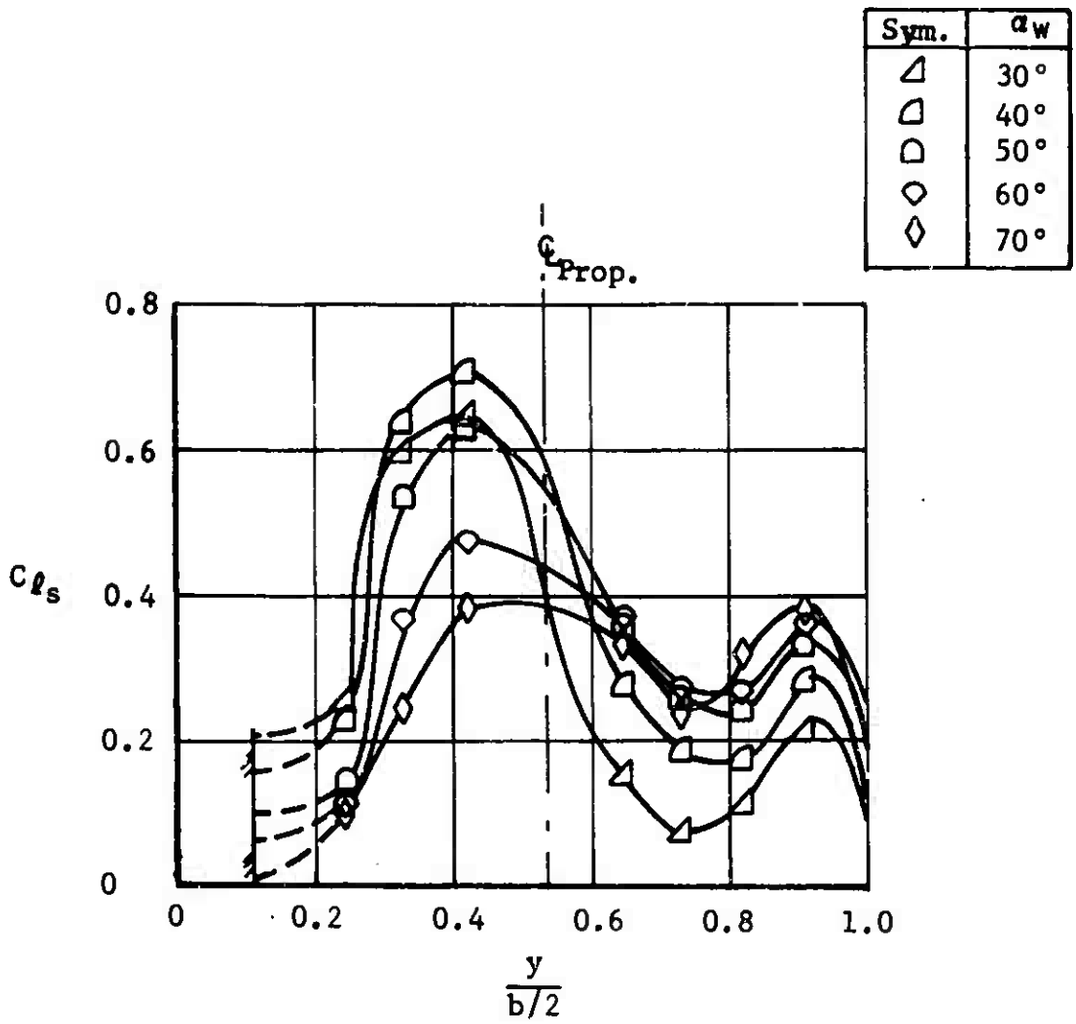

Figure 26. (Continued).

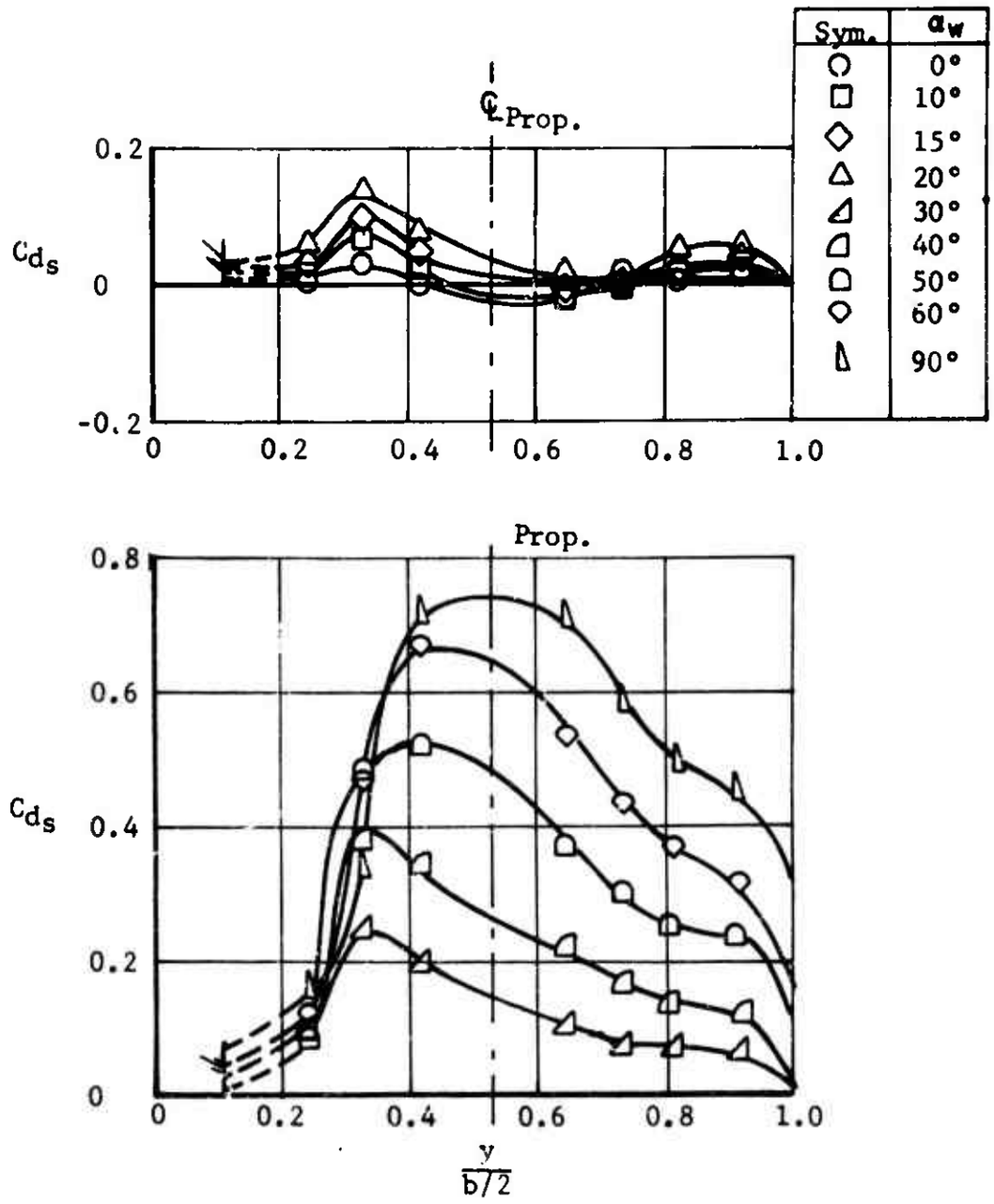

Figure 27. Spanwise Distribution of Slipstream Drag Coefficient, $C_{T_s} = 0.93$.

Configuration: P_1 W_1 B_1.

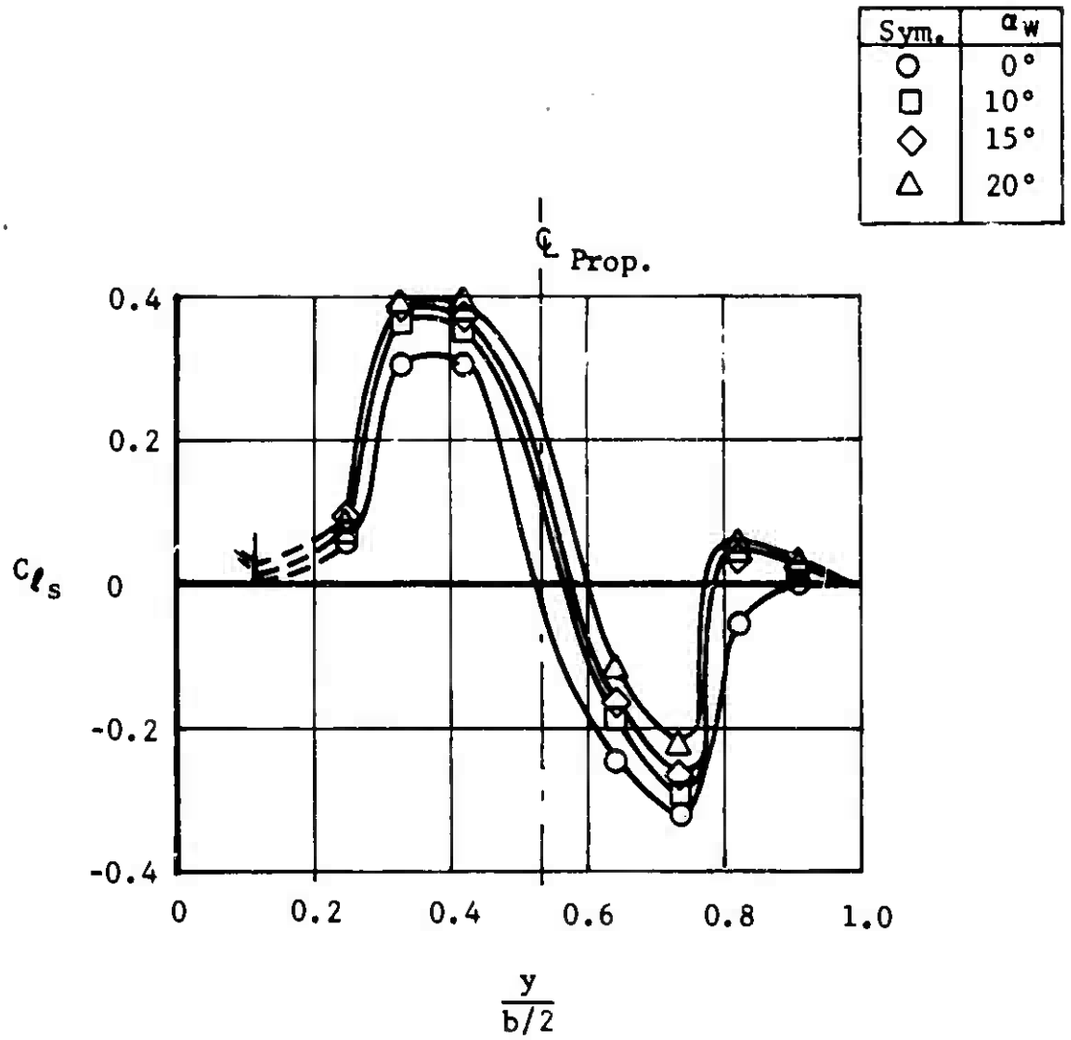

Figure 28. Spanwise Distribution of Slipstream Lift Coefficient, $C_{T_s} = 0.97$.
Configuration: P_1 W_1 B_1.

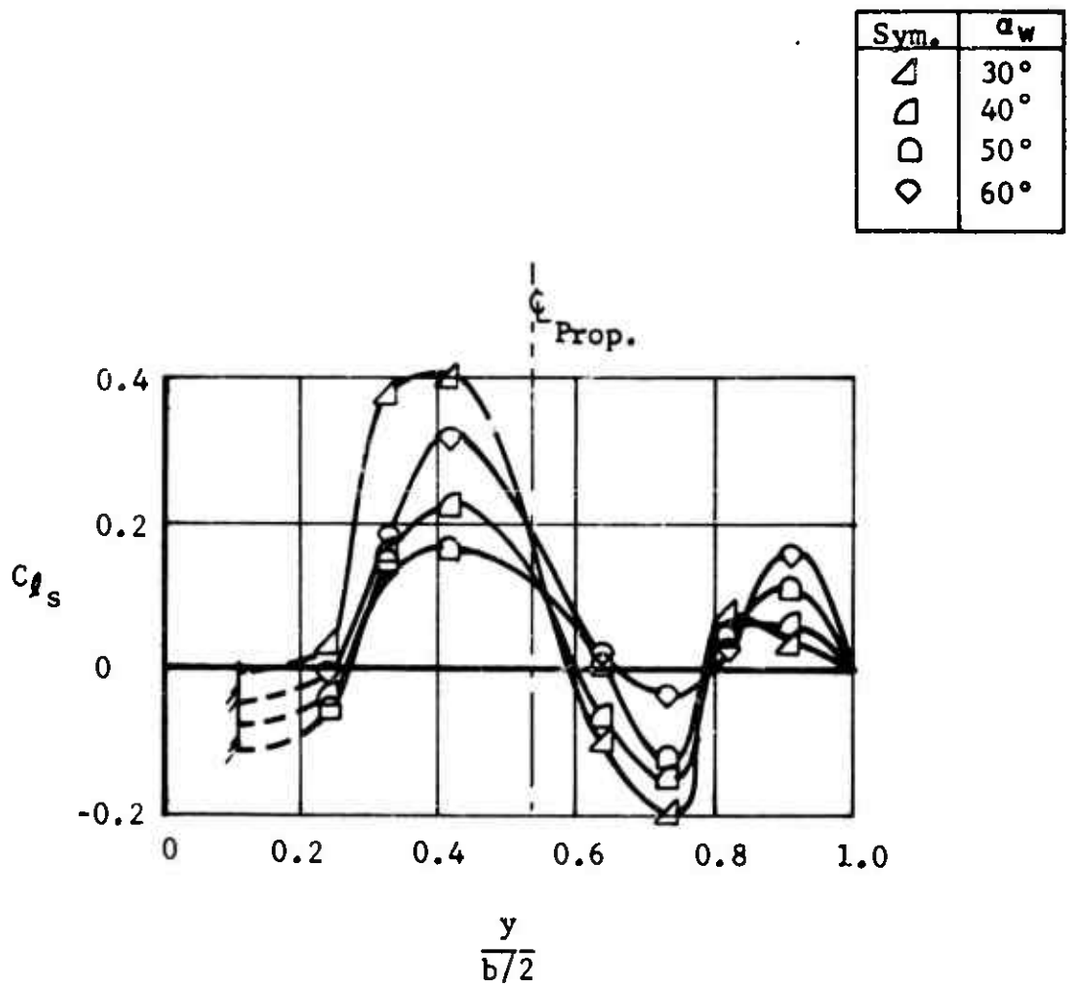

Figure 28. (Continued).

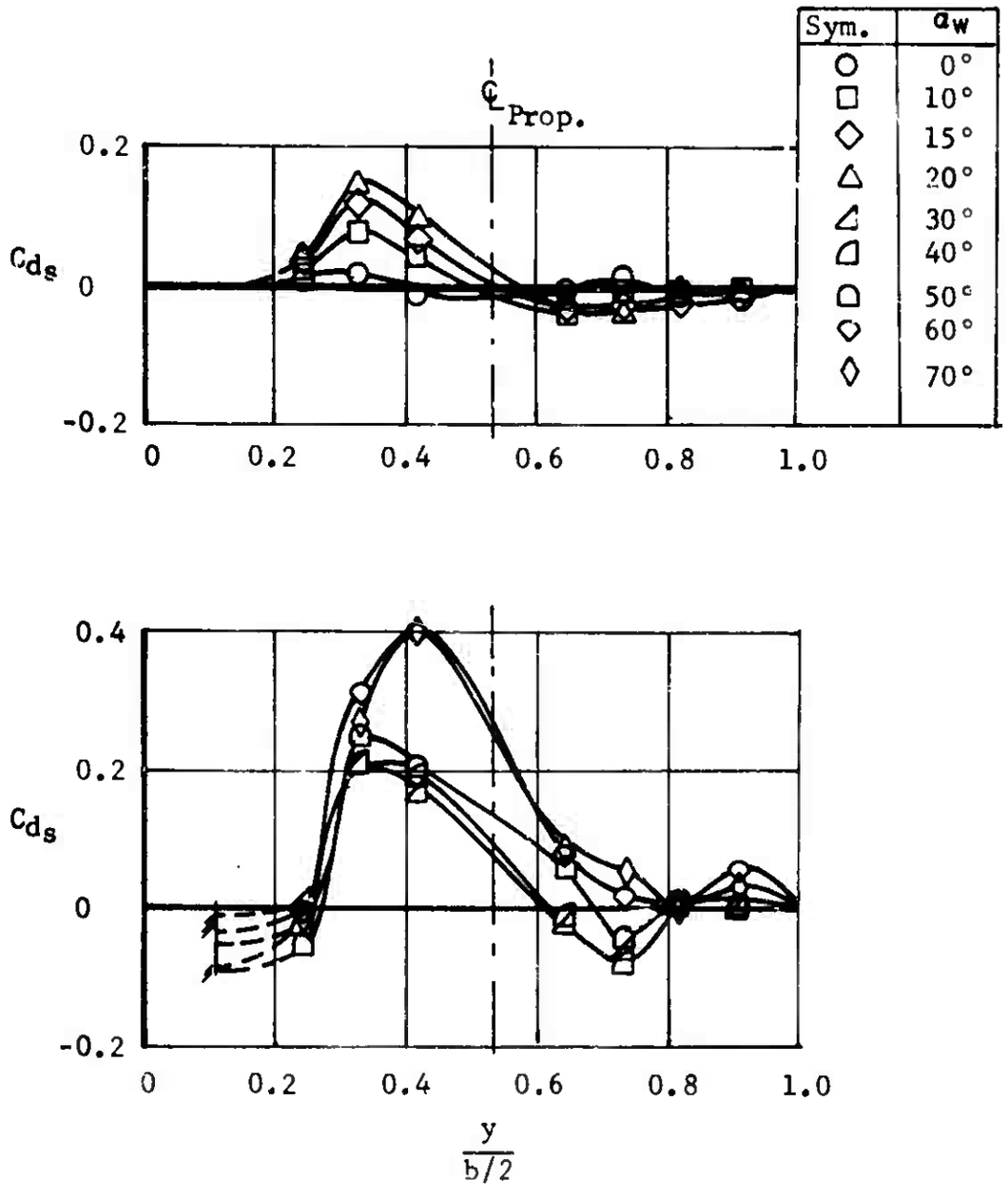

Figure 29. Spanwise Distribution of Slipstream Drag Coefficient, $C_{T_s} = 0.97$.
Configuration: P_1 W_1 P_1.

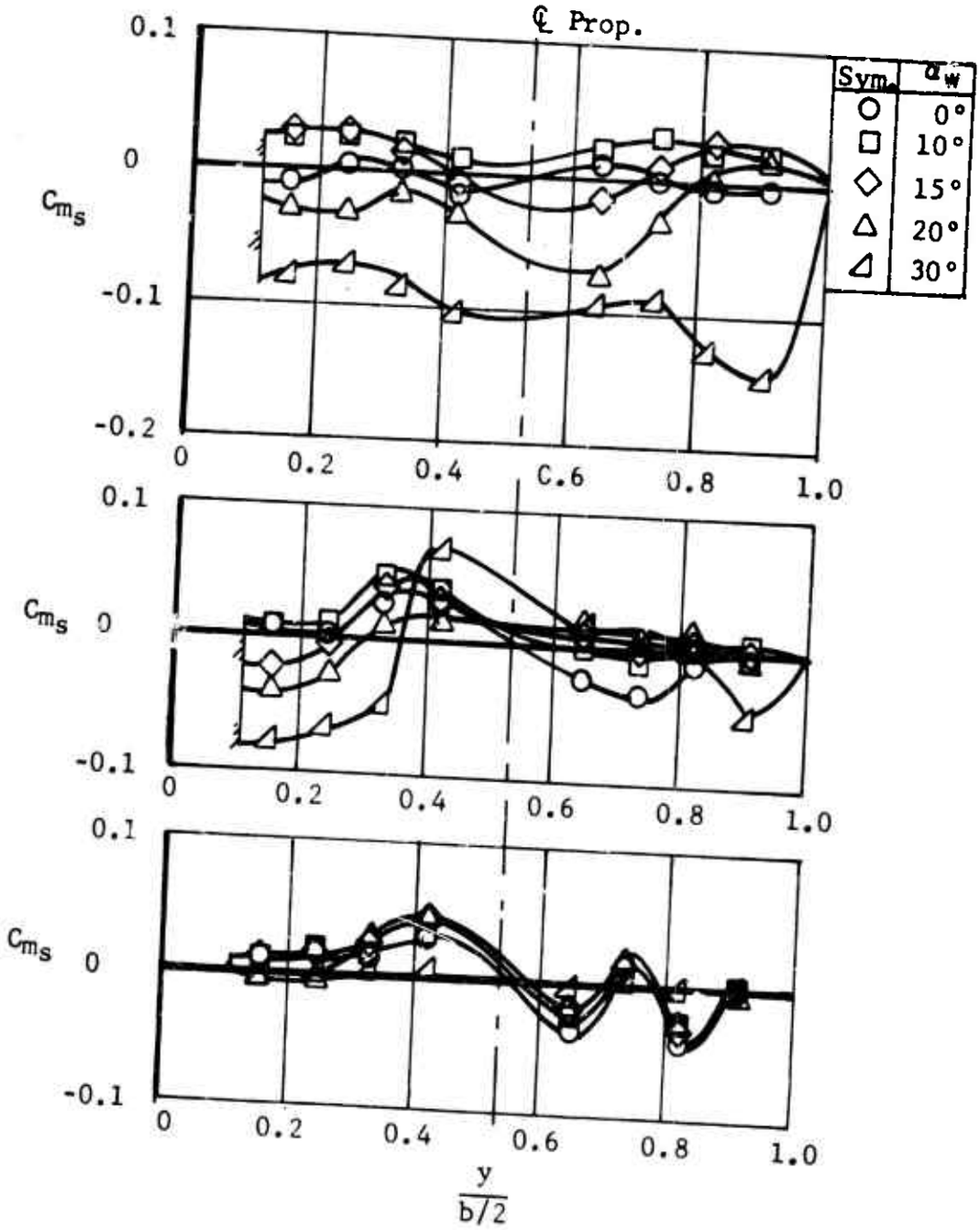

Figure 30. Spanwise Distribution of Slipstream Pitching Moment Coefficient as Function of C_{T_s}. Configuration: P_1 W_1 B_1.

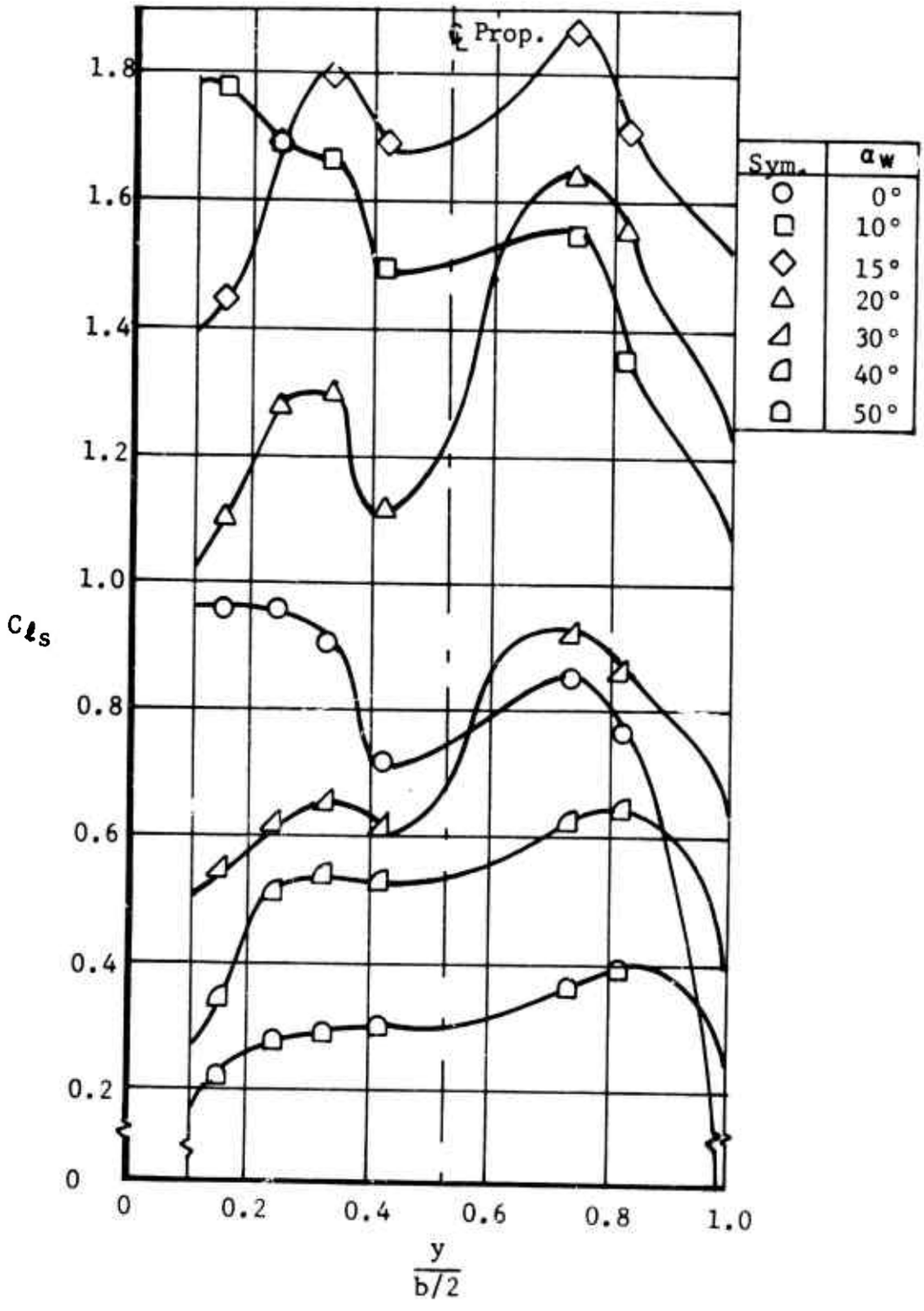

Figure 31. Spanwise Distribution of Slipstream Lift Coefficient, C_{T_s} =-0.1. Configuration: P_1 W_1 F_1 B_1.

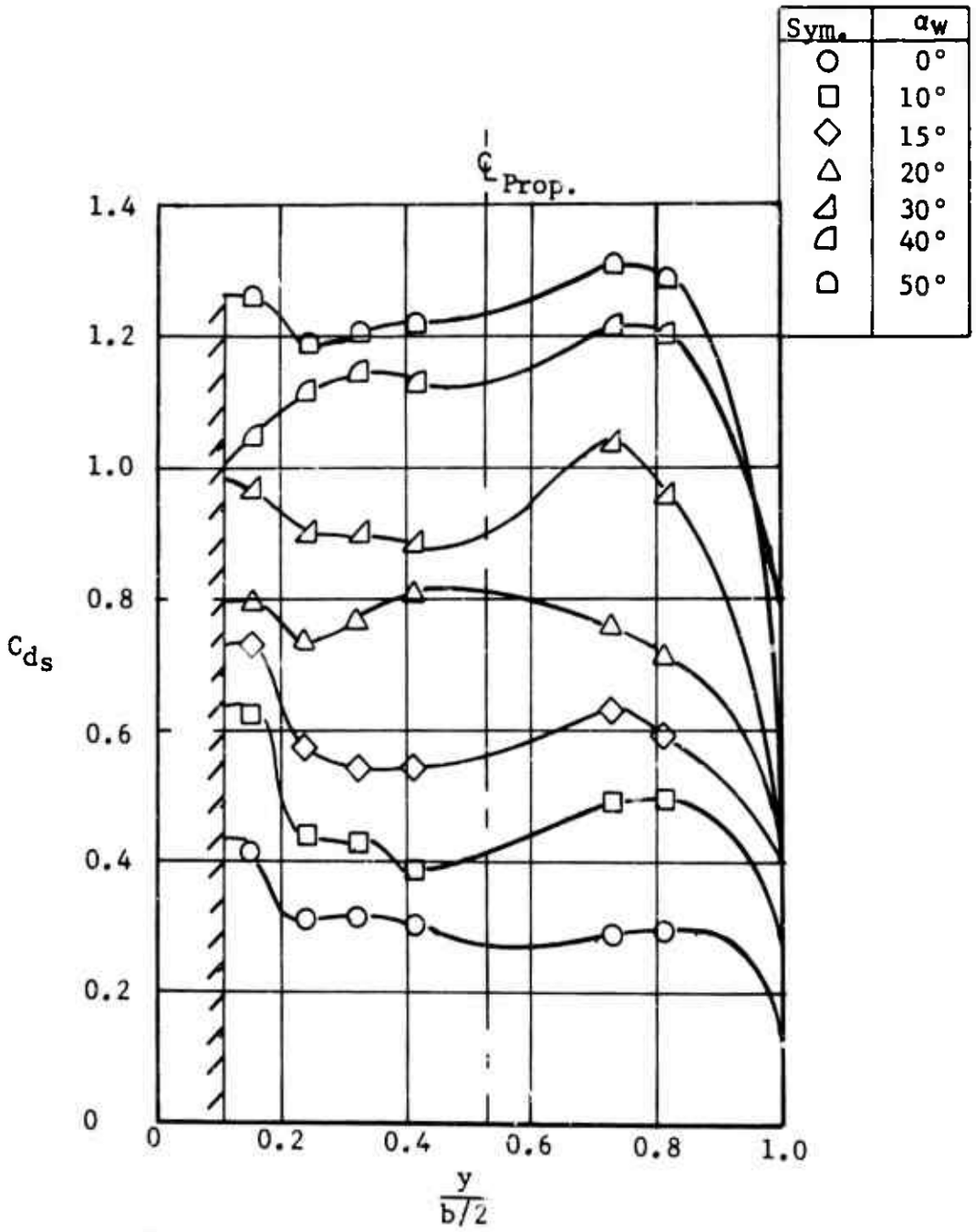

Figure 32. Spanwise Distribution of Slipstream Drag Coefficient, $C_{T_s} = -0.1$. Configuration: P_1 W_1 F_1 B_1.

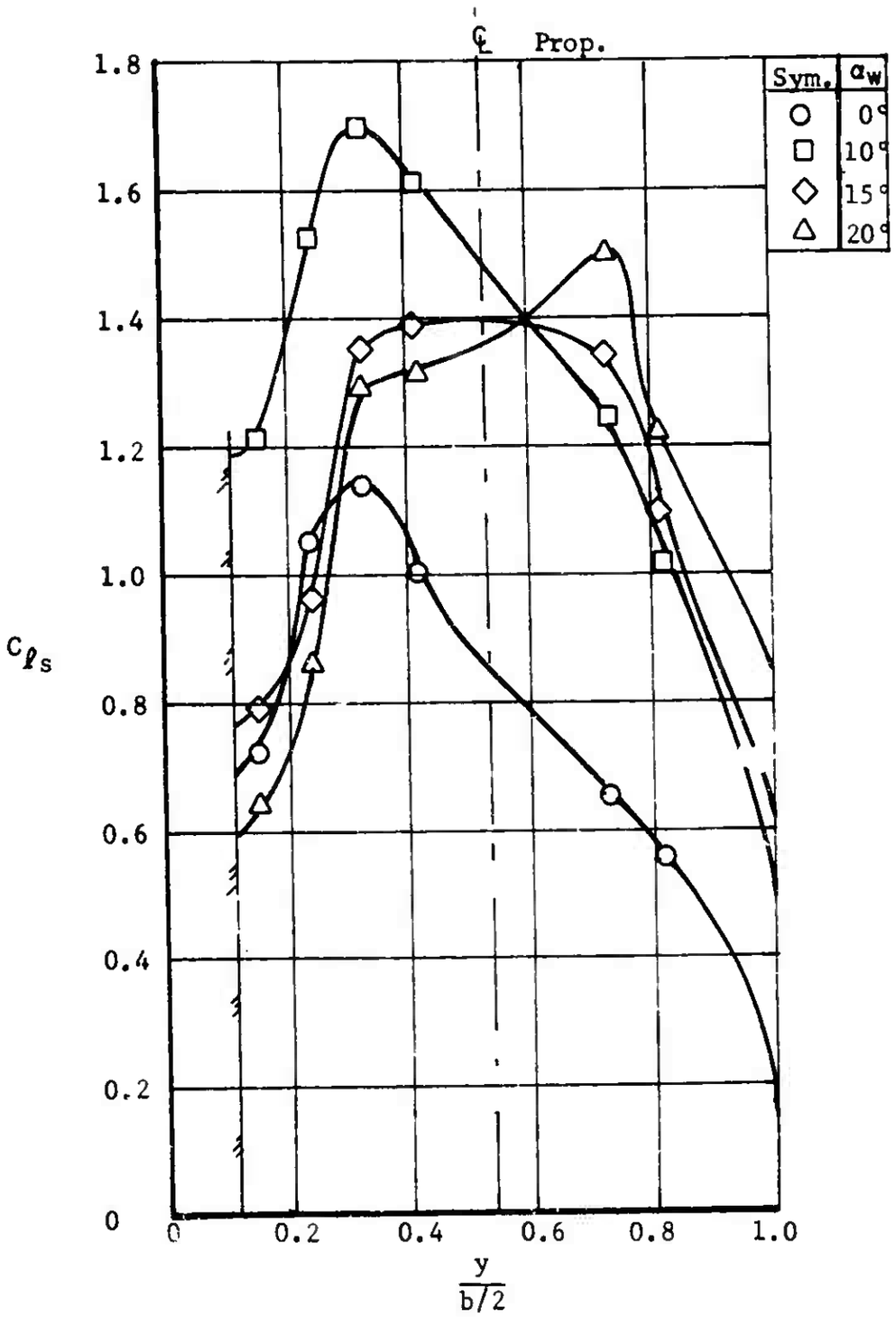

Figure 33. Spanwise Distribution of Slipstream Lift Coefficient, $C_{T_s} = 0.46$. Configuration: P_1 W_1 F_1 B_1.

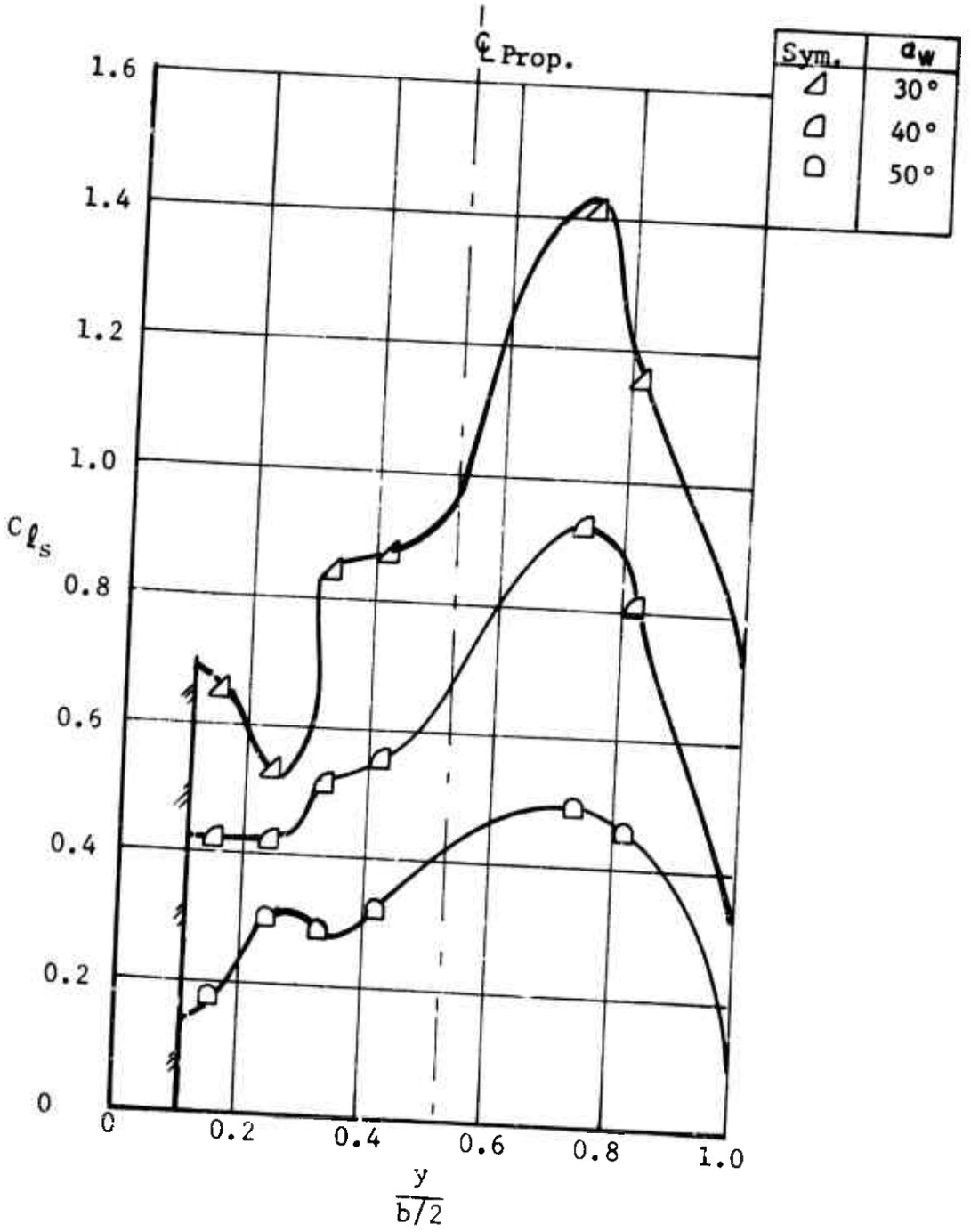

Figure 33. (Continued).

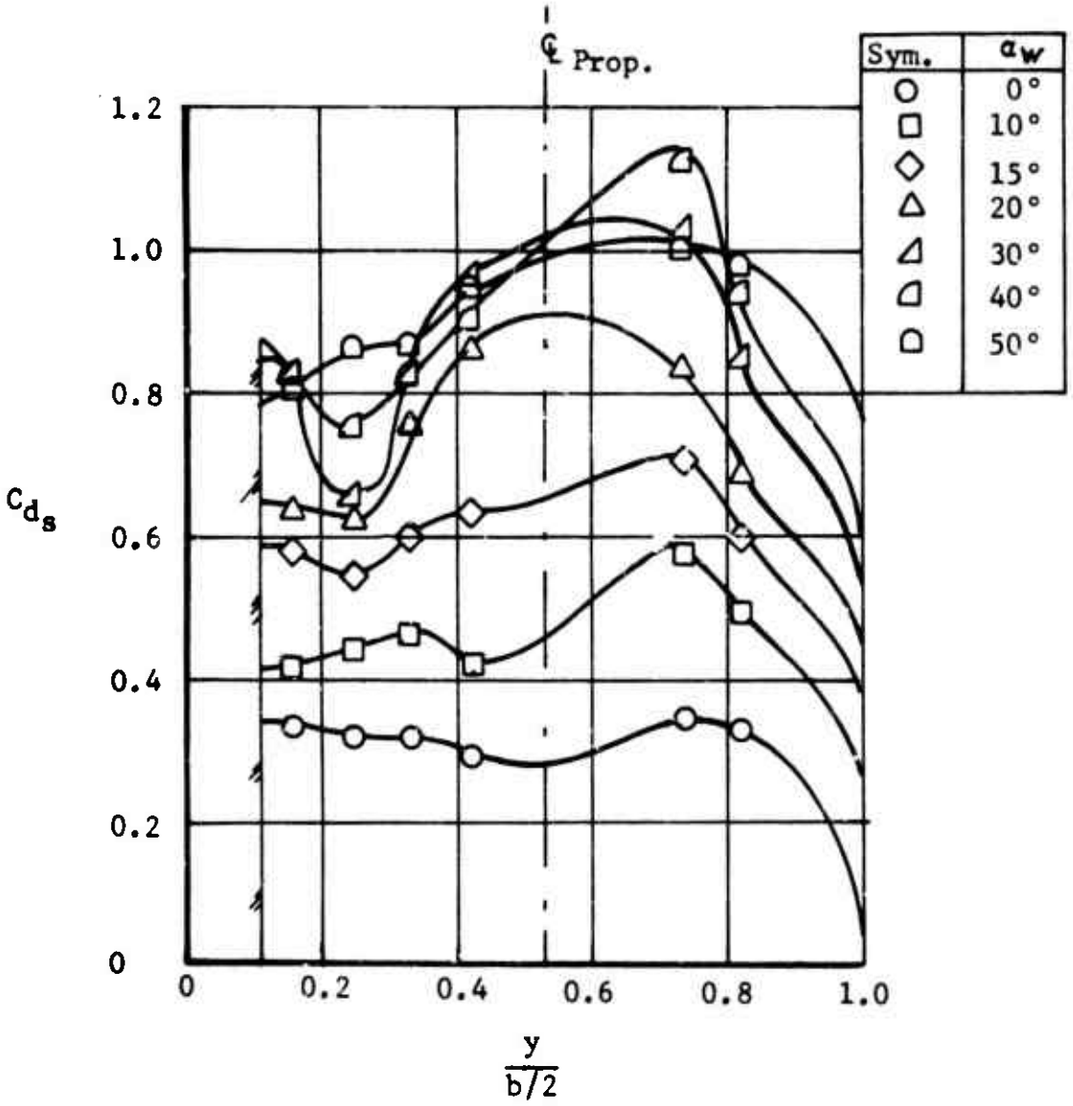

Figure 34. Spanwise Distribution of Slipstream Drag Coefficient, $C_{T_s} = 0.46$.
Configuration: P_1 W_1 F_1 B_1.

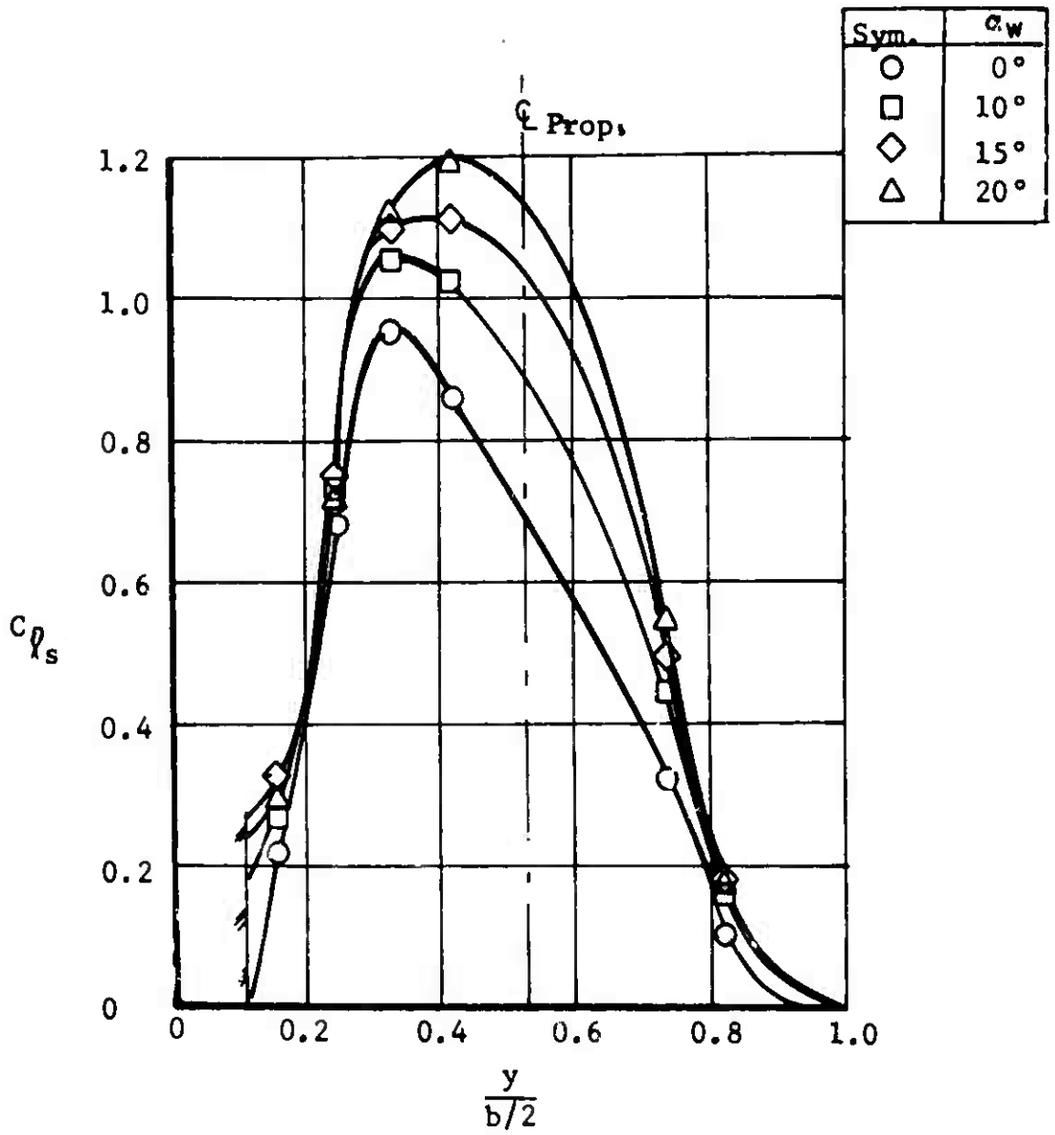

Figure 35. Spanwise Distribution of Slipstream Lift Coefficient, $C_{T_s} = 0.9$.
Configuration: P_1 W_1 F_1 B_1.

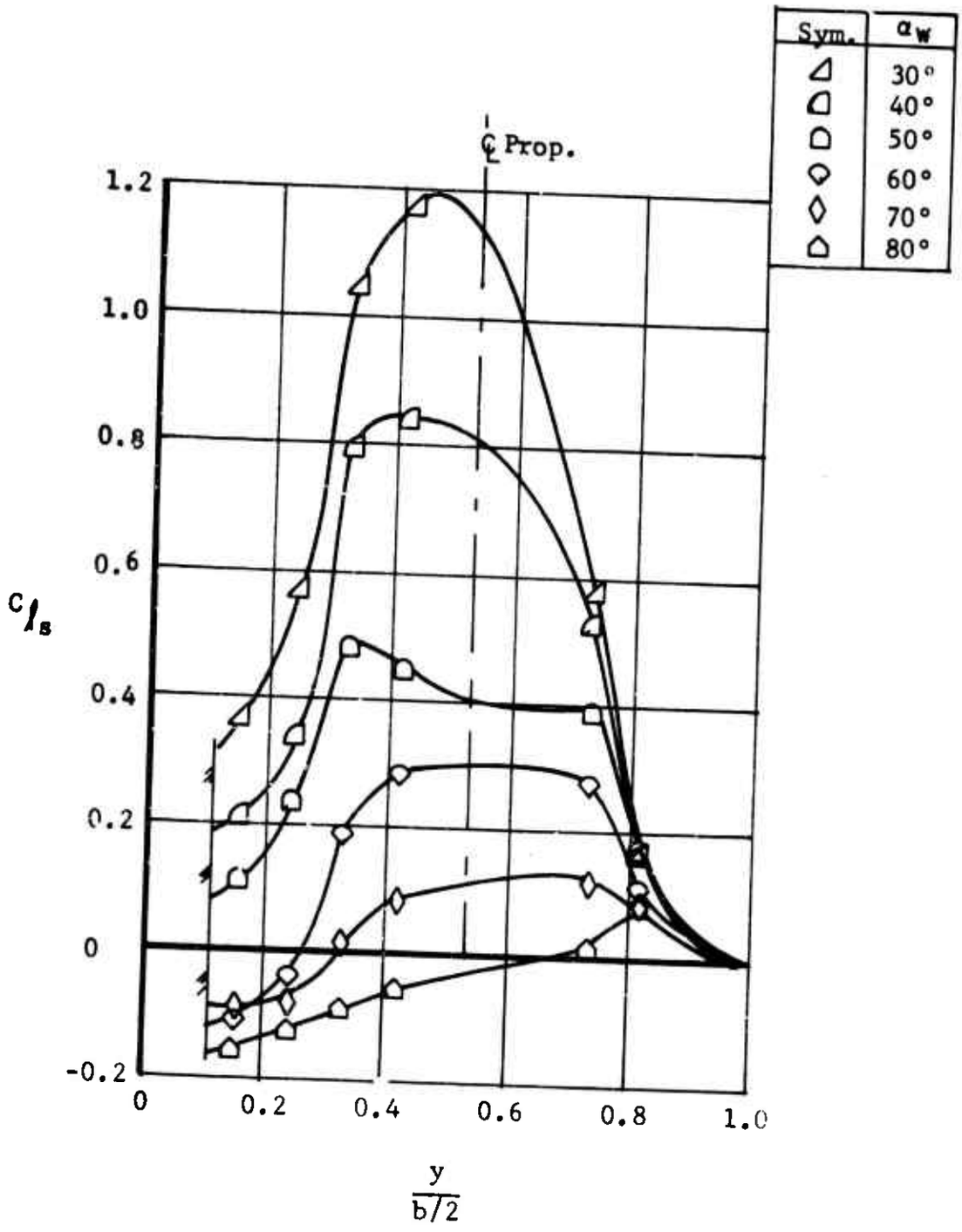

Figure 35. (Continued).

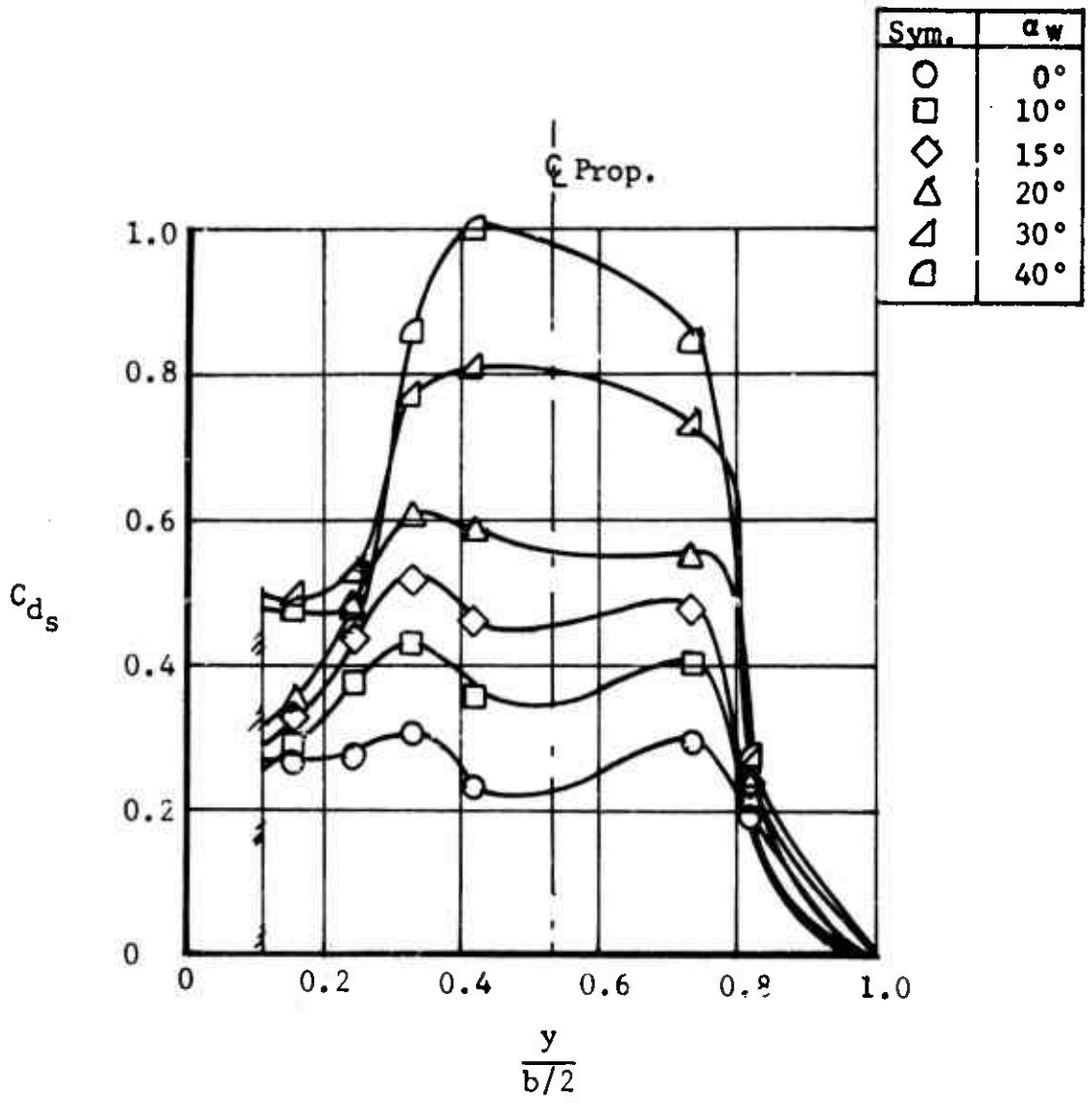

Figure 36. Spanwise Distribution of Slipstream Drag Coefficient, $C_{T_s} = 0.9$.
Configuration: P_1 W_1 F_1 B_1.

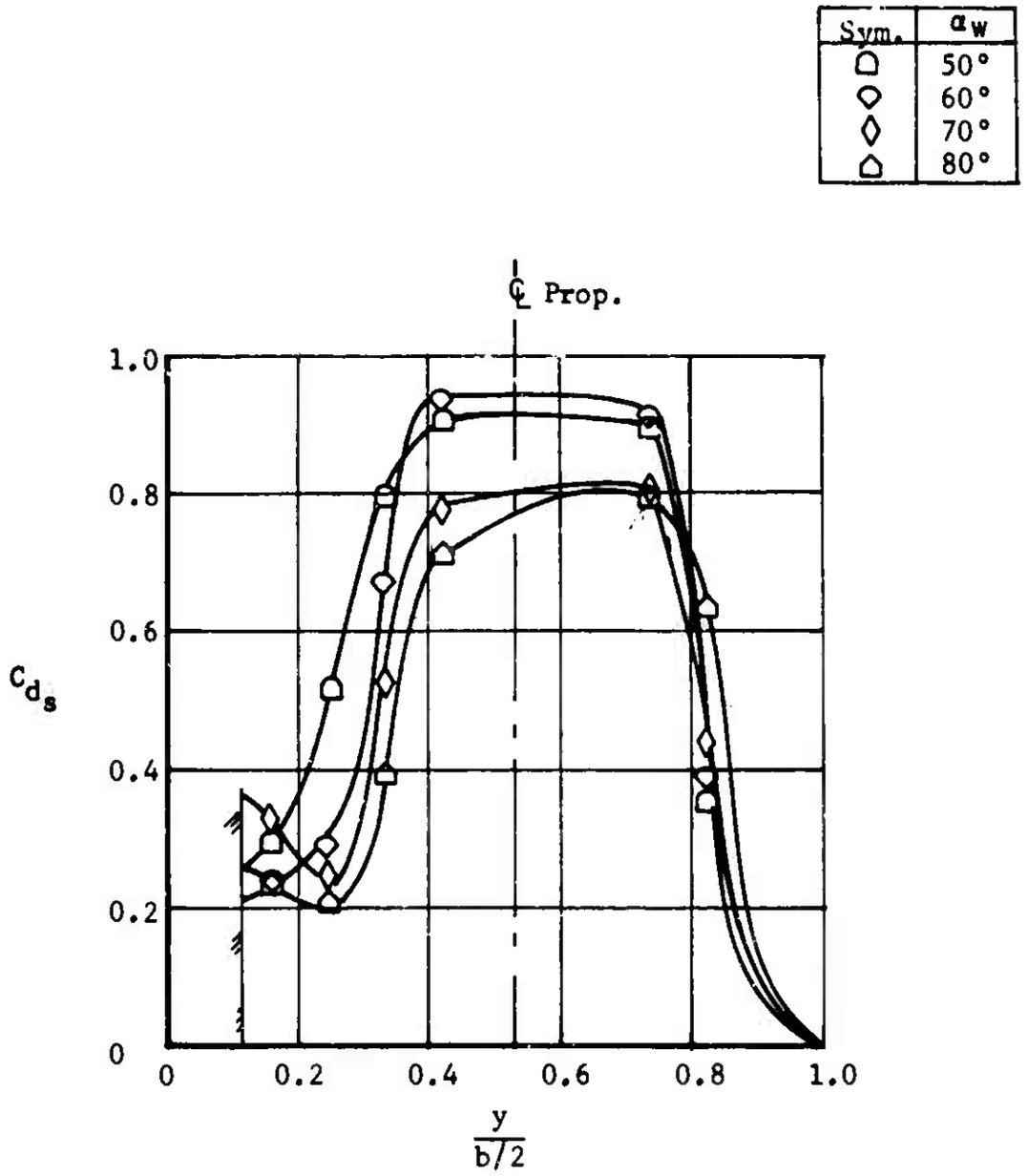

Figure 36. (Continued).

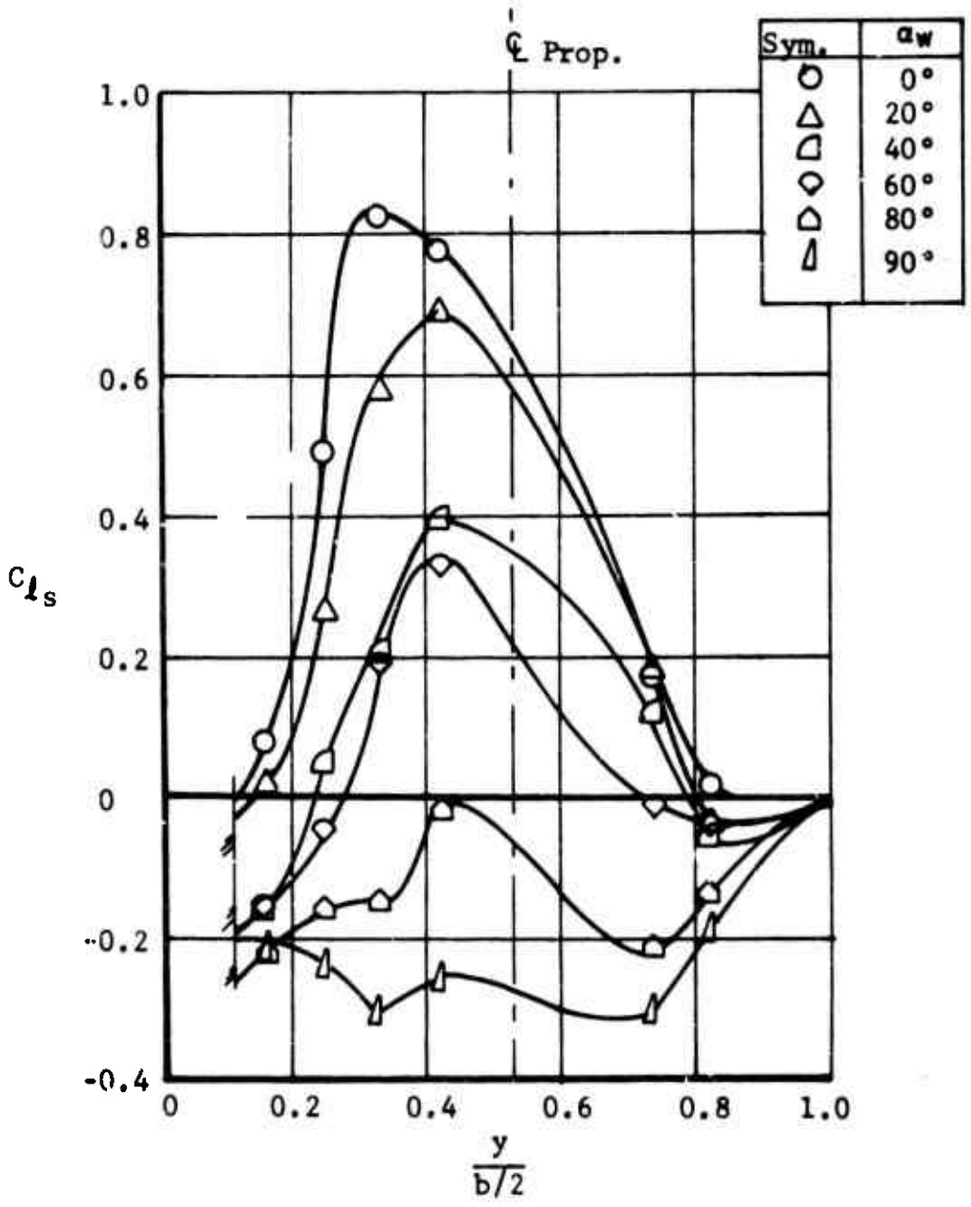

Figure 37. Spanwise Distribution of Slipstream Lift Coefficient, $C_{T_s} = 0.97$.
Configuration: P_1 W_1 F_1 B_1.

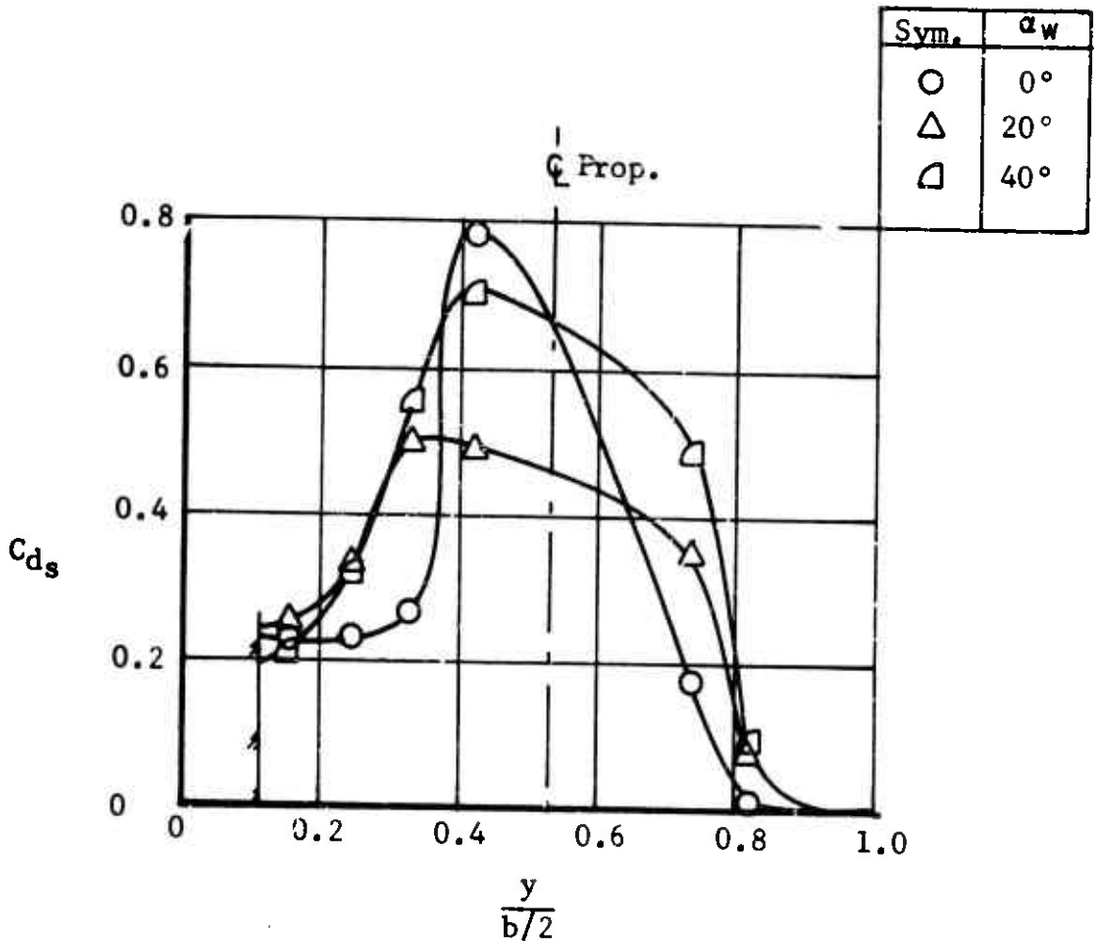

Figure 38. Spanwise Distribution of Slipstream Drag Coefficient, $C_{T_s} = 0.97$.
Configuration: P_1 W_1 F_1 B_1.

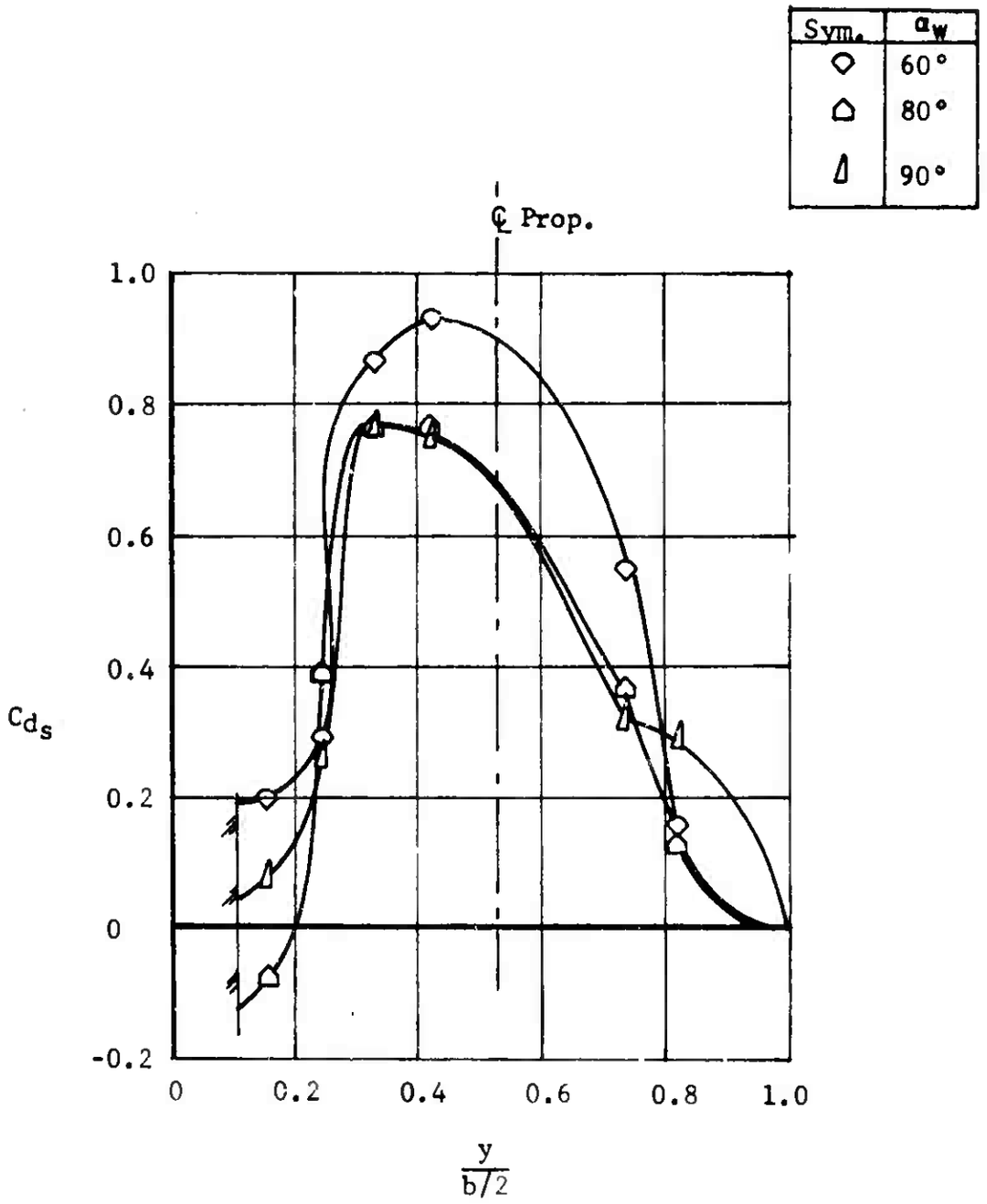

Figure 38. (Continued).

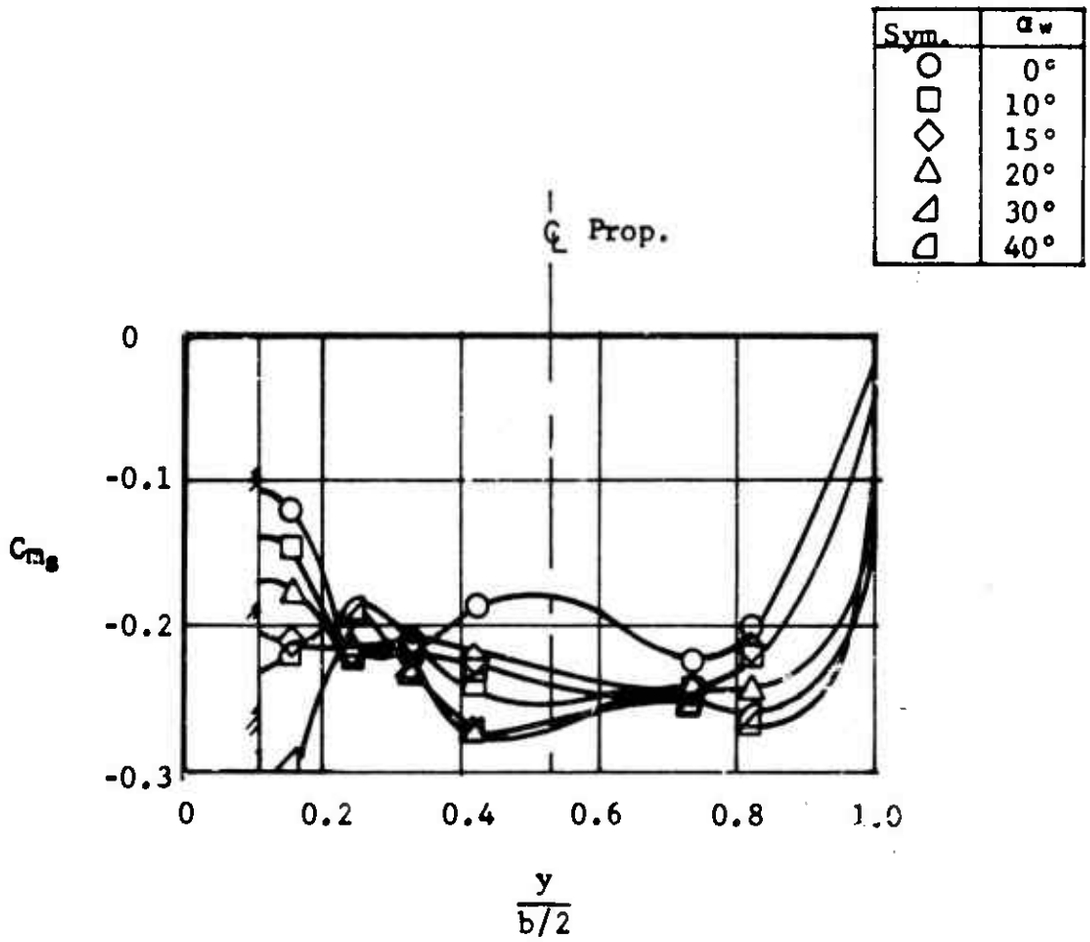

Figure 39. Spanwise Distribution of Slipstream Pitching Moment Coefficient, $C_{T_s} = 0.46$. Configuration: $P_1\ W_1\ F_1\ B_1$.

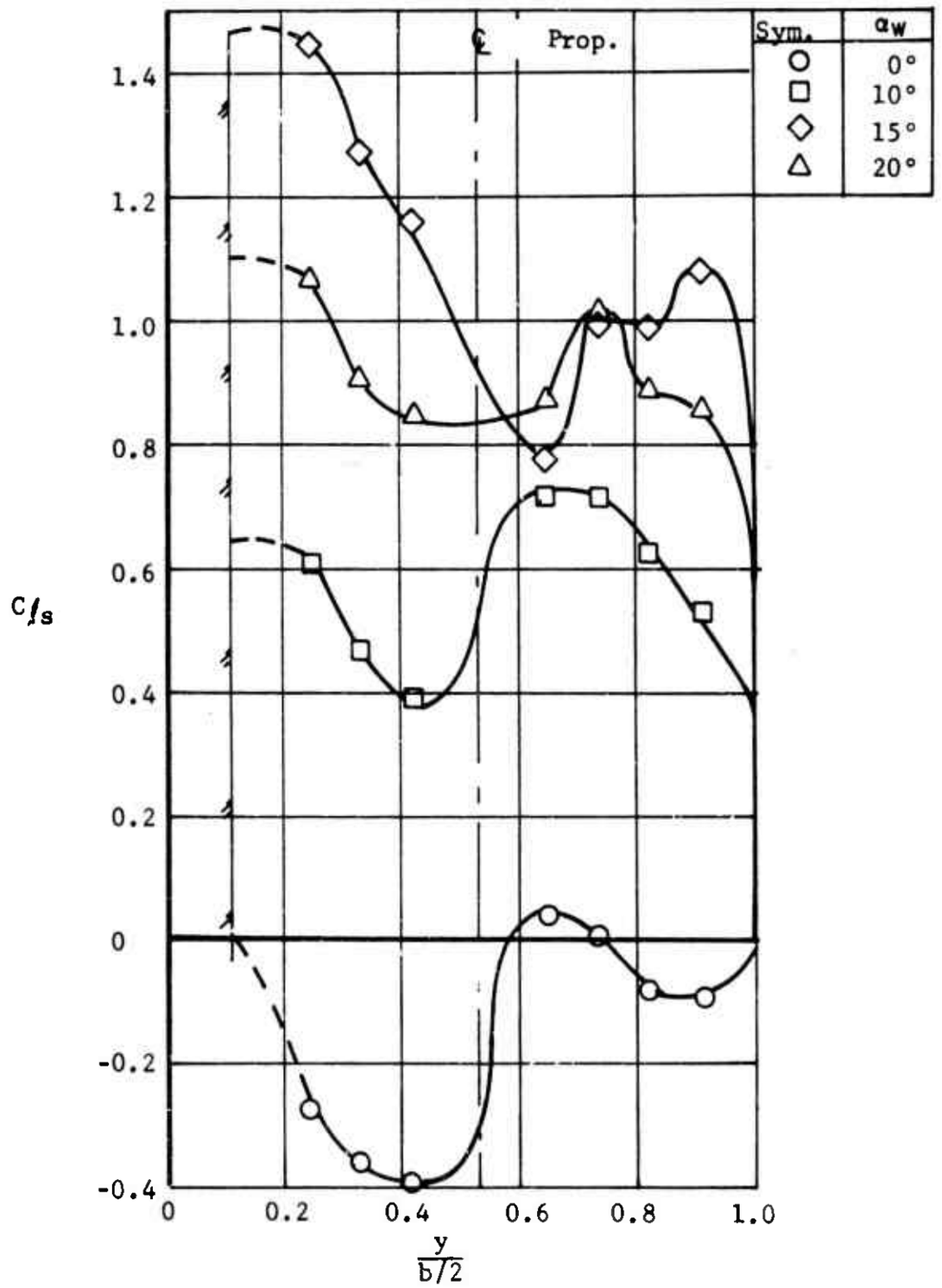

Figure 40. Spanwise Distribution of Slipstream Lift Coefficient, C_{T_s} = -0.5. Configuration: P_2 W_1 B_1.

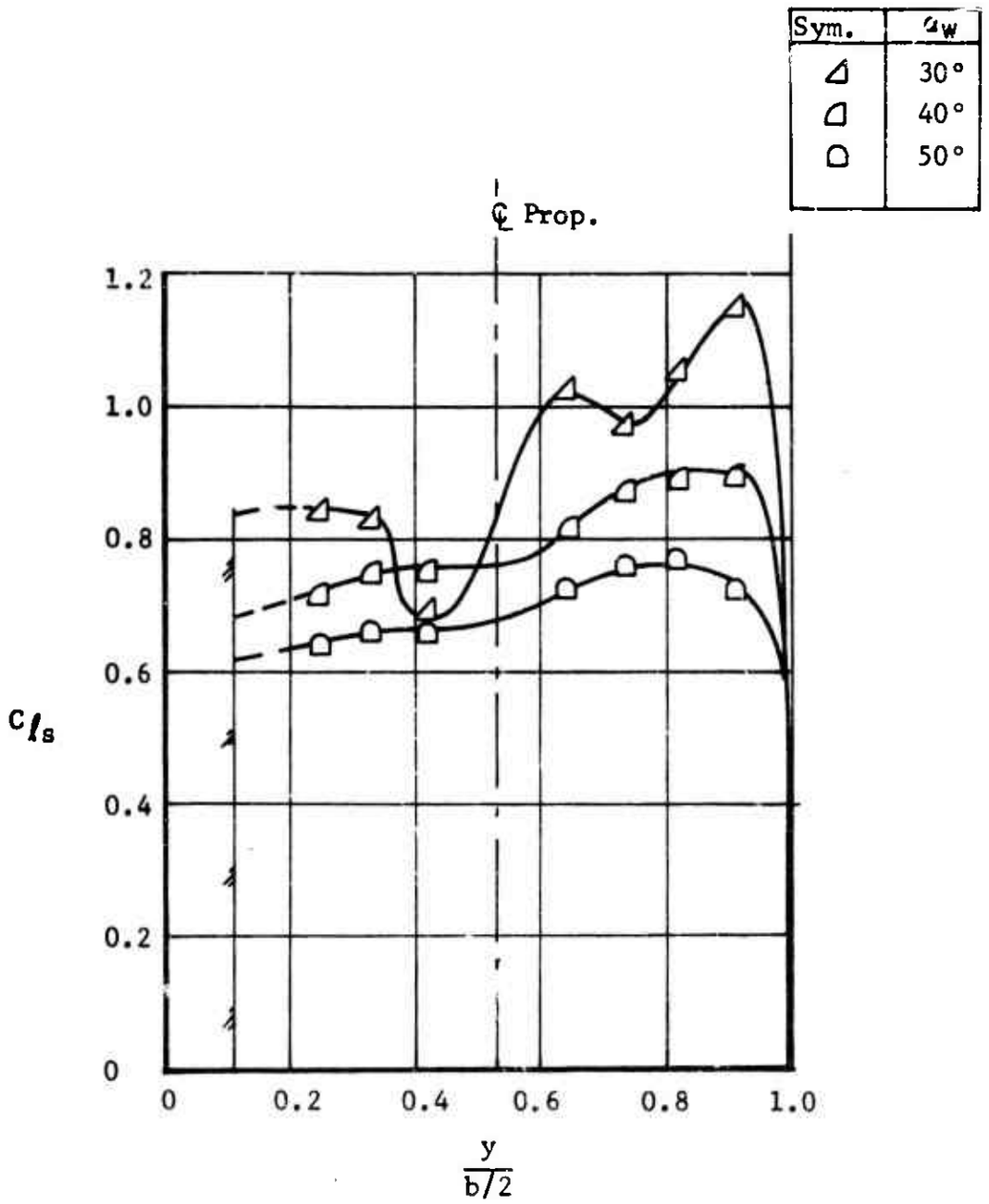

Figure 40. (Continued).

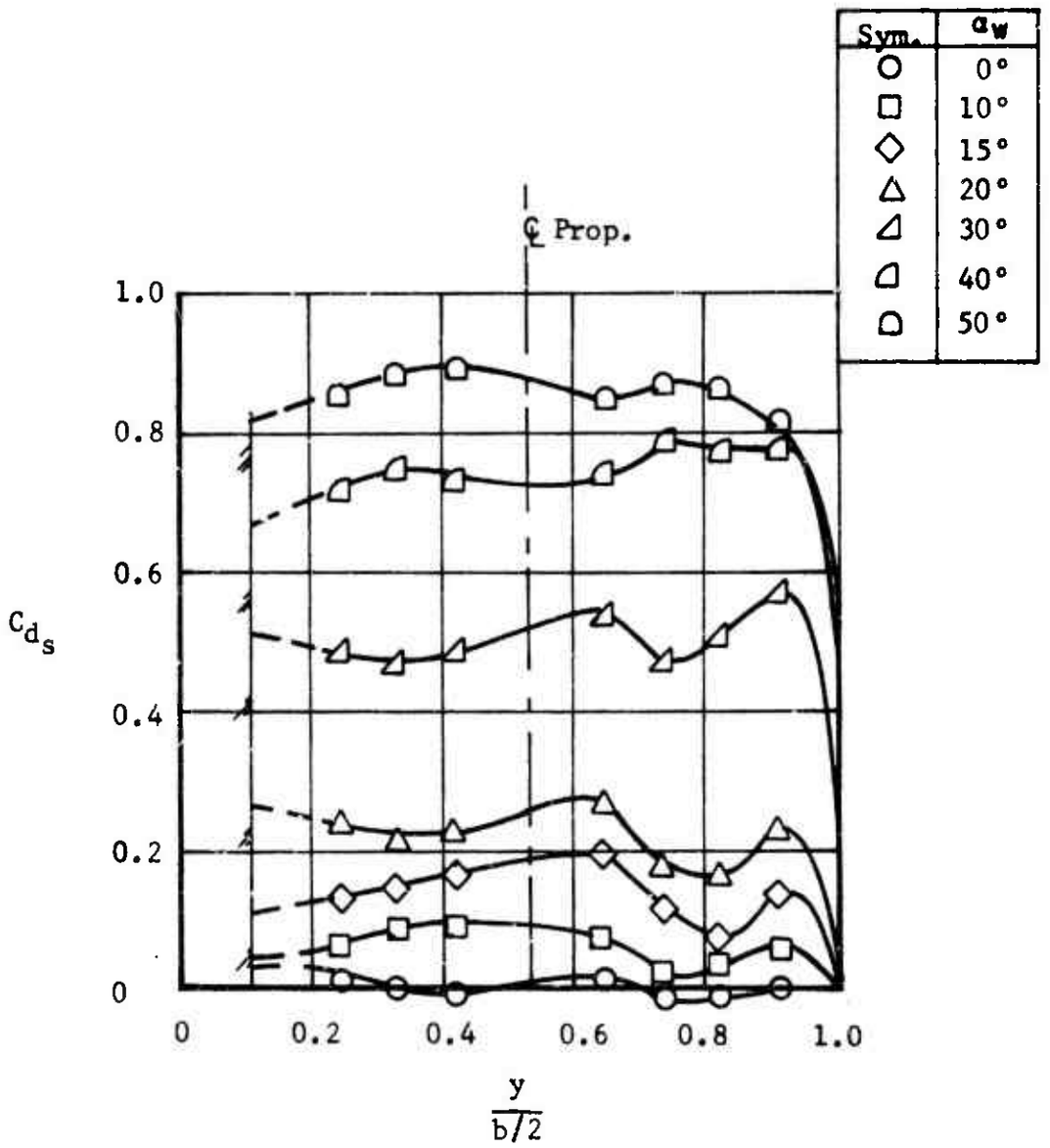

Figure 41. Spanwise Distribution of Slipstream Drag Coefficient, $C_{T_s} = -0.5$.
Configuration: P_2 W_1 B_1.

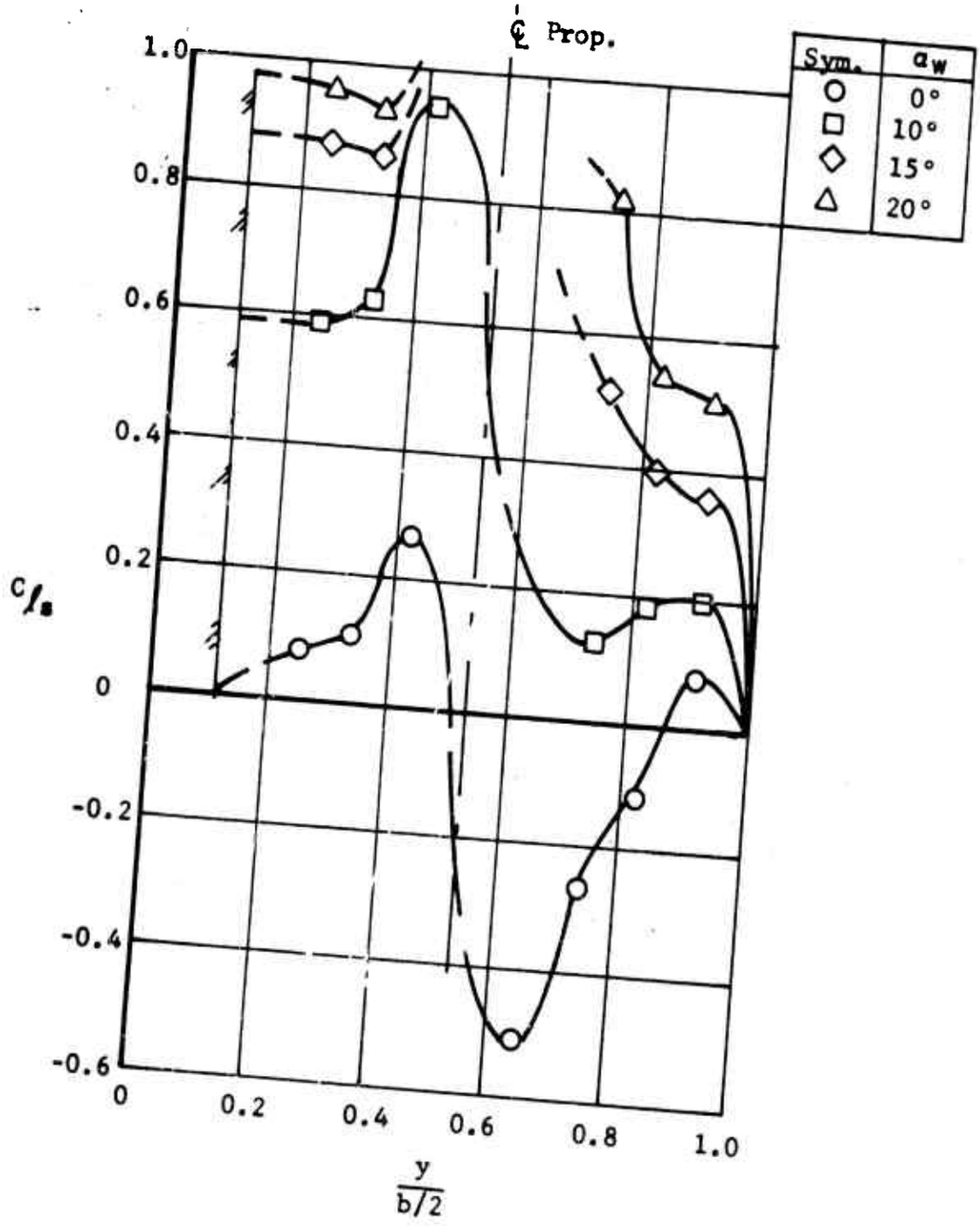

Figure 42. Spanwise Distribution of Slipstream Lift Coefficient, $C_{T_s} = 0.5$.
Configuration: P_2 W_1 B_1.

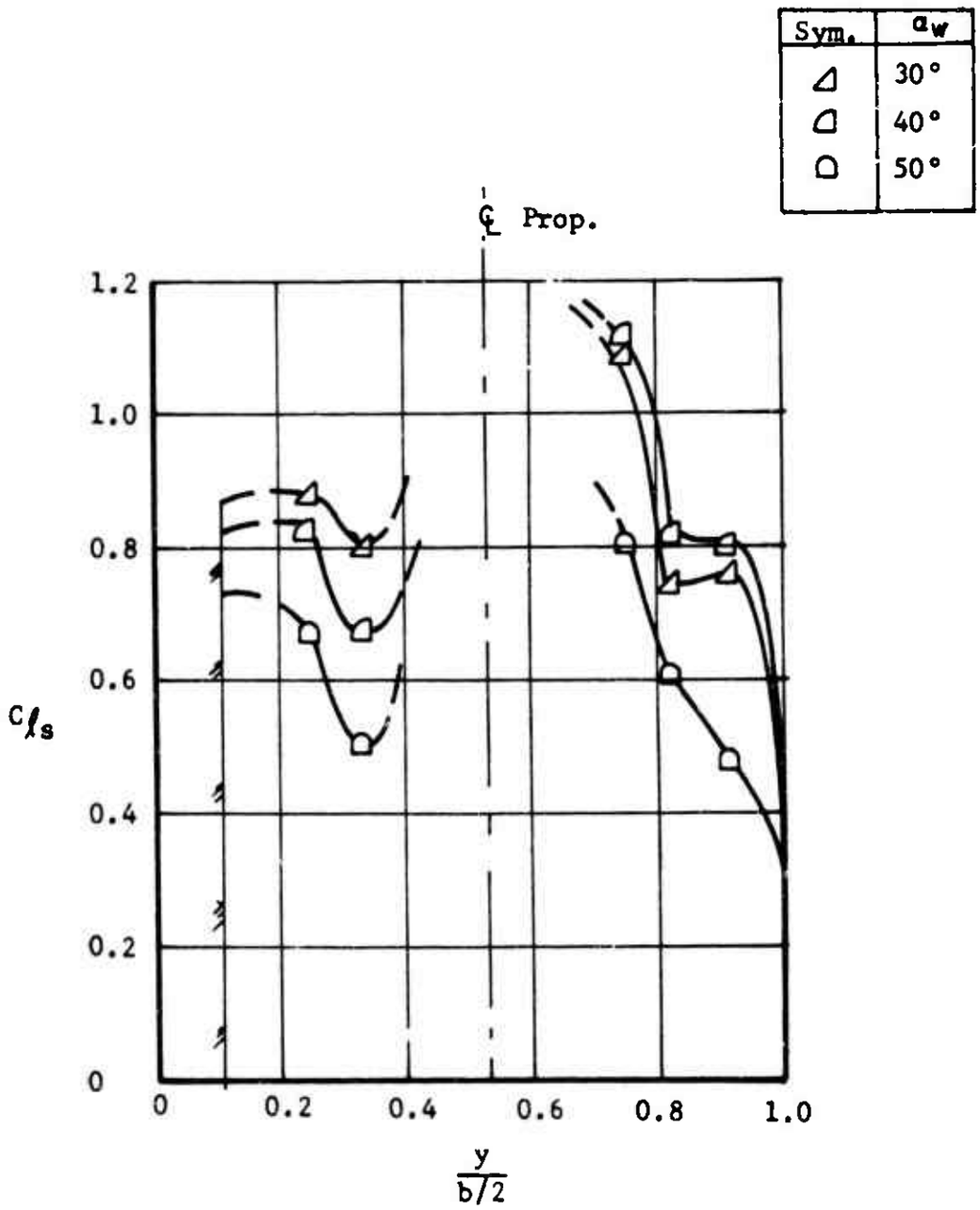

Figure 42. (Continued).

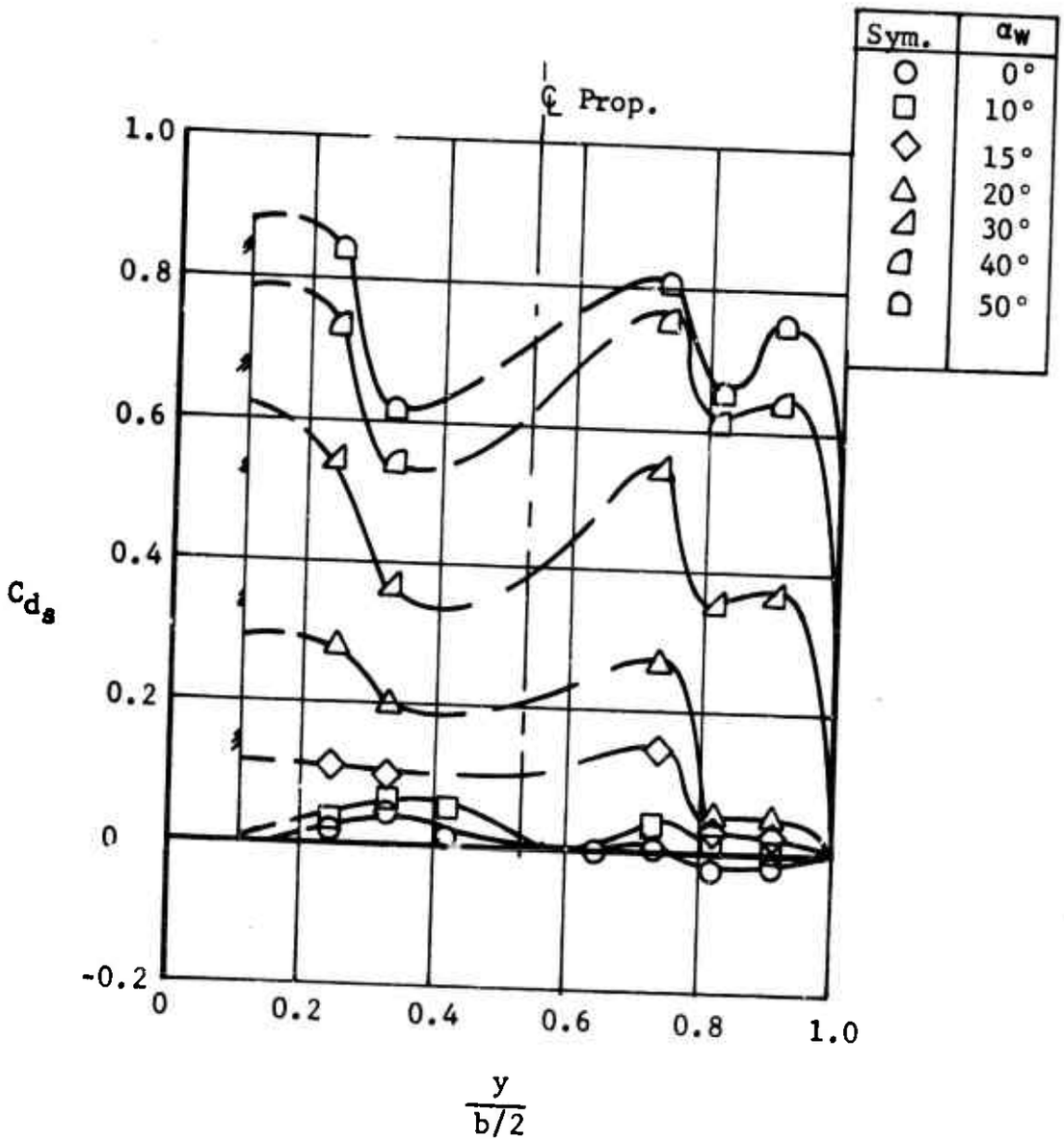

Figure 43. Spanwise Distribution of Slipstream Drag Coefficient, $C_{T_s} = 0.5$.
Configuration: P_2 W_1 B_1.

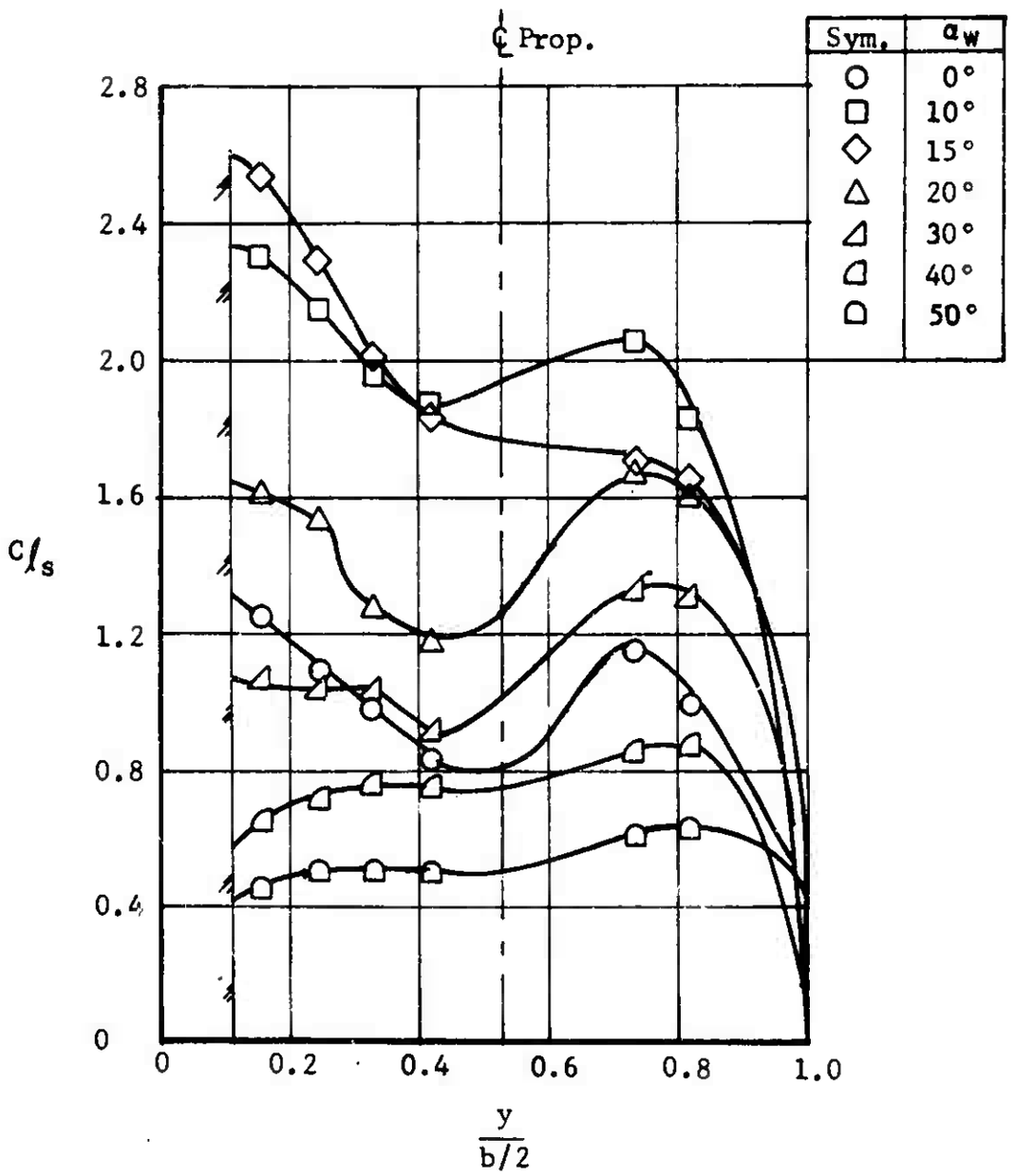

Figure 44. Spanwise Distribution of Slipstream Lift Coefficient, $C_{T_s} = -0.4$.
Configuration: P_2 W_1 F_1 B_1.

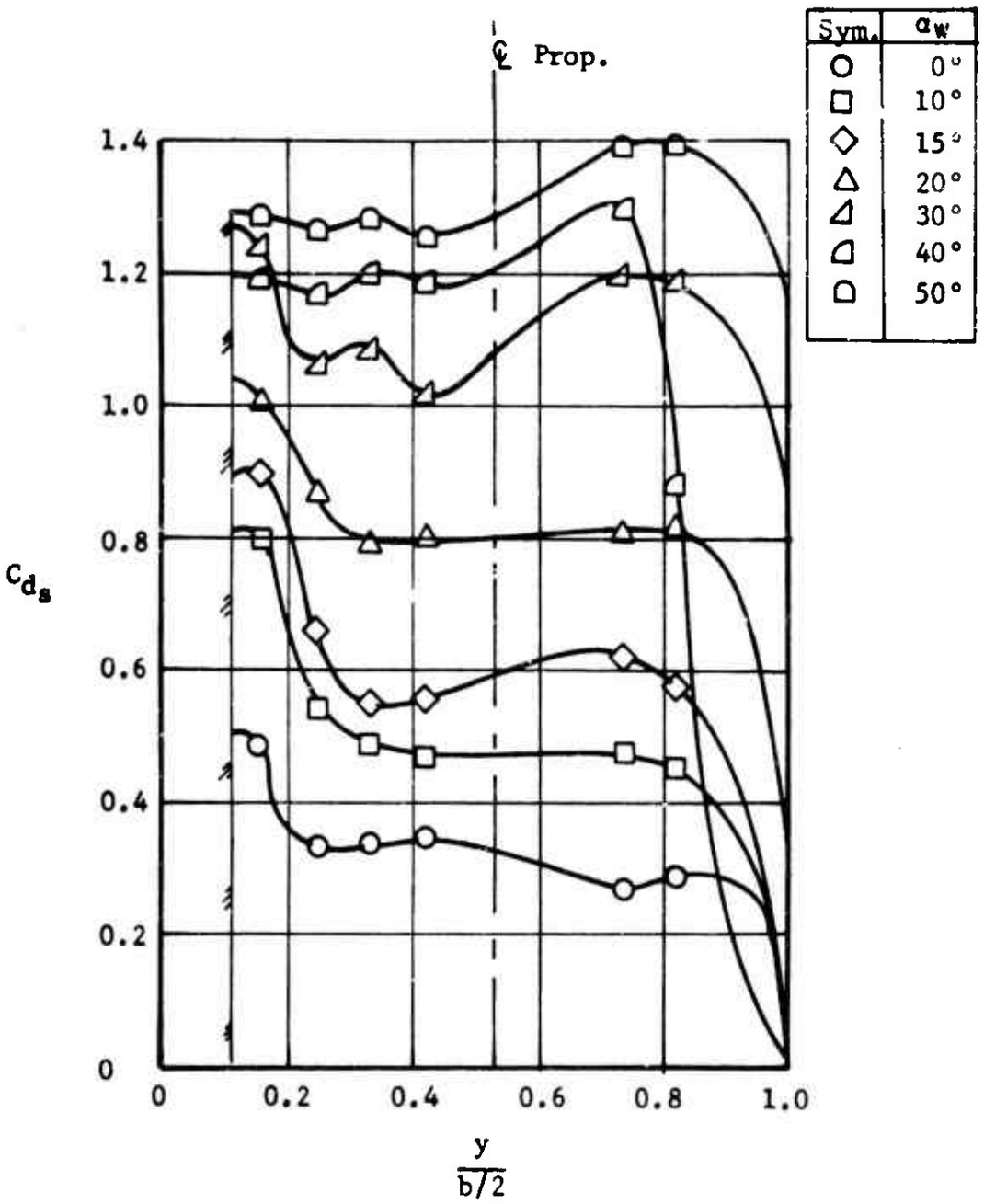

Figure 45. Spanwise Distribution of Slipstream Drag Coefficient, $C_{T_s} = -0.4$.
Configuration: P_2 W_1 F_1 B_1.

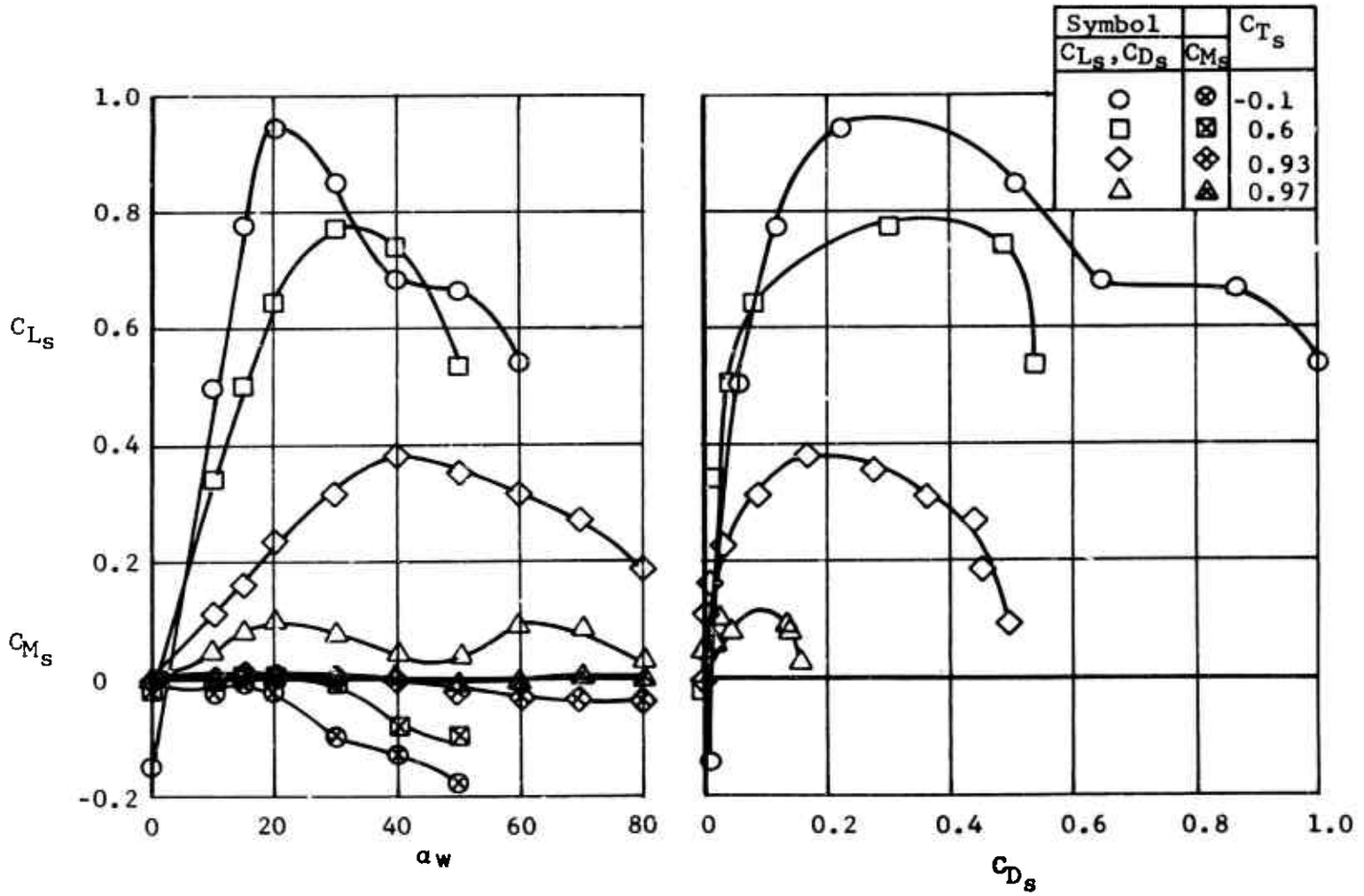

Figure 46. Total Wing Lift, Drag, and Pitching Moment Coefficients. Configuration: P_1 W_1 B_1.

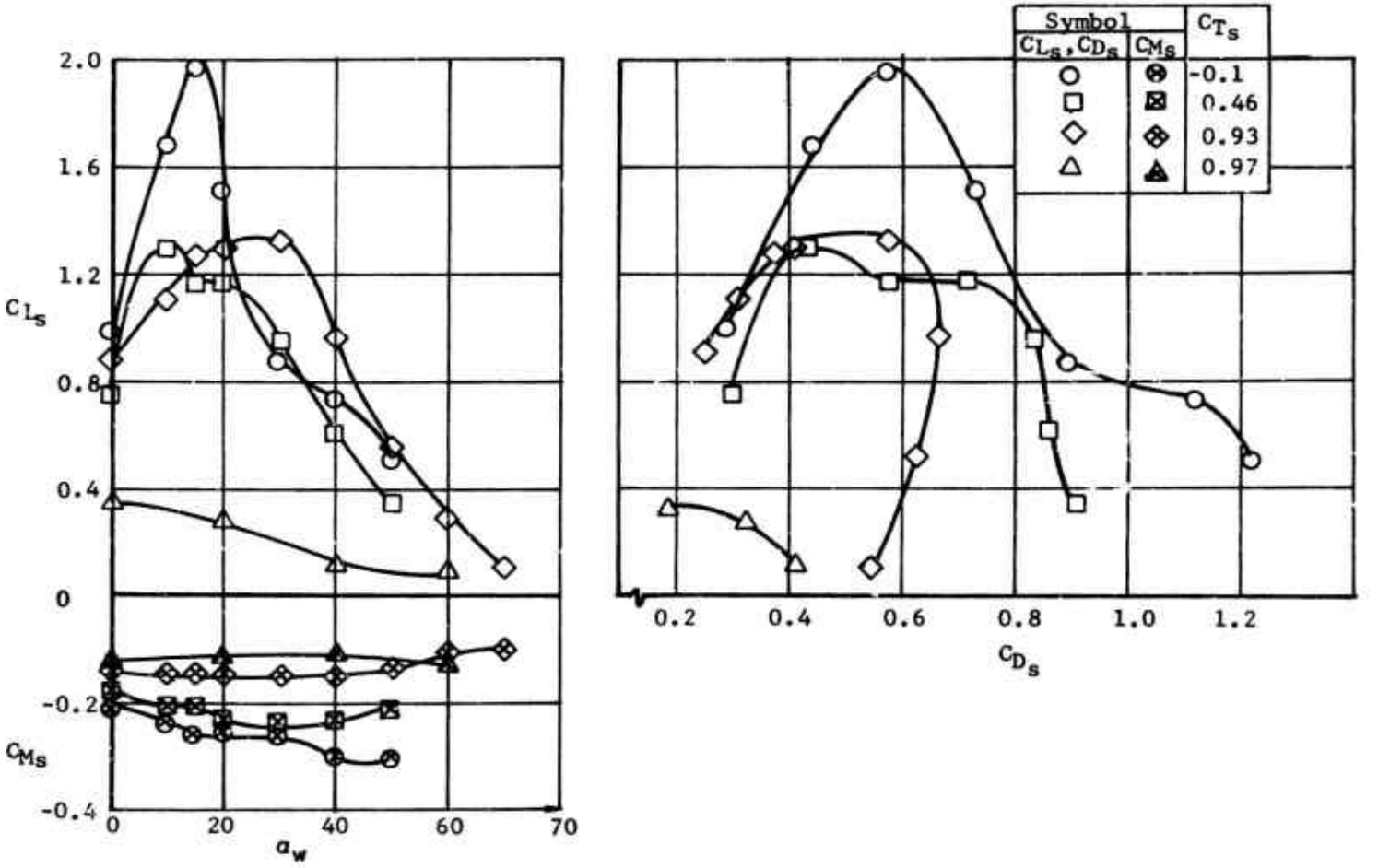

Figure 47. Total Wing Lift, Drag, and Pitching Moment Coefficients. Configuration: P_1 W_1 F_1 B_1.

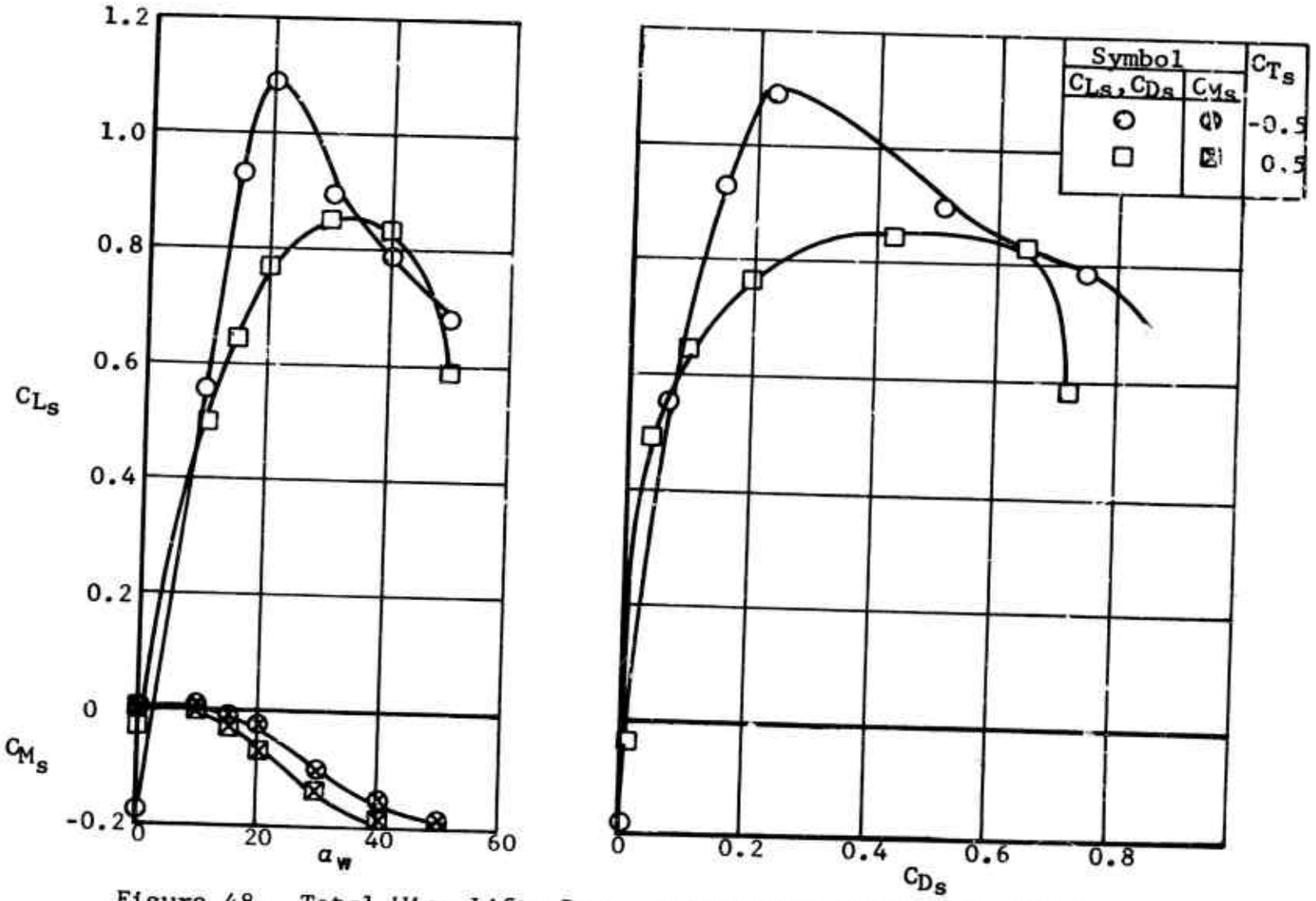

Figure 48. Total Wing Lift, Drag, and Pitching Moment Coefficients. Configuration: P_2 W_1 B_1.

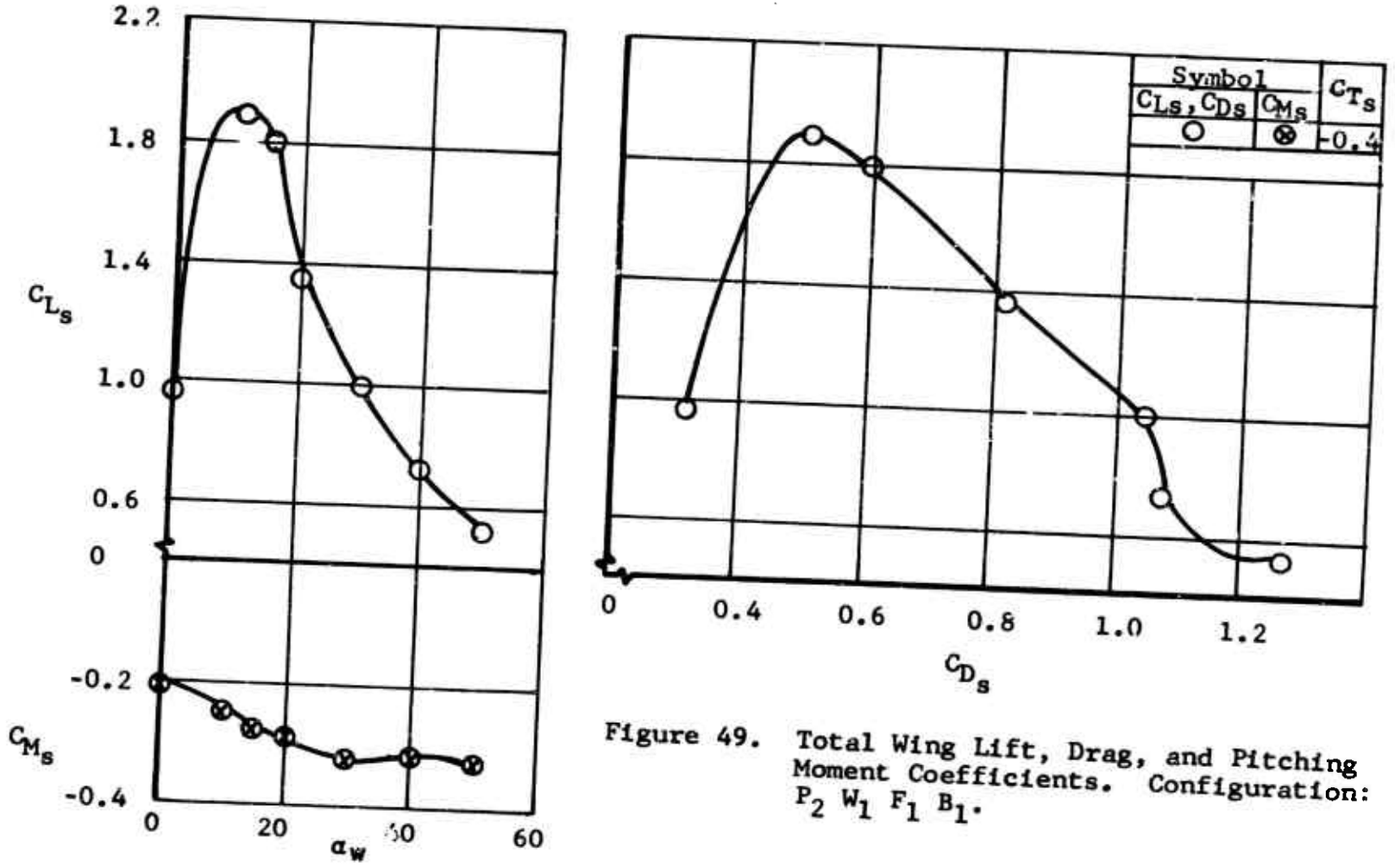

Figure 49. Total Wing Lift, Drag, and Pitching Moment Coefficients. Configuration: P_2 W_1 F_1 B_1.

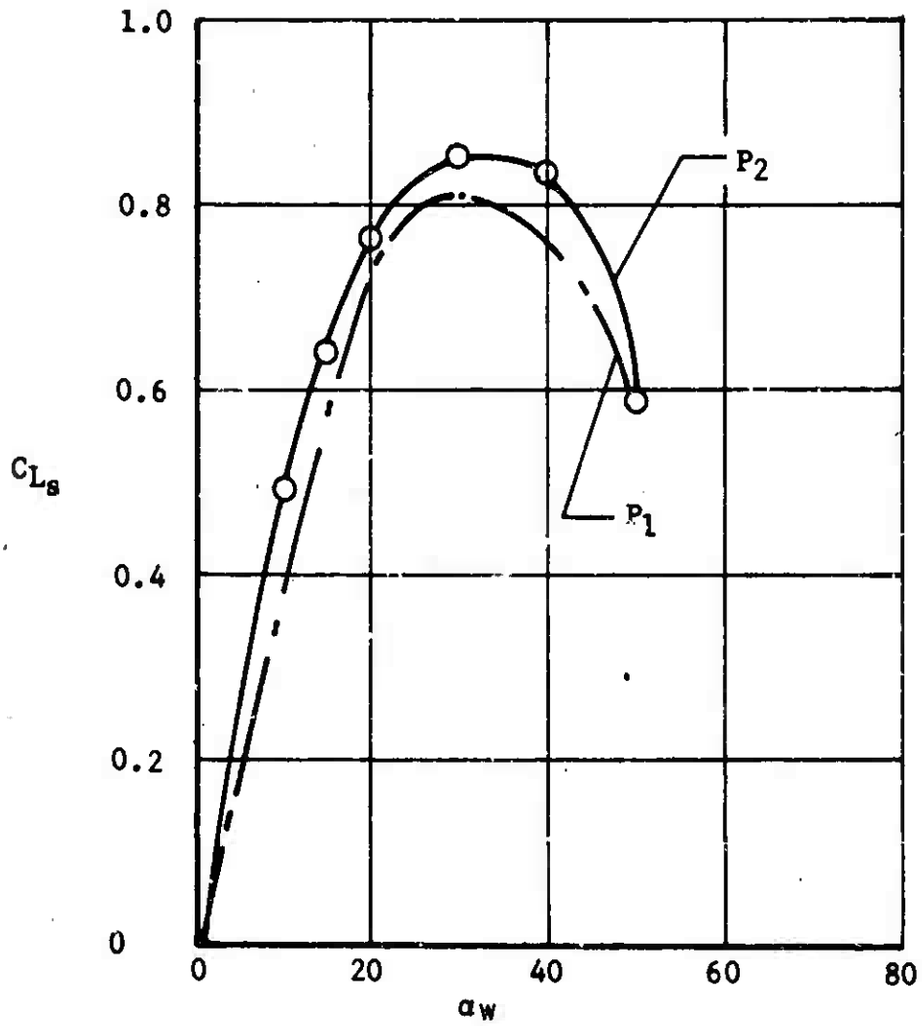

Figure 50. Comparison of Wing Lift Coefficient Generated With P_1 and P_2 Propellers, $C_{T_s} = 0.5$.

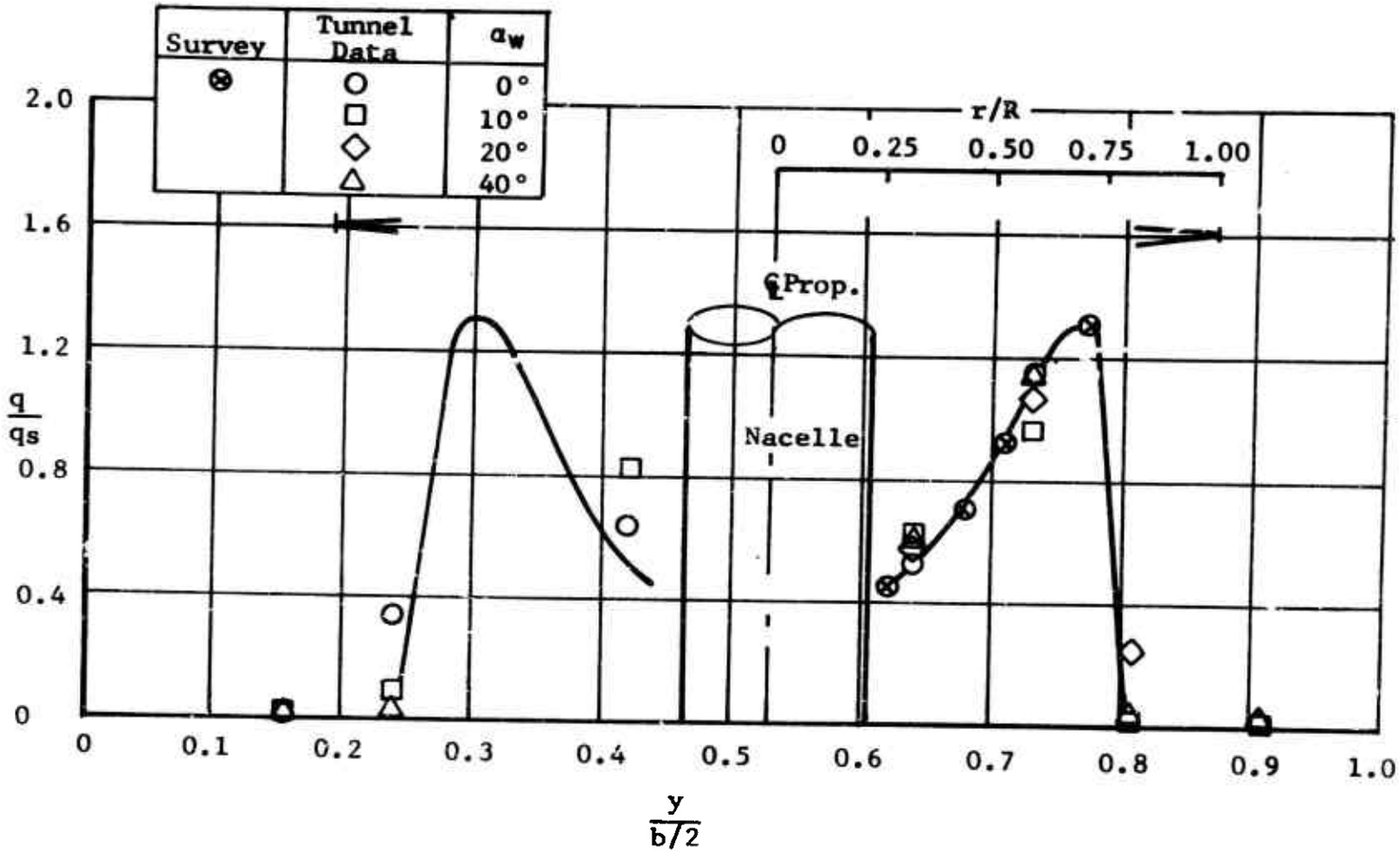

Figure 51. Dynamic Pressure Profiles of Propeller P_1, $C_{T_s} = 0.97$. Configuration: P_1 B_1.

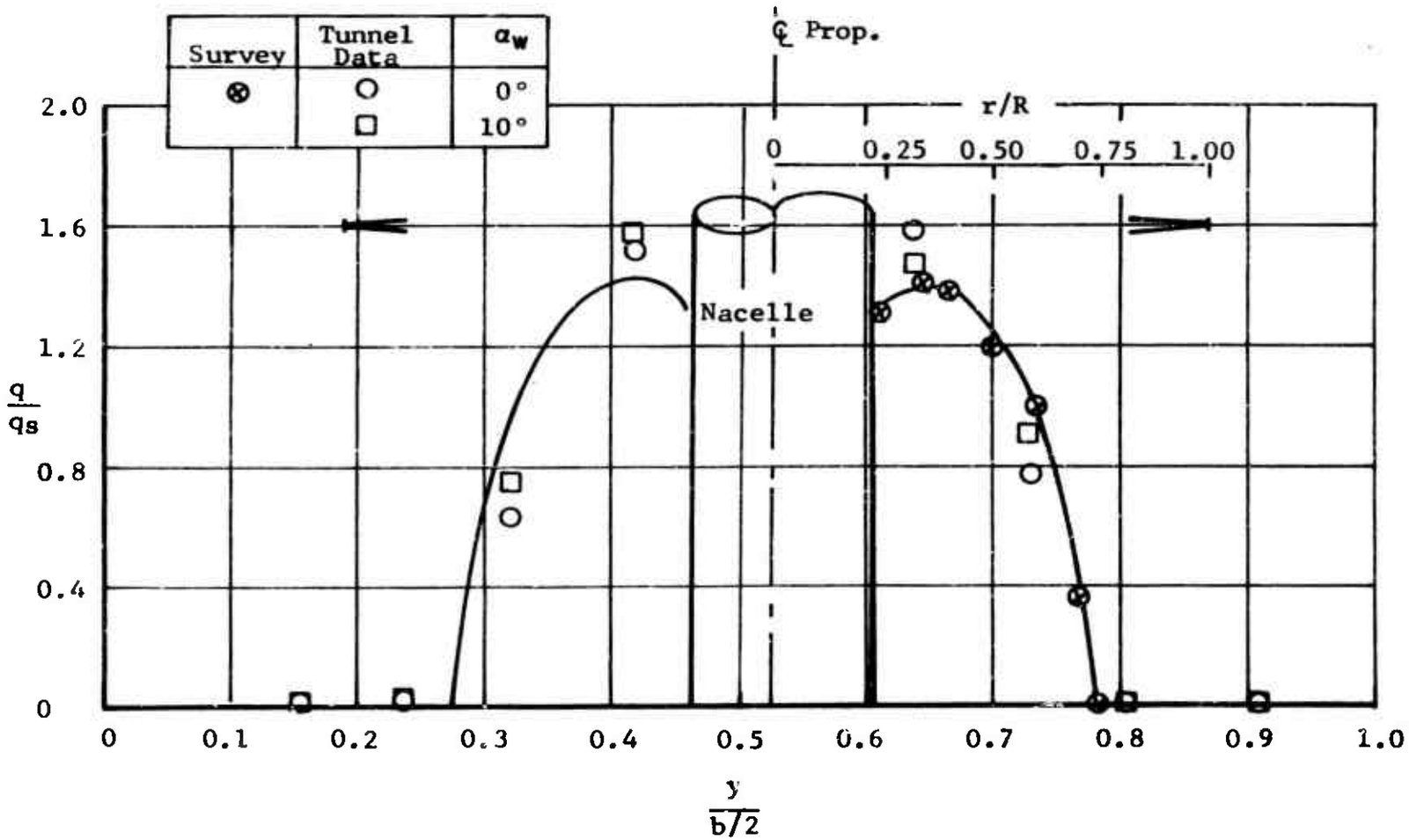

Figure 52. Dynamic Pressure Profile of Propeller P_2, C_{T_s} = 0.97.
Configuration: P_2 B_1.

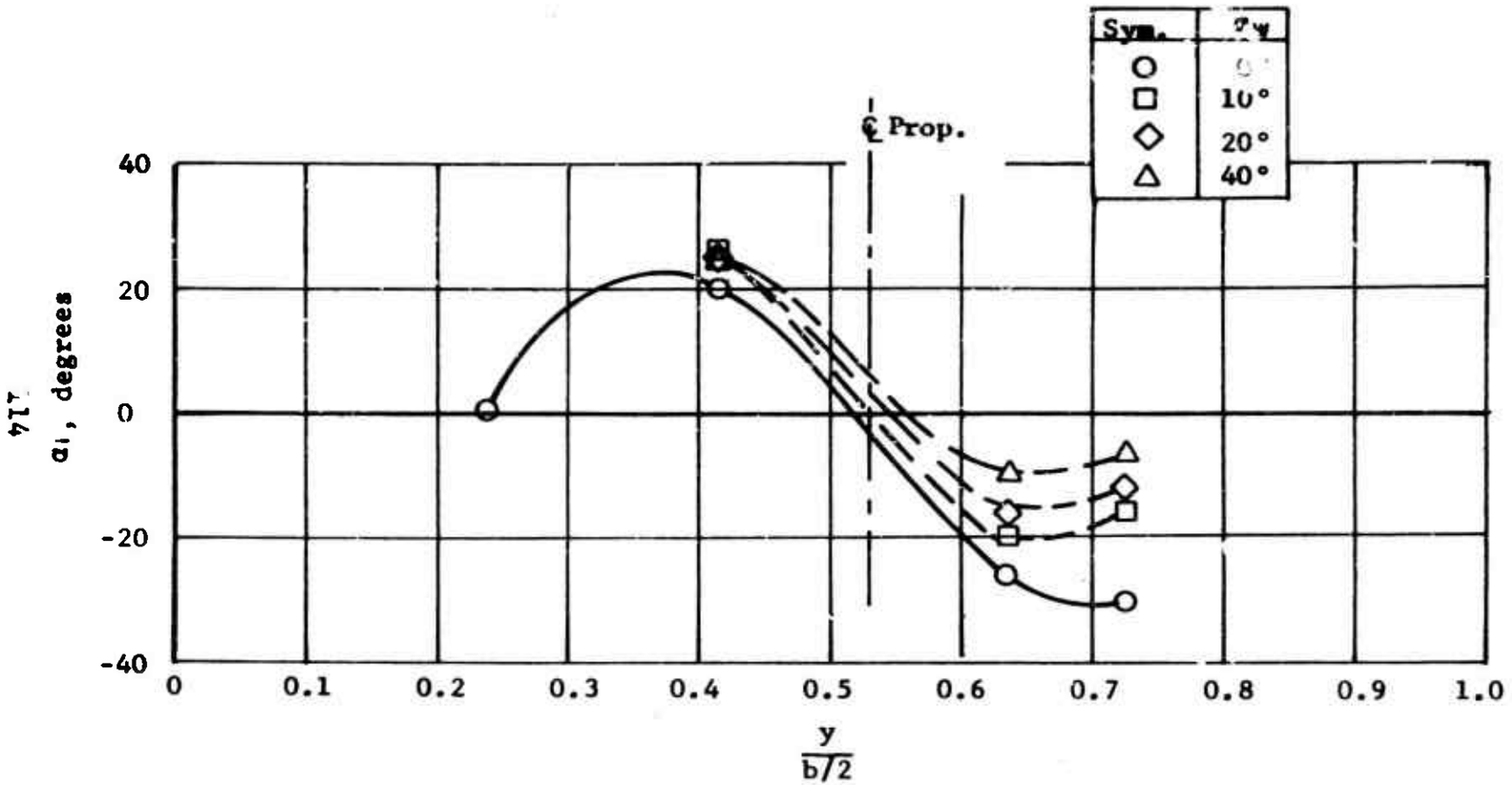

Figure 53. Spanwise Variation of Local Slipstream Angle of Attack, $C_{T_s} = 0.97$. Configuration: P_1 B_1.

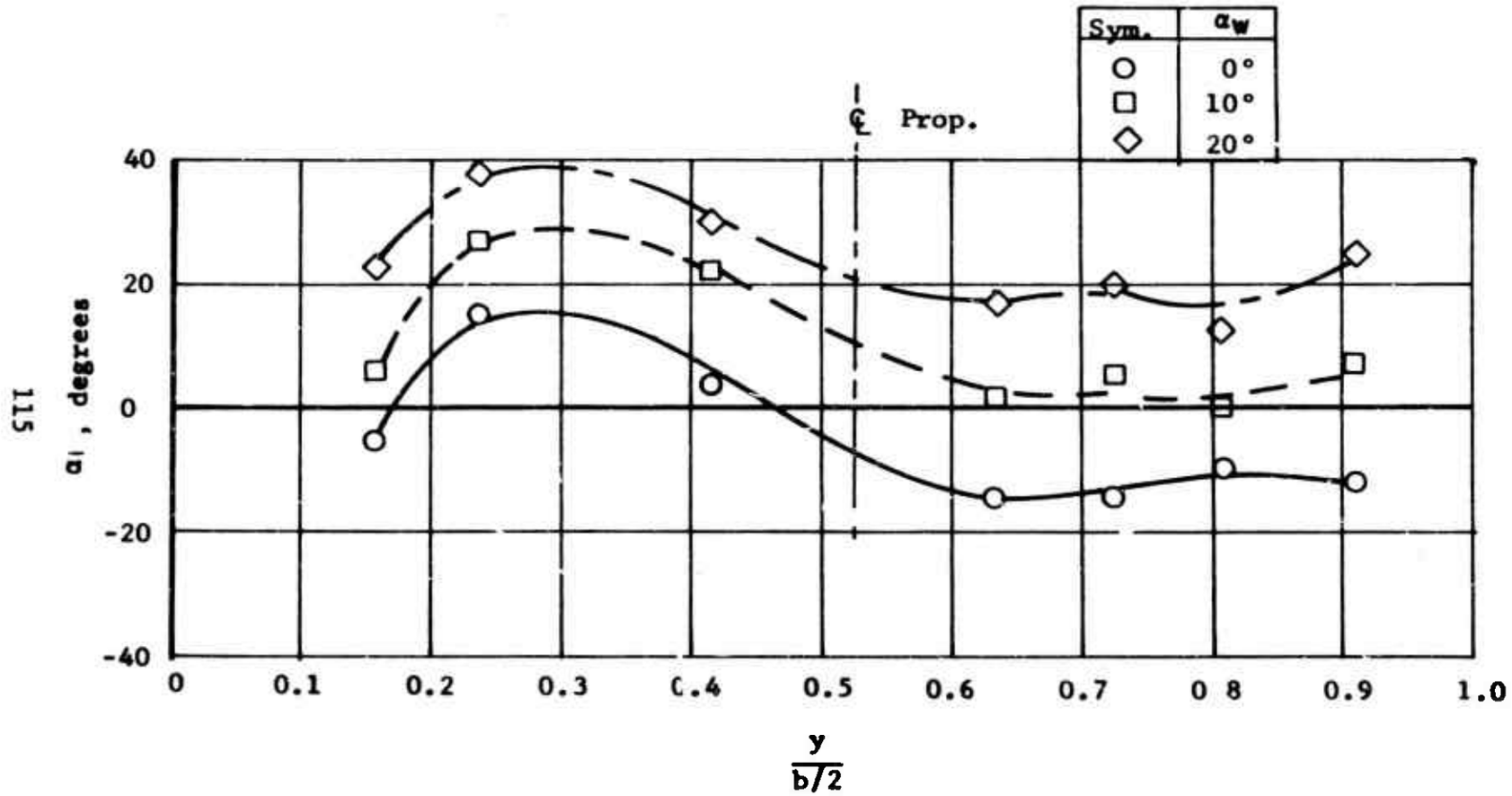

Figure 54. Spanwise Variation of Local Slipstream Angle of Attack, $C_{T_s} = 0.5$. Configuration: P_1 B_1.

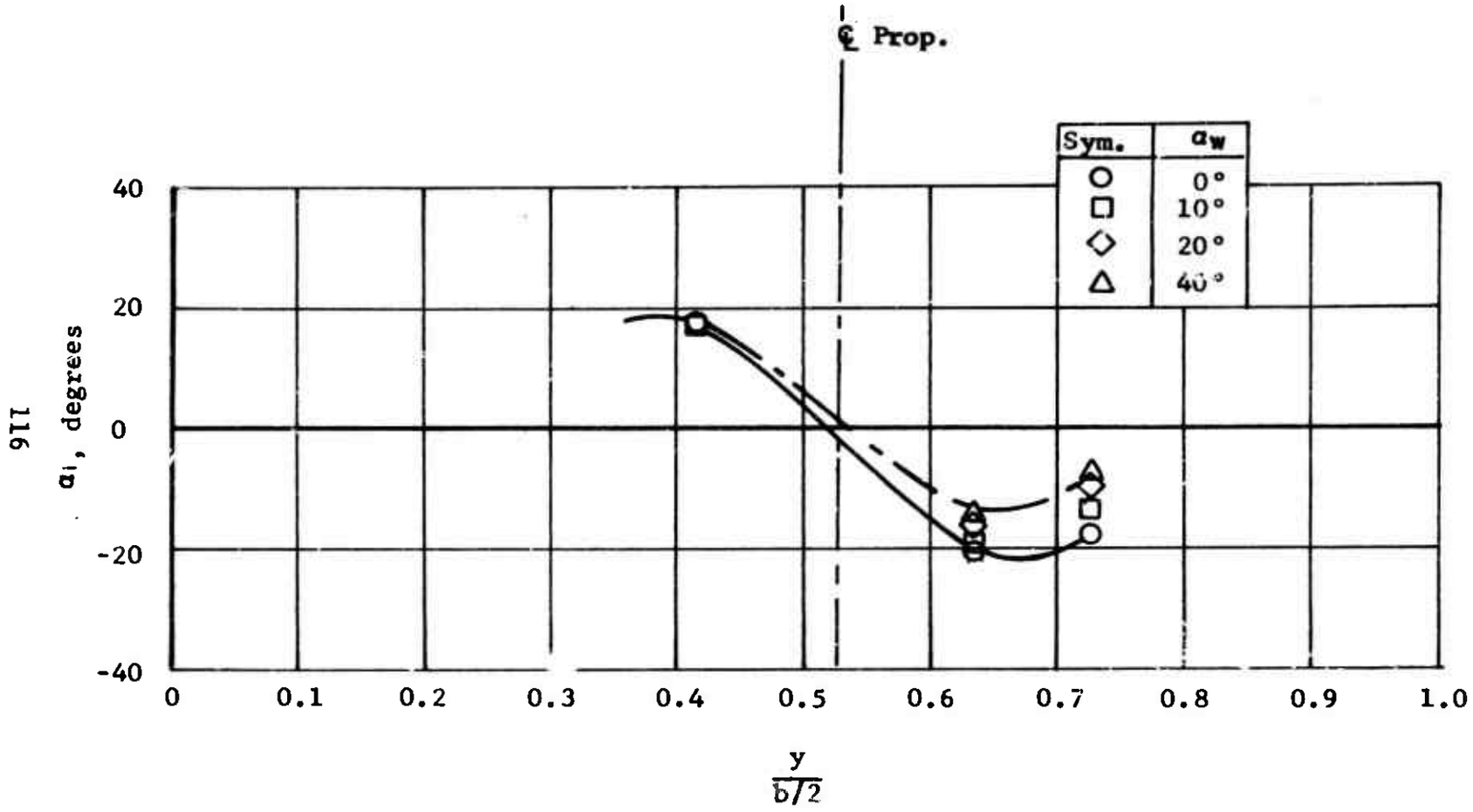

Figure 55. Spanwise Variation of Local Slipstream Angle of Attack, C_{T_s} = 0.97. Configuration: P_2 B_1.

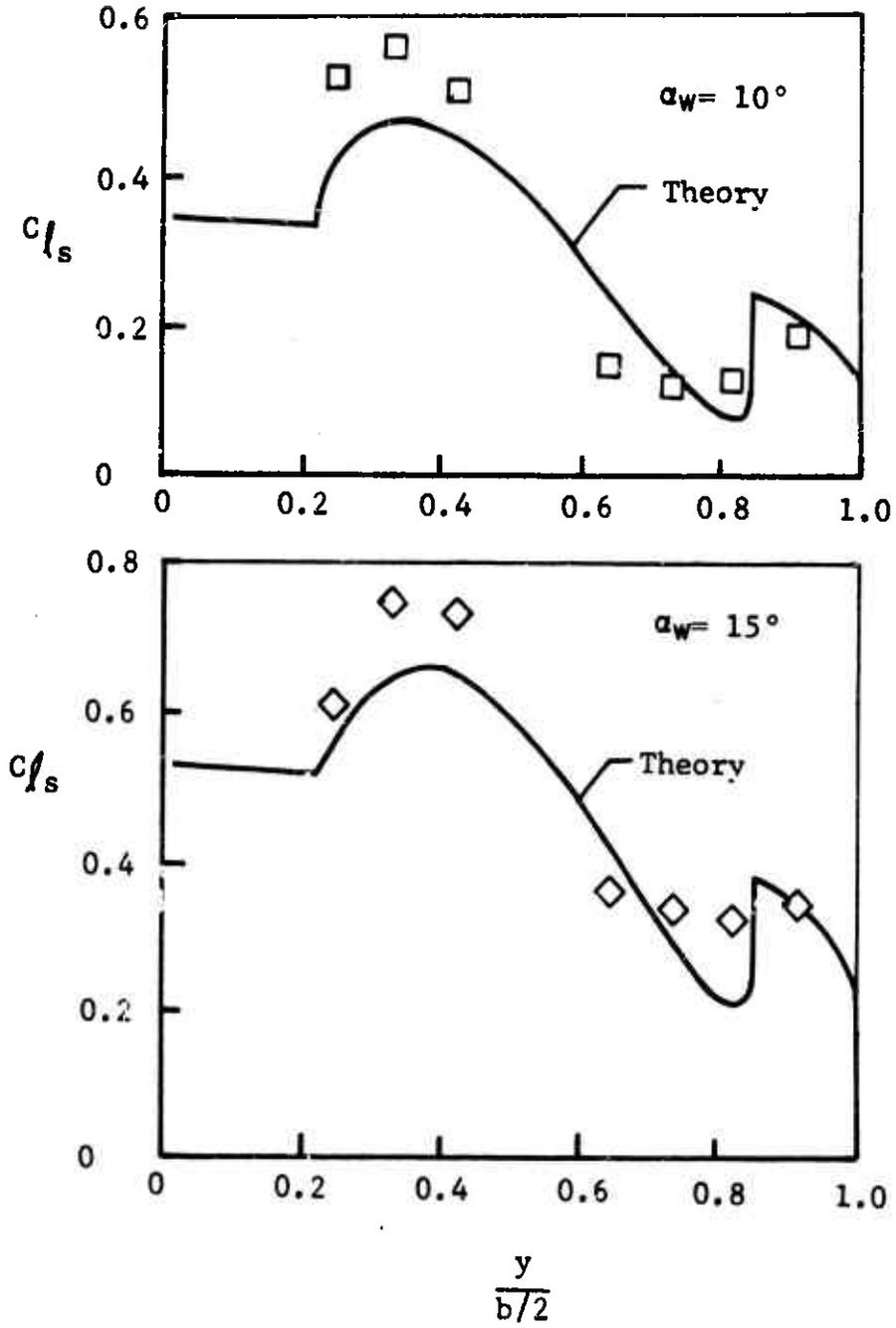

Figure 56. Comparison of Theory With Test Data of the Spanwise Distribution of C_{l_s}, C_{T_s} = 0.6. Configuration: P_1 W_1 B_1.

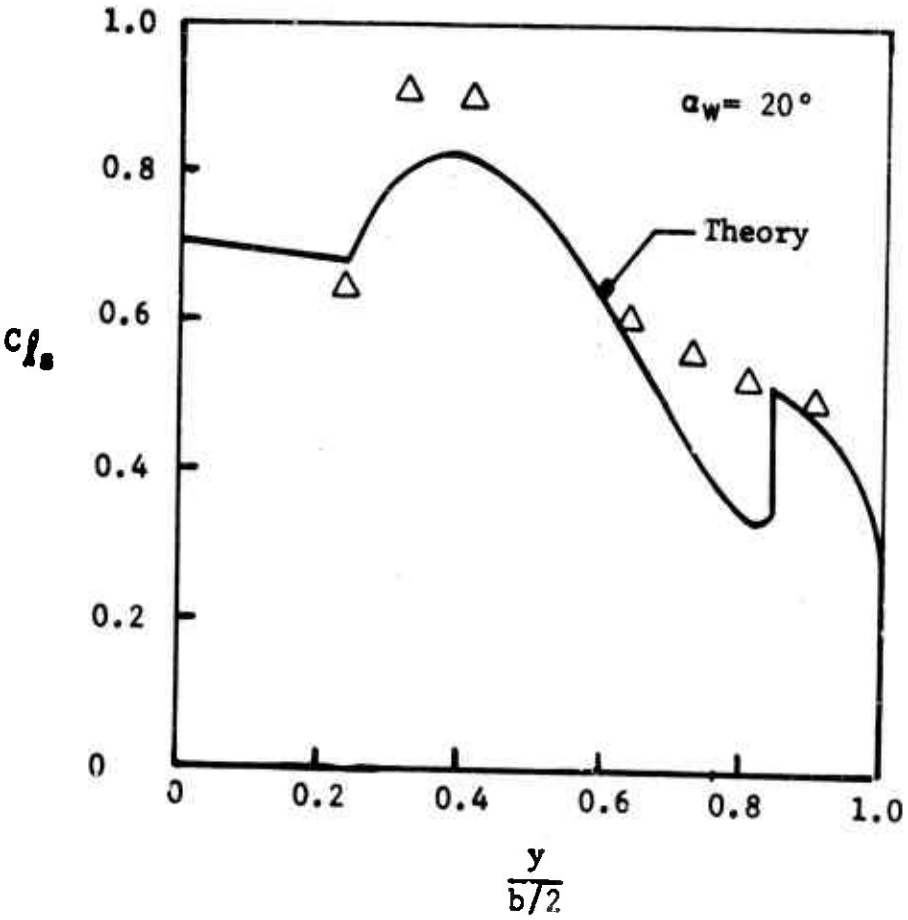

Figure 56. (Continued).

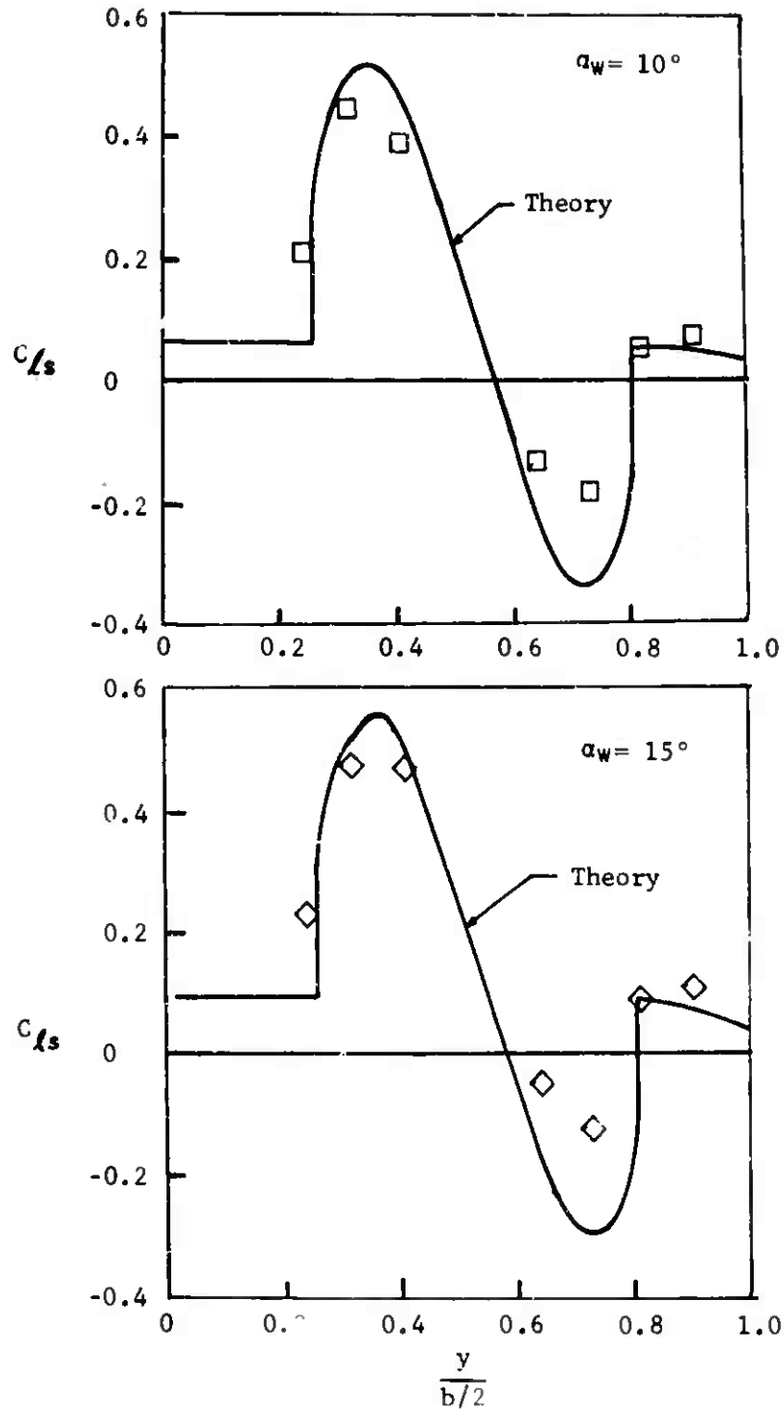

Figure 57. Comparison of Theory With Test Data of the Spanwise Distribution of $C_{\ell s}$, C_{T_s} = 0.93. Configuration: P_1 W_1 B_1.

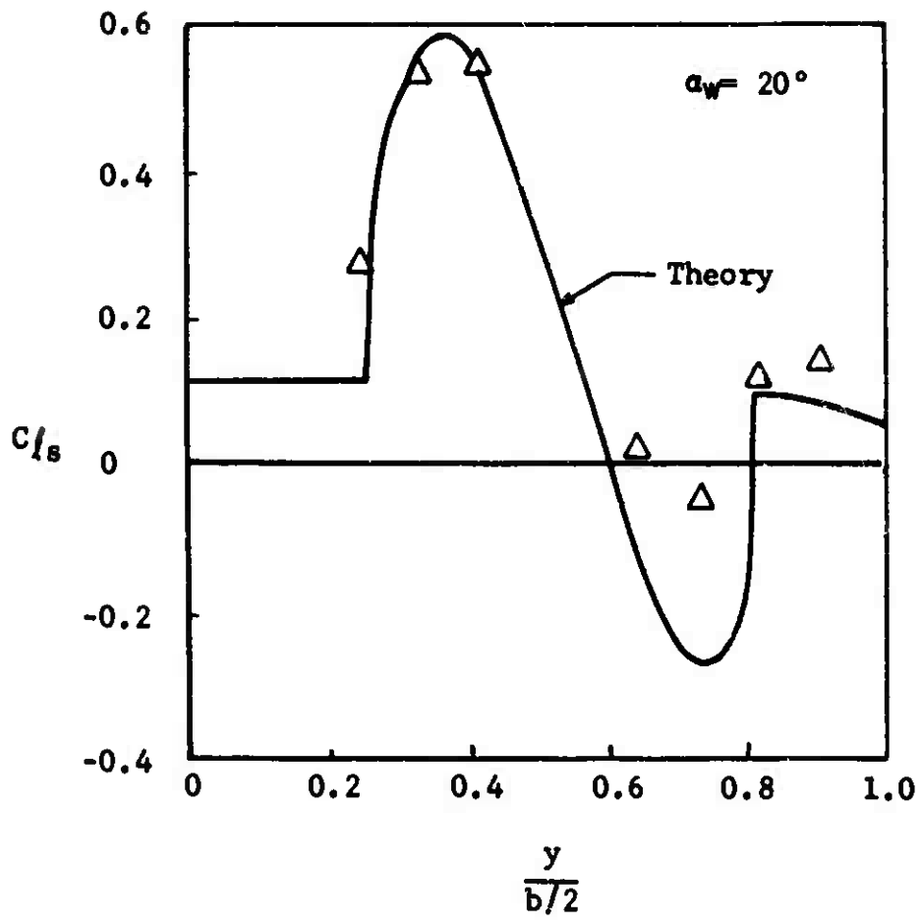

Figure 57. (Continued).

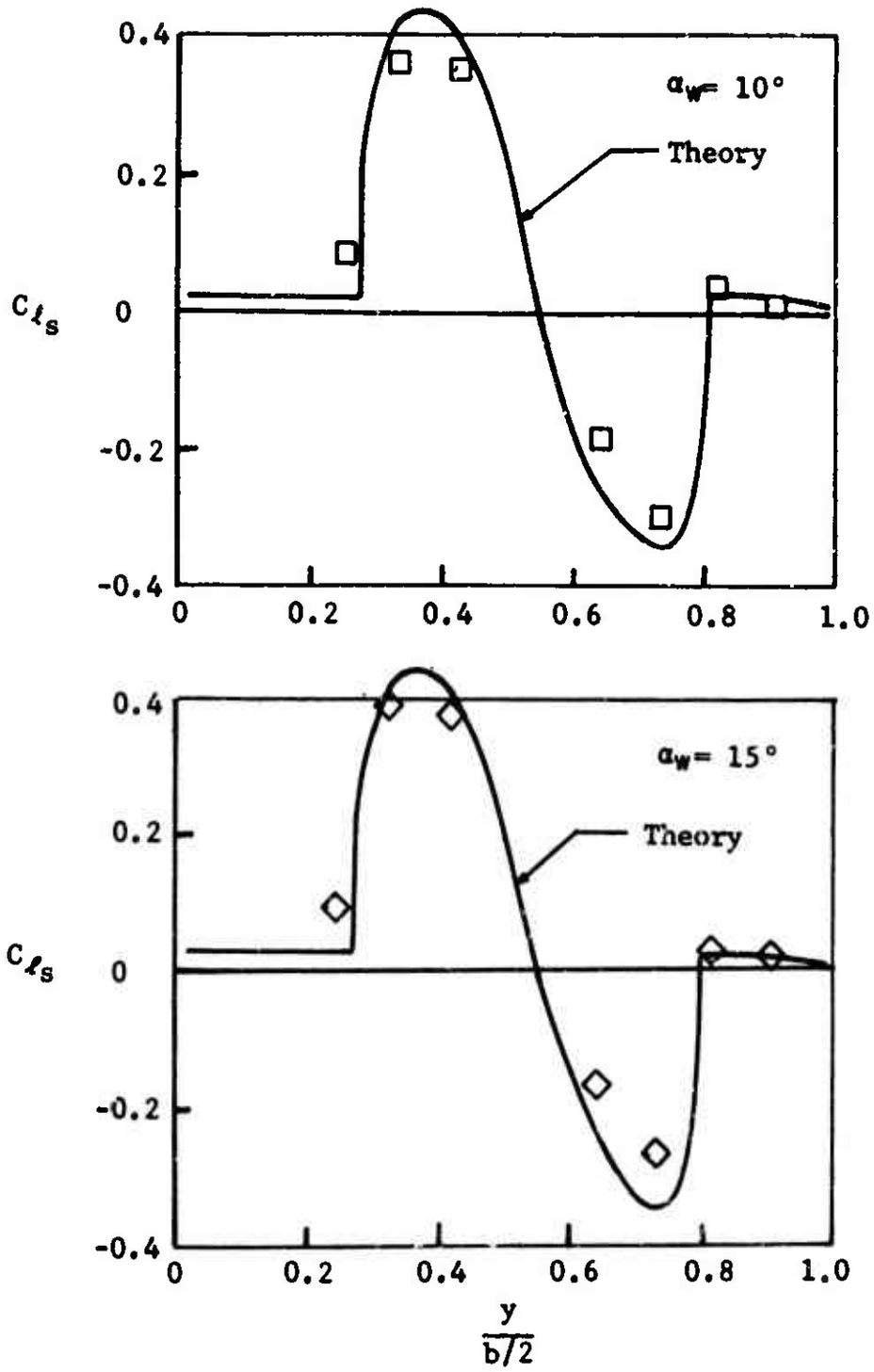

Figure 58. Comparison of Theory With Test Data of the Spanwise Distribution of C_{ℓ_s}, C_{T_s} = 0.97. Configuration: P_1 W_1 B_1.

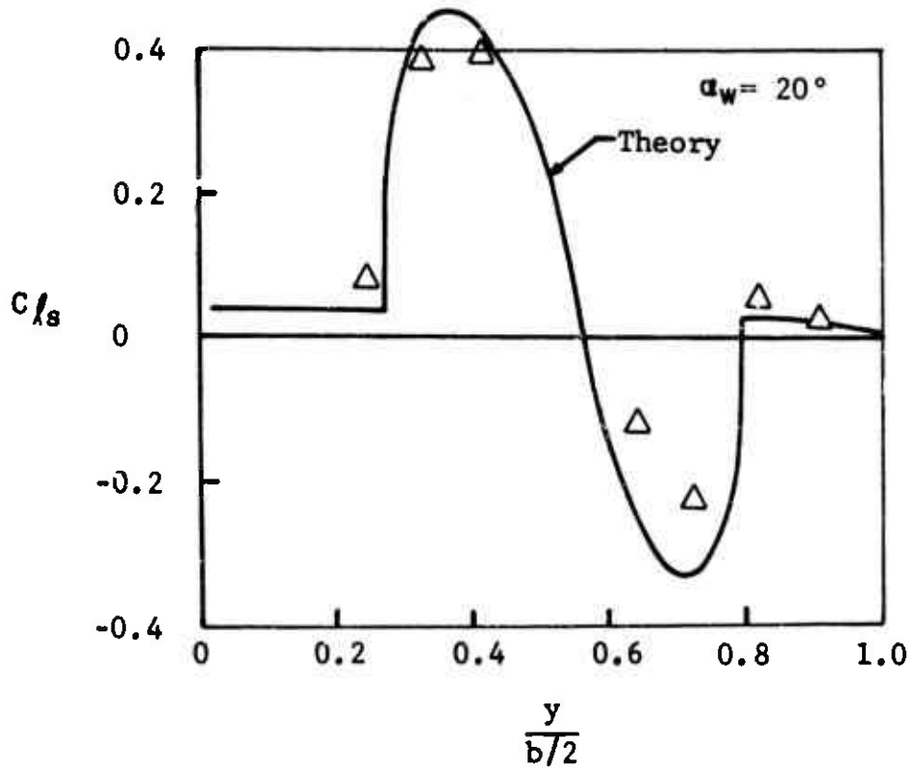

Figure 58. (Continued).

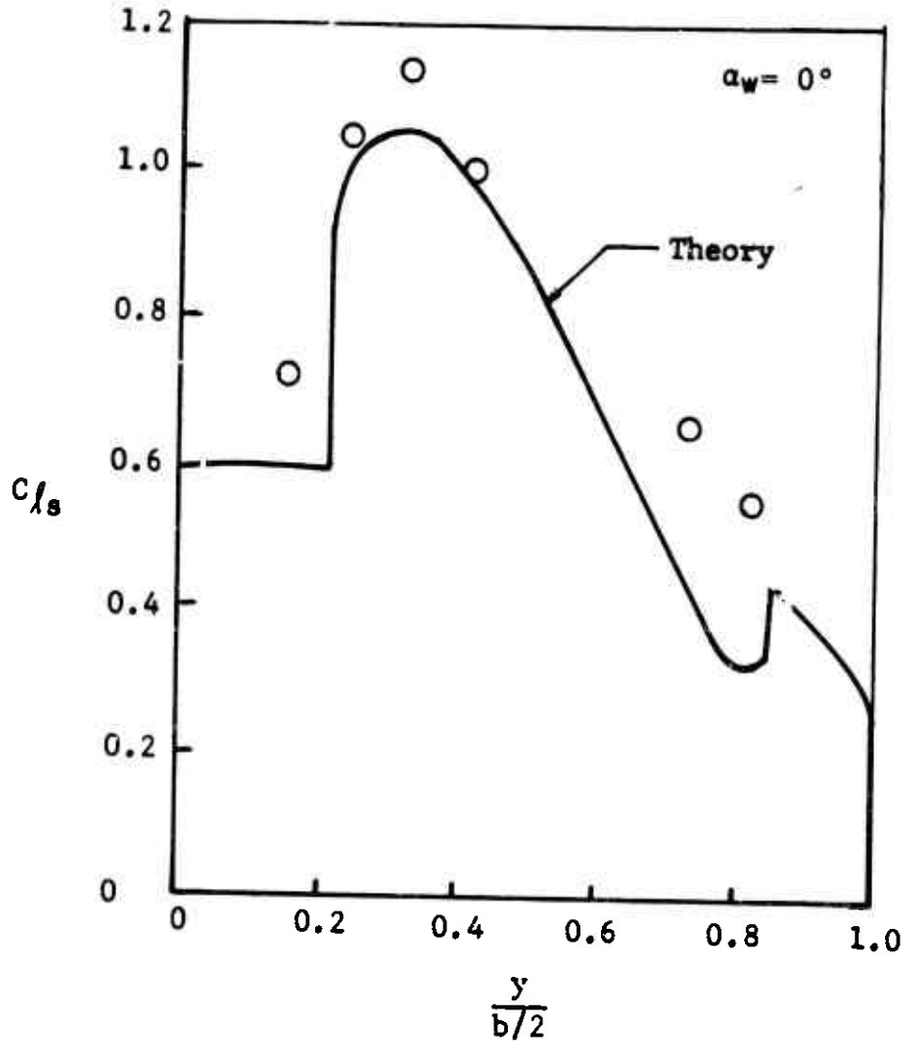

Figure 59. Comparison of Theory With Test Data of the Spanwise Distribution of C_{ℓ_s}, $C_{T_s} = 0.46$. Configuration: P_1 W_1 F_1 B_1.

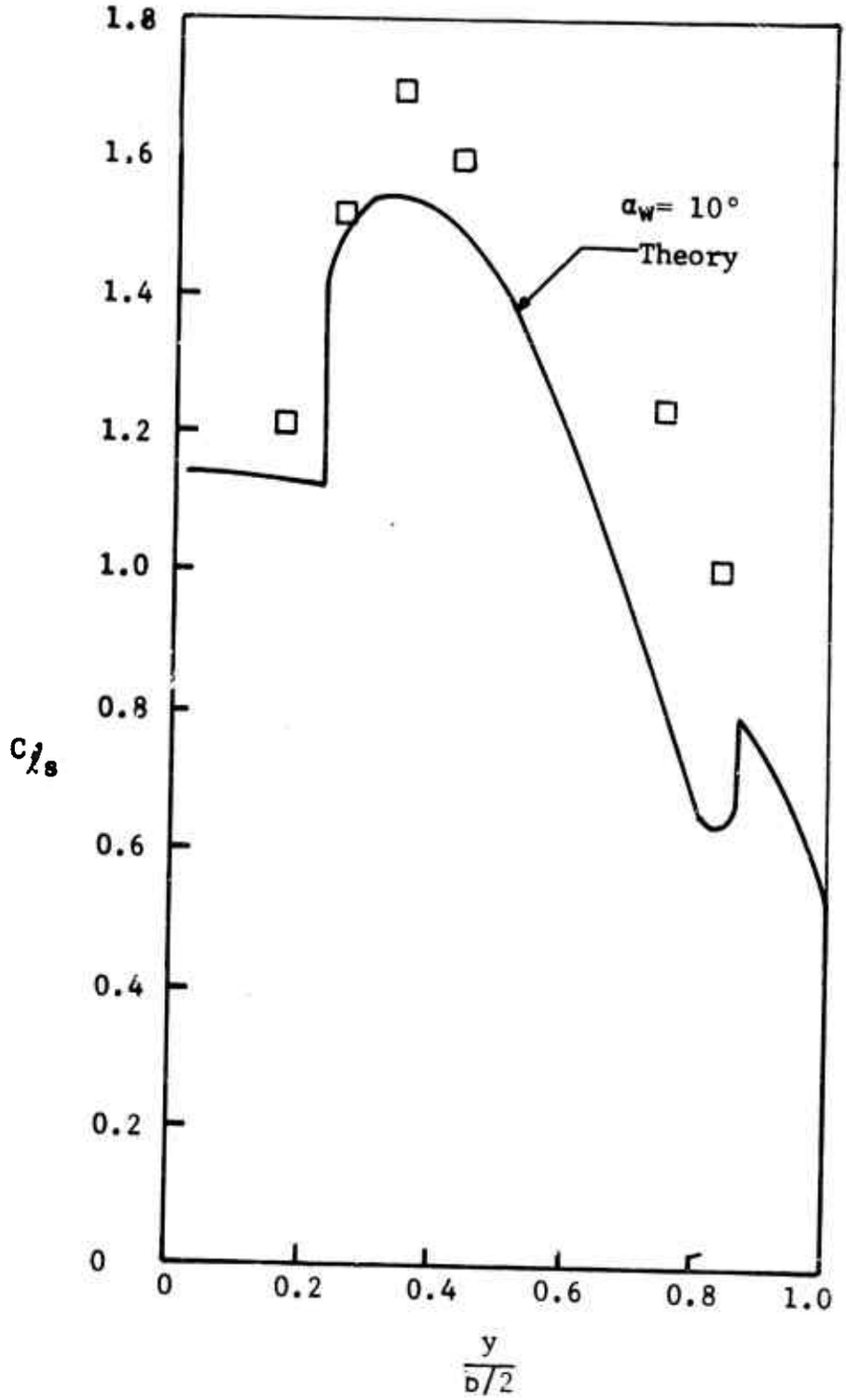

Figure 59. (Continued).

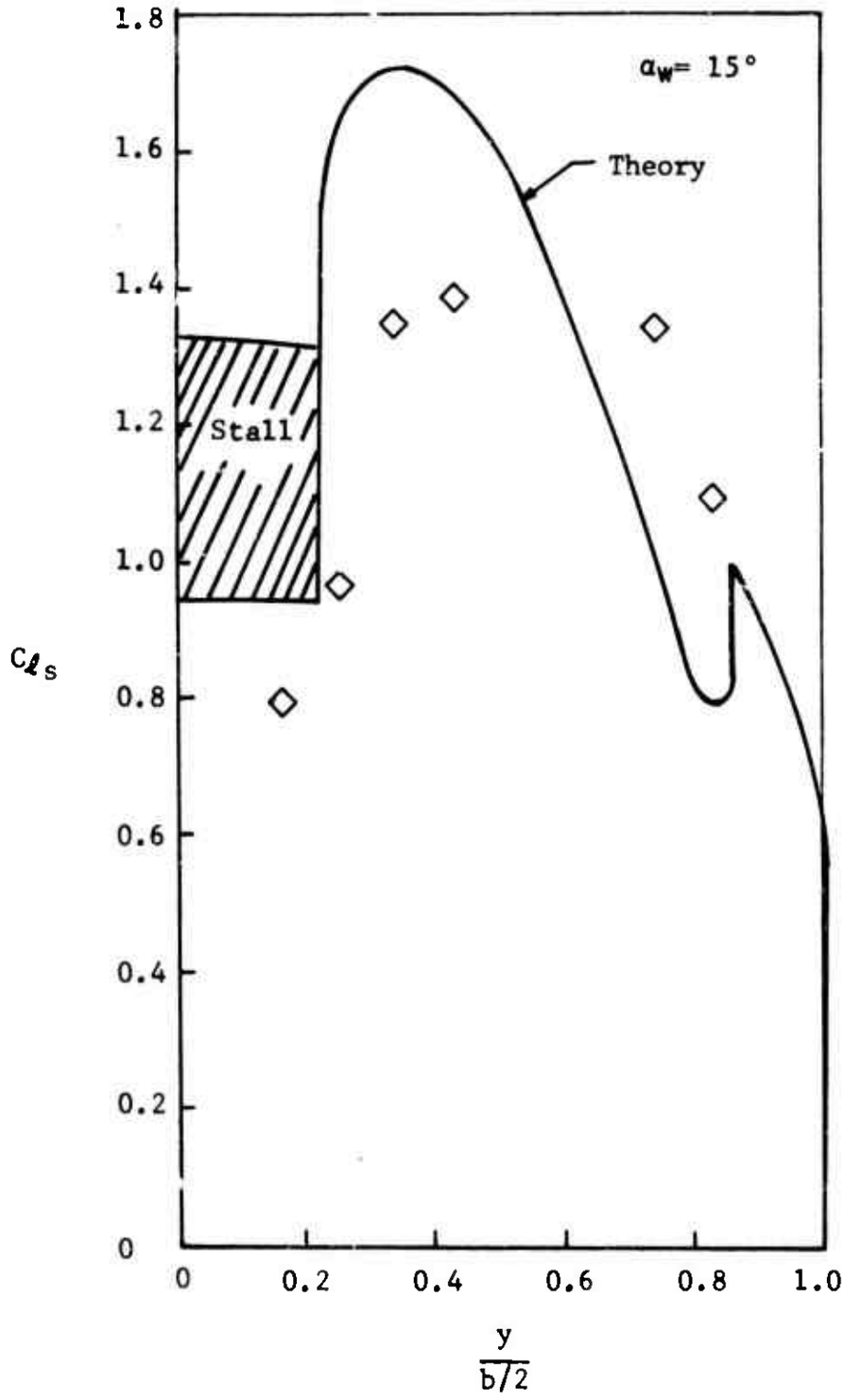

Figure 59. (Continued).

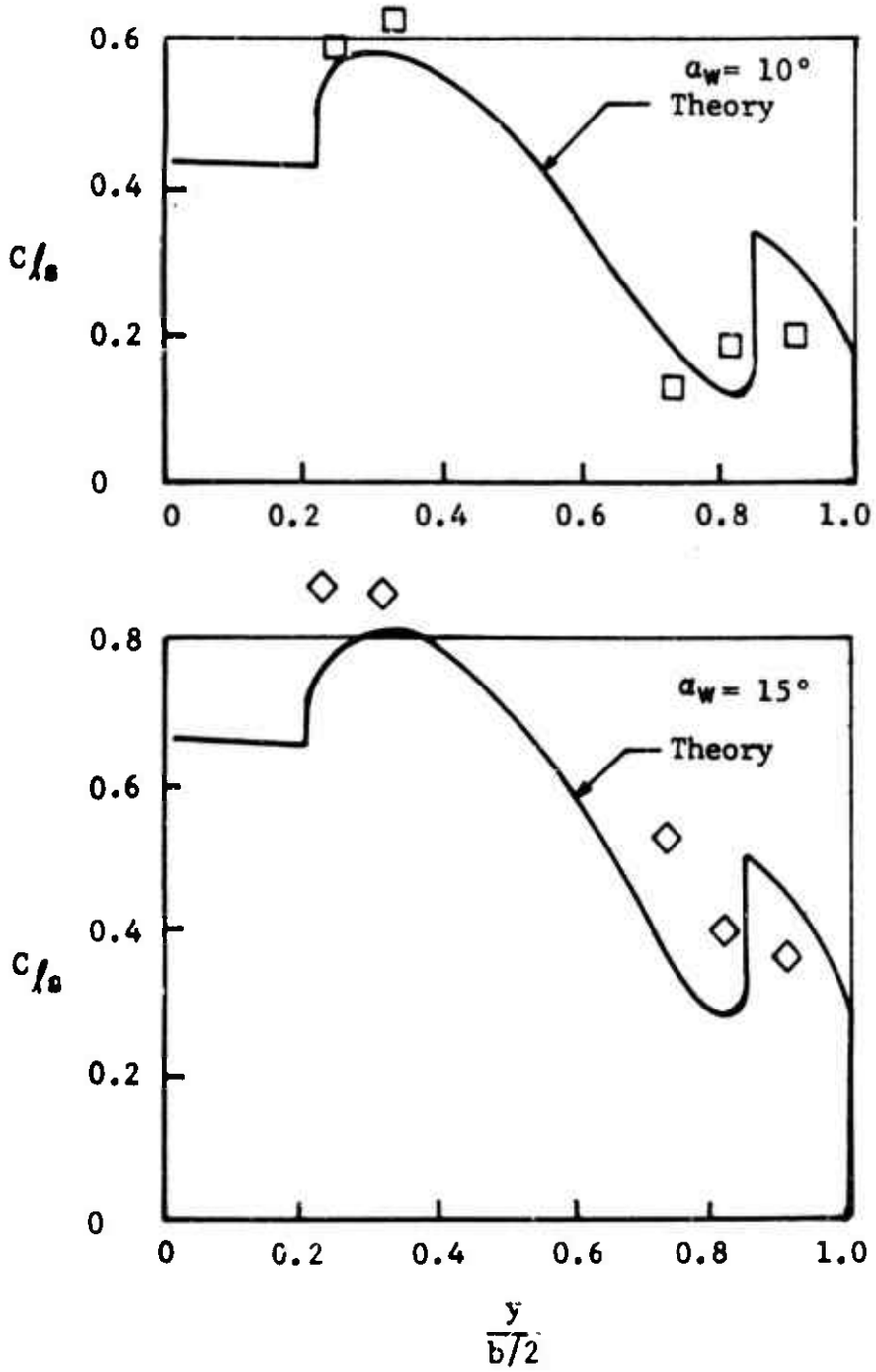

Figure 60. Comparison of Theory With Test Data of the Spanwise Distribution of C_{ℓ_s}, C_{T_s} = 0.5. Configuration: P_2 W_1 B_1.

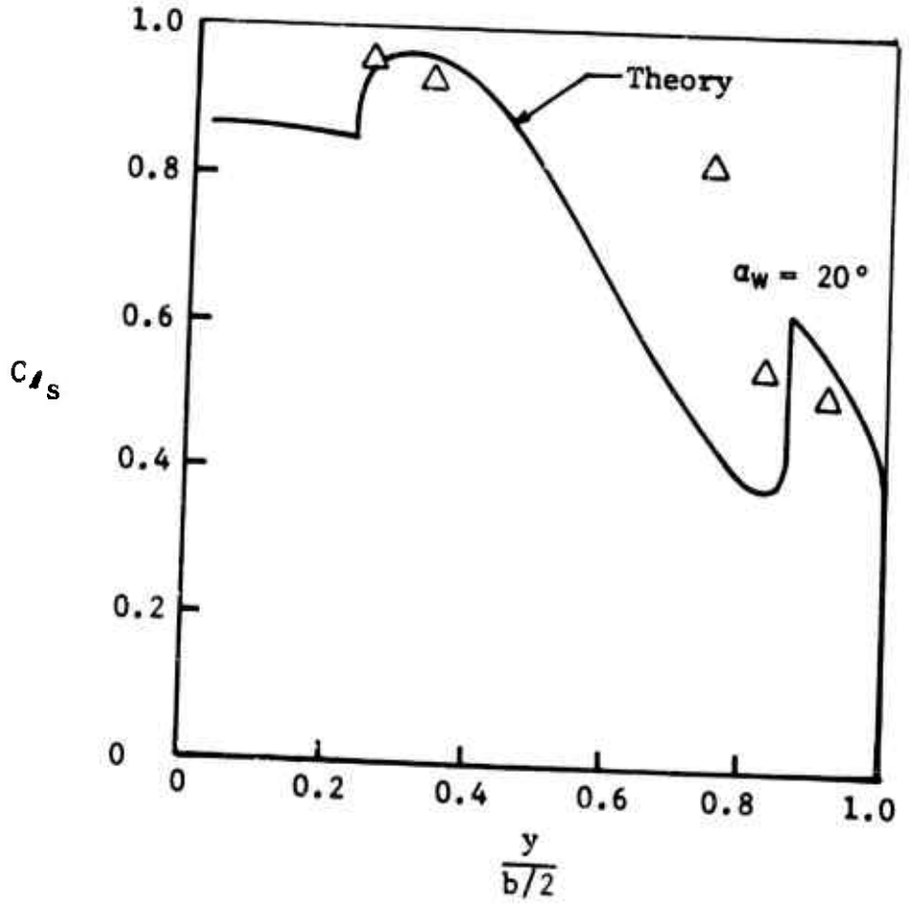

Figure 60. (Continued).

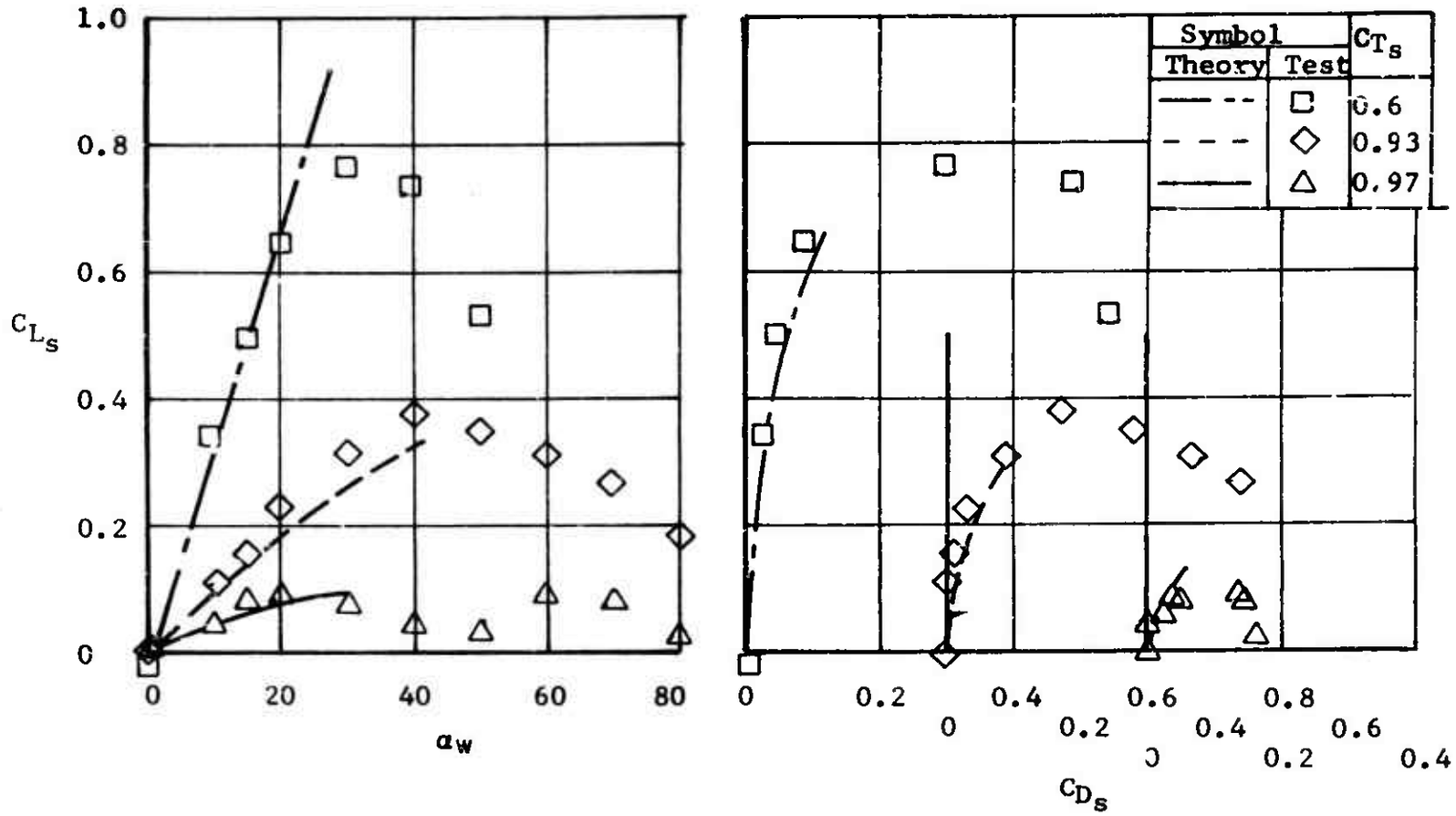

Figure 61. Comparison of Test Results With Theory.
Configuration: P_1 W_1 B_1.

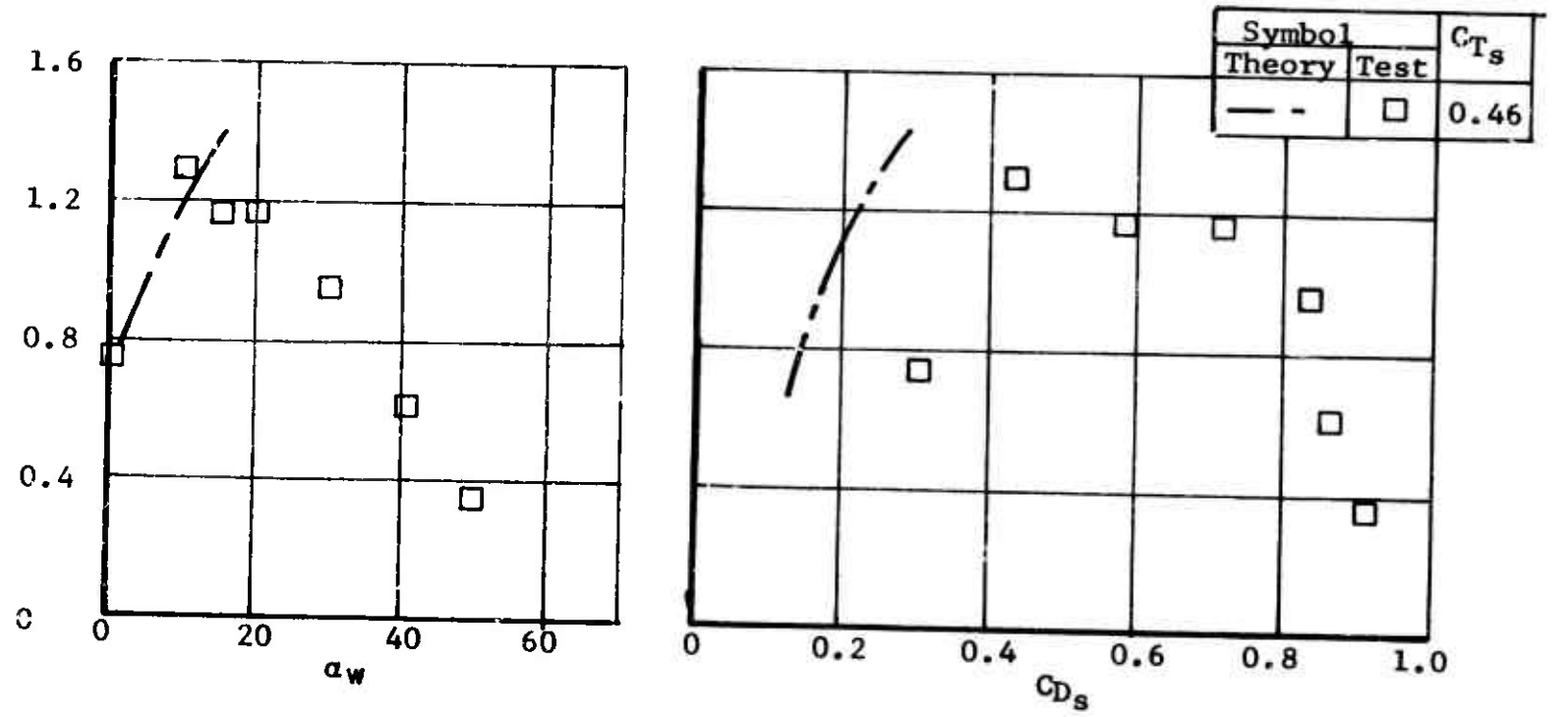

Figure 62. Comparison of Test Results With Theory.
Configuration: P_1 W_1 F_1 B_1.

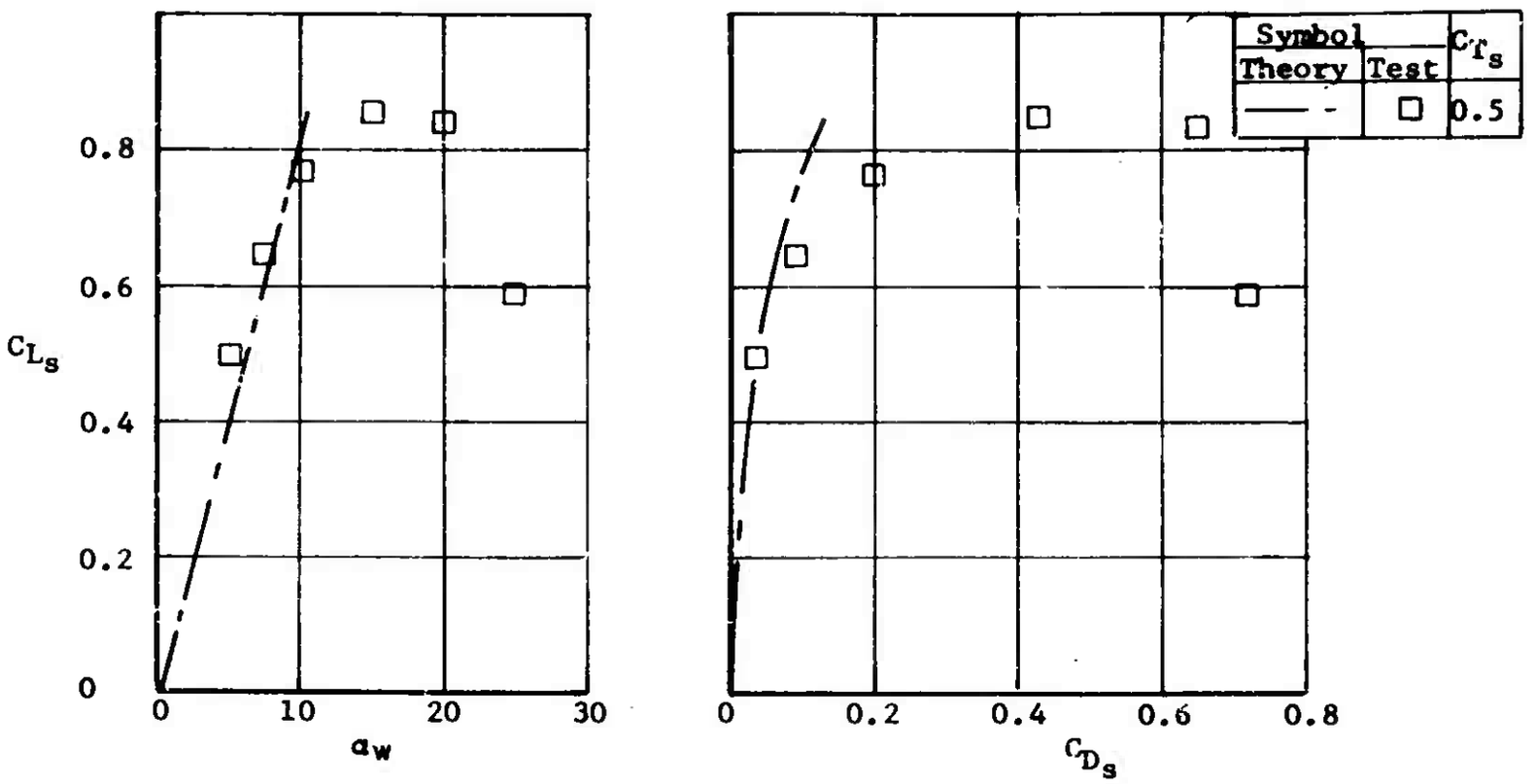

Figure 63. Comparison of Test Results With Theory.
Configuration: P_2 W_1 B_1.

IV. CONCLUSIONS

In reviewing the results of this investigation, the following conclusions are made:

1. The theory of Reference 2, expanded herein to include nonuniform slipstream distribution, gives good correlation with test data for the total wing lift and drag as well as the spanwise lift distribution of a wing partially immersed in a slipstream.

2. The test results obtained indicate that the propeller slipstream swirl causes a large change in wing local angle of attack. Differential angles of attack as much as 10° to 20° have been measured on either side of the propeller, depending upon the propeller thrust coefficient.

3. Methods of reducing onset of stall or increasing lift seem feasible by the use of wing differential flaps, differential twist, or any other method which affects the wing zero lift angle of attack, thus taking advantage of slipstream rotation.

4. An increase in wing lift of as much as 5% is seen to be possible with variation in propeller slipstream distribution. However, the trade-off in propeller efficiency must be considered.

5. The concept of using a segmented wing to obtain spanwise force and moment data distribution has been proven practical.

V. REFERENCES

1. Goland, L., et al, "Effects of Propeller Slipstream on V/STOL Aircraft Performance and Stability", TRECOM Technical Report 64-47, U. S. Army Aviation Materiel Laboratories, Fort Eustis, Virginia, August 1964.

2. Goland, L., et al, "An Investigation of Propeller Slipstream Effects on V/STOL Aircraft Performance and Stability", USAAVLABS Technical Report 65-81, U. S. Army Aviation Materiel Laboratories, Fort Eustis, Virginia, February 1966.

3. Jones, R. T., "Properties of Low-Aspect-Ratio Pointed Wings at Speeds Below and Above the Speed of Sound", NACA Report No. 835, Langley Memorial Aeronautical Laboratory, Langley Field, Virginia, 1946.

4. Kuthe and Schetzer, Foundations of Aerodynamics, John Wiley and Sons, New York, 1950.

5. Gessow, A., and Meyers, G. C., Aerodynamics of the Helicopter, The MacMillan Company, New York, New York, 1952.

6. Fink, M. P., et al, "Aerodynamic Data on Large Semi-Span Tilting Wing With 0.6 Diameter Chord, Single Slotted Flap, and Single Propeller Rotating Down at the Tip", NASA Technical Note, TND-2412, Langley Research Center, Langley Station, Hampton, Virginia, August 1964.

7. Taylor, R. T., "Wind Tunnel Investigation of Effect of Ratio of Wing Chord to Propeller Diameter With Addition of Slats on the Aerodynamic Characteristics of Tilt Wing VTOL Configurations in the Transition Speed Regime", NASA Technical Note TND-17, Langley Research Center, Langley Field, Virginia, September 1959.

APPENDIX

SEGMENTED WING WIND TUNNEL TEST RESULTS

Presented in this appendix is a summary of the test data obtained during this program. The data which are herein presented in tabular form include the total balance wing lift and drag coefficients $C_{L_S'}$ and $C_{D_S'}$, propeller thrust, dynamic pressures q_o and q_s, and wing angle of attack setting α_w for all the test configurations specified in Table IV. It should be noted that the values of C_{L_S} and C_{D_S} include the effects of propeller thrust and normal force coefficients which are not included in the wing segment data presented in the main text.

Also included are the tuft photographs showing the flow characteristics of the propeller-wing model for the conditions and configurations tested.

TABLE VI

SUMMARY OF TEST RESULTS

a. Test Number 2

α_w	q_o	T_p	q_s	C_{T_s}	C_{L_s}'	C_{D_s}'
0	0.25	70.4	8.74	0.97	0.04	-1.26
10	0.24	71.9	8.90	0.97	0.33	-1.22
15	0.22	71.9	8.89	0.97	0.44	-1.19
20	0.20	72.5	8.94	0.97	0.56	-1.15
30	0.12	72.5	8.87	0.98	0.76	-1.04
40	0.09	76.0	9.24	0.99	0.92	-0.89
50	0.07	75.4	9.15	0.99	1.08	-0.70
60	0.04	73.8	8.94	0.99	1.24	-0.46
70	0.04	76.3	9.25	0.99	1.29	-0.23
80	0.02	78.2	9.44	1.00	1.30	-0.04
90	0.00	76.0	9.15	1.00	1.30	+0.21

b. Test Number 3

0.0	0.66	71.2	9.25	0.93	0.06	-1.22
10.2	0.65	72.2	9.36	0.93	0.36	-1.18
15.3	0.65	71.8	9.30	0.93	0.53	-1.13
20.4	0.64	72.7	9.40	0.93	0.69	-1.09
30.5	0.62	72.9	9.41	0.93	0.96	-0.92
40.6	0.60	73.4	9.44	0.94	1.21	-0.69
50.7	0.57	75.1	9.63	0.94	1.36	-0.41
60.8	0.54	75.0	9.58	0.94	1.46	-0.12
70.8	0.52	76.0	9.67	0.95	1.47	+0.15
80.8	0.48	77.1	9.79	0.95	1.42	+0.38
90.7	0.46	77.0	9.75	0.95	1.34	+0.62

TABLE VI (Continued)

c. Test Number 4

α_w	q_o	T_p	q_s	C_{T_s}	C_{L_s}'	C_{D_s}'
0	3.88	51.5	10.1	0.61	-0.02	-0.84
10.3	3.86	49.7	09.8	0.61	0.49	-0.78
15.4	3.87	47.7	09.6	0.60	0.74	-0.70
20.5	3.85	48.1	09.6	0.60	0.98	-0.62
30.7	3.85	47.4	09.5	0.60	1.25	-0.29
40.0	3.84	49.5	09.8	0.61	-0.14	-1.27
50.1	3.84	50.0	09.9	0.61	+0.12	-1.18

d. Test Number 5

-0.1	8.13	-6.42	7.36	-0.10	-0.16	+0.14
10.2	8.11	-6.53	7.32	-0.11	0.44	+0.19
15.3	8.11	-7.19	7.24	-0.12	0.69	+0.25
20.4	8.10	-7.48	7.20	-0.12	0.91	+0.36
30.3	8.12	-4.00	7.64	-0.06	0.79	+0.56
40.3	8.13	-0.56	8.06	+0.01	0.66	+0.64
50.3	8.13	+0.42	8.18	+0.01	0.66	+0.85
60.2	8.12	+3.58	8.55	+0.05	0.60	+0.97
70.2	8.12	+1.25	8.27	+0.02	0.50	1.23

e. Test Number 6

-0.1	8.14	-24.1	5.23	-0.56	-0.26	+0.73
10.1	8.13	-23.0	5.35	-0.52	0.37	+0.71
15.2	8.11	-23.1	5.33	-0.52	0.60	0.76
20.3	8.11	-21.2	5.55	-0.46	0.82	0.76
30.3	8.12	-13.9	6.44	-0.26	0.68	0.76
40.2	8.13	-09.5	6.99	-0.16	0.64	0.84
50.2	8.13	-03.2	7.74	-0.05	0.60	0.89

TABLE VI (Continued)

f. Test Number 7

α_w	q_o	T_p	q_s	C_{T_s}	C_{L_s}'	C_{D_s}'
0.0	3.96	32.2	7.84	0.49	-0.09	-0.64
10.2	3.93	31.7	7.76	0.49	+0.45	-0.62
15.3	3.94	30.7	7.64	0.48	0.76	-0.50
20.4	3.92	32.0	7.79	0.50	0.97	-0.39
30.5	3.93	31.3	7.70	0.49	1.23	-0.06
40.6	3.89	33.2	7.89	0.51	1.30	+0.21
50.5	3.90	35.5	8.19	0.52	1.16	+0.35

g. Test Number 8

0.03	0.67	66.3	8.67	0.92	0.07	-1.17

h. Test Number 9

0.3	8.19	-4.62	7.63	-0.07	0.85	+0.38
10.6	8.17	-4.15	7.66	-0.06	1.44	0.49
15.6	8.18	-7.65	7.25	-0.13	1.65	0.74
20.5	8.15	-2.02	7.90	-0.03	1.34	0.70
30.3	8.20	+6.01	8.93	+0.08	0.85	0.83
40.3	8.18	+3.80	8.63	+0.05	0.75	0.99
50.2	8.18	+6.81	9.00	+0.00	0.57	1.06

i. Test Number 10

0.2	0.78	55.2	7.43	0.89	0.44	-0.92
10.3	0.77	56.5	7.58	0.90	0.79	-0.81
15.3	0.77	56.0	7.50	0.90	0.92	-0.73
20.4	0.76	56.0	7.50	0.90	1.04	-0.62
30.4	0.74	55.4	7.42	0.90	1.23	-0.41
40.5	0.70	58.6	7.77	0.91	1.26	-0.25
50.5	0.68	58.7	7.75	0.91	1.47	-0.01

TABLE VI (Continued)

j. Test Number 11

α_w	q_o	T_p	q_s	C_{T_s}	C_{L_s}'	C_{D_s}'
0.3	4.04	29.1	7.55	0.46	0.71	-0.30
10.4	4.03	24.7	7.02	0.42	1.29	-0.11
15.4	4.03	27.1	7.31	0.45	1.23	+0.00
20.5	4.02	26.7	7.24	0.44	1.35	+0.17
30.4	4.01	31.1	7.76	0.48	1.16	+0.28
40.4	4.02	26.6	7.22	0.44	1.03	+0.51
50.3	4.01	22.5	6.72	0.40	0.88	+0.64

k. Test Number 12

0.1	0 77	56.0	7.52	0.90	0.36	-0.96
50.5	0.68	56.8	7.53	0.91	1.22	-0.10
60.5	0.65	55.2	7.31	0.91	1.23	-0.05
70.5	0.62	58.1	7.63	0.92	1.19	+0.21
80.4	0.59	55.3	7.26	0.92	1.16	+0.35
90.4	0.55	54.3	7.10	0.92	1.12	+0.49

l. Test Number 13

0	0.25	62.5	7.79	0.97	0.34	-1.06
0	0.23	62.4	7.76	0.97	0.40	-1.06
20	0.19	62.7	7.75	0.97	0.72	-0.87
40	0.17	64.0	7.88	0.98	0.96	-0.56
60	0.06	64.4	7.82	0.99	1.15	-0.16
80	0.00	66.1	7.97	1.00	1.15	+0.19
90	0.00	65.9	7.94	1.00	1.07	+0.37

TABLE VI (Continued)

m. Test Number 14

α_w	q_o	T_p	q_s	C_{T_s}	C_{L_s}'	C_{D_s}'
0.3	8.16	-17.1	6.10	-0.34	0.78	0.71
10.6	8.14	-20.8	5.63	-0.44	1.66	1.06
15.6	8.15	18.9	5.88	-0.39	1.54	1.08
20.5	8.18	-13.1	6.60	-0.24	1.26	1.07
30.4	8.19	-08.7	7.15	-0.15	0.94	1.20
40.3	8.20	0.4	8.24	+0.00	0.73	1.15
50.2	8.20	05.6	8.87	+0.08	0.59	1.22

n. Test Number 15

0.2	4.03	25.1	7.06	0.43	0.67	-0.29
10.4	4.03	24.2	6.94	0.42	1.21	-0.11
15.4	4.02	24.3	6.95	0.42	1.25	+0.04
20.4	4.03	23.0	6.80	0.41	1.33	+0.21
30.4	4.01	24.0	6.90	0.42	1.33	+0.44
40.4	4.00	27.8	7.34	0.46	1.10	+0.52
50.3	3.98	26.2	7.14	0.44	0.89	+0.50

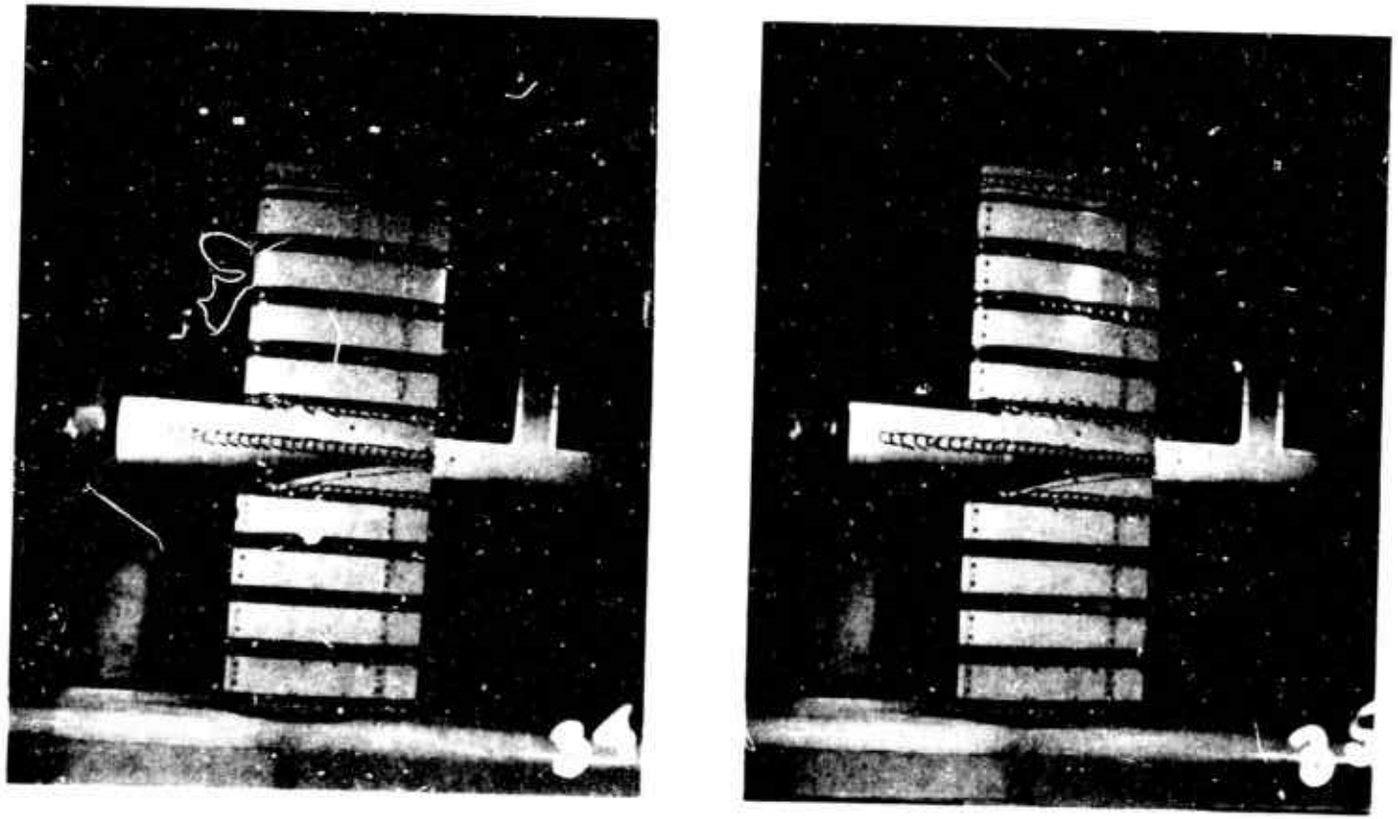

$\alpha_w = 0°$ $\alpha_w = 10°$

Figure 64. Flow Characteristics of Segmented Wing Model, $C_{T_s} = -0.10$. Configuration: P_1 W_1 B_1.

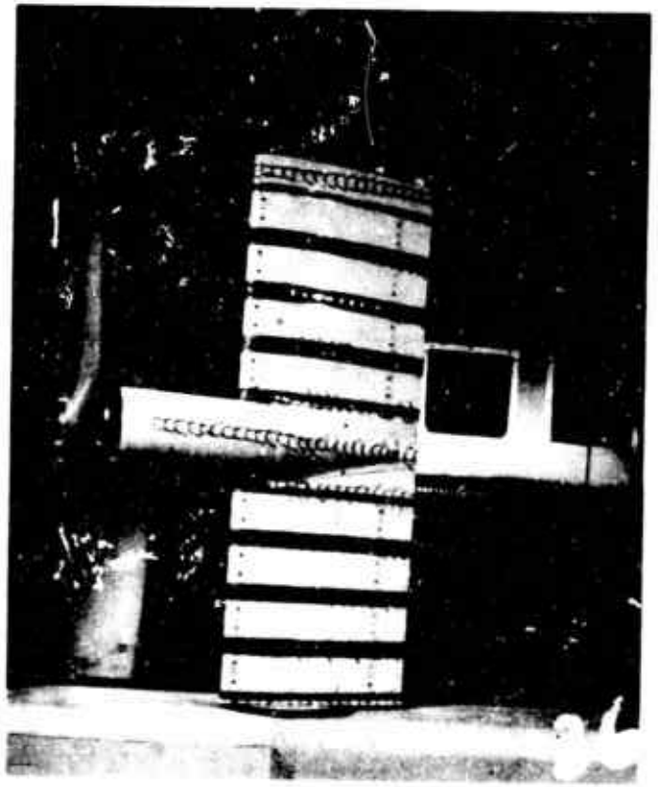

$\alpha_w = 15°$

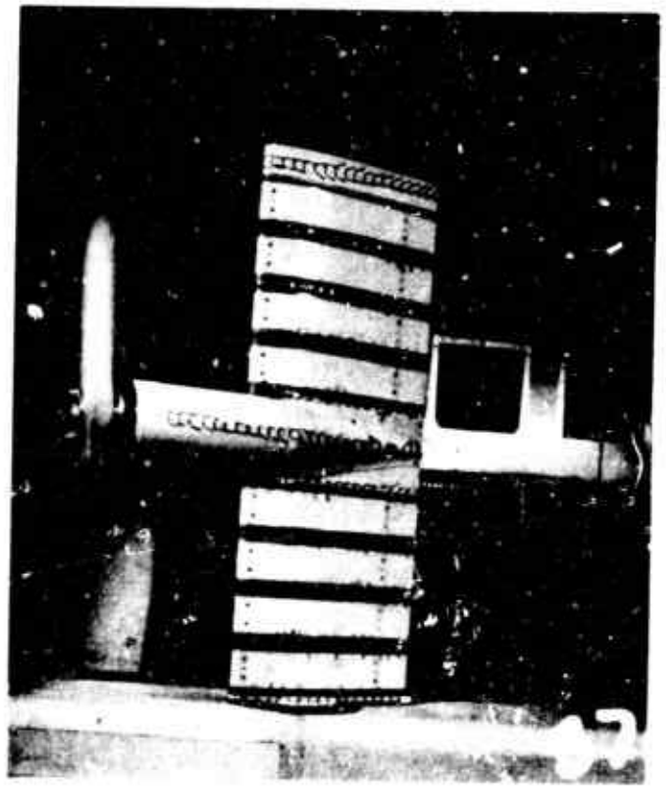

$\alpha_w = 20°$

Figure 64. (Continued).

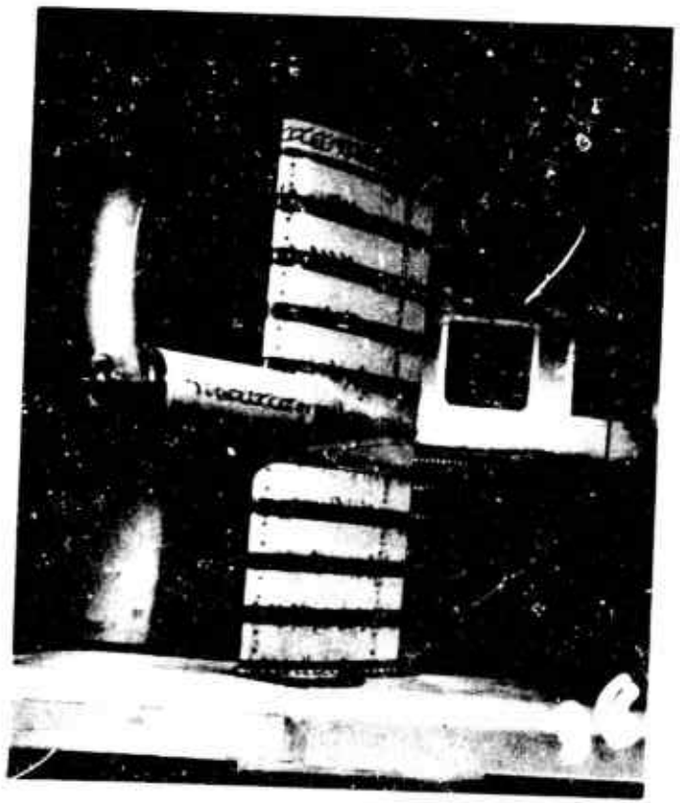

$\alpha_w = 30°$

$\alpha_w = 40°$

Figure 64. (Continued).

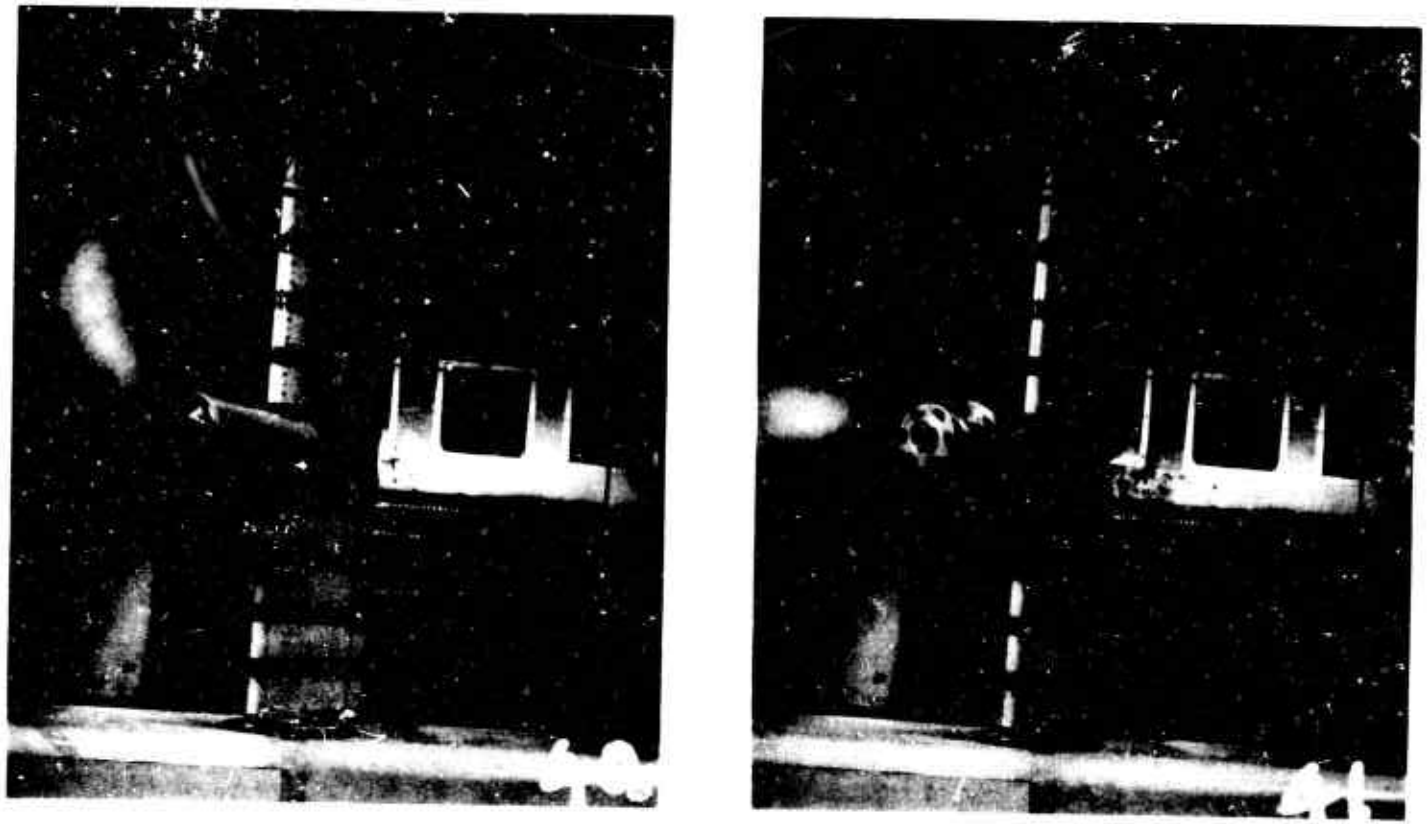

$\alpha_w = 50°$

$\alpha_w = 60°$

Figure 64. (Continued).

$\alpha_w = 70°$

Figure 64. (Continued).

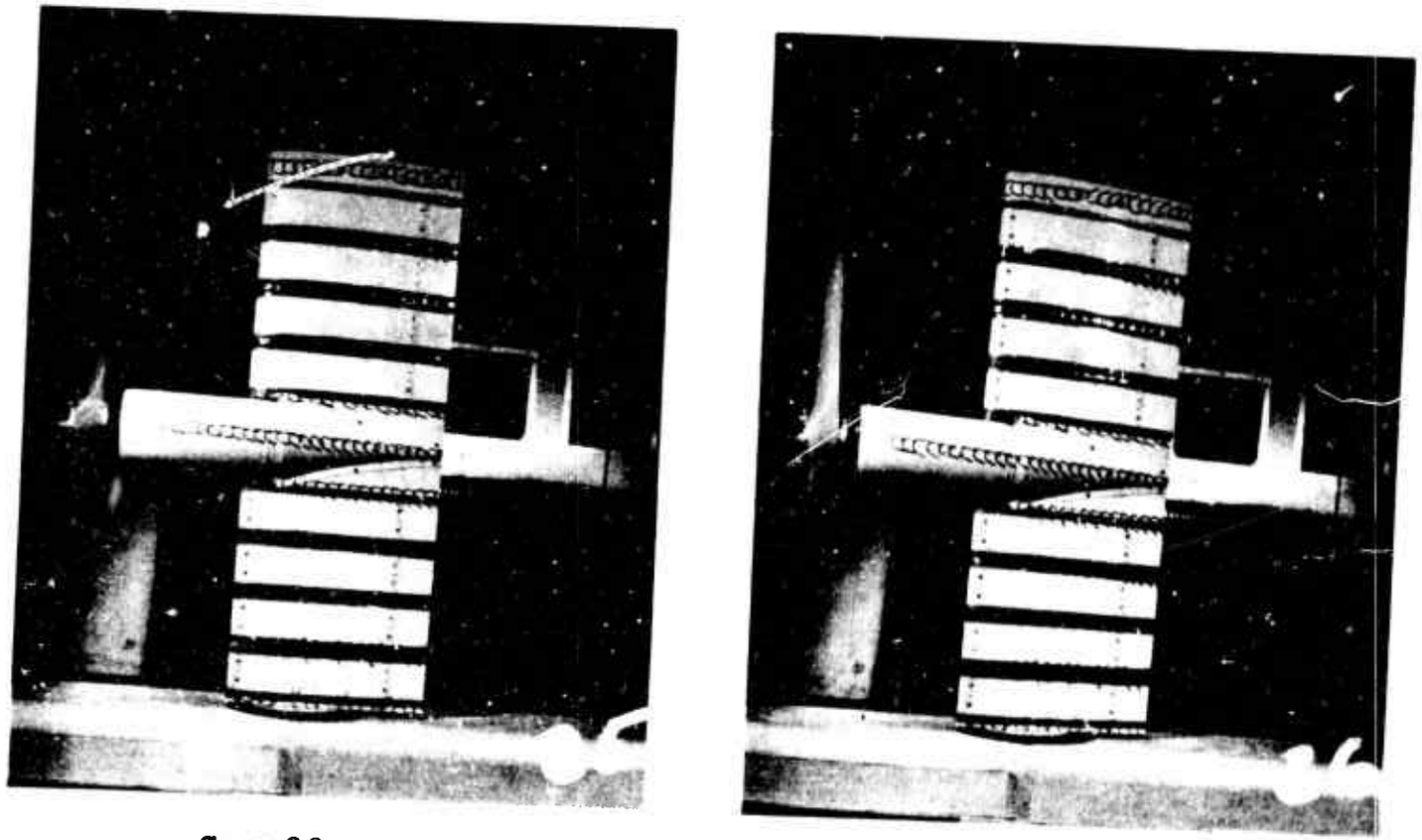

$\alpha_w = 0°$ $\alpha_w = 10°$

Figure 65. Flow Characteristics of Segmented Wing Model, $C_{T_s} = 0.60$. Configuration: P_1 W_1 B_1.

$\alpha_w = 15°$

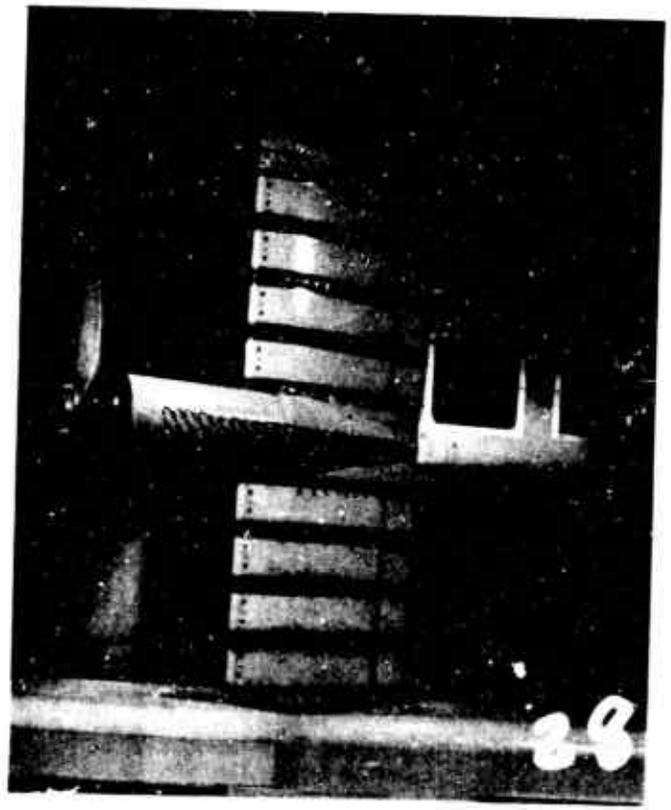

$\alpha_w = 20°$

Figure 65. (Continued).

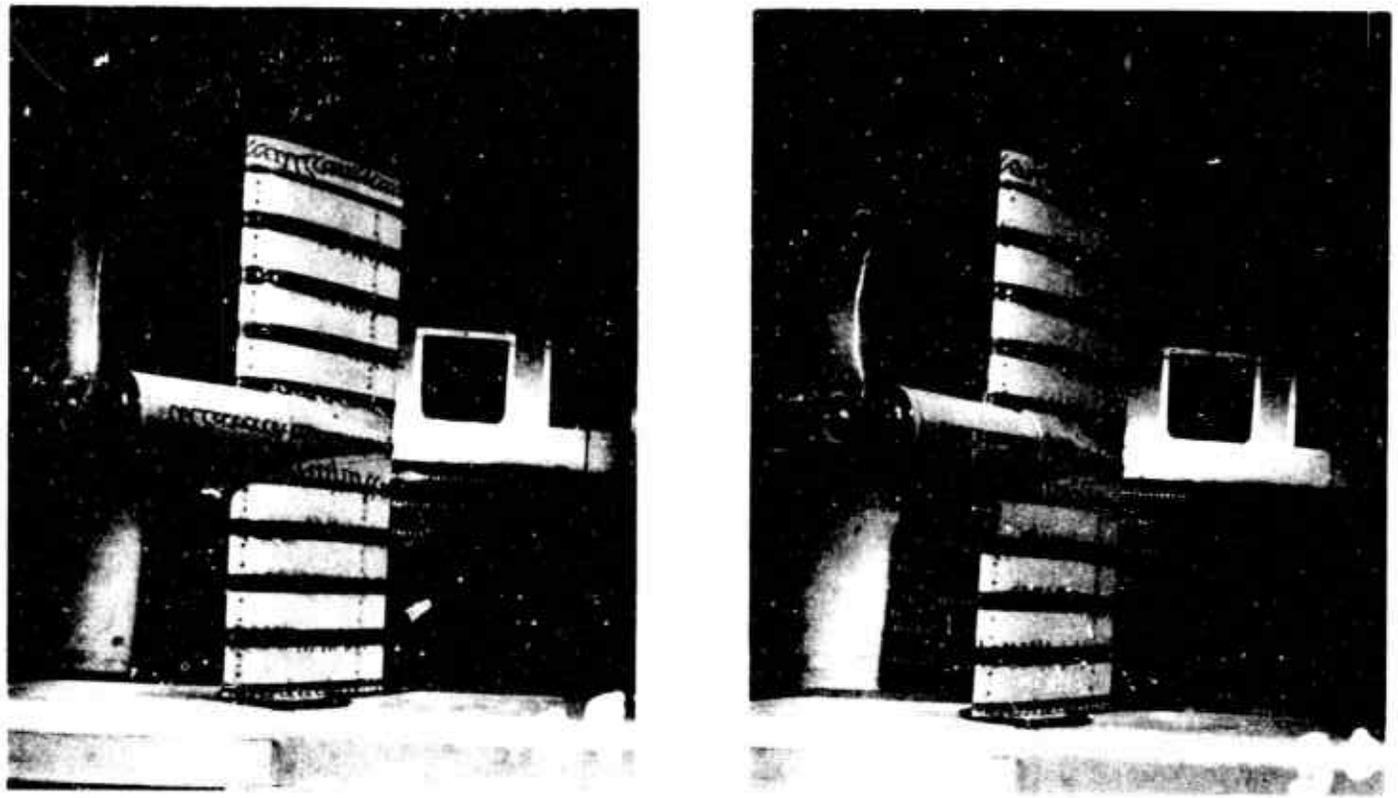

$\alpha_w = 30°$ $\alpha_w = 40°$

Figure 65. (Continued).

$\alpha_w = 50°$

Figure 65. (Continued).

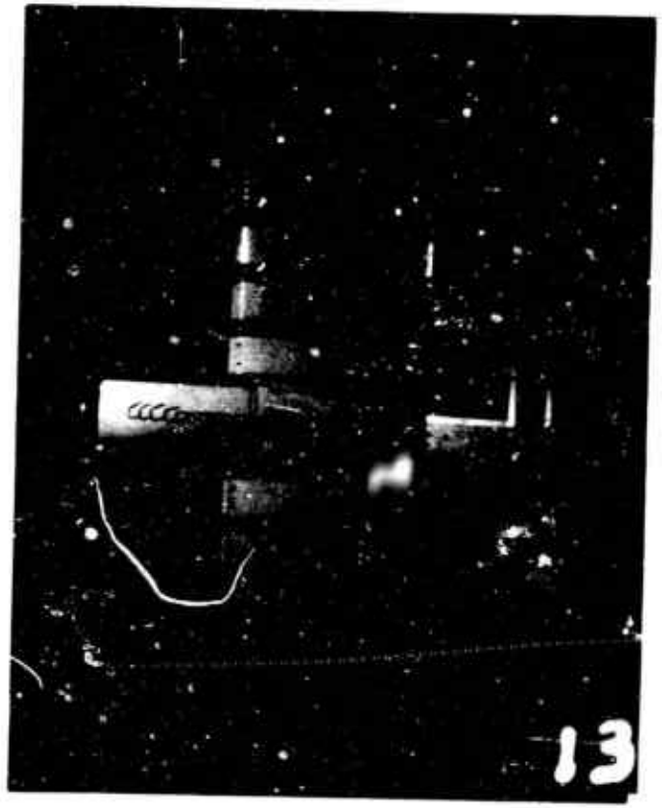

$\alpha_w = 0°$

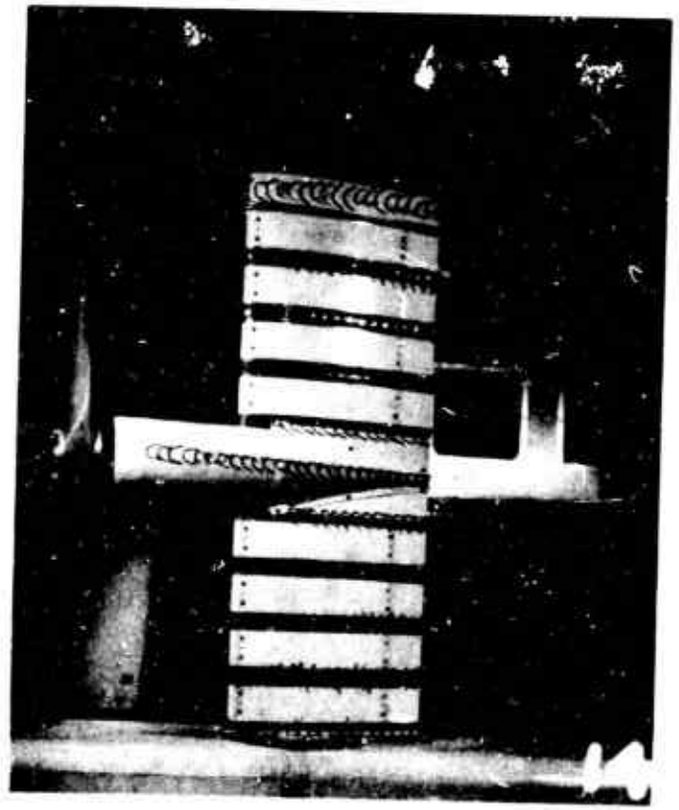

$\alpha_w = 10°$

Figure 66. Flow Characteristics of Segmented Wing Model, $C_{T_s} = 0.93$. Configuration: P_1 W_1 B_1.

$\alpha_w = 15°$

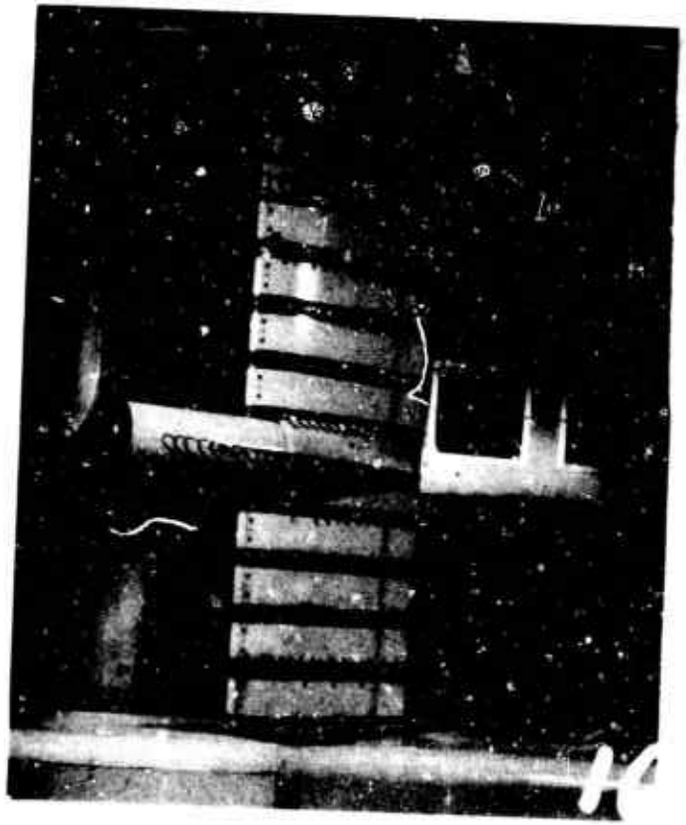

$\alpha_w = 20°$

Figure 66. (Continued).

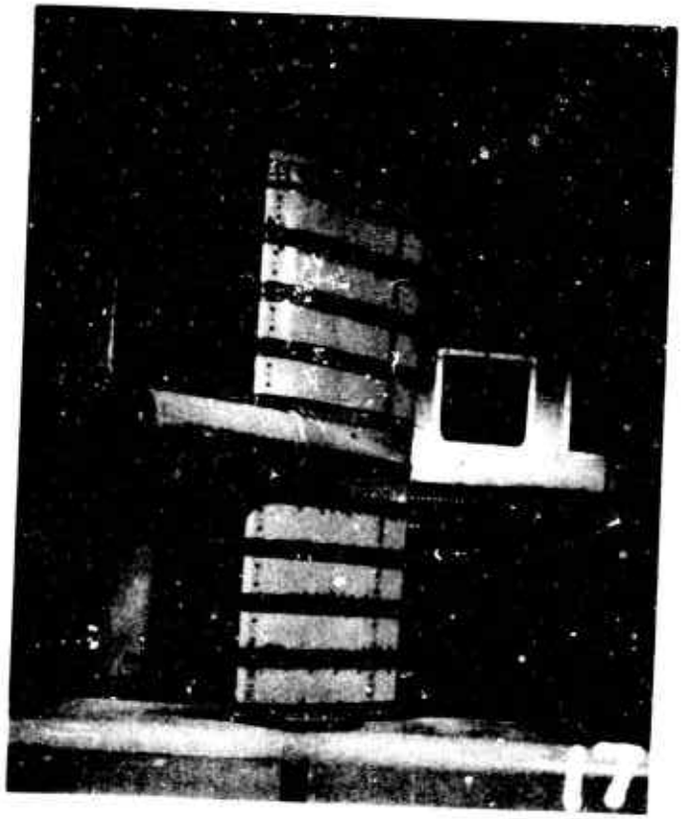

$\alpha_w = 30°$

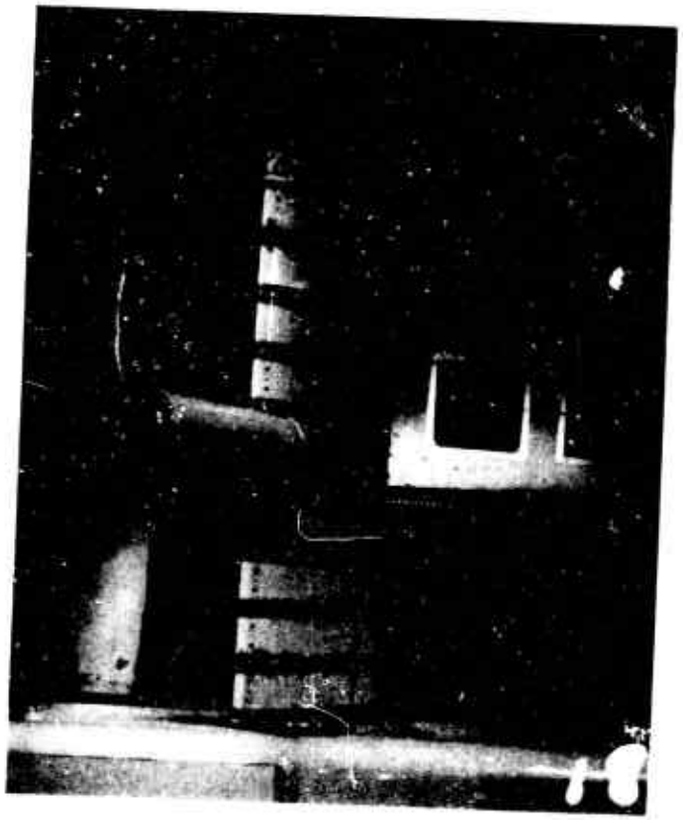

$\alpha_w = 40°$

Figure 66. (Continued).

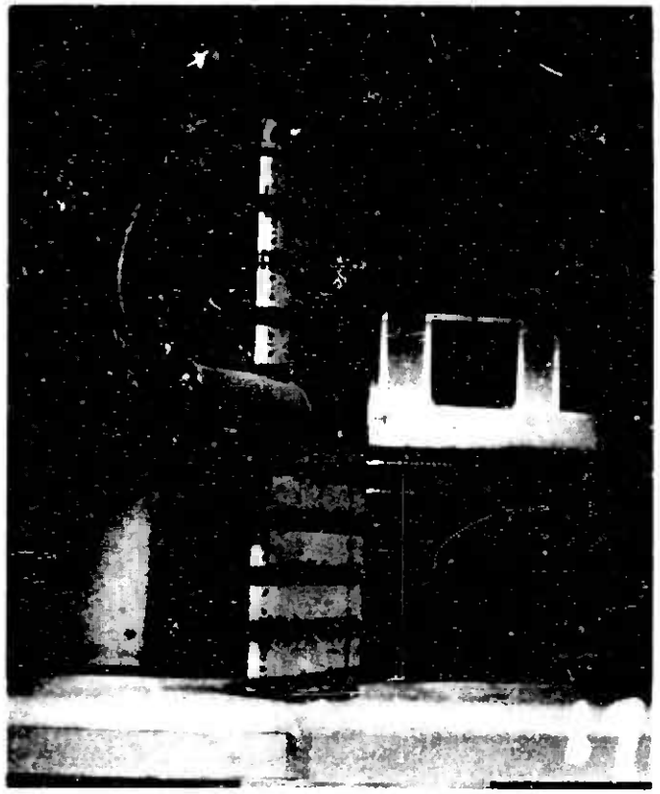

$\alpha_w = 50°$

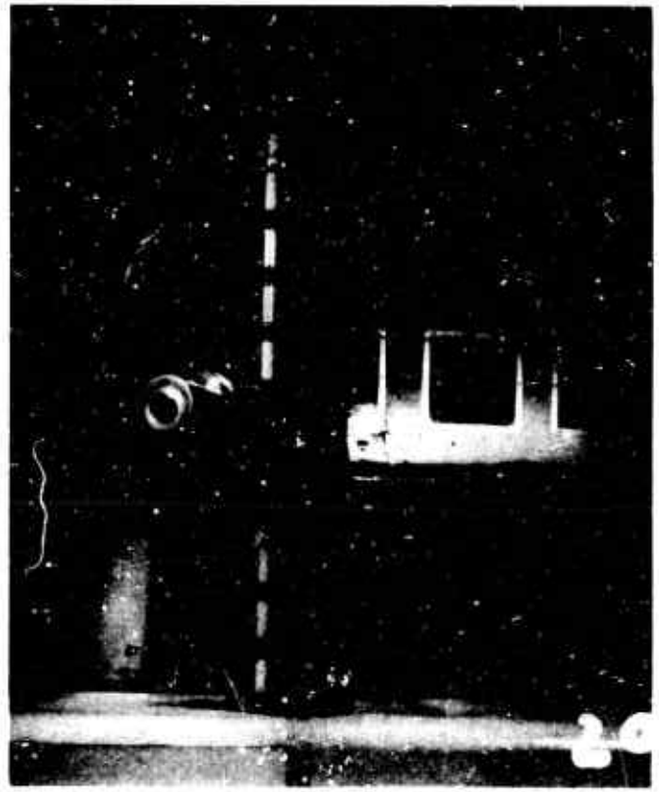

$\alpha_w = 60°$

Figure 66. (Continued).

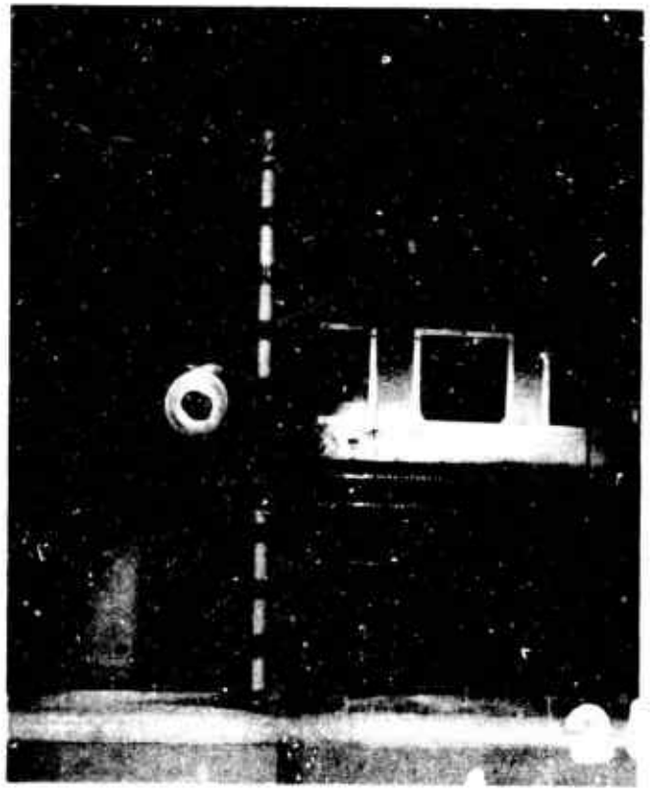

$\alpha_w = 70°$

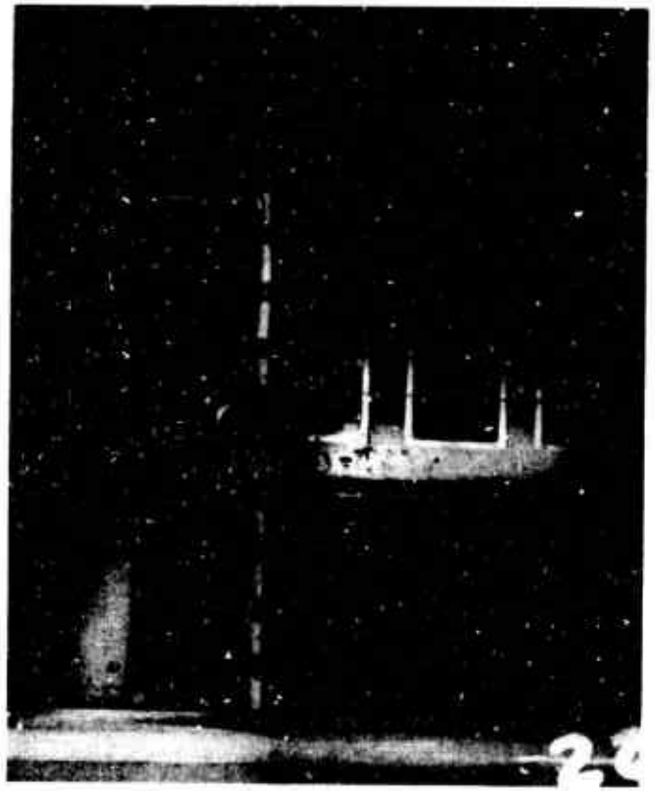

$\alpha_w = 80°$

Figure 66. (Continued).

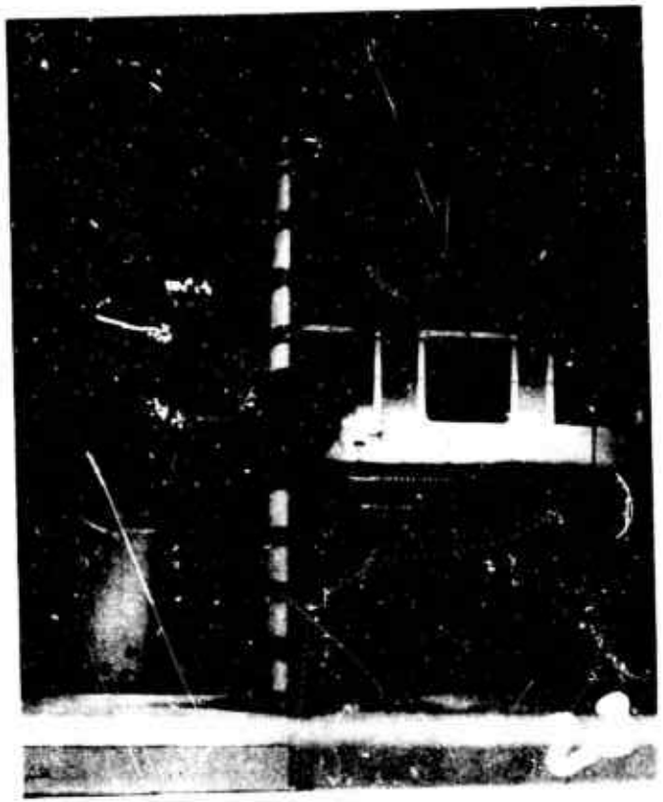

$\alpha_w = 90°$

Figure 66. (Continued).

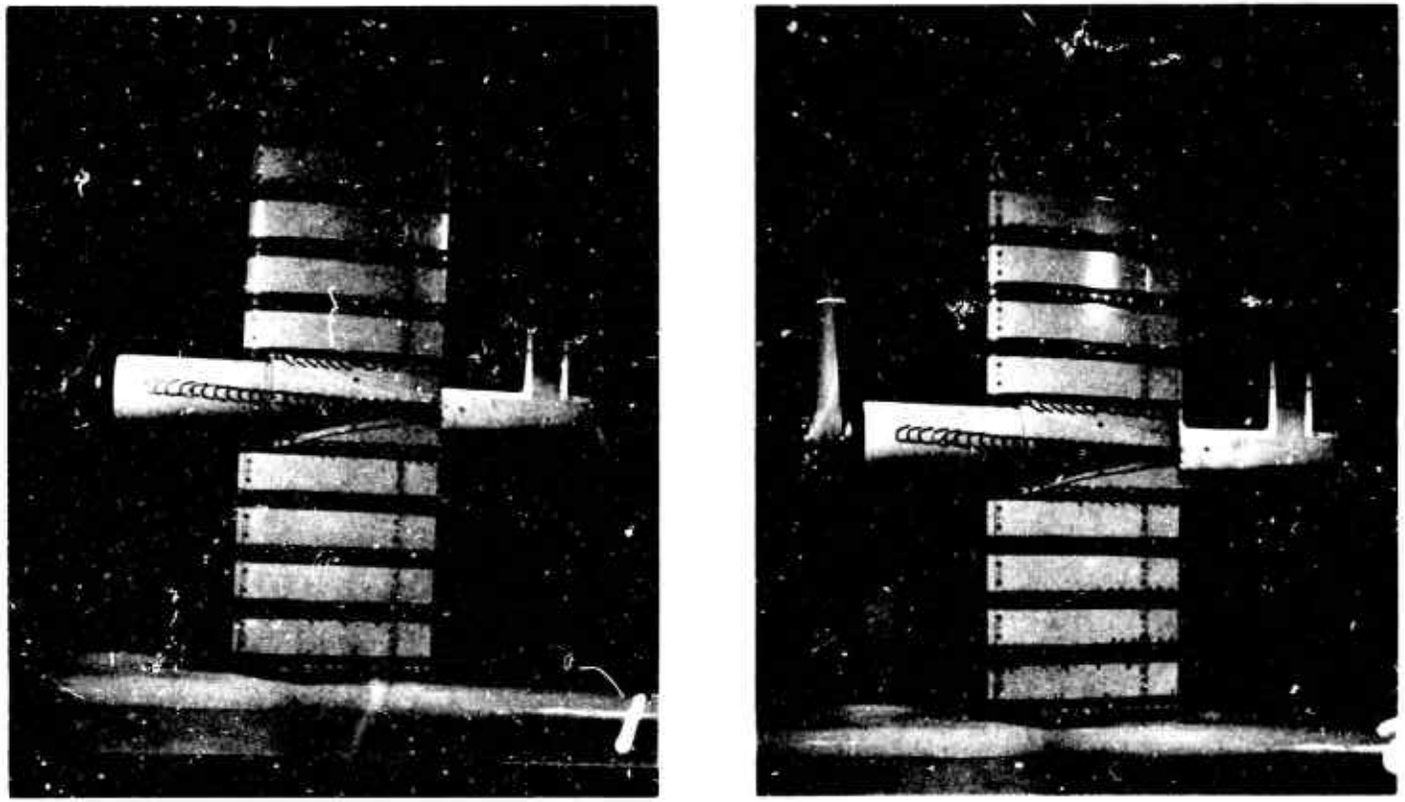

$\alpha_w = 0°$ $\alpha_w = 10°$

Figure 67. Flow Characteristics of Segmented Wing Model, $C_{T_s} = 0.97$. Configuration: P_1 W_1 B_1.

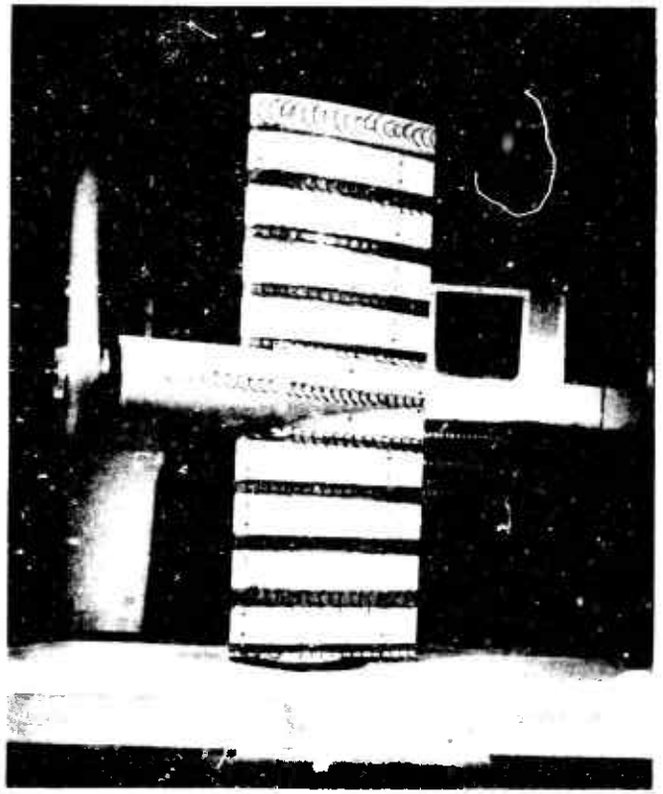

$\alpha_w = 15°$

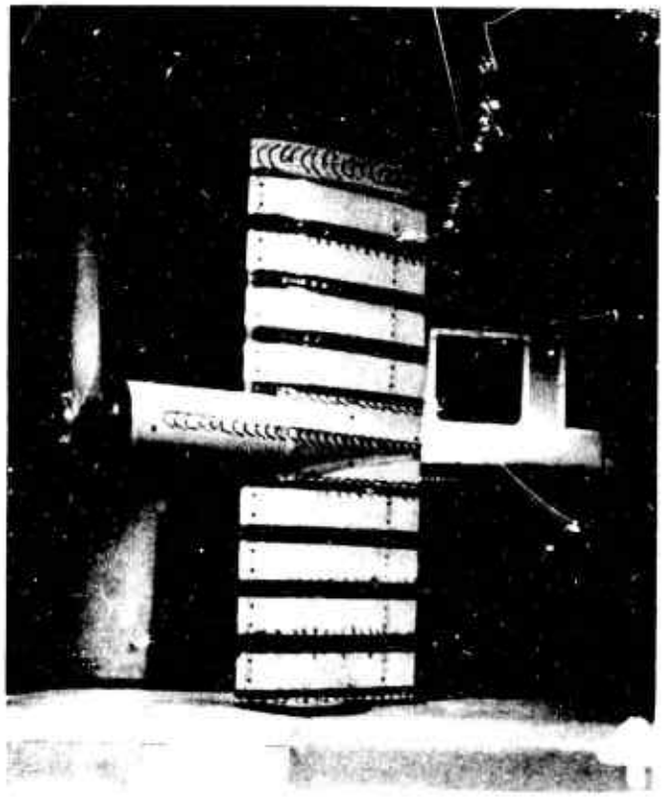

$\alpha_w = 20°$

Figure 67. (Continued).

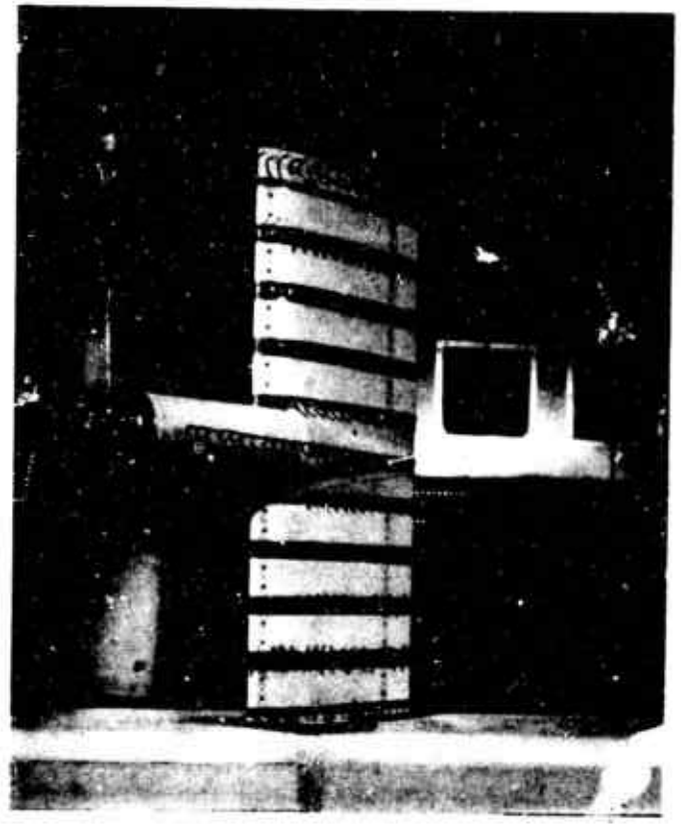

$\alpha_w = 30°$

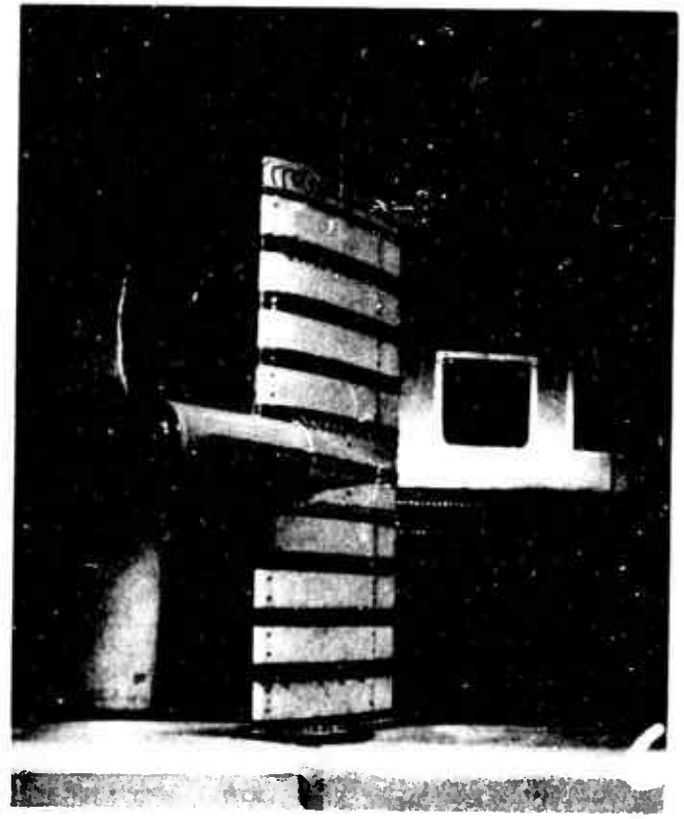

$\alpha_w = 40°$

Figure 67. (Continued).

$\alpha_w = 50°$

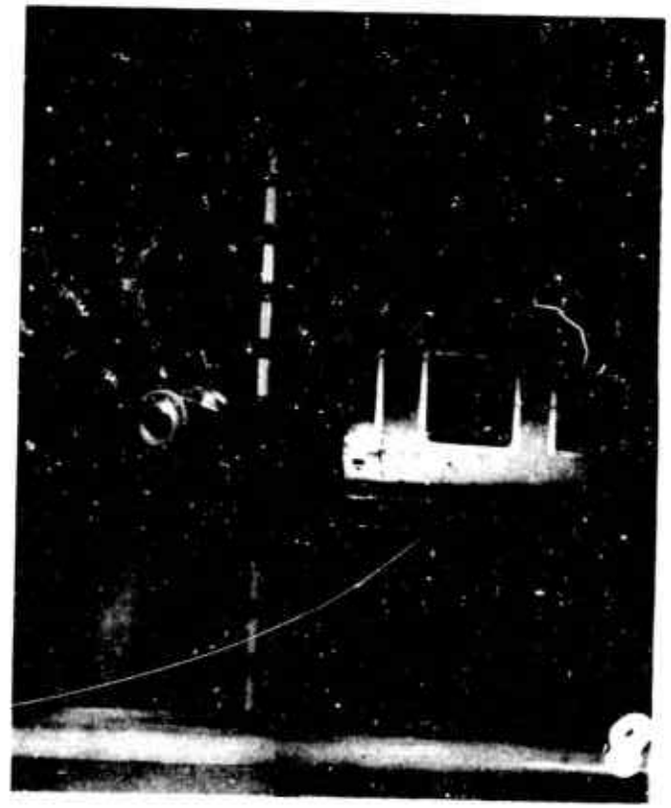

$\alpha_w = 60°$

Figure 67. (Continued).

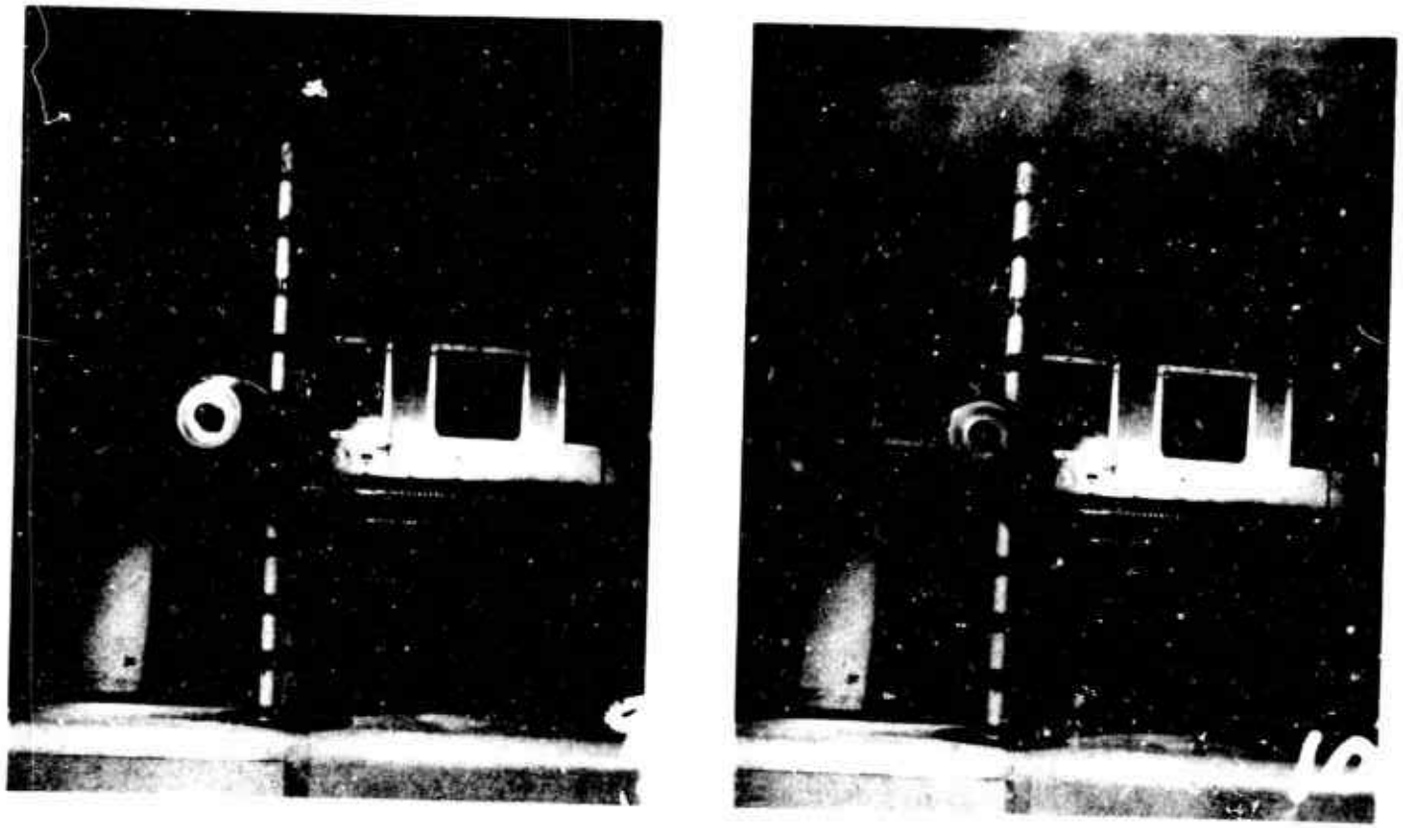

$\alpha_w = 70°$

$\alpha_w = 80°$

Figure 67. (Continued).

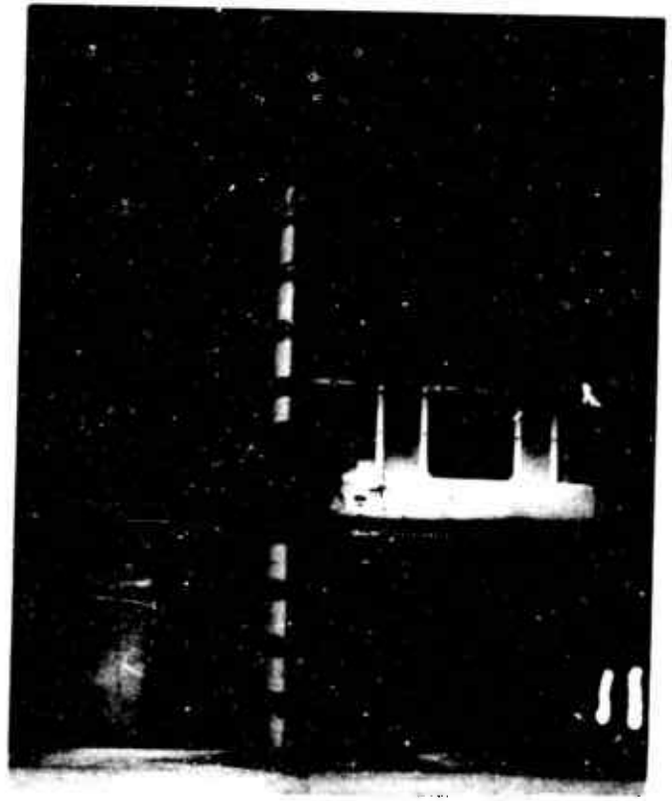

$\alpha_w = 90°$

Figure 67. (Continued).

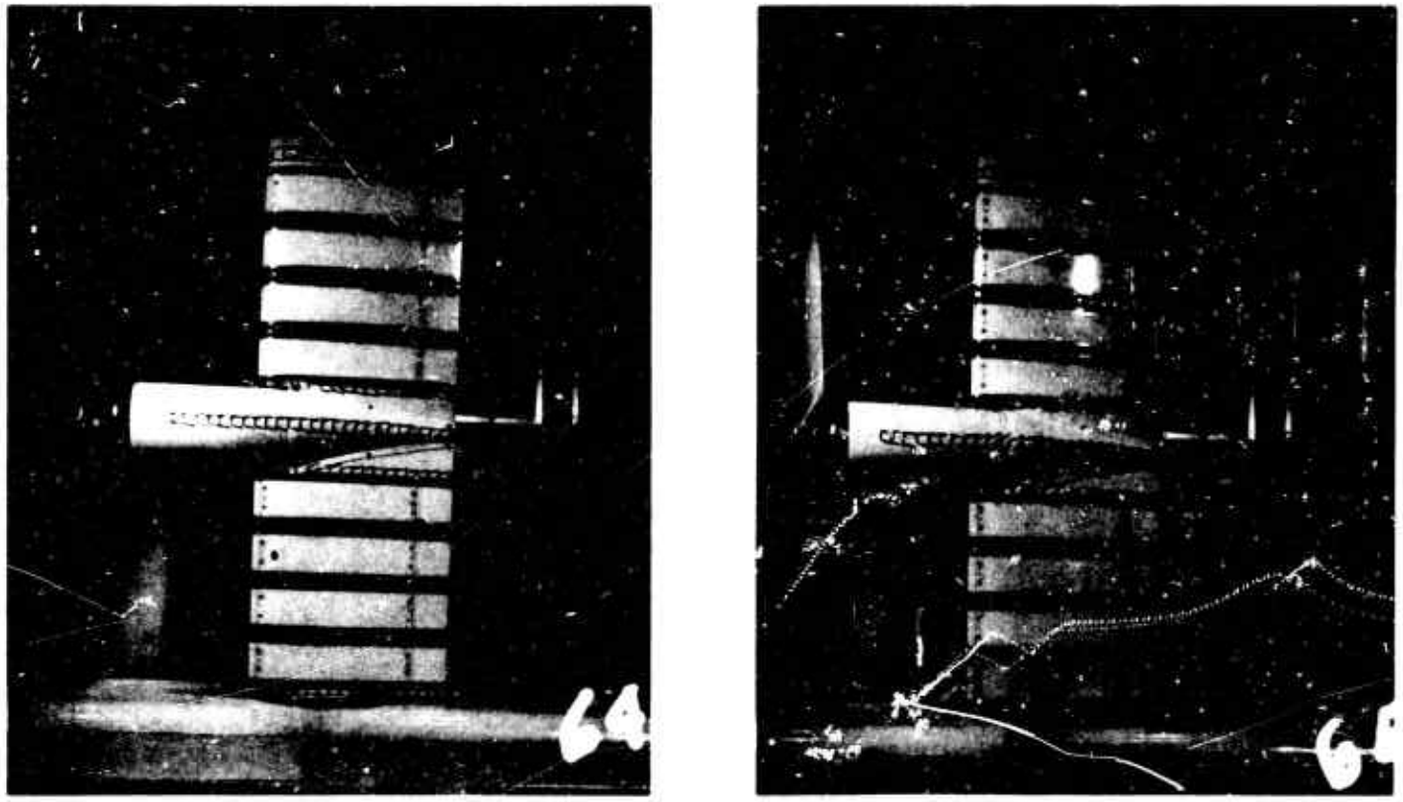

$\alpha_W = 0°$ $\alpha_W = 10°$

Figure 68. Flow Characteristics of Segmented Wing Model, $C_{T_s} = -0.10$. Configuration: P_1 W_1 F_1 B_1.

$\alpha_w = 15°$

$\alpha_w = 20°$

Figure 68. (Continued).

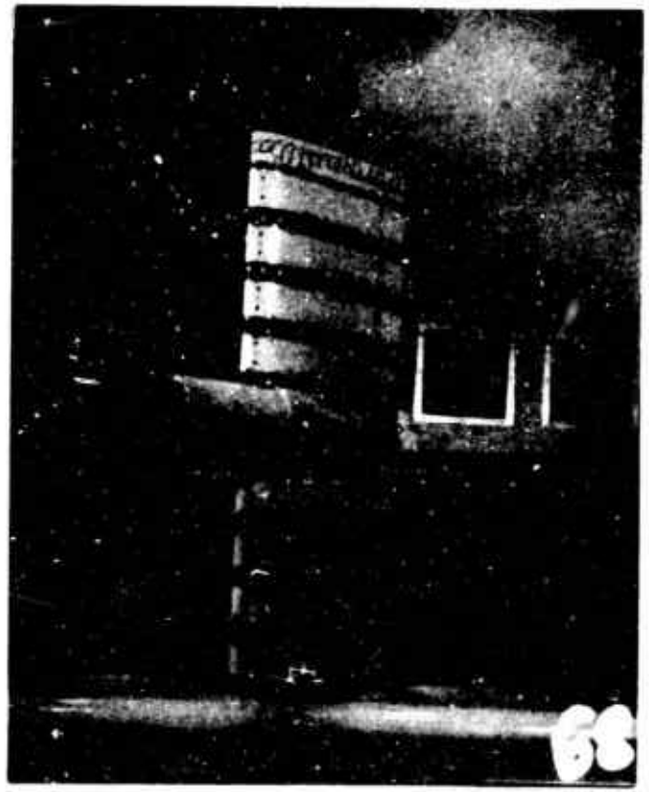

$\alpha_w = 30°$

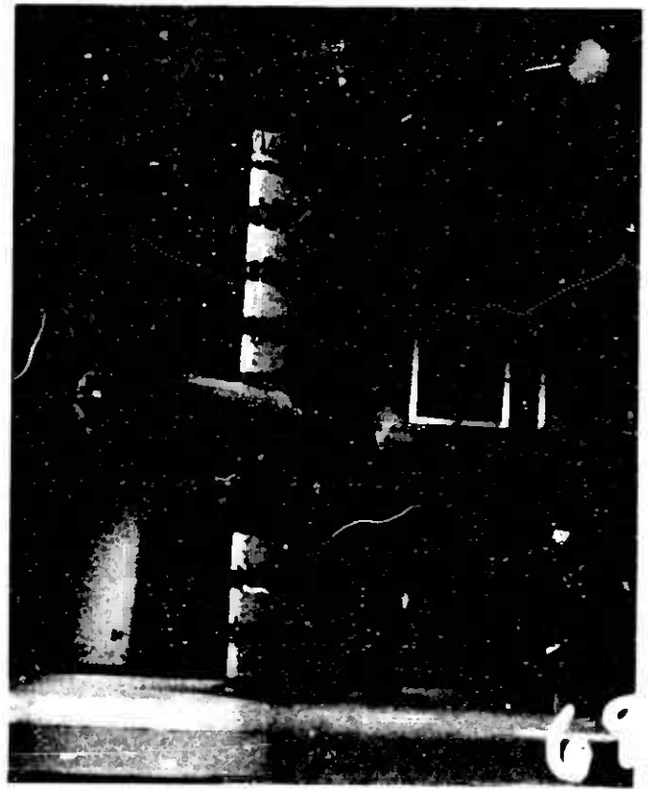

$\alpha_w = 40°$

Figure 68. (Continued).

$\alpha_w = 50°$

Figure 68. (Continued).

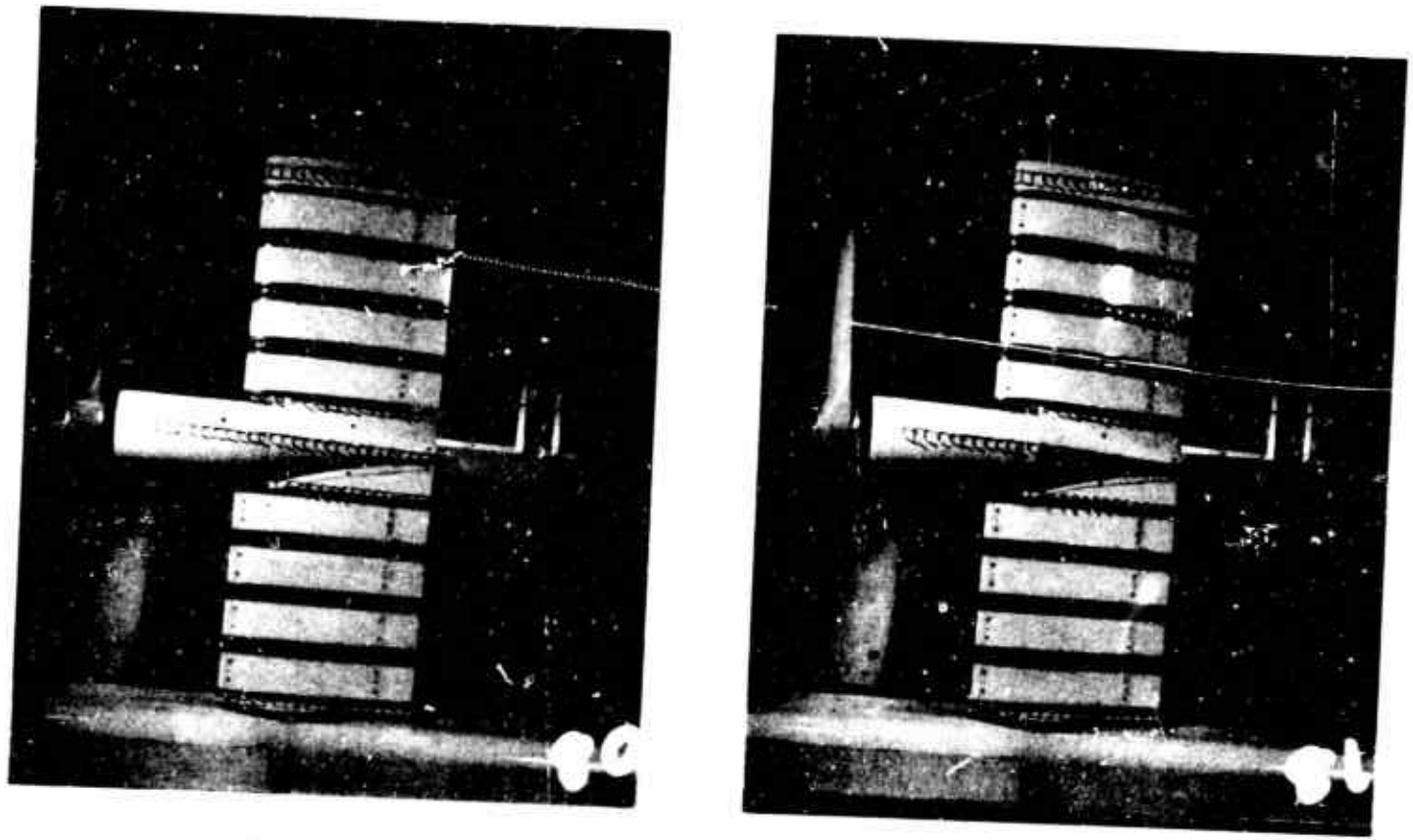

$\alpha_w = 0°$ $\alpha_w = 10°$

Figure 69. Flow Characteristics of Segmented Wing Model, $C_{T_s} = 0.46$. Configuration: P_1 W_1 F_1 B_1.

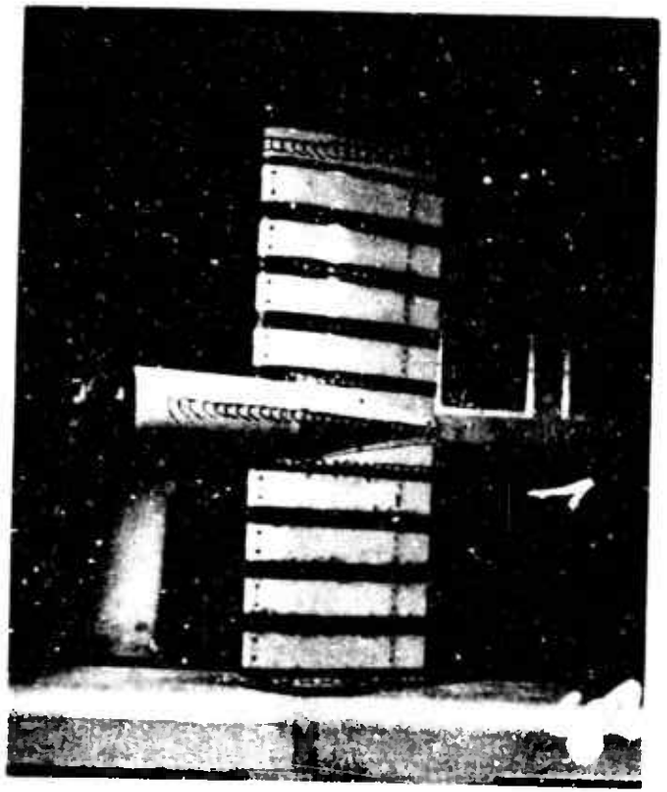

$\alpha_w = 15°$

$\alpha_w = 20°$

Figure 69. (Continued).

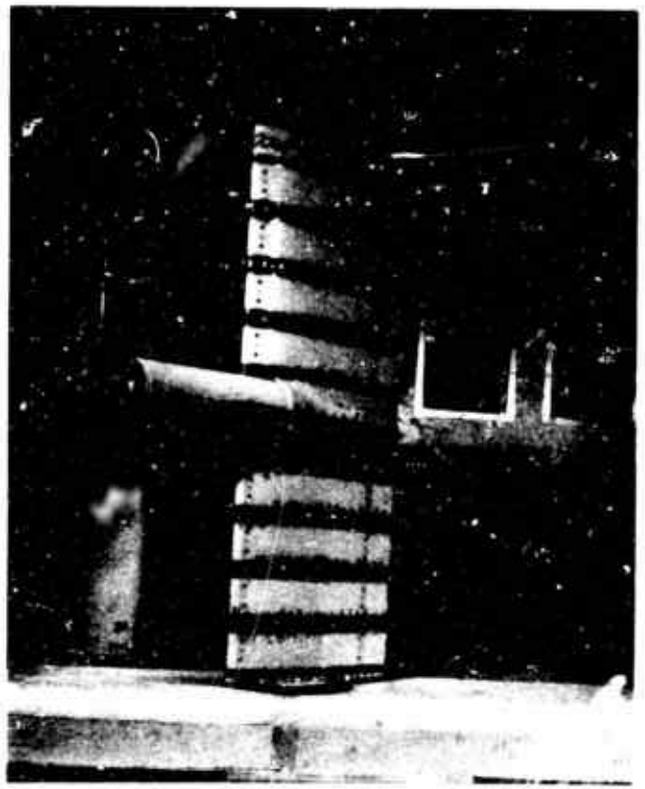

$\alpha_w = 30°$

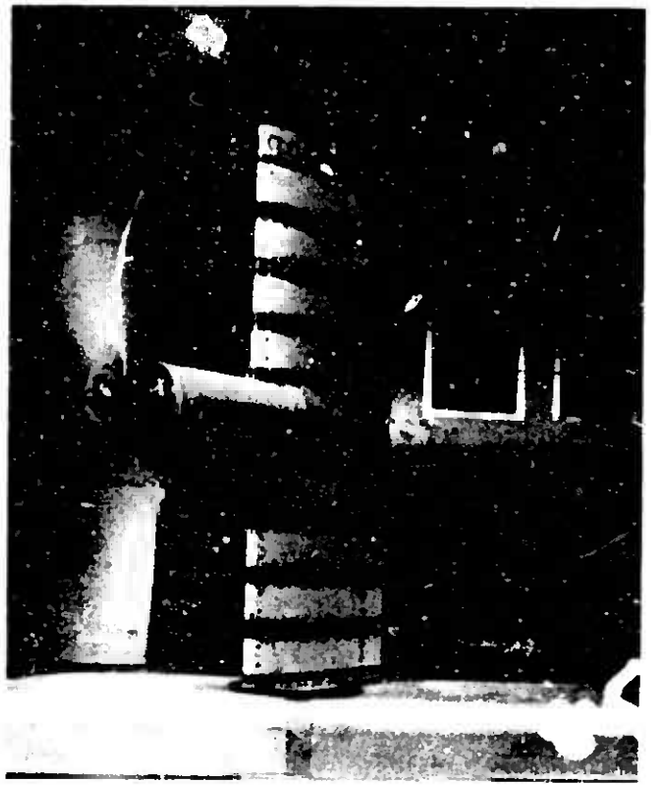

$\alpha_w = 40°$

Figure 69. (Continued).

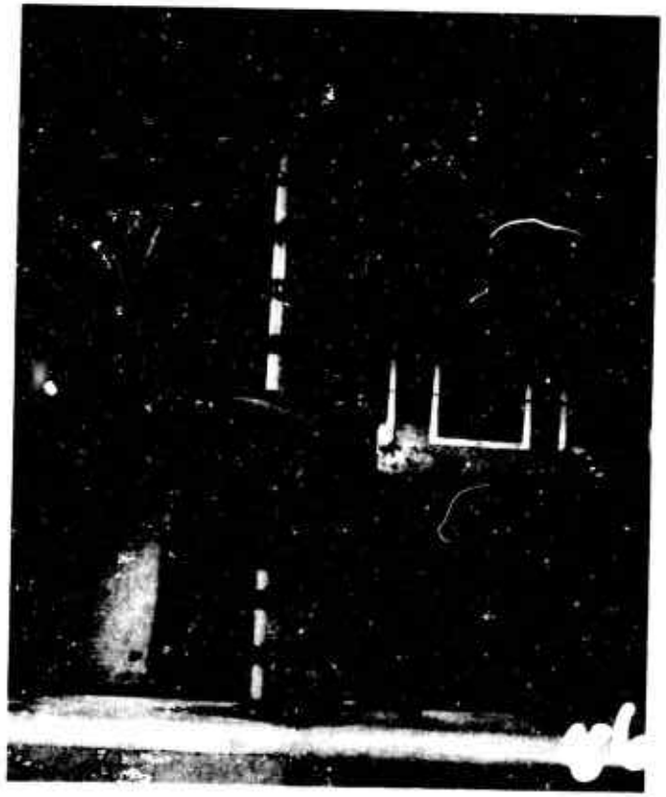

$\alpha_w = 50°$

Figure 69. (Continued).

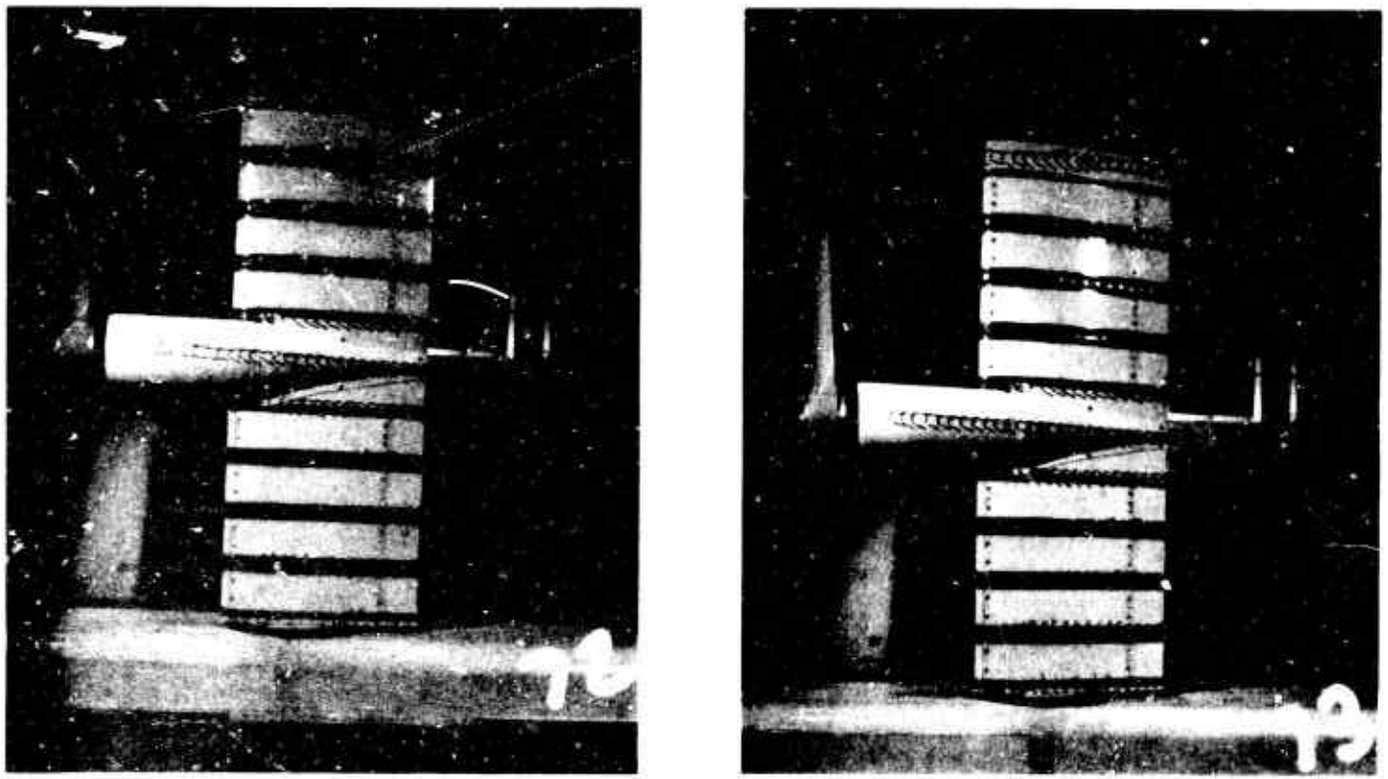

$\alpha_w = 0°$ $\alpha_w = 10°$

Figure 70. Flow Characteristics of Segmented Wing Model, $C_{T_s} = 0.9$. Configuration: P_1 W_1 F_1 B_1.

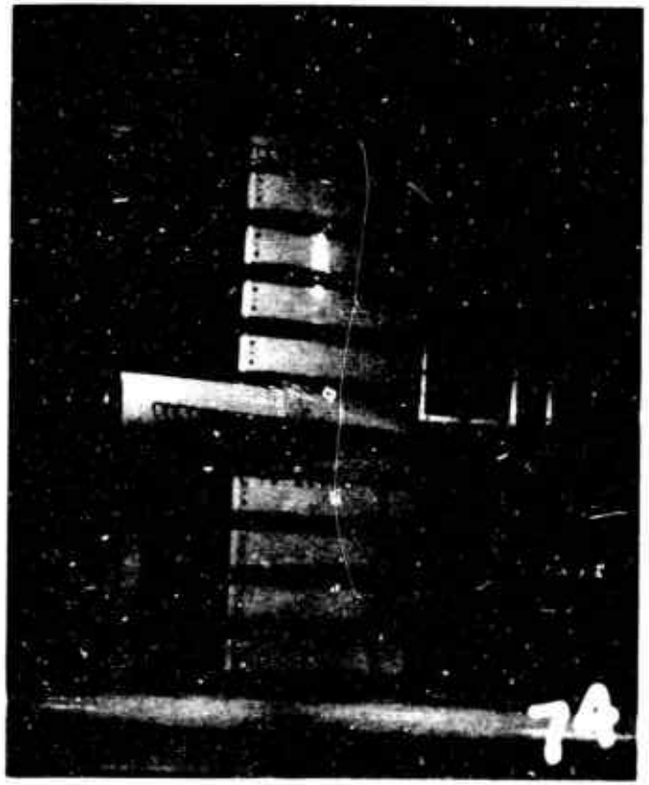

$\alpha_w = 15°$

$\alpha_w = 20°$

Figure 70. (Continued).

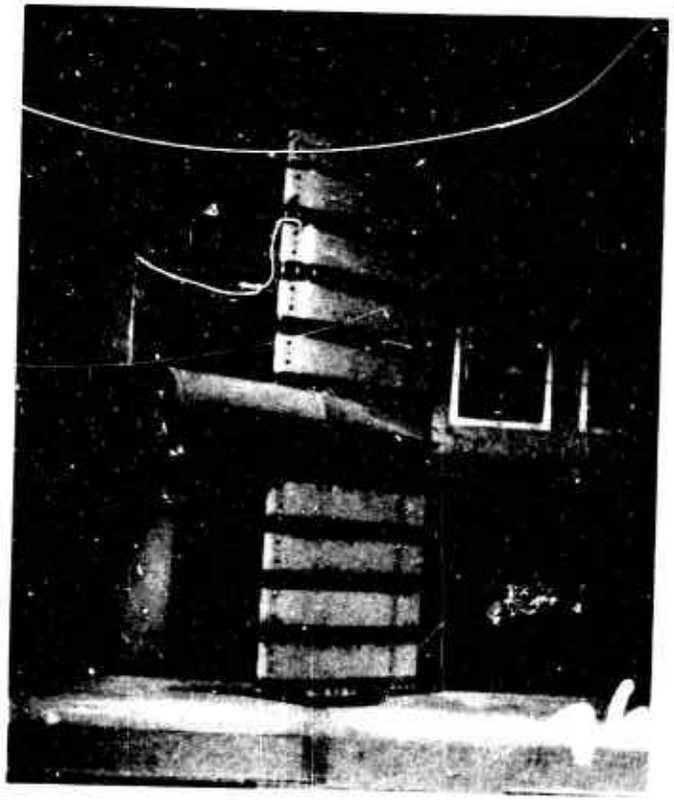

$\alpha_w = 30°$

$\alpha_w = 40°$

Figure 70. (Continued).

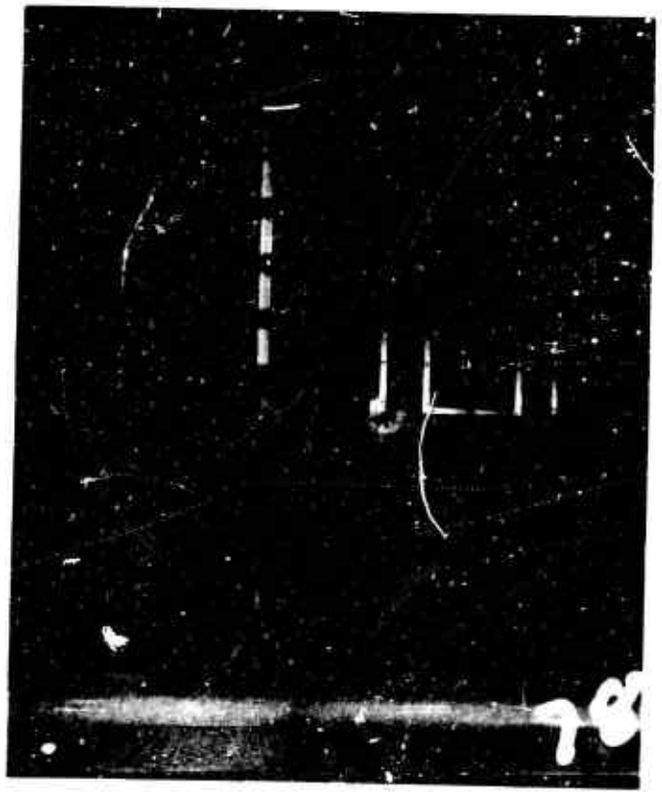

$\alpha_w = 50°$

$\alpha_w = 60°$

Figure 70. (Continued).

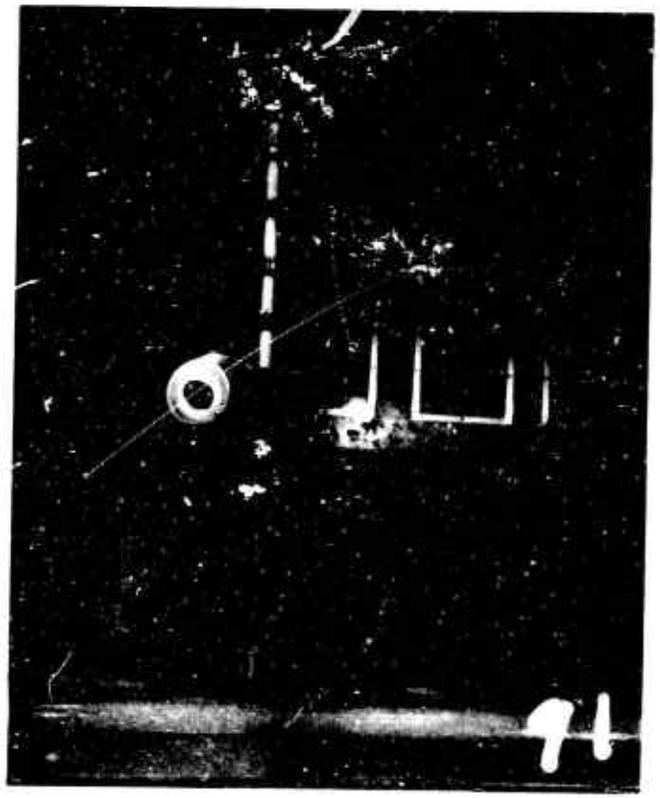

$\alpha_w = 70°$

$\alpha_w = 80°$

Figure 70. (Continued).

$\alpha_w = 90°$

Figure 70. (Continued).

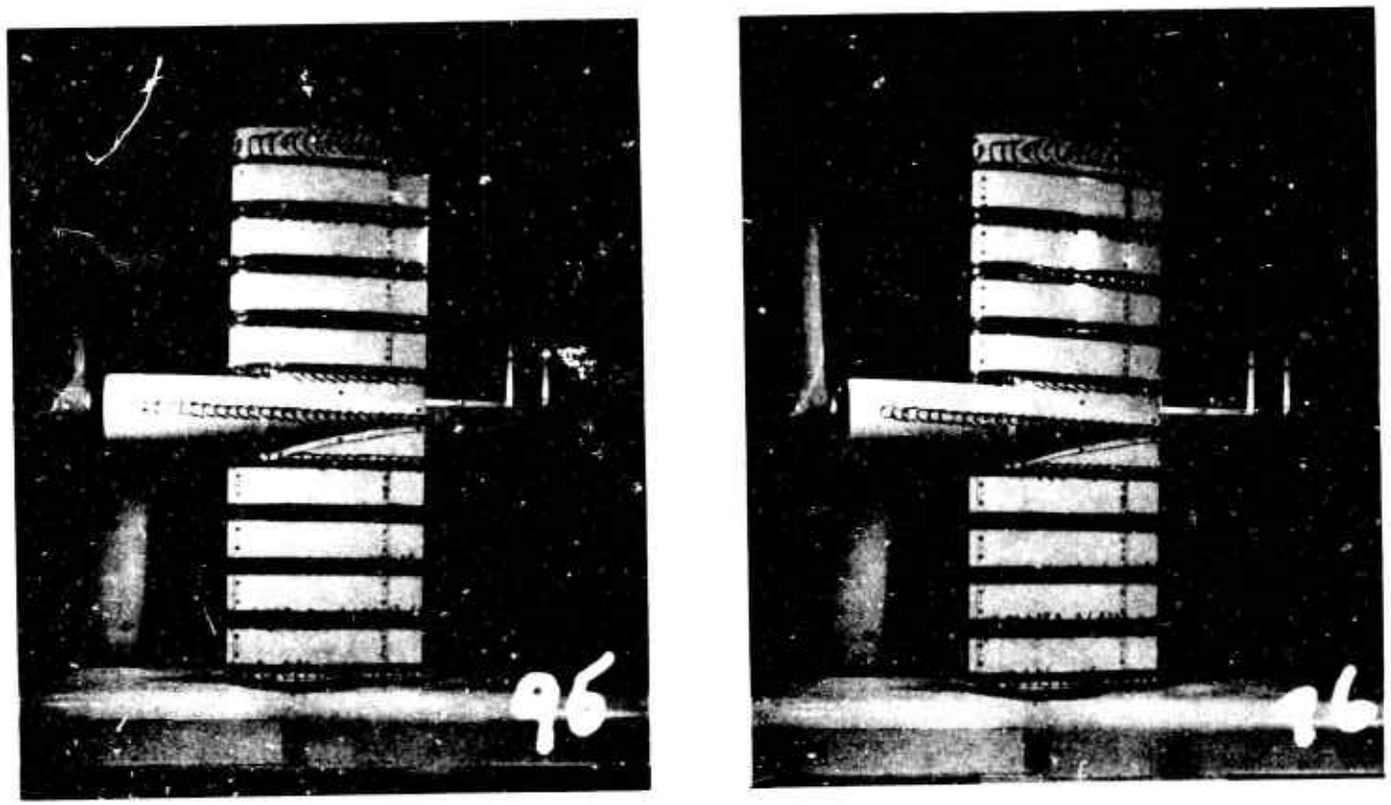

$\alpha_w = 0°$ $\alpha_w = 10°$

Figure 71. Flow Characteristics of Segmented Wing Model, $C_{T_S} = 0.97$. Configuration: P_1 W_1 F_1 B_1.

$\alpha_w = 20°$

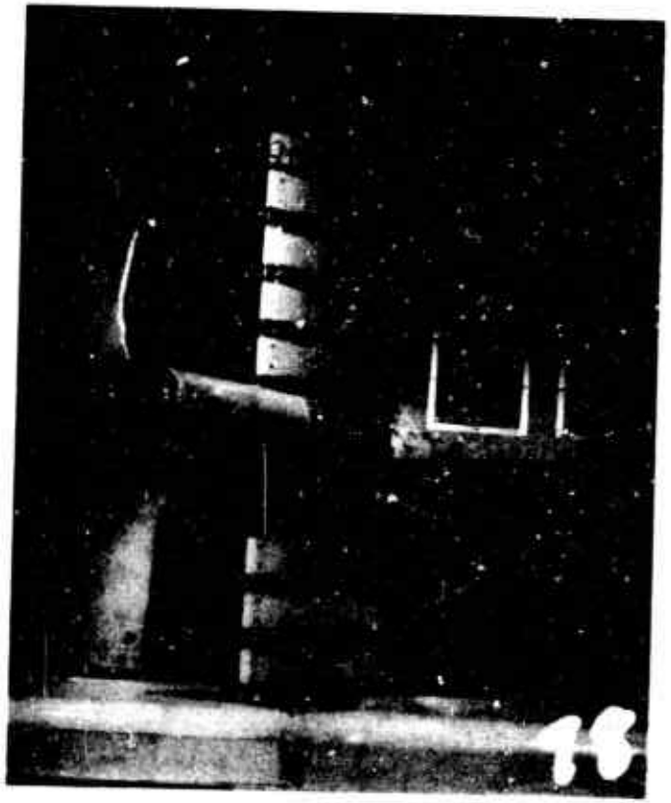

$\alpha_w = 40°$

Figure 71. (Continued).

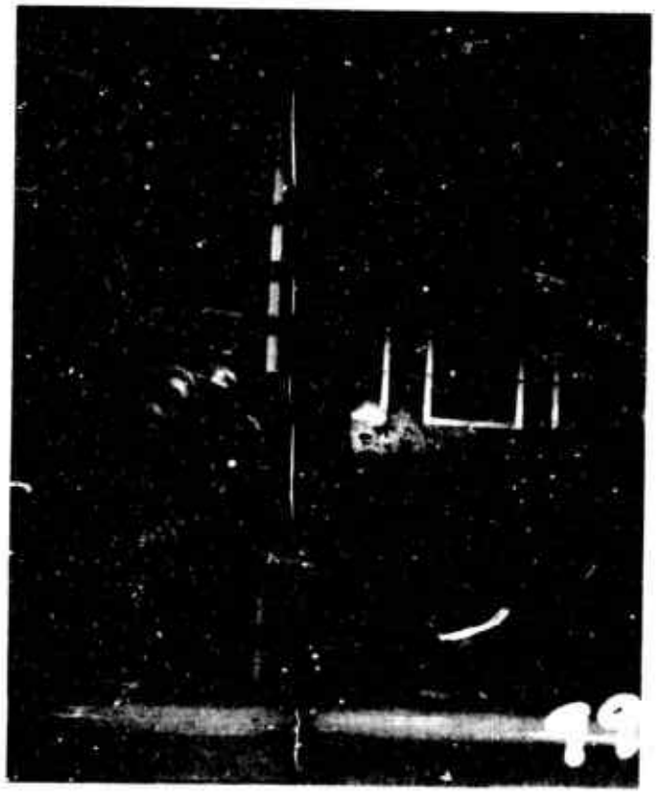

$\alpha_w = 60°$

$\alpha_w = 80°$

Figure 71. (Continued).

$\alpha_w = 90°$

Figure 71. (Continued).

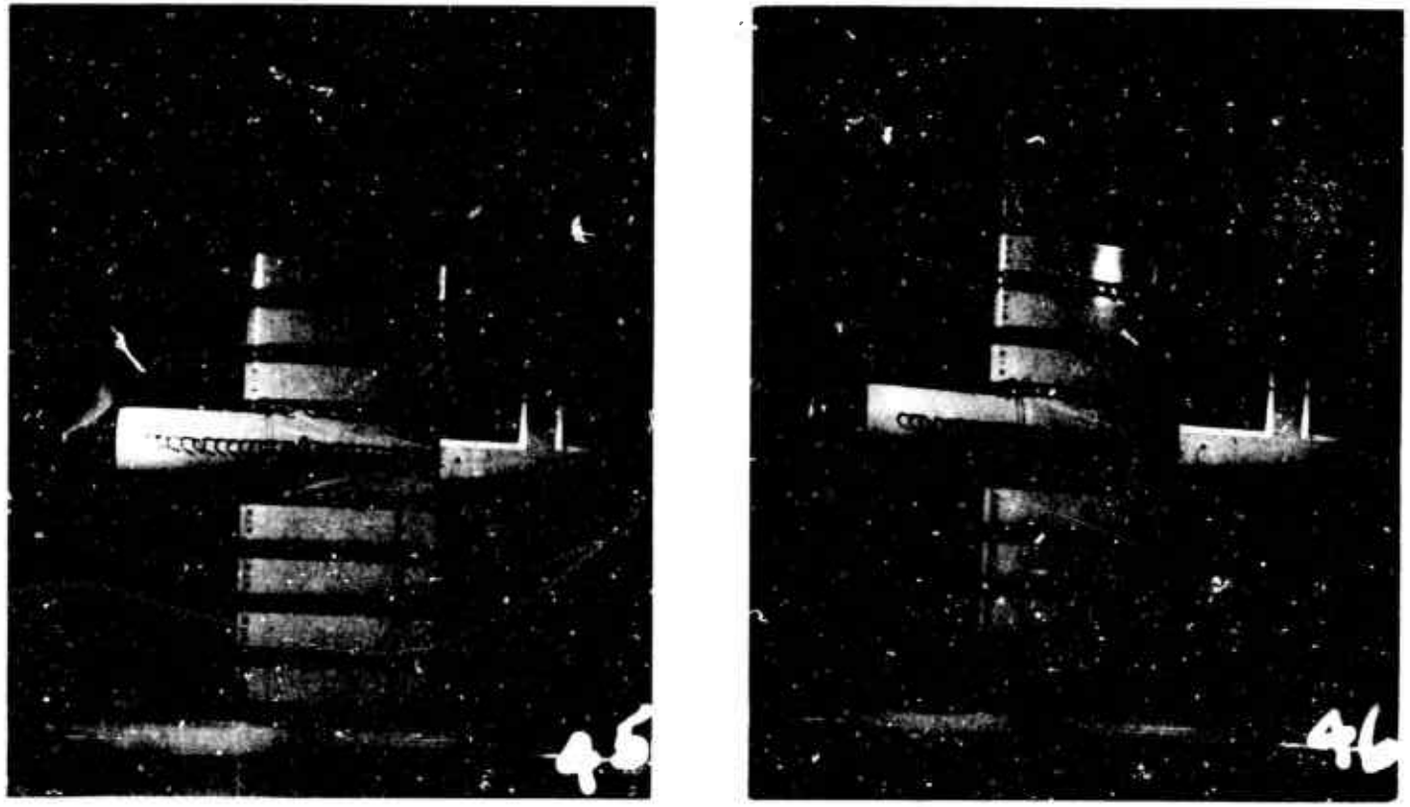

$\alpha_w = 0°$ $\alpha_w = 10°$

Figure 72. Flow Characteristics of Segmented Wing Model, $C_{T_s} = -0.50$. Configuration: P_2 W_1 B_1.

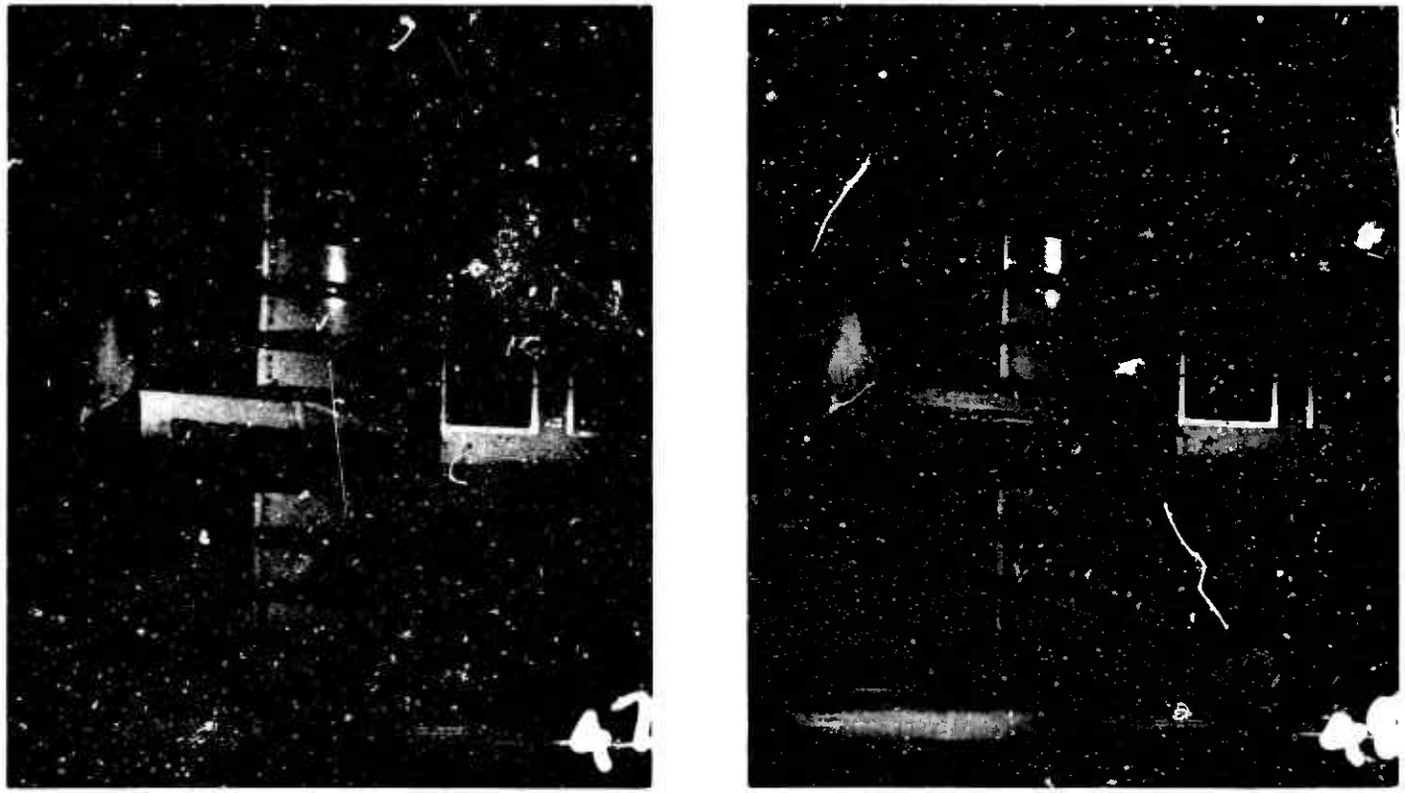

$\alpha_w = 15°$ $\alpha_w = 20°$

Figure 72. (Continued).

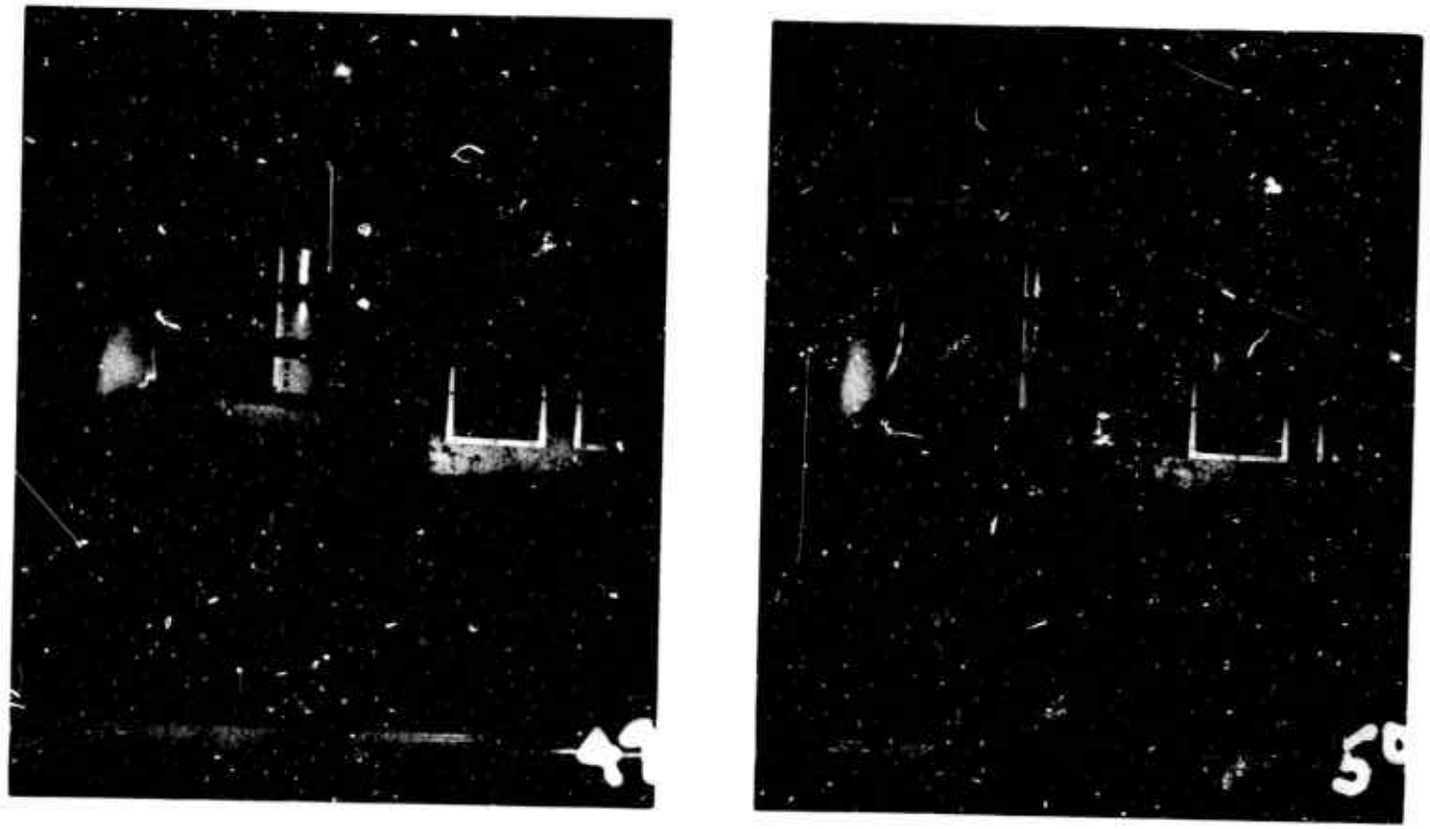

$\alpha_w = 30°$

$\alpha_w = 40°$

Figure 72. (Continued).

$\alpha_w = 50°$

Figure 72. (Continued).

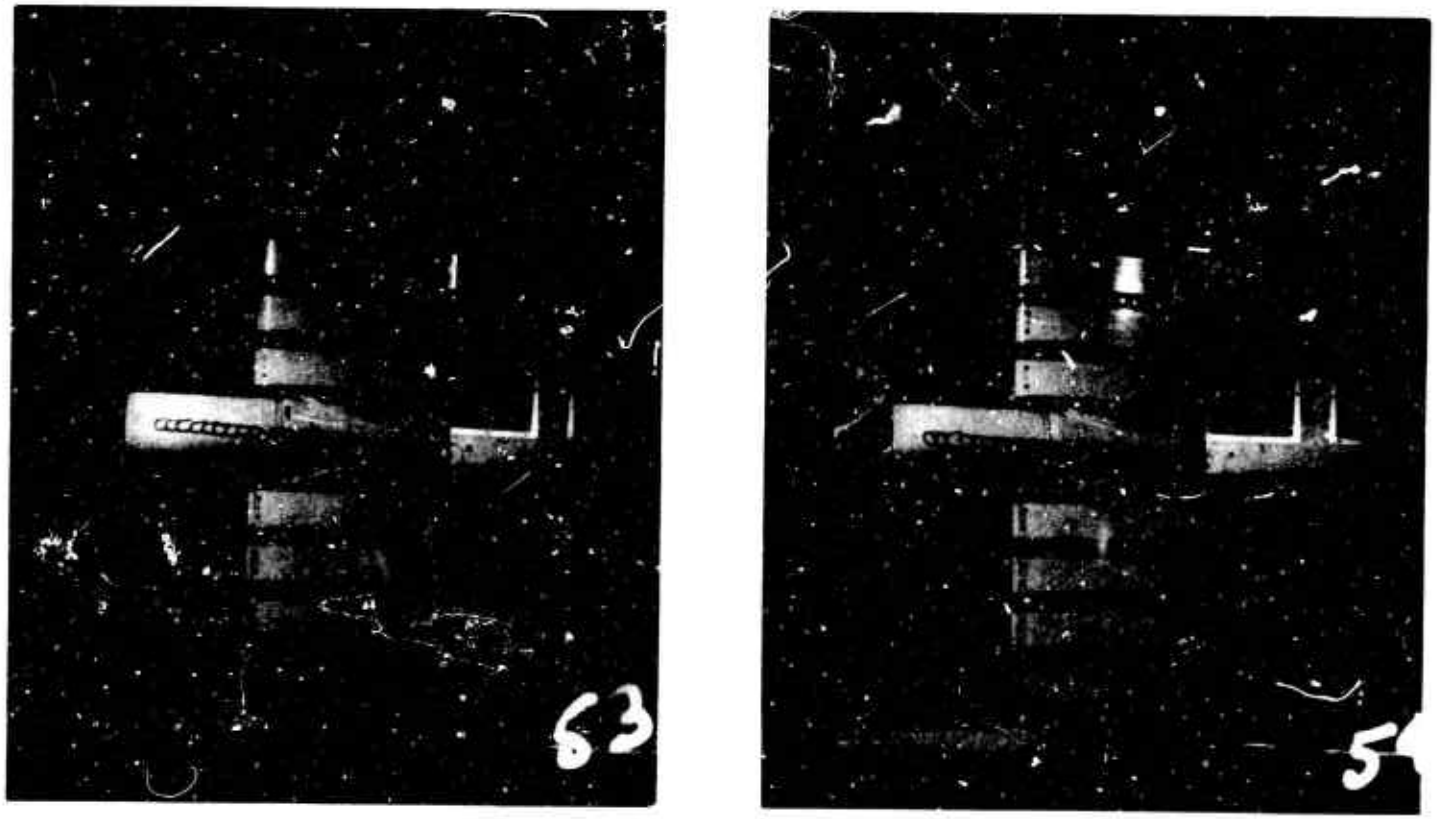

$\alpha_w = 0°$ $\alpha_w = 10°$

Figure 73. Flow Characteristics of Segmented Wing Model, $C_{T_s} = 0.50$. Configuration: P_2 W_1 F..

α_w = 15°

α_w = 20°

Figure 73. (Continued).

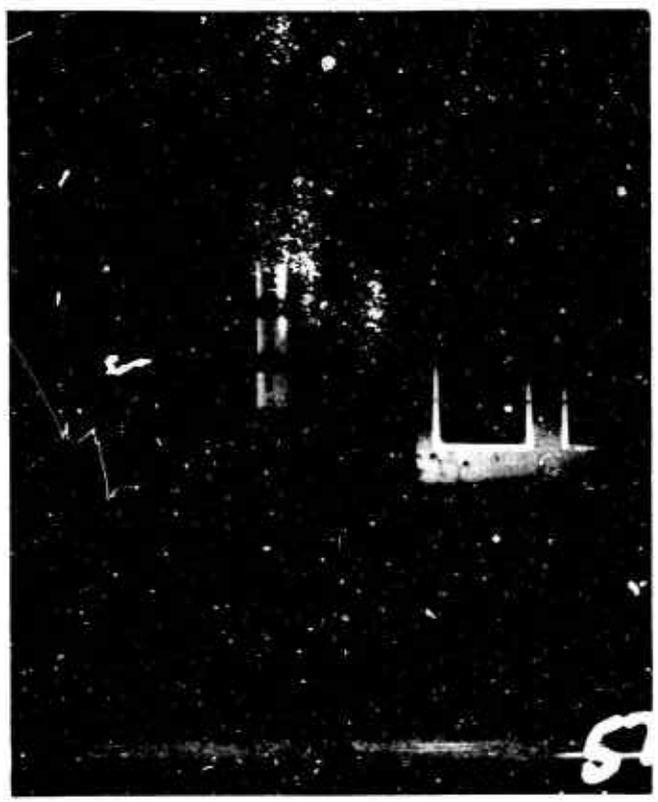

$\alpha_w = 30°$

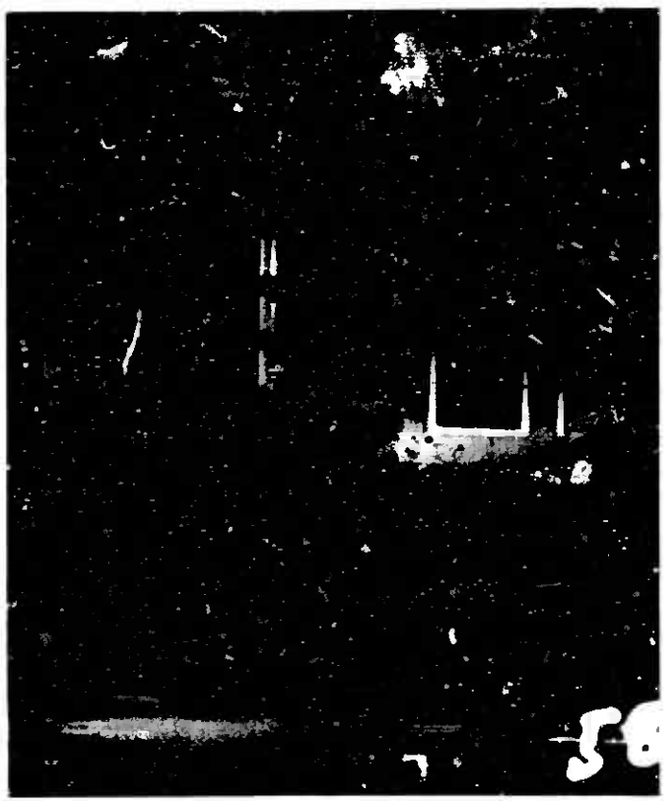

$\alpha_w = 40°$

Figure 73. (Continued).

$\alpha_w = 50°$

Figure 73. (Continued).

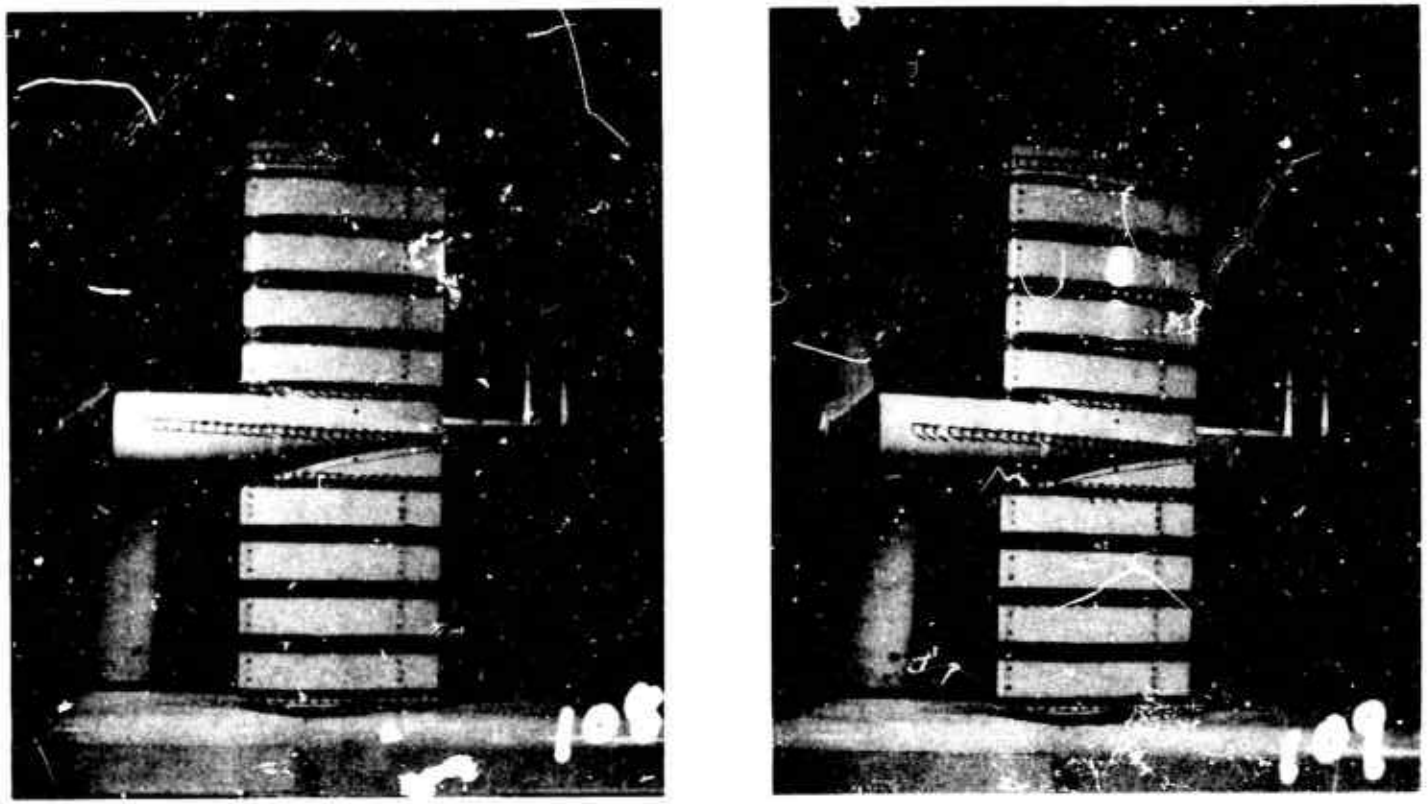

$\alpha_w = 0°$ $\alpha_w = 10°$

Figure 74. Flow Characteristics of Segmented Wing Model, $C_{T_s} = -0.40$. Configuration: P_2 W_1 F_1 B_1.

$\alpha_w = 15°$

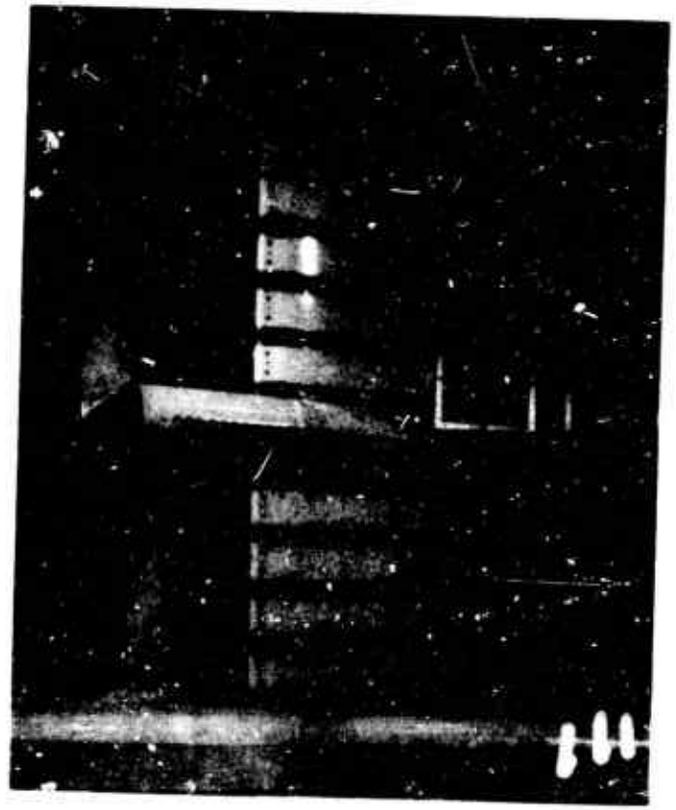

$\alpha_w = 20°$

Figure 74. (Continued).

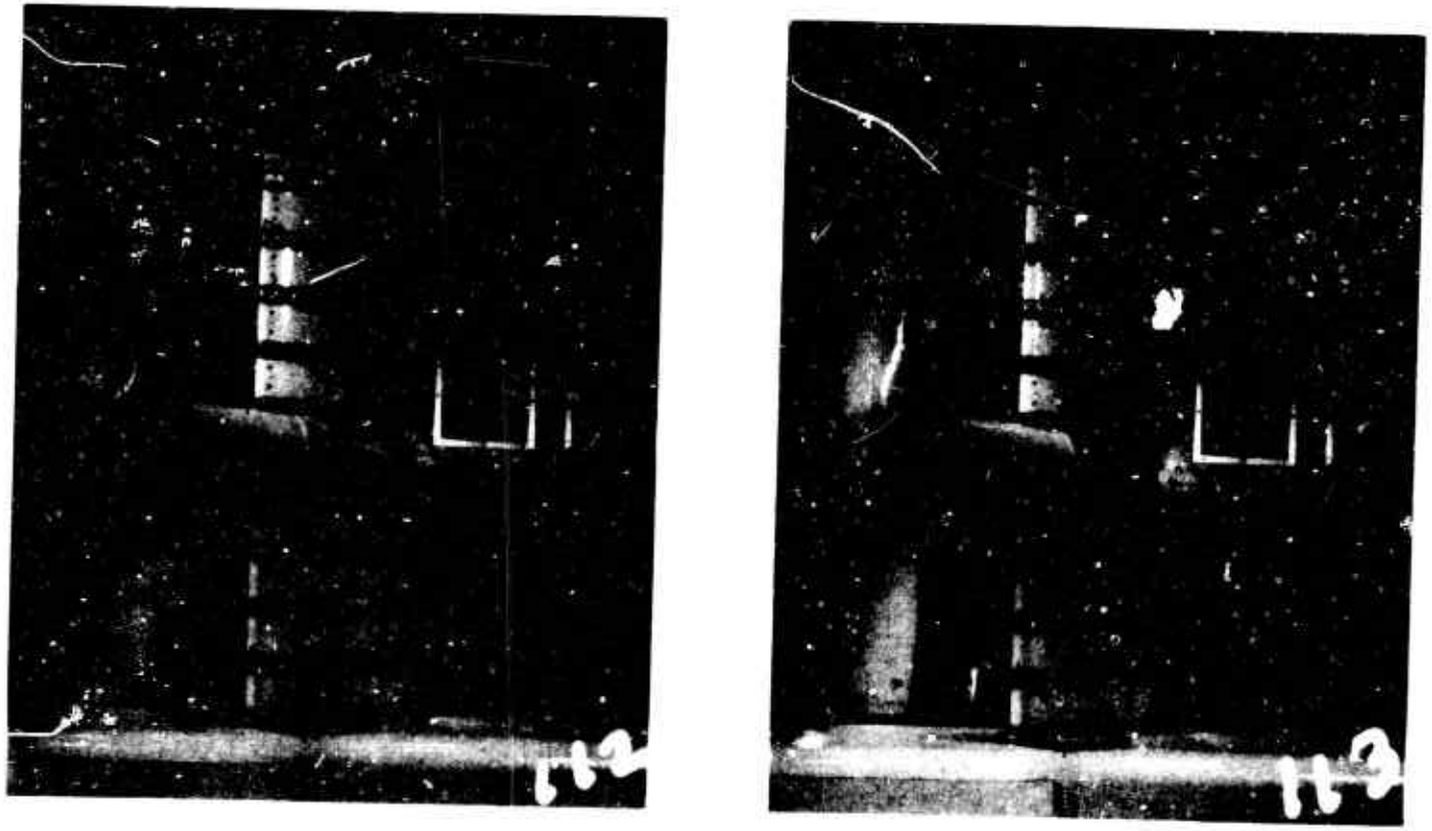

$\alpha_w = 30°$ $\alpha_w = 40°$

Figure 74. (Continued).

$\alpha_w = 50°$

Figure 74. (Continued).

Unclassified

Security Classification

DOCUMENT CONTROL DATA - R & D

(Security classification of title, body of abstract and indexing annotation must be entered when the overall report is classified)

1. ORIGINATING ACTIVITY *(Corporate author)*

Dynasciences Corporation
Blue Bell, Pennsylvania

2a. REPORT SECURITY CLASSIFICATION

Unclassified

2b. GROUP

3. REPORT TITLE

Investigation of Propeller Slipstream Effects on Wing Performance

4. DESCRIPTIVE NOTES *(Type of report and inclusive dates)*

Final Report

5. AUTHOR(S) *(First name, middle initial, last name)*

George, M.
Kisielowski, E.

6. REPORT DATE	7a. TOTAL NO. OF PAGES	7b. NO. OF REFS
November 1967	212	7

8a. CONTRACT OR GRANT NO.	9a. ORIGINATOR'S REPORT NUMBER(S)
DA 44-177-AMC-394(T)	USAAVLABS Technical Report 67-67
b. PROJECT NO. Task 1F125901A14231	9b. OTHER REPORT NO(S) *(Any other numbers that may be assigned this report)* Dynasciences Report No. DCR-234
c.	
d.	

10. DISTRIBUTION STATEMENT

This document has been approved for public release and sale; its distribution is unlimited.

11. SUPPLEMENTARY NOTES	12. SPONSORING MILITARY ACTIVITY
	U.S. Army Aviation Materiel Laboratories, Fort Eustis, Virginia

13. ABSTRACT

A theoretical and experimental study was conducted to determine the effects of propeller slipstream on wing performance. Previously developed theoretical analyses were expanded and modified to account for radial variation of the propeller slipstream velocity.

The experimental program consisted of wind tunnel tests conducted with a motor-propeller system mounted on a semispan wing model. The wing model utilized has a chord to propeller diameter of 0.46, an aspect ratio of 6.37 (3.18 for semispan), a taper ratio of 1.0, and a NACA 0015 airfoil section. The wing model has eight floating wing segments with and without a 45-degree simulated split flap. Located within each floating wing segment is a three-component strain gage balance to provide measurements of lift, drag, and pitching moment. The measurements of total wing lift, drag, and pitching moment were obtained with the six-component main wind tunnel balance. The test data obtained included the effects of the variation of propeller slipstream velocity by utilizing two propellers of different geometries. Propeller rotation for all tests was down at the wing tip. The experimental and theoretical results are compared; in general, good correlation is observed.

The results obtained from this investigation substantiate the feasibility of the segmented wing approach for the measurement of the spanwise variation of aerodynamic forces and moments. In addition, it is also shown that significant increases in wing lift can be achieved by suitable propeller and wing design.

DD FORM 1 NOV 68 1473 REPLACES DD FORM 1473, 1 JAN 64, WHICH IS OBSOLETE FOR ARMY USE.

Unclassified

Security Classification

Unclassified

Security Classification

14. KEY WORDS	LINK A		LINK B		LINK C	
	ROLE	WT	ROLE	WT	ROLE	WT
Propeller Slipstream-wing Interaction Slipstream Analysis Wind Tunnel Tests Spanwise Distribution Lift, Drag, Pitching Moment						

Unclassified

Security Classification